Gold Copper Based Catalysts in the Development of Direct Formic Acid Fuel Cells

By:

Charles Ijogbemeye Oseghale

A thesis submitted in partial fulfilment of the requirements for the degree of
Doctor of Philosophy

The University of Sheffield
Faculty of Engineering
Department of Chemical and Biological Engineering

December 2017

Abstract

There is a growing awareness of the need for fundamental and applied research in energy storage and conversion due to the global climate issue with energy sources, environmental and human health challenges. In this work, development of a new synthesis route for catalysts, physicochemical and electrochemical research is reported for direct formic acid fuel cells. The synthesis method is based on the sodium borohydride reduction of (Pd^{2+}, Cu^{2+}, Au^{3+}) precursor, stabilised by polyvinylpyrrolidone for the preparation of a highly stable catalysts with, well-controlled particle size distribution. The surface and bulk properties of the catalysts were characterised by scanning electron microscopy (SEM), transmission electron microscopy (TEM), X-ray diffraction (XRD), energy dispersive X-ray spectroscopy (EDS), atomic force microscopy (AFM), and electrochemically by cyclic voltammetry and chronoamperometry.

The results obtained for Pd-C showed that a uniform XRD estimated the size distribution in a narrow particle size range with an average size of 1.4 ± 0.11 nm. Electrochemical studies for formic acid electrooxidation reveals that Pd-$C_{H3BO3\ +\ NH4F(21wt.\%)}$ presents superior catalytic activity (over 44 %) than that of the Pd-$C_{PVP(43.5wt.\%)}$ synthesis route. For an equivalent electrode paste, Pd-$C_{PVP(43.5wt.\%)}$ exhibited a greater electrochemical surface area (ECSA) than Pd-$C_{PVP(43.5wt.\%)}$ but achieved a lower utilisation of palladium.

The electrooxidation of the catalyst shows three times higher activity for formic acid oxidation than commercial gold nanoparticles dispersed on the carbon support. The enhanced catalytic performance is attributed to the electronic synergistic effect of copper and the specific gold structure promoting oxidation of adsorbed intermediate species. Overall, these findings have significant implications for practical direct formic acid fuel cells (DFAFCs) technology by the controlled Au-shell Cu-core anode catalysts application. Overall, palladium catalysts demonstrated better electrocatalytic activities for formic oxidation than Au and gold copper catalysts. This work is part of the initial stages of the effort to develop a low-cost gold-catalyst for DFAFCs technology.

Dedication

To all the great teachers

- To my parents: Philip Ebhodaghe Oseghale and Margaret Ebosele Oseghale

Acknowledgements

I would like to express my gratitude to my supervisors Professor Peter J Hall and Professor Peter Styring for their help, guidance and support throughout the duration of this research. I also appreciate all the professional opportunities provided by Professor Hall, and the direction and involvement in shaping my career path.

Going back in time, I appreciate the people and place that made possible from the early beginning my accomplishments, but will not mention names for the list is very long. I would like to thank them for their invaluable guidance, advice, encouragement and constructive ideas without which this work would not be successfully accomplished.

I would like to acknowledge and with sincere gratitude thank the University of Port Harcourt and the Nigerian Government for allowing me to conduct my research and providing the financial assistance.

I would like to thank my fellow PhD students and the Postdoctoral researchers I shared time with for making the last 4 years enjoyable. I would like to thank Miss Alison R Thompson for all her help with proofreading my thesis. Your suggestions, revisions and the extra effort I know you gave have greatly enhanced the quality of the thesis.

Finally, I would like to express my wholehearted gratitude to my family, especially my children Oseluonamen and Omoefe who always welcome me home with smiles. Ose will ask me 'Daddy, what's you doing in the office?' For the motivation and deepest joy I gained from them daily, knowing I must have a good response to Ose's question. Most importantly, special appreciation to my wife, Margaret for her support, patience and endurance throughout my Ph.D. research.

To all, I will always be indebted.

Table of Contents

List of Tables

List of Figures

Nomenclature

Atomic force microscopy	*AFM*
Balance-of-plant	*BOP*
Capital expenditure	*CAPEX*
Chemical surface area	*CSA*
Chronoamperometry	*CA*
Counter electrode	*CE*
Cross sectional surface area	*CSSA*
Cyclic Voltammetry	*CV*
Direct formic acid fuel cell	*DFAFC*
Direct liquid fuel cells	*DLFCs*
Direct methanol fuel cell	*DMFC*
Electrochemical active surface area	*ECSA*
Electrochemical energy technologies	*EETs*
Energy dispersive spectroscopy	*EDS*
Face-centered cubic	*fcc*
Flame atomic absorption spectroscopy	*AAS*
Formic acid oxidation	*FAO*
Fuel cells	*FCs*
Gold nanoparticles	*AuNPs*
High angle-annular dark-field scanning TEM	*HAADF-STEM*
High-Resolution transmission electron microscopy	*HRTEM*
Hydrogen adsorption-desorption	*HAD*
Inductively coupled plasma atomic emission spectroscopy	*ICP-AES*
Inductively coupled plasma mass spectroscopy	*ICP-MS*
Internal diameter	*ID*
International Centre for Diffraction Data	*ICDD*
Outer diameter	*OD*

Oxygen reduction reaction	*ORR*
PEM fuel cell	$H_2\text{-}PEMFC$
Platinum group metals	*PGMs*
Poly (diallyl dimethyl ammonium chloride)	*PDDA*
Polymer electrolyte membrane	*PEM*
Polyvinyl alcohol	*PVA*
Polyvinylpyrrolidone	*PVP*
Reversible hydrogen electrode	*RHE*
Scanning electron microscopy	*SEM*
Surface area (XRD)	S_{XRD}
Tetrahydro methyl phosphonium chloride	*THMP*
Tetrahydroxymethyl phosphonium chloride	*THPC*
Texture coefficient of the facet [hkl]	TC_{hkl}
Thermogravimetric analysis	*TGA*
Three-electrode electrochemical cell	*3-EEC*
Transmission electron microscopy	*TEM*
Working electrode	*WE*
X-ray diffraction	*XRD*

Symbols

E^o	Ideal (or standard) potential of the cell
ΔG^o	Change in Gibbs free energy
E_{anode}	Half-cell potential at the anode
$E_{cathode}$	Half-cell potential at the cathode
η	Efficiency
η_{thermo}	Thermodynamic efficiency
$\eta_{voltage}$	Potential efficiency
η_{fuel}	Fuel efficiency
ϑ	Scan rate
n	Number of electrons
λ	Specific wavelength
hkl	Miller's indices
δ	Rayleigh criterion minimum distance
μ	Rayleigh criterion reflection index
d_{hkl}	Interplane spacing (d-spacing)
h	Plank's constant
p	Relativistic momentum
m	Rest mass
v	Velocity of the particle
c	Speed of light in vacuum
$\mathring{A}$	Angstrom
β	Peak width
θ	Peak position

Chapter 1   Introduction

1.1   Brief Background of the study

The world primary energy supply was estimated to consist of over 80% of oil, natural gas and coal. Figure 1.1[1], indicates the high dependence on fossil energy sources. These also serve as the primary raw materials for a variety of products such as gasoline, diesel, synthetic materials (fine chemicals), plastics, and pharmaceuticals, which has caused continued significant depletion and increased the cost of energy sources [2]. There is also the global climate issue as a consequence of the use of these energy sources, with the negative impact on the environment and increasing human health challenges.

The world population is increasing at 1.2-2% annually and by 2050 is expected to reach 12 billion. This growing population will continue to drive economic development and spike up the increasing global demand for energy services; as a result the primary energy demands are projected to increase by 1.5-3 times as shown in Figure 1.2 [3]. Therefore, there is a well-established need for a more sustainable energy future regarding energy supply and consumption, the development of new generation, conversion and renewable energy storage technologies acceptable to the public and to fulfill social needs.
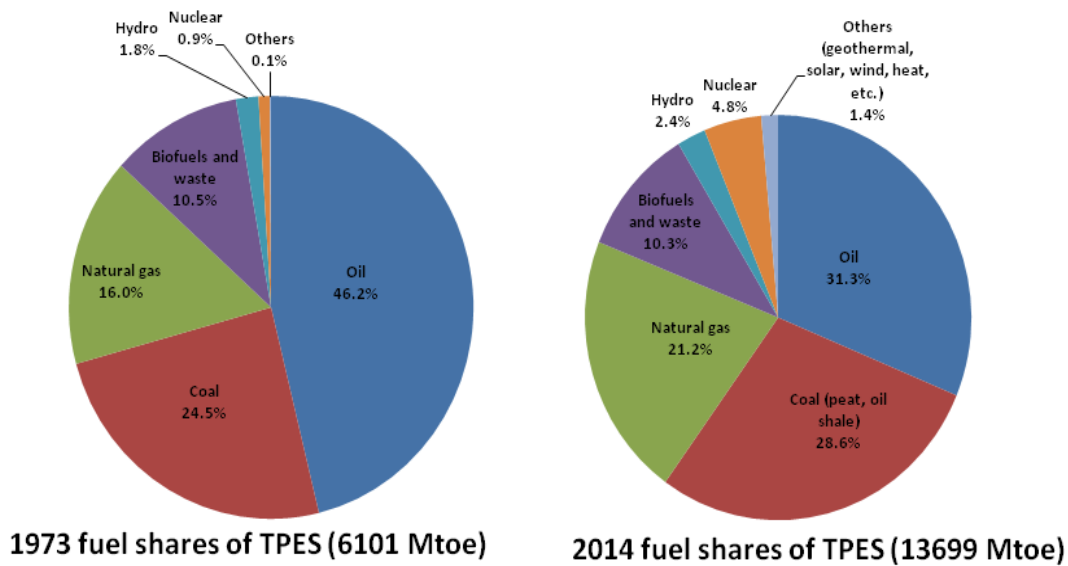
Figure 1.1: *World total primary energy supply (TPES) indicating the high dependence on fossil energy sources [1]*

In recent years, there has been rapid development in fundamental and applied research due to a) the impact of energy use on the environment, b) the limited supply of fossil fuels and c) energy requirements and storage being a motivating factor in the new research direction for alternative energy options [4]. There are many technological energy options at different developmental stages; electrochemical energy technologies (EETs) (batteries, fuel cells, capacitors, etc.) are excellent candidates to be considered. EETs will play a vital role in the future energy mix: in energy conversion/storage, conservation and energy sustainability [5].
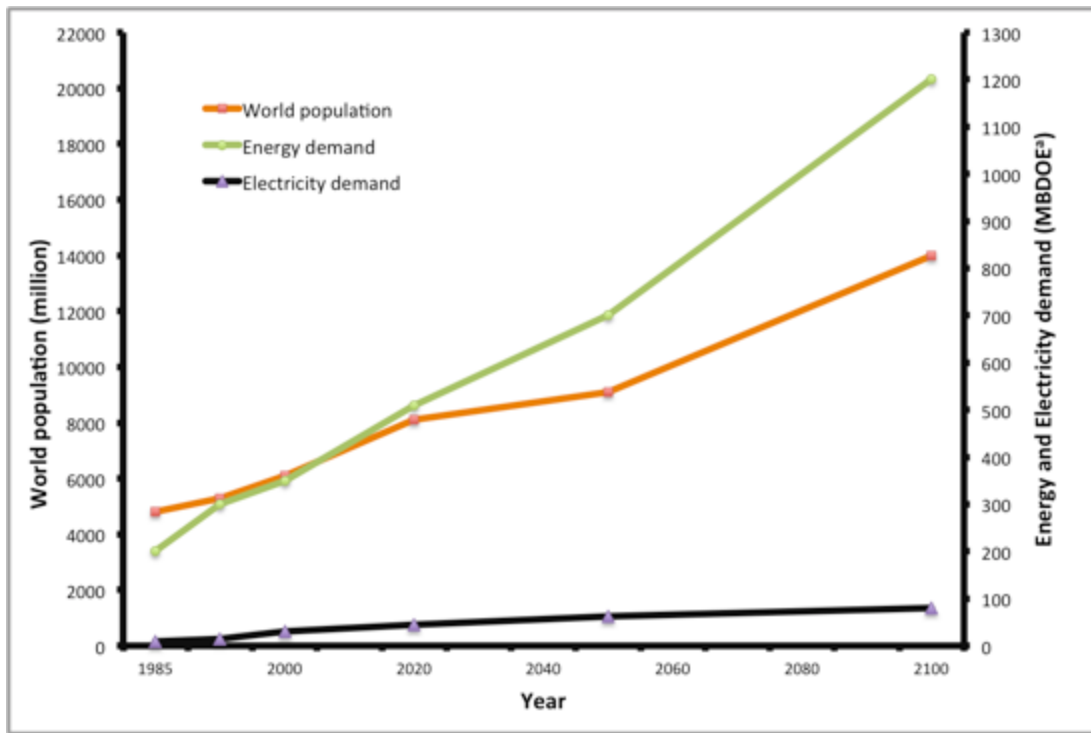
Figure 1.2:   Actual and estimated world population, energy and electricity demand ([a]Millions of barrels per day of oil equivalent) [6]

Electrochemical energy storage (EES) devices such as batteries (primary and secondary) and fuel cells primarily convert stored chemical energy into electrical energy. Batteries utilise built-in chemical components to store electrical energy while fuel cells have chemically bound energy supplied (hydrogen, methanol, formic acid) from outside the device [7]. Fuel cells have the advantage unlike heat-engines and conventional batteries to be miniaturised while maintaining higher stored energy densities [8-10]. The impact is expected to transform future energy technologies just like the microelectronic chip over vacuum tubes, which changed the communications technology, if fuel cells are miniaturised. The adoption of fuel cells will displace internal combustion engines to improve the existing transportation technologies and be used to replace batteries in portables/communication devices [9].

Fuel cells (FCs) convert the fuel from chemical energy through electrochemical reactions directly into electricity [11, 12] and heat with a high theoretical thermodynamic efficiency. The development of energy production or conversion technologies will directly or indirectly decrease the CO_2 emissions, for example, by using hydrogen energy with about 83% conversion efficiency in fuel cell vehicles, molten carbonate fuel cells in electricity generation. Fuel cells will generate clean energy continuously so long as the fuel and oxidant are in supply. Fuel cells emit low levels of NO_x and particulates (air quality) making it a more environmentally friendly energy option. Fuel cells, however, face some operational challenges, which decrease their performance such as the effect of electrolyte concentration, loading of catalysts, membrane fuel crossover and flooding at the cathode electrode [13]. Although extensive research has been carried out on fuel cell technology, development of new electrodes (anode catalysts), membrane materials and current collectors remain very expensive. This indicates a need to understand the various challenges of fuel cells components to efficiently reduce the material cost for the deployment of FCs technologies.
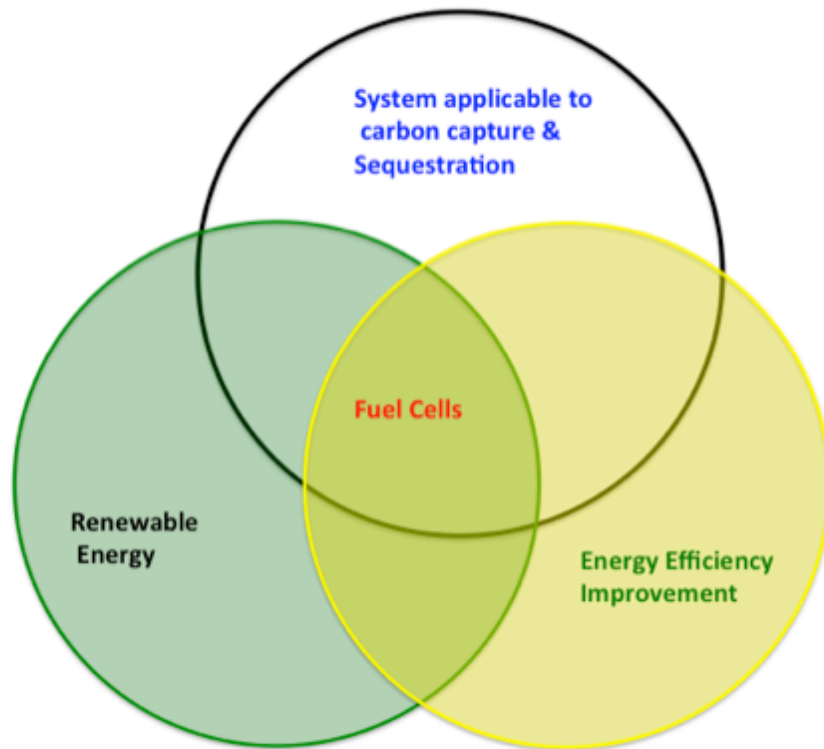
Figure 1.3: Options for CO_2 emission reduction in energy use and the role of fuel cells [14]

In Figure 1.3, Wee (2010) proposed three major options for the reduction of CO_2: (i) improving the conversion efficiency of energy devices (e.g. boiler, turbine), (ii) using renewable and sustainable energy sources (solar, hydrogen, wind) and (iii) carbon capture and storage technology development. The synergy effect of combining these methods will significantly decrease CO_2 emission. A fuel cell can, directly and indirectly, reduce CO_2 emissions depending on the application. Fuel cells and their hybrid system represent one of the most promising technologies to reduce greenhouse gas emissions (GHGs) on transport as shown in Figure 1.4 [14]. In using a molten carbonate fuel cell system, it can directly double electricity generation whilst decreasing CO_2 emission by 13.4% when it is separated from the combustion mixture. Depending on the H_2 production system, Polymer electrolyte membrane fuel cell (PEMFC)

vehicles could decrease CO_2 emissions by 70-80% of the current emission standards. Figure 1.4 indicates the contribution of PEMFCs to the reduction of CO_2 and the effect of the production method. PEMFC showed a significant decrease in CO_2 emissions from the H_2 produced from renewables compared to the internal combustion engine sources [14]. The synergy between these factors could positively contribute to reducing the overall effect of GHGs to the challenges of climate change.
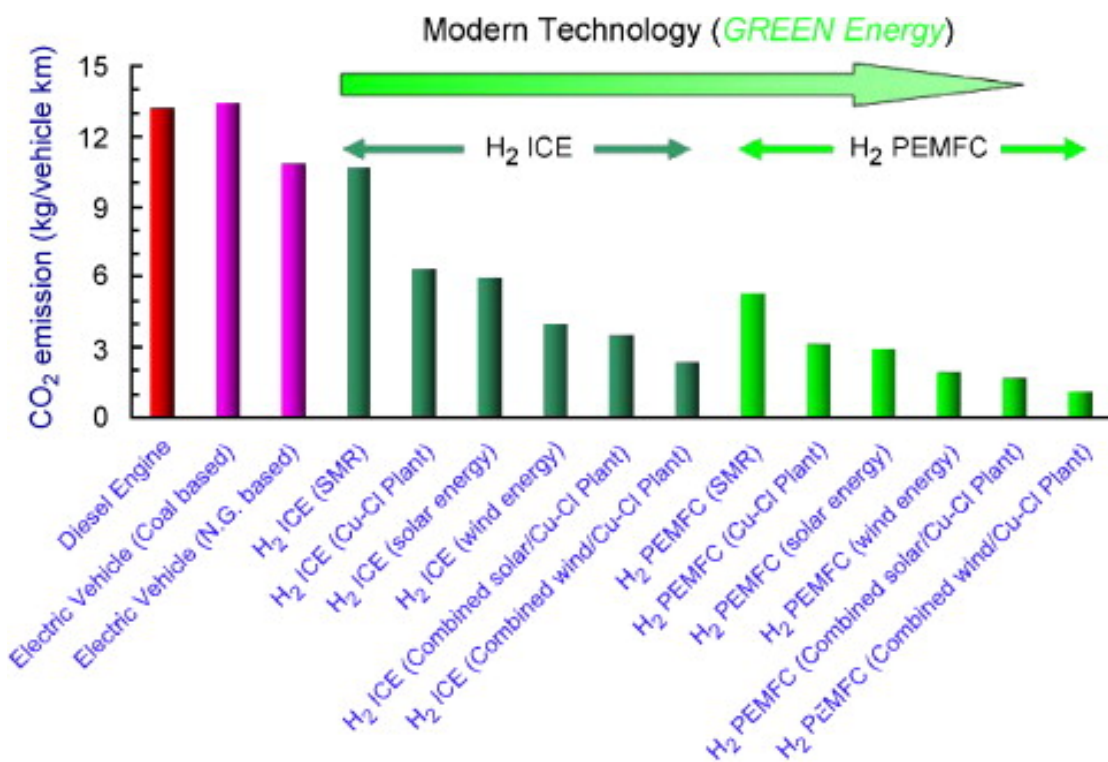
Figure 1.4 Greenhouse gas emissions from different trains with various fuel production methods (Adapted with permission from [15])

1.2 Objectives

The overall objective of this study is to find ways to reduce the cost of the catalyst for direct formic acid fuel cells (DFAFCs) by investigating new synthesis routes.

The reduced catalysts loading utilisation and evaluation of catalyst performance are two foci of interest.

The specific objectives are as follows:

i. To formulate and prepare an anodic catalyst through a new synthesis route to increase Pd utilisation by increasing electrochemical surface area (ECSA)

ii. To develop a low-cost gold (Au) electrocatalyst that is efficient with good performance, increased stability for DFAFCs and to decrease catalyst loading

iii. To design a suitable formulation/preparation method for bimetallic gold copper (AuCu-C_{PVP}) catalysts for electrooxidation of formic acid in DFAFC

iv. To investigate structural effects of AuCu-C_{PVP} anodic catalysts developed in objective (iii) for formic acid electrooxidation activity

1.3   Significance of the Study

Immobilisation of gold sols represents a suitable method for producing gold catalysts characterised by excellent/high metal dispersion and narrow distribution of the metal nanoparticles, which is a prerequisite for high-performance catalyst activity. Metal-on-carbon catalysts are very active and selective in liquid-phase oxidation [16-18], and this activity is governed by two factors: particle dimensions and metal (gold) exposure on the carbon surface. This is linked to the nature of the carbon support surface oxygenated groups or anchor sites. Gold particle activity increases with decreasing particle size and increasing gold exposure. Zhang and Weaver demonstrated the lack of CO poisoning of formic acid oxidation (FAO) on

gold electrodes and suggested that the reaction follows the direct pathway mechanism [19].

The rationale behind this study is the need to develop a new low cost synthesis routes for core shell nanocatalysts for electrochemical oxidation. This research should be of interest to a broad group of readership including those interested in the synthesis of nanocatalysts materials for hydrogen production, electrochemical energy storage/conversion and direct liquid fuel cells technology.

1.4 Layout of thesis

This thesis is arranged as follows: Chapter 1 is the introduction, starting with the background, the objectives and the significance of the study. Chapter 2 introduces the relevant background through an extensive literature review of formic acid catalysis by gold and gold-based catalysts, the role of catalyst supports and effects of bifunctionality properties of bimetallic catalysts. Chapter 3 presents the experimental techniques for elucidating the electrochemical and physical characteristics of the prepared catalyst. Chapter 4 presents the experimental procedures used for physically characterising the electrocatalysts and for the electrochemical performance testing of the anode catalysts. Chapters 5-7 show the detailed performance analysis of Pd-C, AuNPs-C, Au-C and AuCu-C catalysts for formic acid electrooxidation, respectively. The overall discussion includes a comparison of the mechanism, kinetics, and stability of each catalyst for formic acid oxidation. Chapter 8 provides a summary of the work, conclusions and suggests new directions for future research.

Chapter 2   Literature Review

2.1   Introduction

This chapter is a review of the literature on fuel cell development, comparative overview of the various types of PEMFCs, and gives a background understanding of commercially available PEMFCs such as hydrogen PEMFCs and direct methanol FCs. It further explores the catalyst formulation and preparation methods, alongside the availability and potential application of gold in catalysis. The effect of particle size and the nature of the active sites on the gold catalyst are investigated. The influence of the catalyst support material and the role in catalyst activity is examined. Finally, an evaluation of extant literature was made towards understanding bimetallic catalysis in an acid medium with the view of investigating gold-based catalysts for DFAFC application.

2.2   History of Fuel Cells

Swiss scientist Christian Friedrich Schönbein pioneered the principle of the fuel cell in 1838. Sir William Grove, a chemist, physicist and lawyer, developed the first fuel cell that reversed the electrolysis of water in 1839, which he called a gas voltaic battery. Grove's experiments produced an electric current by the electrochemical reaction of hydrogen and oxygen over a platinum catalyst. Then in 1959, Francis Bacon successfully developed a 5 kW alkaline fuel cell (AFC), which was used by NASA space mission instead of large backup batteries in the 1960s. To boost research into fuel

development, the very high installation cost (CAPEX) became a major drawback. However, the need for clean air and greater energy efficiency, higher oil price and environmental problems lead to further development of fuel cell research, in various developmental and application stages as shown in Figure 2.1 [11, 20].
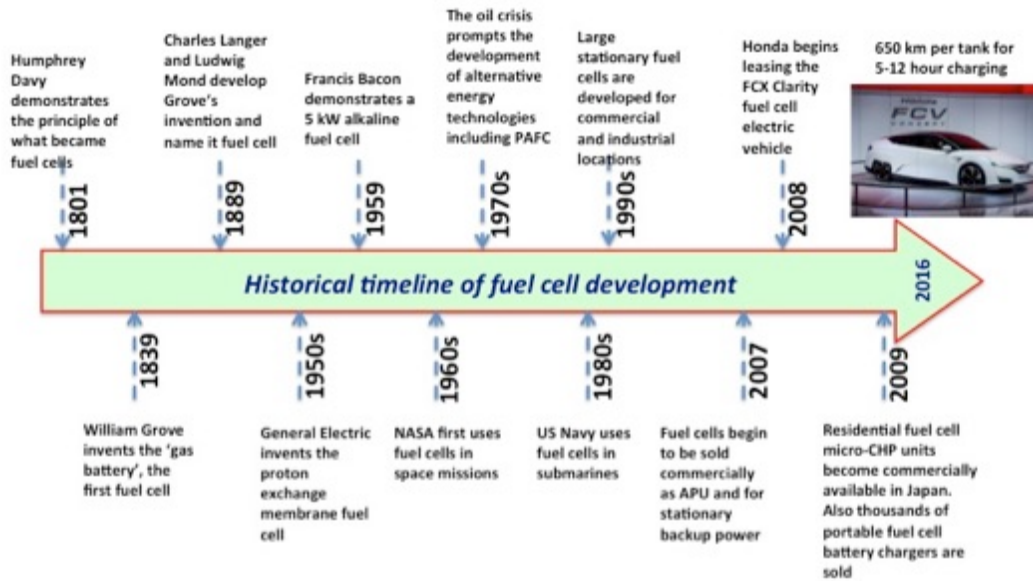
Figure 2.1: Historical timeline of fuel cell developmental and application stages [20]

There are different types of fuel cell suitable for portable, stationary and transportation applications. Table 2.1 gives a general comparison of the type of FCs: the electrolyte used, the conducting species and the internal charge carrier, which flows through the external circuit. In this research, the focus will be on low temperature direct formic fuel cells and the development of the anode catalysts.

Extensive effort has been devoted to the development of fuel cells with significant advances, but their commercialisation is yet to became widespread. One problem is the prohibitive cost of component materials such as bipolar plates, membranes and electrocatalysts. With economies of scale, the cost of production is expected to decrease

substantially for bipolar plates and membranes. However, the price of Pt and platinum group metals (PGMs) with limited natural resources has continued to increase as time goes on. There have been several strategies to decrease the usage of Pt and PGMs by increasing the mass specific activity, adding other metals to reduce cost or finding alternative non-noble metal catalysts with an acceptable catalytic performance. There remain the problems of low durability and Pt agglomerating or detaching from support materials, which makes it easily oxidised, degrading the performance of fuel cells and reducing their lifetime [21].

2.3 Polymer electrolyte membrane (PEM) fuel cells

2.3.1 H$_2$-PEMFC

PEM-based fuel cells are considered as a viable candidate to replace batteries in portable devices like mobile phones and laptops, etc. in the near future [22]. Mobile phones could be operated for up to 30 days without recharging and laptops up to 20 hours, showing superior power than current available batteries [11].
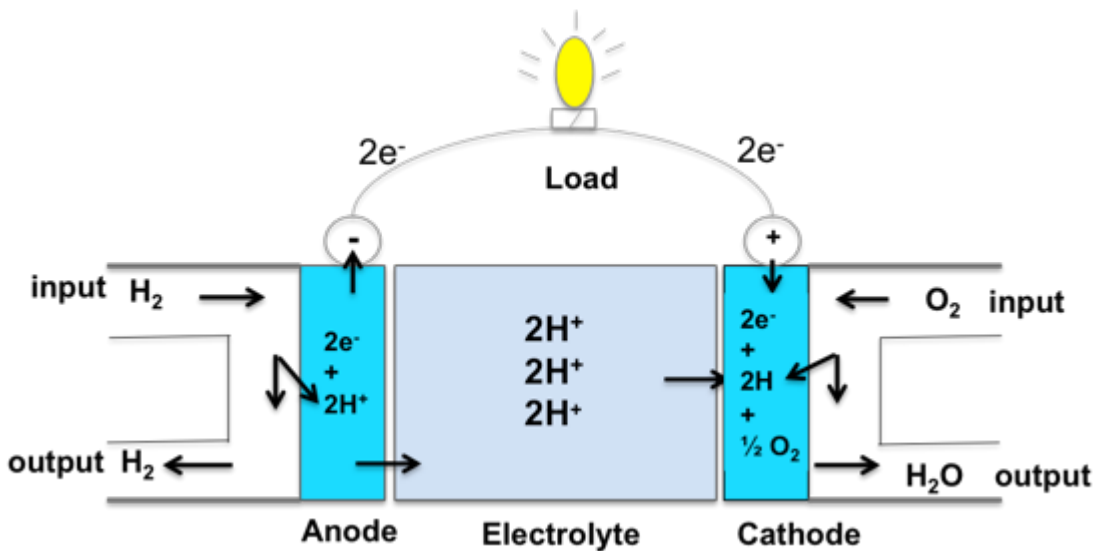
Figure 2.2: Schematic drawing of a hydrogen/oxygen fuel cell and its reactions based on the proton exchange membrane fuel cell (PEMFC)

Figure 2.2 gives a visual description of a typical proton exchange membrane (PEM) fuel cell, the input/output of fuel and oxidants at the electrodes, with the passage of H^+ ions (protons) through the electrolyte/PEM. Similarly, using methanol and formic acid as a fluid with free H^+ ions is expected to serve this purpose very well. It shows the movement of electrons between the anode and cathode through the external circuit.

Table 2.1 shows a comparison of the different types of fuel cells based on parameters such as fuel type, catalyst materials, cost, and efficiency. The low temperature (50-100 °C) PEM fuel cells are most suitable for portable devices, residential and transportation applications, while medium and large scale applications need high temperature FCs with high efficiency (80%), fuel flexibility and cogeneration of heat [11].

Table 2.1: General comparison of polymer electrolyte membrane fuel cells [11]

Parameters	Fuel cell types						
	PEMFC	**AFC**	**PAFC**	**MCFC**	**SOFC**	**DMFC**	**DFAFC**
Electrolyte	Solid polymer membrane (Nafion)	Liquid solution of KOH	Phosphoric acid (H_3PO_4)	Lithium and potassium carbonate $(LiAlO_2)$	Stabilized solid oxide electrolyte (Y_2O_3, ZrO_2)	Solid polymer membrane	Solid polymer membrane (Nafion)
Operating temperature (°C)	50-100	50-200	~200	~650	800-1000	60-200	
Anode reaction	$H_2 \rightarrow 2H^+ + 2e^-$	$H_2 + 2(OH^-) \rightarrow 2H_2O + 2e^-$	$H_2 \rightarrow 2H^+ + 2e^-$	$H_2 + CO_3^{2-} \rightarrow H_2O + CO_2 + 2e^-$	$H_2 + O^{2-} \rightarrow H_2O + 2e^-$	$CH_3OH + H_2O \rightarrow CO_2 + 6H^+ + 6e^-$	$HCOOH \rightarrow CO_2 + 2H^+ + 2e^-$
Cathode reaction	$\frac{1}{2}O_2 + 2H^+ + 2e^- \rightarrow H_2O$	$\frac{1}{2}O_2 + H_2O + 2e^- \rightarrow 2(OH)^-$	$\frac{1}{2}O_2 + 2H^+ + 2e^- \rightarrow 2H_2O$	$\frac{1}{2}O_2 + CO_2 + 2e^- \rightarrow CO_3^{2-}$	$\frac{1}{2}O_2 + 2e^- \rightarrow O^{2-}$	$3O_2 + 12H^+ + 12e^- \rightarrow 6H_2O$	$\frac{1}{2}O_2 + 2H^+ + 2e^- \rightarrow H_2O$
Charge carrier	H^+	OH^-	H^+	CO_3^-	O^-	H^+	H^+
Fuel	Pure H_2	Pure H_2	Pure H_2	H_2, CO, CH_4, other hydrocarbons	H_2, CO, CH_4, other hydrocarbons	CH_3OH	HCOOH
Oxidant	O_2 in air	O_2 in air	O_2 in air	O_2 in air	O_2 in air	O_2 in air	O_2 in air
Efficiency	40-50%	~50%	40%	>50%	>50%	40%	≤50%

Parameters	Fuel cell types						
	PEMFC	AFC	PAFC	MCFC	SOFC	DMFC	DFAFC
Cogeneration	-	-	Yes	Yes	Yes	No	No
Reformer is required	Yes	Yes	Yes	-	-	-	-
Cell Voltage	1.1	1	1.1	0.7-1.0	0.8-1.0	0.2-0.4	0.3-0.72[23]
Power density (kW/m^3)	3.8-6.5	~1	0.8-1.9	1.5-2.6	0.1-1.5	~0.6	0.2-4.8[23]
Installation Cost (US $/kW)	<1500	~1800	2100	~2000-3000	3000	-	-
Capacity	30 W, 1 kW, 2 kW, 5 kW, 7 kW, 250 kW	10-100 kW	100 kW, 200 kW, 1.3 MW	155 kW, 200 kW, 250 kW 1 MW, 2 MW	1 kW, 25 kW, 5 kW, 100 kW, 250 kW, 1.7 MW	1 W to 1 kW, 100 kW to 1 MW (Research)	1 W to 1 kW, 100 kW to 1 MW (Research)
Applications	Residential; UPS; emergency services such as hospitals and banking; industry; transportation; commercial	Transportation; space shuttles; portable power	Transportation; commercial cogeneration; portable power	Transportations (e.g. marine-ships; naval vessels; rail); industries; utility power plants	Residential; utility power plants; commercial cogeneration; portable power.	It is used to replace batteries in mobiles; computers and other portable devices	It is used to replace batteries in mobiles; computers and other portable devices
Advantages	High power density; quick start up; solid non-corrosive electrolyte	High power density; quick start up	Produce high grade waste heat; stable electrolyte characteristics	High efficiency; no metal catalysts needed	Solid electrolyte; high efficiency; generate high grade waste heat	Reduced cost due to absence of fuel reformer	Low crossover effect, increase reactant flow rate/concentration
Drawbacks	Expensive platinum catalyst; sensitive to fuel impurities (CO, H_2S)	Expensive platinum catalyst; sensitive to fuel impurities (CO, CO_2, CH_4, H_2S)	Corrosive liquid electrolyte; sensitive to fuel impurities (CO, H_2S)	High cost; corrosive liquid electrolyte; slow start up; intolerance to sulphur	High cost; slow start up; intolerance to sulphur	Lower efficiency and power density	Low volumetric energy density, expensive Pt- and Pd-based anode catalysts

2.3.2 Direct methanol fuel cell (DMFC)

Direct liquid fuel cells (DLFCs), using small organic liquid fuels at the anode, are considered to be the next generation of energy sources for mobile phones and laptop applications [23, 24]. Methanol is a very promising liquid fuel especially if it can be oxidised directly and completely into carbon dioxide [25]. A direct methanol fuel cell (DMFC) is a *polymer electrolyte membrane* (PEM) fuel cell that is fed directly with an aqueous methanol solution instead of reformed hydrogen gas fuel [11, 26].
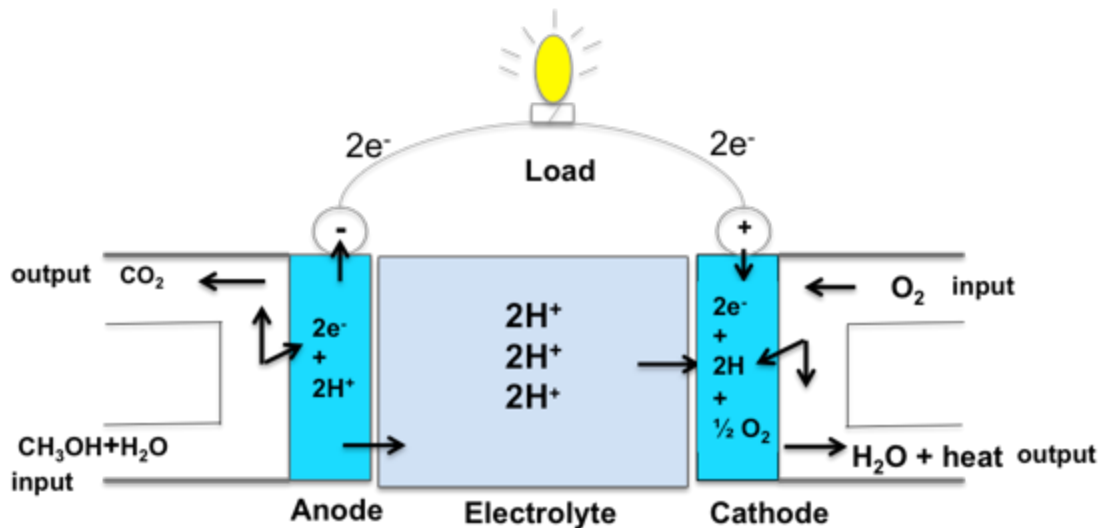
Figure 2.3: Schematic diagram illustrating the operating principle of the direct methanol fuel cell (DMFC)

Methanol is widely available and can be easily reformed from gasoline or biomass [26]. The application of hydrogen-fed PEM fuel cells (H_2-PEMFC) is impaired because of the challenges of lack of infrastructure for hydrogen distribution, hydrogen storage and safety concerns with hydrogen gas leakage [27]. The principle of DMFCs is that methanol flows through the anode and is broken down into protons, electrons, and CO_2

(see Figure 2.3), which in turn reduces the overall cost due to the absence of reformer installation and bulky balance-of-plant (BOP) [26, 27].

There are some challenges associated with DMFC development and application, which have hindered their widespread commercialisation. These include the electrooxidation of methanol at the anode, which produces hydrocarbon intermediates that deactivate the anode catalysts. There is the problem of slow kinetics at the anode, which requires a large overpotential for high power output. There is also the need for water at the anode, which limits the methanol concentration [28]. The crossover of unreacted methanol flows from the anode to the cathode and reacts with the supplied oxygen, creating a parasitic loss. This has been reported to account for up to 40% of system losses in DMFCs [26, 29].

2.3.3 Direct formic acid fuel cells (DFAFCs)

DFAFC is PEM-based fuel cell using the formic acid electrolyte as fuel. It is a promising alternative to DMFC because of the simpler oxidation mechanism, being a byproduct of the complex methanol oxidation (see details in section 2.3.5). It is non-toxic and non-flammable even at high concentration [30-32], and has a lower crossover effect in FC operating condition [33]. Hence, formic acid can be used at a high concentration (up to 20 M) [34], which overcomes the lower electron transfer per molecule of the fuel (formic acid compared to methanol) [27, 35]. However, formic acid has a low volumetric density of 2104 Wh/L, compared to 4690 Wh/L for methanol [36, 37]. This is overcome by the use of high concentrations of formic acid. The limited the crossover in direct formic acid fuel cells (DFAFCs) is due to the anodic repulsion between the Nafion sulfonic groups [38-41]. Also, the partial dissociation of formate

anions in formic acid reduces the crossover effect. Thus, DFAFCs are a promising technology for commercialisation compared to DMFCs [13] with above mentioned limitations.

Another advantage for the choice of formic acid as a fuel is that the anodic oxidation reaction occurs at -0.25 V (vs. RHE), with overall higher theoretical voltage of 1.48 V, compared with hydrogen (H_2-PEMFC, 1.23 V) and methanol (DMFC, 1.18 V) [11, 13, 34, 42, 43]. In FC operating conditions, formic acid has higher OCV of approximately 0.96 V compared with 0.70 V for methanol (DMFC) [4, 44, 45].

Anode: $HCOOH \rightarrow CO_2 + 2H^+ + 2e^-$ $E^o = -0.25\,V\,(SHE)$ 2.1

Cathode: $\frac{1}{2}O_2 + 2H^+ + 2e^- \rightarrow H_2O$ $E^o = +1.23\,V\,(SHE)$ 2.2

Net Reaction: $HCOOH + \frac{1}{2}O_2 \rightarrow CO_2 + H_2O$ $E^o = +1.48\,V$ 2.3
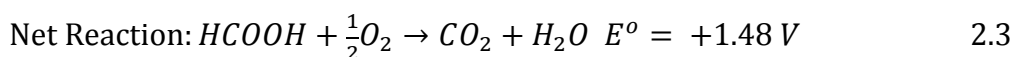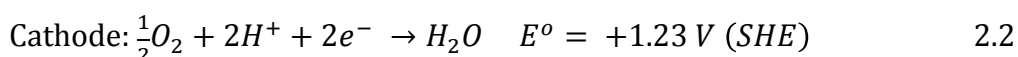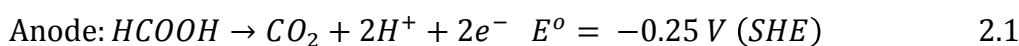
The reactions, Equations 2.1-2.3, proceed continuously. At the anode, formic acid ionises, releasing electrons and creating protons and carbon dioxide (Equation 2.1). The electrons produced at the anode must pass through an external circuit to the cathode. At the cathode, oxygen reacts with electrons taken from the electrode, and protons from the electrolyte to form water (Equation 2.2). The overall redox reaction of the DFAFC gives a theoretical (maximum) open circuit voltage (OCV) of 1.48 V (Equation 2.3) [43, 46, 47].

2.3.4 Methanol economy

A methanol based economy can lead to sustainable energy security, where methanol is produced from biomass and recycled CO_2 using other technologies such as CO_2 capture

and utilisation [48]. Compared to the hydrogen economy when the primary energy source is hydrogen gas, a methanol economy does not face the challenges of storage at high pressure and transportation of a volatile liquid, with potential explosive leakages. Hydrogen (liquid or gas) currently lacks the infrastructure to achieve the high purity for FCs fuel condition, whereas methanol, on the other hand, has no need for liquefaction [49, 50]. Currently, hydrogen production (fossil, renewable and nuclear energy sources) and use still requires high-energy consumption and costly processing. Hydrogen fuel cell performance and cost are not economically competitive with battery technology due to these limitations [50]. Methanol has great potential because of its different production options, broad applications in transportation, fuel cell, stationary and portable devices. Methanol can be produced from the catalytic conversion of syngas, oxidation of methane and biomass. There is a large market economy for methanol with China the biggest consumer. There are several blends of methanol with gasoline in the market such as M5 (5% methanol and 95% gasoline), M10, M15, M85 and M100. M15 remains the most common because greater fractions of methanol would require engine modification of a conventional internal combustion engine, thus limiting the market recognition. These, in turn, lower the harmful emission of CO_2, NOx and particulates [48, 51] reducing their contribution to the climate change problem.

Table 2.2: Environmental half-lives in days of methanol

	Soil	Air	Surface water	Ground water
Methanol	1-7	3-30	1-7	1-7
Ethanol	0.1-1	0.5-5.1	0.25-1	0.5-2.2
Benzene	5-6	2-21	5-16	10-720
Toluene	4-22	0.4-4.3	4-4.3	7-28

Methanol is easily biodegraded in the environment, when compared to the benzene and toluene, used for adding octane to gasoline, and has much shorter half-life in soil and

water mediums as shown in Table 2.2. In air, methanol is more resistant to oxidation (longer half-life) compared to gasoline and ethanol. The slow oxidation is beneficial for the reduction in the amount of volatile organic compounds for ozone production [52, 53].

2.3.5 Mechanism of methanol oxidation

The overall oxidation reaction for the direct methanol fuel cell can be expressed by equation 2.6 [54, 55]:

Anode: $CH_3OH\ (l)\ +H_2O(l)\ \rightarrow\ 6H^+\ +\ 6e^-\ +\ CO_2\ (g)$ $E^o = 0.02\ V$ 2.4

Cathode: $6H^+\ +\ \frac{3}{2}O_2(g)\ +\ 6e^-\ \rightarrow\ 3H_2O\ (l)$ $E^o = 1.23\ V$ 2.5

Overall: $CH_3OH\ (l) + \frac{3}{2}O_2\ \rightarrow CO_2\ (g) + 2H_2O\ (l)$ $E^o = 1.21\ V$ 2.6
$\Delta H(298\ K) = 50\ kJ\ mole^{-1}$
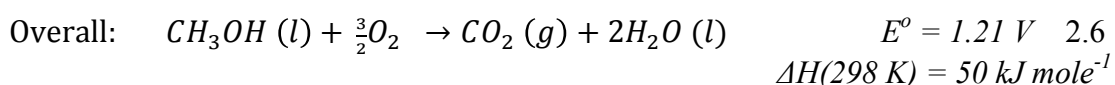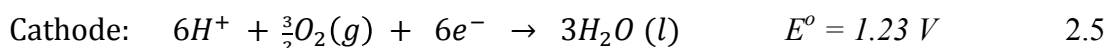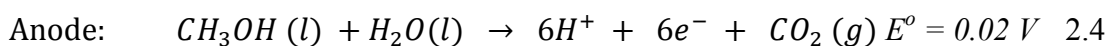
In the overall equation of methanol oxidation (Equation 2.6), six electrons are produced for each molecule of methanol, which is why it is a promising fuel for fuel cells. However, Equation (2.6) does not proceed simply but through a variety of stages as shown in Figure 2.4. Previous literature has reported that the oxidation products of methanol depend on several factors such as temperature, concentration, electrode roughness and time of electrolysis [47, 54].

a
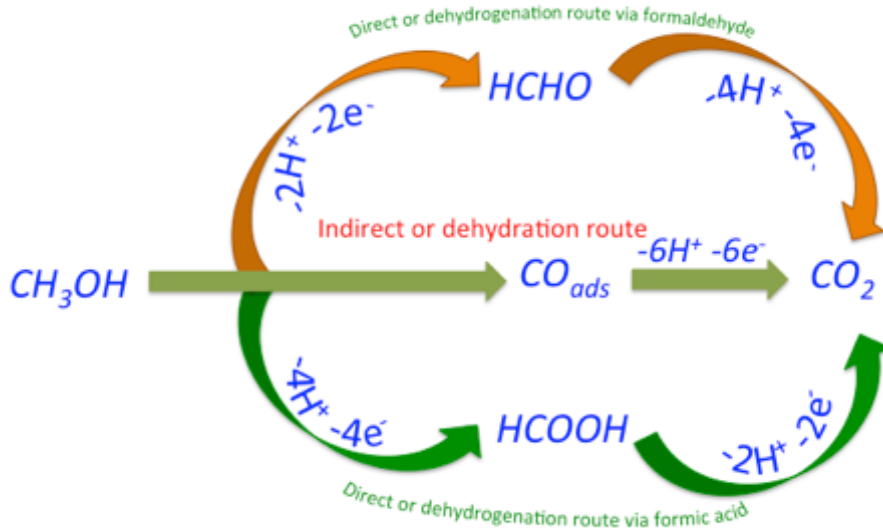
b
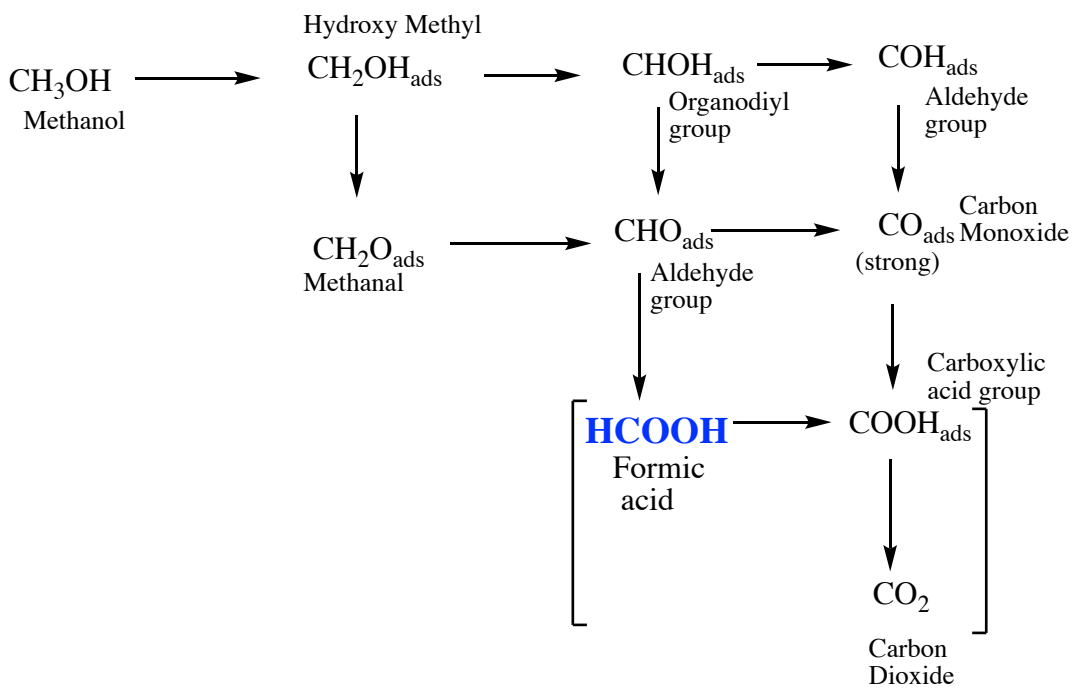
Figure 2.4:   Methanol oxidation parallel pathways on platinum-based anode catalysts – (a) General direct-indirect pathway (b) Specific intermediate reaction pathways [47, 56, 57].

The performance of DMFC is hindered by the complex mechanism of the reaction and the different intermediate products formed as shown Figure 2.4. In this thesis, the focus will be on the last three steps of methanol mechanism (Figure 2.4b and direct route on

Figure 2.4a). The byproduct, formic acid, from the methanol oxidation process will be the focus of this thesis by using mono- and bi-metallic catalysts to investigate its electrooxidation. Therefore, to improve the viability of DMFCs, an understanding of their operating mechanism is pivotal on the choice of electrocatalysts suitable for direct and complete oxidation to CO_2 (direct or dehydrogenation route). Also, the following research goals must be addressed for progress in DMFCs [26]:

1. Improve membrane to have higher selectivity (ratio of conductivity to crossover rate) and durability.

2. Develop anode materials for improved methanol oxidation catalysis (slow kinetics and overpotential).

3. Increase methanol-tolerant oxygen for reduction reaction (ORR) catalysts for better cathode performance and improve air electrode for lower active metal loading.

4. Improve understanding of factors influencing electro-osmosis.

2.3.6 Types of catalysts

An optimised electrocatalyst for methanol oxidation remains a major challenge in the deployment of DMFC technology. The catalyst should be able to catalyse the dissociation of the methanol molecules, favour adsorbed oxygenated species (OH) at the catalyst surface at low potentials and quickly remove poisonous species from active sites. Platinum catalysts remain the most suitable for methanol dissociation while ruthenium handles the adsorption of (OH) at low potentials. However, the problematic

CO poisoning of the anode catalysts remains a major drawback, which is due to inability of Pt to dissociate water [54, 58]. It was suggested that the use of a multimetallic platinum-based anode, Platinum-Ruthenium-Molybdenum, could improve the adsorption of OH species, however the easily corroded Mo resulted in deactivation of the anode electrode [25, 54]. From the crystallographic viewpoint, Batista *et al* (2004) suggested that Pt (111) crystal plane catalysts enhanced the formation of methoxide species $(H_3CO)_{ad}$, which oxidises to formic acid and formaldehyde via the Eley-Rideal mechanism and CO_2 via the Langmuir-Hinshelwood mechanism without CO poisoning [59]. Other binary Pt-based alloys investigated are PtOs [60], PtMo and PtRuMo [61]. Also, PtRuIr [62], PtAu [63], Pt-Pd core shell nanocatalysts [64], have demonstrated improved oxidation of methanol due to the synergistic effect of the bimetallic structure of the catalyst.

2.4 Electrochemical oxidation of formic acid on noble metals

To understand the catalysis and electrochemistry of formic acid over noble metals, it is important to compare it with commercially available and well-researched studies of methanol oxidation. Formic acid is a by-product along with formaldehyde from the complex methanol oxidation processes (*refer to Figure 2.4, Section 2.3.5 above*).

Formic acid oxidation is comparable with methanol in their oxidation over Pt catalysts, which is known to be the best catalyst for breaking the C-H bond [54] via two (direct and indirect) pathways [13, 22, 65]. For the simplified overall methanol oxidation (see Figure 2.4) the direct (or dehydrogenation) pathway, which is a poison-free route from HCOOH or HCHO produce CO_2 and the indirect (dehydration) pathway leads to the CO poisonous intermediate route. Methanol and formic acid are known to favour the

CO route (indirect pathway) on pure Pt catalysts since the electrooxidation into CO_2 cannot begin below 0.45 V versus RHE. However, at 0.4 V, adsorption of the intermediate starts, resulting in competition between oxidation and blocking of active sites on the Pt catalyst surface (activation potential losses). However, no viable reactivity on the adsorbate layer occurs below 0.7 V on a pure Pt surface [54, 66].

The anodic oxidation of methanol received a remarkable boost from the pioneering work of Entina and Petry (1968) and Binder et al. (1972) with the discovery that platinum-ruthenium (Pt-Ru) catalysts produced higher catalytic activity than pure platinum and no activity with pure ruthenium [67]. Their catalytic performance was attributed to the synergetic effect of the bimetallic catalysts, due to changes in the electronic structure of Pt when alloyed with Ru. So far, this remains the most electroactive catalyst for methanol oxidation to date.

The electrooxidation of small organic molecules is generally complex, and the reaction kinetics cannot be fully completed with a pure monometallic catalyst, as proven with methanol oxidation. Multifunctional catalysts are the most suitable for catalysing the various chemical bonds on these organic fuels because of this electronic effect, such as demonstrated in Cu-Pd [68, 69], Pd-Au [70, 71].

Fuel cell performance is affected by several operating variables such as temperature, reactant utilisation and current density, which results in the magnitude of potential losses influencing the ideal cell potential. The actual potential in a fuel cell generally decreases due to the contribution of several types of irreversible losses, see Figure 2.5 below [72]. The slow kinetics causes activation-related losses at the electrode surface, causing significant losses generated at the anode as compared with the cathode. Therefore, one solution to minimise these losses is the formulation and development of

active anode catalysts that are robust, eco-friendly and economically viable. A considerable amount of research has been devoted to anode catalysts, but mainly to platinum group metals (Pt, Pd-based) [22, 46, 63, 68, 69, 71, 73-80]. However, less holistic attention has been paid to the catalyst's utilisation and performance versus cost strategies such as is taken into account in this work. This research relied mainly on the experimental evidence, and the conclusions stated here are mostly based on the experimental observations.

2.4.1   Mechanistic pathways of formic acid oxidation on metal surface

Several mechanistic studies on Pt metal surfaces have shown that formic acid electrooxidation occur via a dual parallel pathways: the complete oxidation to water molecule and CO_2 (the *direct or dehydrogenation pathway*) and the indirect or dehydration pathway leading to self-poisoning of strongly absorbed CO intermediate species. [13, 22, 65]. Pt has been widely used as anode catalyst due to its high catalytic activity but suffers seriously from CO intermediate poisoning in the dissociation of HCOOH. [46, 81]. Figure 2.5 displays the dual (dehydrogenation and dehydration) pathways of FAO on Pt catalyst surface.is shown below.

dehydrogenation

$HCOOH$

$$CO_2 + 2H^+ + 2e^-$$ poison free route

dehydration

$$CO_{abs} + H_2O \rightarrow CO_2 + 2H^+ + 2e^-$$
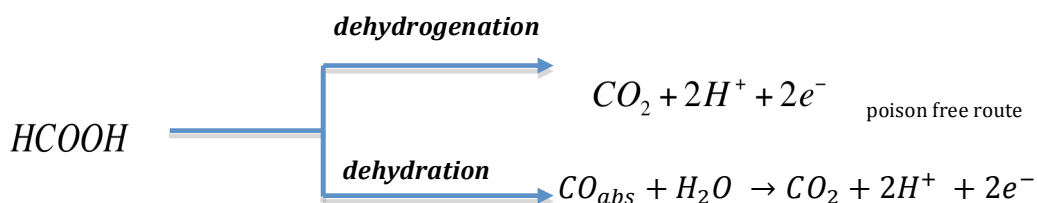
Figure 2.5: The dehydrogenation and dehydration pathway of formic acid on Pt metal surface

The chemisorption of CO_{abs} poisoning species on the Pt anode in the FA oxidation suppresses the overall decomposition reaction by blocking the Pt active sites, resulting in low efficiency and performance activity [39]. Several research findings have shown a better catalytic enhancement of Pd and Pd-based than Pt catalysts in FAO mechanism proceed via the dehydrogenation pathway at lower potentials [39, 43, 82-86]. There is improved performance of DFAFCs on Pd and Pd-based catalysts because there is no strongly absorbed CO_{abs} poisoning intermediate species [81]. Equation 2.7 shows the multistep FAO mechanism on Pd proposed by Lui *et al.* [87] similar to the Zhang *et al.* [88] proposed reaction mechanism for Pt.

$$HCOOH + Pd \rightarrow Pd - (COOH)_{abs} + H^+ + e^- \qquad (a)$$
$$Pd - (COOH)_{abs} \rightarrow Pd + CO_2 + H^+ + e^- \qquad (b) \qquad 2.7$$
$$Pd + H_2O \rightarrow Pd - OH + H^+ + e^- \qquad (c)$$
$$Pd - (COOH)_{abs} + Pd - OH \rightarrow 2Pd + CO_2 + H_2O \qquad (d)$$
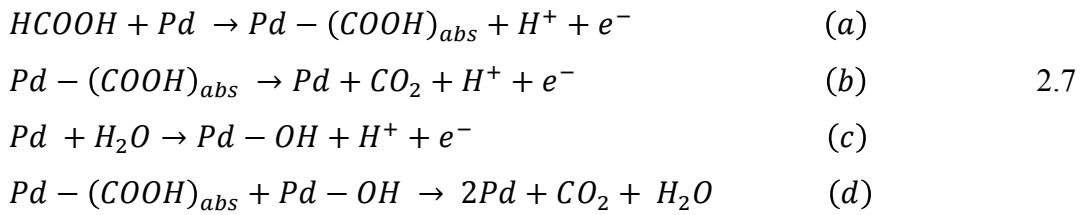
Equation 2.7a is a mass-transfer reaction at lower potential for FAO proposed by Lui *et al.*, which proceeds to the evolution of CO_2 from the initial decomposition of the reactive carboxyl radical (COOH). The cleavage of the C-H bond in HCOOH molecule in equation 2.7a results in the transfer of electron and is considered to be the rate-determining step. The water molecules added from FA dilution are absorbed as hydroxyl (OH) ions on the surface of Pd and then decomposed into water and CO_2 (equation 2.7c and d) [40, 84, 85]. However, unfortunately, Pd intrinsic surface reaction mechanisms show instability of the Pd catalyst for FAO during operation, remained challenging and unclear [44]. These findings show that some absorbed poisoning intermediate species (*e.g. side reaction*) may be contributing to the main dehydrogenation reaction processes. Furthermore, the formation of absorbed

intermediate species is still a controversy issue and more investigations using *in-situ* techniques to elucidate Pd deactivation processes. Cheng *et al.* reported that catalyst active site poisoning due to Pd nanoparticle size effect, (SO_4^{2-}) anions from the electrolyte and other physical properties could be responsible for the Pd deactivation [40].

2.5 Fuel cell electrochemistry, materials and operations

The change in Gibbs free energy (ΔG) is the maximum electrical work obtainable in a fuel cell operating at constant temperature and pressure (see equation 2.8):

$$\Delta G^o = -nFE^o_{cell} \qquad\qquad 2.8$$

where *n* is the number of electrons participating in the reaction, *F* is Faraday's constant (96487 coulombs/g-mole electron), and E^o_{cell} is the ideal (or standard) potential of the cell (e.g. 1.48 V for DFAFC, provided the system is reversible and no has losses). The overall theoretical cell (or Nernst) potential for the two half-cell reactions at the anode and cathode is given as (see Equation 2.9):

$$\Delta E_{cell} = E_{anode} - E_{cathode} \qquad\qquad 2.9$$

The Nernst potential (or open circuit potential) corresponds to the maximum performance achievable by a fuel cell. This is strongly influenced by the purity of the anode and cathode reactants. This potential increases linearly with the partial pressure or concentration of the reactants, and inversely with the partial pressure of the products. For low-temperature fuel cells (DFAFCs, DMFCs, and H_2-PEMFCs), a noble metal electrocatalyst is the key to achieving reasonable reaction rates at the fuel cell electrodes.

Fuel cells provide an environmentally friendly energy solution compared to combustion engines with moving parts, to produce electricity with a high energy conversion rate [89]. Unlike combustion engines, fuel cell performance is not subject to Carnot's theorem (Equation 2.10):

$$\eta = 1 - \frac{T_1}{T_2} \qquad\qquad 2.10$$

where T_1 and T_2 are the surrounding and internal engine operating temperatures, respectively. Instead the efficiency of the fuel cell (η) is the product of the thermodynamic (η_{thermo}), potential ($\eta_{voltage}$), and the fuel (η_{fuel}), efficiencies (Equation 2.11) [66, 90]:

$$\eta = \eta_{thermo} \times \eta_{voltage} \times \eta_{fuel}$$

$$= \frac{\Delta G}{\Delta H} \times \frac{V}{E_{cell}^o} \times \frac{i/nF}{v_{fuel}} \qquad\qquad 2.11$$

where ΔG is the maximum electrical energy, ΔH is the total thermal energy, V actual or operating voltage, E_{cell}^o is the ideal (or standard) potential of the cell, i is electric current generated, n is the number of electrons participating in the reaction, and F is Faraday's constant (96487 coulombs/g-mole electron).
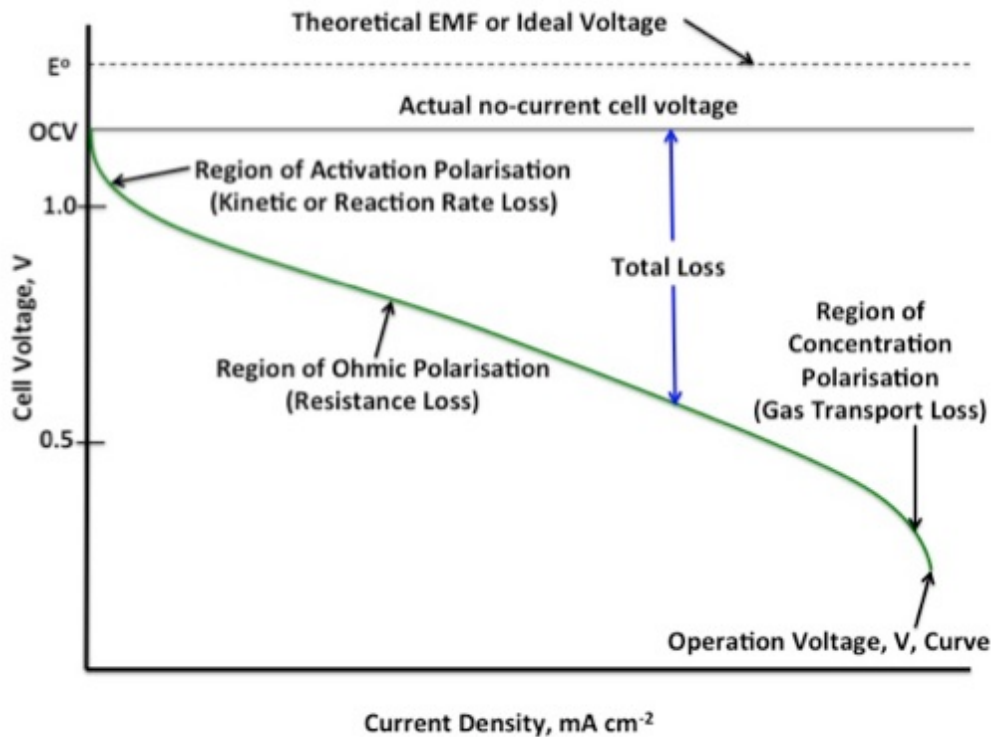
Figure 2.6:   *Ideal and actual fuel cell potential/current polarisation characteristics*

In practice, as shown in Figure 2.6, there are irreversible losses that reduce the actual potential. The performance characteristics of the fuel cell can be improved by the thermodynamic and electrical efficiency of the FC system. The electrical polarisation characteristics include:

- *Ohmic losses* (ionic resistance in the electrolyte and electrodes, electronic resistance in the electrode, current collectors and interconnects, and contact resistance),

- *Kinetic activation losses* (caused by sluggish rate of the reactions at the electrode surface),

- *Mass (concentration) losses* (losses due to change in concentration of the reactants at the surface of the electrode),

- and *fuel crossover/internal current losses* (due to fuel diffusion and electron flow through the electrolyte) [66, 72, 90]. The thermodynamic efficiency

28

depends on the fuel efficiency, water management and temperature control of the system [6]. The difference between the ideal and the actual voltage in a fuel cell is that for the ideal potential, the system is reversible with 100% efficiency, whereas actual irreversible systems have efficiencies < 100% attributed to loss due to wasted energy.

2.6 Half cell electrochemistry: Anode electrode

Electrochemical characterisation of the oxidation and reduction half-cell reactions can be estimated using the three-electrode electrochemical cell (3-EEC). The 3-EEC allows for the reliable controlled study of the electrode/electrolyte interface kinetics/mechanism of the oxidation and reduction half-cell reaction(s). It measures only one half of the electrochemical cell, allowing for the isolation of particular reaction(s) so they can be studied with confidence and accuracy. In 3-EEC system, the *working electrode* (WE) measures the current voltage characteristic independent of changes that may occur at the counter electrode. The *counter electrode* (CE) ensures that current flows to and from the working electrode, and not through the reference electrode. The *reference electrode* (RE) controls the potential without passing current. The CE and WE form the circuit; the RE provides a stable potential for these two. The WE should be close to the RE to avoid any voltage drop owing to electrolyte resistance. When high current passes through an electrode, it changes the potential, therefore, if careful control and measurement of both potential and current through the cell is required, 3-EEC should be used. The 3-EEC is, therefore, the appropriate choice for investigating the anode catalyst electrode materials developed for the oxidation of formic acid.

2.7 Catalyst Support

The desire for high catalyst performance means it is necessary to use of a support for high dispersion and narrow distribution of metal nanoparticles due to their high specific area. Catalyst supports help to stabilise nanoparticles for optimum catalyst utilisation, reduce the metal loading required and subsequently reduce the overall catalyst cost [91]. Catalyst supports can improve other properties such as mechanical strength, catalytic reactivity, stability, and selectivity of the catalyst. The effect of the catalyst support has a strong influence on overall catalyst properties. These include metal particle size, dispersivity, morphology, mass transport and electronic conductivity of the catalyst [92]. Generally, supports are physical carriers, but there is some co-functioning; the so-called metal-support interaction (MSI). In general, the properties of catalyst support should include [93]:

- Creating interplay with catalytic metals to influence the catalytic activity and durability
- Low combustive reaction at low temperatures
- High electrochemical stability under fuel cell conditions
- High conductivity and easy-to-recover metal nanoparticles of the used catalyst
- Desirable mechanical properties such as attrition resistance, hardness and compressive strength
- Porosity, average pore size and pore size distribution (these are considered to be beneficial to improve catalyst utilisation and mass transport properties of the fuel cell electrode structure)

2.7.1   Vulcan XC72 carbon support

Vulcan XC72 is extensively used as an electrocatalyst support and at the moment is widely used by E-TEK and Johnson Matthey as support in commercial electrocatalysts. A reason why Vulcan XC72 is used is the suitable pore structure; it has a large mesoporous structure, which is preferred for PEM fuel cells. Small micropore structures decrease the catalyst utilisation because of poor mass transport of reactant and product. Also electrical resistance will increase with reduced surface area. Vulcan XC72 is the most extensively used carbon support because of the good distribution of various support properties (see Table 2.3). In view of its favourable electrical conductivity, mesoporous qualities, low cost and frequent use in fuel cell electrocatalysts, it allow for easy comparison to catalyst performance in previous research.

Table 2.3: Physical properties of Vulcan XC-72[66]

Product	Vulcan XC-72
Carbon Source	Carbon Black
Total Fluoride (%)	0
Colour	Black
True Density (g ml^{-1})	1.7-1.9
Bulk Density (g ml^{-1})	0.02-0.55
Median Particle Size (µ)	<1
Surface Area (m^{2}g^{-1})	250
Particle Size (nm) **[94]**	30-60
Electrical Resistivity (Ω cm)	>2
Pore Volume (ml g^{-1}) **[95]**	1.74

Vulcan XC72 (Cabot, Boston, MA, USA) is a commonly used carbon support to facilitate electron transfer but nanostructured carbon materials such as carbon nanotubes, graphene and mesoporous carbon are increasingly being applied in fuel cell electrocatalysts. Carbon nanotubes have very high curvature and chemical inertness but

have an insufficient number of binding sites for anchoring metal nanoparticles. This causes large particle size and poor dispersion, which leads to significant reductions in catalytic activities and overall fuel cell performance [21, 91, 96].

Table 2.4 shows a comparison of different carbon supports with their physical properties as a function of cost. This will help determine the choice of support to use based on the cost-performance strategy concerning the overall electrochemical performance. The cost of carbon support affects the utilisation efficiency of noble metals and remains a difficult challenge. However, conventional strategies employed to mitigate these effects include modification of supports by introducing suitable functional groups or molecules onto its surface. These functional groups, such as nitrogen atoms, sulfonic groups and metal oxide groups, serve as anchor sites; and improve solubility and assembly/dispersion of metal nanoparticles [97].

Table 2.4: Comparison of carbon materials for catalyst supports [98]

Carbon material	Specific surface area (m^2 g^{-1})	Pore volume (cm^3 g^{-1})	Density (g cm^{-3})	Electrical conductivity (S cm^{-1})	Cost
Graphite	10-100	0.01-0.1	2.26	104	Low
Activated carbon	1000-3500	0.6-2	0.4-0.7	0.1-1	Low
Template porous carbon (include Starbon, carbon monoliths)	500-3000	0.7-2	0.5-1	0.3-10	High
Carbon fibers	1000-3000	0.3-0.7	0.3-0.8	5-10	Medium
Carbon aerogels	400-1000	2-6	0.5-0.7	1-10	Low
Carbon nanotubes	120-500	2.5	0.6	10^4-10^5	High
Graphene	1500-2500	2-3.5	>1	106	High

2.7.2 Supported gold catalysts

For heterogeneous catalysts; the aim is to achieve enhanced diversity of available active sites by tuning the catalytic properties, and understanding the structure-property correlations to achieve catalyst architecture for improving stability and performance. Preparations of gold catalysts are often loaded on pristine supports, such as metal oxides and carbon via deposition-precipitation, co-precipitation, or colloidal dispersion. Catalyst supports provide active sites and influence the oxidation state of gold when dispersed and stabilised as nanoparticles [99, 100]. Efforts to improve the structural and catalytic properties of gold catalysts through modification of existing synthesis routes will lead to new material-driven research strategies and a better scientific understanding of catalyst preparation [99]. Bulk gold is completely inert towards reacting with molecules but when finely dispersed, it shows high activity and selectivity in oxidation and hydrogenation reactions. The nanoparticle size determines the level of activity: the smaller the size, the higher the activity [101]. Gold nanoparticles finely dispersed on metal oxide supports exhibited high activity in CO oxidation at low temperature, discovered by Haruta and others (1987), which inspired a tremendous amount of research into catalysis using supported gold catalysts. Pristine supports (e.g. TiO_2, CeO_2, Fe_2O_3, ZrO_2, Al_2O_3, SiO_2, and C) are commercially available and relatively easy for establishing structure-property correlation in the development of supported gold catalysts [102].

To our knowledge, there are as yet no fundamental studies of direct formic acid electrooxidation on gold catalysts with the exception of this research in which gold is proposed as a potential catalyst for use in the electrooxidation of HCOOH at low temperature. Gold nanoparticles on a carbon support has demonstrated excellent activity

33

for oxidation of different small organic hydrocarbons such as CO oxidation, alcohol and formic acid [103, 104]. For example, Haruta (2001) confirmed that the Au catalysts demonstrated excellent activity for the water gas-shift reaction, hydrogenation of unsaturated hydrocarbons and liquid-phase selective oxidation on Au/TiO_2 [105]. Redina *et al.* used Au-Cu catalysts prepared by a redox method in the selective oxidation of ethanol to acetaldehyde. Au and Au-based supported catalysts show promise as viable candidates for application in other systems (e.g. formic acid oxidation). In this thesis, AuCu on Vulcan XC72 carbon is investigated for the oxidation of formic acid for application in direct formic acid fuel cells.

2.8   Catalyst Formulation and Preparation

2.8.1   Palladium catalysts

Platinum (Pt) and platinum-based catalyst electrodes have been widely used and investigated for low-temperature fuel cells due to their high reactivity. However, extensive studies of Pt catalyst electrodes were found how they follow the indirect electrooxidation pathway, which is often severely poisoned by the strongly adsorbed CO intermediate [11, 13, 20, 58, 63, 84, 106-110]. Also, the high cost and limited availability of Pt prevents the wide deployment and commercialisation of DFAFCs. In order to increase utilisation and reduce cost (*less use of material*), supporting materials with a large surface area and bimetallic catalysts are viable options for investigation [111-115]. In recent years Pd (or Pd-based) catalysts have attracted more attention for formic acid electrooxidation [43, 82, 84-86, 116-118] because of their better performance towards anodic oxidation of formic acid in direct formic acid fuel cells

(DFAFCs). In contrast to Pt, Pd follows the direct pathway with no-CO absorbed intermediate species and deactivation [23, 34, 81, 119-126]. Also, the application of Pd and Pd-based catalysts in rechargeable lithium-air batteries have shown an excellent performance of up to 336 mAh (g solid)$^{-1}$ discharge capacity compared to other catalysts (Pt-C, Ru-C, RuO$_2$-C and MnO$_2$-C) [127]. These studies strongly suggest that Pd and Pd-based catalysts have potential in a range of energy storage/conversion applications. However, the electrooxidation activity and durability of Pd anode catalysts are still insufficient due to several, poorly understood oxidation mechanisms of Pd surface reactions, poisoning from non-CO organic species [128], the effect of temperature, and anchorage of the metal particles on the carbon support.

So far recent research based on different synthesis routes for Pd or Pd-based catalysts for have been investigated. Among them, Xin *et al.*, using an impregnation method, prepared Pd on phosphorus-doped carbon nanotubes. They concluded that the electron transfer from Pd to the Phosphorus-doped carbon support was due to the Pd3d electron density improving the FAO catalytic performance [129]. Hu *et al.* synthesised Pd-C, PdNi-C, PdCu-C, and PdNiCu-C alloys with a polyvinyl alcohol capping agent through an aqueous solution reduction using sodium hypophosphite as the reducing agent [130]. They conclude that the relationship between electronic structure and the electrochemical activity towards FAO was achieved via a metal salt reduction method.

2.8.2 Gold catalysts

It is well known that gold and gold-containing catalysts are very effective for heterogeneous and homogeneous catalysis. In particular, gold is widely recognised

since pioneering work on low-temperature CO oxidation and acetylene hydrochlorination reaction [105, 131-135]. Gold is an excellent catalyst for redox reactions and selective oxidation of small organic molecules, such as alcohols and formic acid [136]. Most recently, gold and gold-based catalysts have been reported to show a very promising performance in the C-H activation reaction [137].

Early researchers identified that the methods of preparation of gold catalyst play a vital role in its catalysis. This is especially true for the CO oxidation reaction when co-precipitation and deposition-precipitation methods were used to prepare small nanoparticles. This led to the misinterpretation that the observed high reactivity was solely due to the particle size. With advances in aberration-corrected STEM, Au supported catalysts CO oxidation was associated with small bilayer clusters.

Another unique observation of gold catalysis is the influence of support material, for example, the replacement of carbon support in acetylene hydrochlorination reaction leads to inactive catalysts. This strongly suggests the influence of the type of support material and the presence of peripheral sites for gold anchor and on its reactivity [137]. Superior qualities due to cooperative effects of support materials have been reported for noble metals in practical applications: high-resolution biomarkers and long-term durable catalysts [138]. Gold and gold-based catalysts have potential in a broad range of potential in biosensor and biomedical applications because of the stability in neutral aqueous and acidic environments. Because of the Au-specific surface functionality and the unique surface plasmon resonance absorption band, AuNPs can be used for treatment with chemical or biomedical agent: An example gold application is colorimeter sensors for detection of Melamine in infant formula [139, 140]. Gold catalysts' oxidative selectivity is earning praise because of the promising response to environmental restrictions for a progressive shutdown on tradition preparation methods, causing undesired toxic by-products [141].

The electrochemical oxidation of formic acid confirmed that on Au catalyst showed favourable kinetics given the high selectivity of gold catalysts and its high resistance against surface oxides for small organic molecules [142-144]. Pt-based catalysts suffer CO poisoning at the operating temperature of PEMFCs (80-120 ^{o}C), but monometallic Au catalysts have been reported to reach 100% CO conversion without any poisoning effects. However, the problem of agglomeration and deactivation constrains the Au practical application of Au in FCs [18, 145-150]. There have been previous studies that identified Au and Cu catalysts to possess an intermediate binding strength favourable for C_1 hydrocarbon reduction, and as a starting point to tune the energetics of the intermediate binding to achieve higher electrochemical activity [151].

2.8.3   Catalysis by Gold

Gold is a noble metal. The nobility of a metal is the ability of the metal to chemisorb dissociated oxygen, i.e. the ability of the metal surface to oxidise. Metals located above and to the left of Au in the periodic table show increasingly high chemisorption energies but Au binds weakly to oxygen (see Figure 2.6). Au metal has an endothermic chemisorption energy which indicates that it does not bind to oxygen at all (Au is inert in air).

37

Cr	Mn	Fe	Co	Ni	Cu
		-6.30	-5.07	-3.90	-2.51
Mo	Tc	Ru	Rh	Pd	Ag
-7.48		-4.62	-4.03	-1.20	-0.65
W	Re	Os	Ir	Pt	Au
-8.62			-4.65	-2.17	+0.54

Figure 2.7: Oxygen dissociative chemisorption energies on some transition metal surfaces [152]

The chemical bond associated with Au and oxygen the coupling valence state and *d*-state of Au is net repulsive because of the low energy interaction with oxygen $2p$-state [152]. Therefore, Au is not likely to be a suitable catalyst at all for the oxidation of methanol and formic acid. Au is chemically inert but at the nanoscale level (<5 nm) can be a very reactive catalyst. These dramatic changes may be attributed to several explanations in the literature including quantum size effects [101, 153], and the role of the very low-coordinated Au oxidation state [30, 154, 155]. Others are charge transfer to and from the support [156] and oxygen spill-over to and from the support [157, 158]. All these effects may occur simultaneously or interplay with different factors during the reaction process.

Gong and Mullins (2009) reported the unique properties of gold, which make it a potential model system for investigating oxidation chemistry. Gold has a high ionisation

potential (9.2 eV), work function (5.3 eV), electron affinity (2.3 eV) and is a weak electron donor. When oxidised by chemical treatment, cationic gold shows high reactivity [159]. Small gold particles (both polycrystalline and single-crystalline) under electrochemical conditions can significantly oxidise formic acid in acidic media, whereas it is inactive for methanol and formaldehyde [150]. The properties and behaviour of Au nanoparticles differ completely from bulk material. For example, their melting point, density, lattice parameter, and electrical or optical properties change when particles are nanosized. From the studies above, the exact catalytic properties of a particular catalyst are subject to the interplay of different effects. These effects would depend on other factors such as system temperature and electrode properties (size, shape, crystallinity, electrolyte-electrode interface). The most dominant effects will be considered in the determination of the catalytic property of a catalyst. The improved activity, selectivity and stability of gold catalysts in various reactions advanced the research and progress to numerous commercially oriented patents [105, 160]. However, the origin of the unique nature of gold reactivity at the nanoscale level is still not understood.

2.8.4   **The effect of temperature on the properties of nanoparticles**

The properties of Au nanoparticles, such as crystallinity, can be affected by the change in temperature as a function of particle size. The state of crystallinity can be defined as the deviation of each Au atom from its location in a perfect face-centred cubic (fcc) crystal structure, i.e. the degree of disorder. Heating at elevated temperatures (e.g. sintering process) results in the formation of multiple grains (polycrystalline particles)

that transform into a single crystal at sufficiently long sintering conditions. In their report, Goudeli and Pratsinis demonstrated the effect of the melting temperature of Au nanoparticles (1.5-11 nm) using the Lindemann index method to trace the thermally driven disorder of the sintering process.
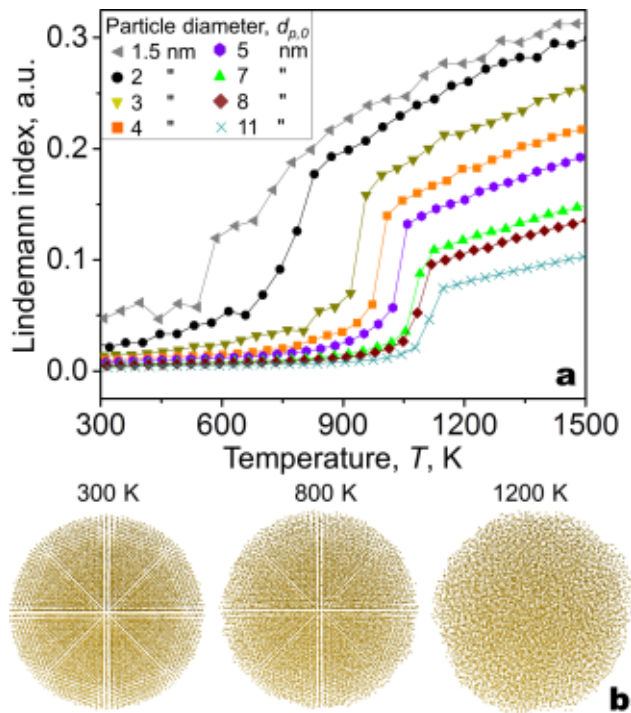
Figure 2.8: Evolution of the average Lindemann index of Au particles of various diameters as function of temperature during heating from 300 to 1600 K for 5 ns. (b) Snapshots of Au nanoparticles with $d_{p,} = 8$ nm at T = 300, 800, and 1200 K. (Reproduced with permission from [161])

Figure 2.7 shows that at low temperatures, the Lindemann index was small but change abruptly as the temperature increases indicating melting (liquid-like state). For small nanoparticles (1.5-2 nm), the index value increases gradually with temperature compared to the abrupt/steep increase in the Lindemann index for large nanoparticles. The perfect Au fcc structures say at 300 K fades away inwards from the surface of smaller nanoparticles to amorphous or liquid state (layer of disordered atoms) at 800 K (see Figure 2.7b). Figure 2.8 shows that at even higher temperatures, the crystalline fcc

structure is completely lost at about 1200 K when the melting point is exceeded. However, larger Au nanoparticles (≥10 nm) maintain their fcc structure, indicating that increasing the particle size increases the melting point, which gradually approaches that of the bulk Au (T_m = 1337 K). Goudeli and Pratsinis in their study concluded that the nanoparticle grain orientation as a function of temperature affects the morphology of the nanoparticle depending on the crystal surfaces exposed and the temperature conditions.
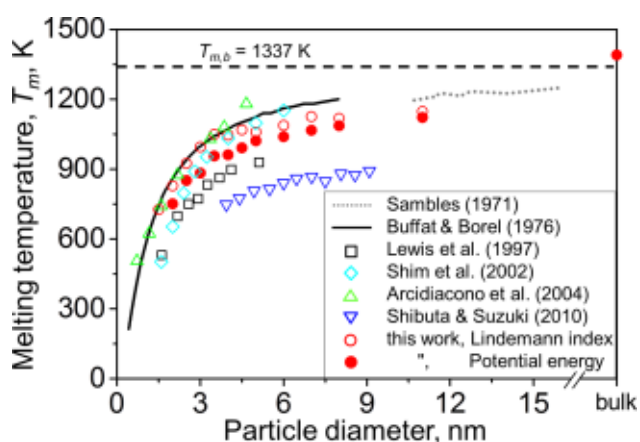
Figure 2.9: Melting temperature, T_m, of Au nanoparticles obtained by the Lindemann index and the change in potential energy as a function of their nanoparticle diameter (Reproduced with permission from [161])

In their study, Guisbiers and co-workers demonstrated the effect of size and shape on the catalytic properties of palladium from a thermodynamic approach [162]. Pd can exhibit different geometries, which affect the thermodynamic properties such as melting temperature, melting enthalpy, and catalytic activation energy of the system. For nanoparticle size below 4nm, the surface energy change significantly with by the size, edges and corners of the Pd nanostructures and also depends on the geometric shapes as shown in Figure 2.9. On the basis of their findings, they confirmed that a dodecahedron is the most stable geometry for palladium, but it depends on the synthesis process and

thermodynamic equilibrium of the system under investigation. These studies do not indicate any optional particle size depends on several factors such shape stability, thermal fluctuations, synthesis procedure than just minimization of the area volume ratio.
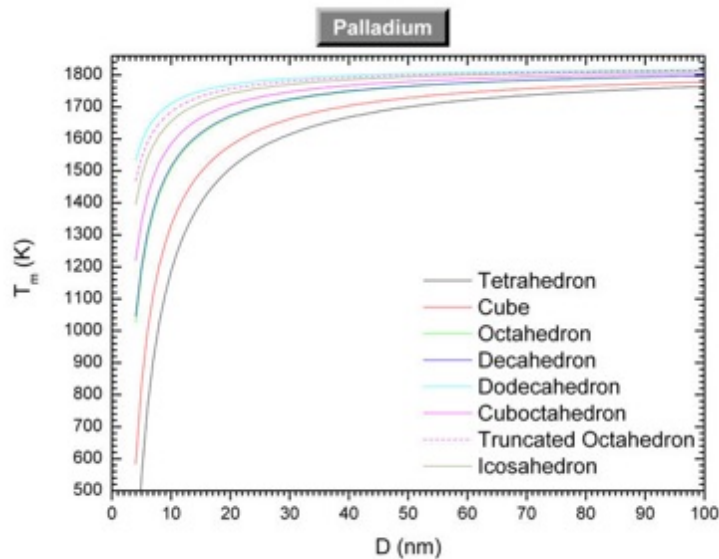
Figure 2.10: Size-dependent melting temperature of palladium versus the size of the different shapes [162]

2.8.5 Availability

Fuel cell technology currently uses platinum group metals (PGMs) as choice catalysts. Advances in fuel cells concerning cost-performance strategy require the decreased use of PGMs contents in catalysts and the development of non-noble metal catalysts (i.e. US$/kW price Metal) [163, 164]. The shift from Pt-based catalysts has shown a trend in the volume of research efforts to develop new non-noble metal catalysts. The decline in the mining of Pt, Pd and the increasing application of Au has led to a higher volume

of Au mining. The significant higher cost of Au is in line with industrial demand and the drop in usage of Pt and Pd in vehicle exhaust cleanup catalysts (see Table 2.5).

Table 2.5: The price of Pt, Pd and Au precious metals in Oct 2017

	Pt (USD)	Pd (USD)	Au (USD)
Price (USD)	963.00/Troy ounce	969.00/Troy ounce	1266.50/Troy ounce
	30.96/gram	31.15/gram	40.72/gram
Ratio	1	1.006	1.315

Source: https://apps.catalysts.basf.com/apps/eibprices/mp/defaultmain.aspx (1 Troy ounce = 31.1035 gram)

The potential benefits that gold catalysts offer compare to other precious metals is the greater stability of price, greater abundance in comparison with Pt and Pd, and Au being substantially cheaper (on a weight for weight basis). Gold has shown a remarkably stable price compared to widely fluctuating Pt and Pd, which have exceeded that of gold since 1998 [163, 165].

2.8.6   **Potential applications**

The superior performance of PGMs was attributed to the strong tendency towards chemisorption processes. Gold was believed to fail as a catalyst due to the low strength of chemisorption [166]. The earliest catalytic application of gold as catalysts was in research work by Bone and Wheeler (1906) in the oxidation of hydrogen in 1906 [166, 167]. High activities of gold were demonstrated with only 0.01 – 0.05% silica supported

gold contents showing 7000 times the turnover frequencies in comparison with other catalysts for double-bond isomerisation reaction [168].

Nanoparticle gold (AuNPs) catalysts under mild conditions have continued to show excellent catalytic activity, even below 0^oC which if this property is suitably tailored may lead to many useful applications. Gold and Au-based catalysts have found applications in pollution and emission control, chemical processing of speciality chemicals, clean hydrogen production/fuel cells, sensors, biomarkers and drug delivery [165, 169]. In fuel cell applications, three distinct areas where gold catalysts can be used have been identified: water gas shift for clean H_2 production, oxidative removal of CO from H_2 feedstock within fuel cell membranes, and gold as electrocatalysts for fuel cells [164]. Gold and Au alloys have significant applications in dentistry and drugs for the treatment of arthritis, and excellent potentials for chemotherapy [165]. Previous studies have reported that AuNPs have unusual optical properties, size-dependent electrochemistry, drug delivery, and catalysis [170, 171].

AuNPs are used in cancer therapy applications such as cancer therapeutic agents or cancer cell imaging and are critical components in hyperthermia and thermoablation treatment methods [172]. Gold nanoparticles are used in conjugation with antibodies or grafted to other carriers for surface property enhancement. Other important properties of nanoscale gold materials are its low electrical resistivity (2.21 $\mu\Omega$ cm), its inertness and resistance to sulphur-based tarnishing. These unique attributes of gold render it suitable for implantation due to its biocompatibility when compared to most metals, for electrical interfacing with cells and tissues in the nanobiological applications [173]. The unique properties of gold nanoparticles demonstrated the wide application in medical, environmental, catalysis and energy technologies giving it a broad spectrum of its potential application.

2.8.7 **Effect of particle size**

The effect of particle size is key in the determination of the properties and in particular, the unique characteristic of any nanomaterial in catalysis. In electrochemistry, the particle size of the nanomaterial plays great role in determining the available surface area (ECSA, CSA) for the electrochemical activity of the particular system. The larger the active metal surface area the greater the reactive surface and the amount of energy generated from such systems. To be more specific, electrooxidation reaction involves surface atoms; reducing particle size is cost effective because of the increased dispersity (ratio of surface atoms to the total number of atoms) of the catalysts. The cuboctahedral geometry provides a model for the description of the metal nanoparticle surface atoms. With decreasing size these surface atoms have a relatively abundant corner, edge and reducing terrace surface atoms. This effect leads to an undercoordinated catalyst with altered *d*-band energetic and interatomic lattice spacing, which negatively impacts particular catalyst activity [174-176]. Lopez and Norskov, and Liu *et al.*, demonstrated the role of gold in gold-based catalysts by a density function theory study on CO oxidation on Au. The effect of particle size of the Au nanoparticles on the electroactivity were confirmed by Rice and Wieckowski in their study of the electrocatalysis in fuel cells using a non- and low-platinum approach.

The effects of Au particle size in various reactions (homogeneous/heterogeneous) have been investigated [177-181]. It is clear that with decreasing Au particle size, there are a number of effects [166]:

a) There is an increased fraction of surface atoms, leading to a decrease in melting temperature and increased mobility of surface atoms.

b) There is a weakened bond structure because of the decreased overlap of electron orbitals, making atoms display unique characteristics.

c) Increased fraction of atoms in contact with the support.

d) Small Au particles on support extracts oxygen ions to give surface anion vacancies on which oxygen molecules can absorb as superoxide ions (O_2^-)

Au catalysts general show a remarkably structure-sensitive quantum size effect for most reactions, particularly below 5 nm particle sizes [182, 183]. It has been reported that the size, shape and activity depend on synergistic relationships between the synthesis method and the interaction between the support with a varying fraction of edges, corner and terrace atoms [177, 184-187]. Sun *et al.* demonstrated the electrocatalytic changes with the variation of the core size and shell thickness of Au-based catalyst leading to enhanced performance.

2.8.8 Nature of active sites

The function-structure relationship at the nanoscale depends strongly on the thermal, mechanical and optical properties, and also on the particle size, shape, composition, crystallinity and chemical interface [177, 188]. The structure of the active site remains elusive, because (1) the sites are on or near tiny gold particles that are structurally difficult to characterise, and (2) the Au surfaces are heterogeneous and structurally ill-defined. However, the following reasons for the high activity of Au catalysts have been proposed [189]:

- Active sites are a combined synergy between the surface of the oxides (usually defects or edges) and the Au nanoparticles.

- The presence of neutral gold atoms on the Au NPs. These atoms are different in 3 ways:

  (i) They have few near neighbour atoms (high degree of coordinative unsaturation)

  (ii) They alter the electronic band structure of Au NPs due to quantum size effects

  (iii) Partial electron donation to Au clusters due to electronic modification between the oxides support and Au NPs.

The nature of active sites remains a matter of debate in catalysts, especially over Au-based catalysts. However, it is clear that the size of metal crystallites, crystal planes, strain defects, the catalyst support interface, or the electronic effect for alloys and core-shell architectures are important properties to understanding their catalyst activity. Metal surface properties (electronic effects, nanosize) play a key role in the modification of the catalytic activity of nanocatalyst. From a crystallographic point of view, metal with a fcc crystal structure has arrangements of low index atoms (100), (110) and (111). These low index planes are reported to be very stable compared to higher index planes and can be polished to give very smooth and uniform surfaces. The electrode properties depend strongly on the index plane, which is limited by defects from grain boundaries, dislocations, pits and depression. The focus of nanomaterial scientists is to develop a low index plane catalyst with an efficient catalysis process. The most common crystal structure is the polycrystalline structure (a mixture of low and high indexes), which comprises different planes exhibiting different electrochemical behaviour and reactivity.

2.8.9 Influence of preparation methods on catalyst properties

The synthesis method depends on the preparation procedure employ, and the support used. Catalyst particle size and metal-support interaction have a profound influence on the activity and selectivity of the whole catalyst. The choice of a suitable preparation method depends strongly also on the desired application (homogeneous or heterogeneous catalysis). Chemical synthesis is an excellent and efficient method for the preparation of well-controlled size and shape, with a slight small amount of crystal defects. However, most synthesis methods are limited to one form of nanocrystallinity, i.e. single-domain or polycrystalline [177].

There are two methods of preparation of metal nanoparticles via physical and chemical methods. Physical methods involve subdividing bulk precursors to nanoparticles (e.g. solid grinding). In chemical methods, metal precursor ions or molecules are reduced to metal atoms, followed by aggregation of the atoms to particles, clusters and grains. Chemical methods are most suitable for obtaining small and uniform particle size distribution, with control of atoms as the most important step for determining the size and uniformity. Two processes involved in chemical synthesis are the (i) reduction of metal ions or molecules to zero-valent atoms and (ii) coordination of the stabilised polymer/ ligands to metal nanoparticles [190]. Chemical preparation methods found in recent literature can be subdivided: impregnation, deposition-precipitation, and co-precipitation. Other special impregnation techniques are chemical and vapour-phase deposition, metal-sol immobilisation, and solid grinding [191-193]. Haruta and coworkers concluded that impregnation could not lead to the high dispersion of gold over metal oxide supports using precipitation and deposition-precipitation methods [194]. Further study is required to determine the most suitable method depending on support materials and type of application for the specific catalyst.

In chemical synthesis, nanoparticles are produced from metal precursors using reducing agents and suitable stabilisers. Using a stabilising agent offers an easy method for controlled nanoparticle synthesis to prevent excessive size increase and agglomeration of as-synthesized nanoparticles. There are different types of chemical synthesis and catalysis of polymer- and ligand-stabilized NPs such as the alcohol-reduction method, organic ligands- phosphine group, thiol, citrate [123, 190, 195-202]. For example, different Au nanoparticle size ranging from $2 - 10nm$, were obtained by reducing chloroauric acid with $NaBH_4$ in the presence of stabilising agents such as polyvinyl alcohol (PVA), polyvinylpyrrolidone (PVP) and tetrahydro methyl phosphonium chloride (THMP) and glucose [203-205]. The choice of a stabiliser depends on the role required for a particular synthesis route. These ligands or polymers are generally solvent soluble, with an affinity for metals. They control the rate of metal ion reduction and the growth processes of nanoparticles. Biella *et al.* reported that using tetrahydroxymethyl phosphonium chloride (THPC) resulted in 2-3 nm-sized particles of Au but the protection provided by the phosphonium salt was unable to preserve the mean particle diameter when immobilised on the carbon support. Also, using poly (diallyl dimethyl ammonium chloride (PDDA) with $NaBH_4$ as reducing agent suffered the same fate as THPC with enlargement of nanoparticles being observed. It is clear that a synergy between the reducing agent and types of precursors, stabilising agent, and other synthesis conditions require interplay between parameters to determine the optimal conditions for nanoparticle preparation.

The effect of the presence of reducing agent on the dimension and size distribution of the gold particle is very high, the decrease in particle size correlates to an increased amount of $NaBH_4$ (i.e. increasing the rate of the reduction). Sodium borohydride has a small reaction-initiation temperature, is stable in air and nonflammable in solution. It

also has an environmentally benign hydrolysis product: sodium metaborate, $NaBO_2$ (Equation 2.1) [206].

$$NaBH_4 + 2H_2O \rightarrow NaBO_2 + 4H_2 \qquad\qquad 2.1$$
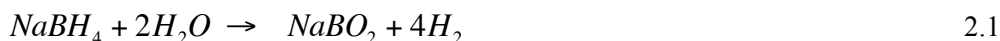
Biella *et al.* found that Au particle dimension was 5.4-5.9 nm for carbonate and 8.8-10 nm for hydroxides and concluded that the type of anion principally influenced or determined the particle size, while the cations determined its location. For carbonates activity increased $Na^+ > Li^+ > K^+$, whereas for hydroxides $Li^+ > Na^+ > K^+$ [16]. Li_2CO_3 as base showed very poor catalyst for pH control to 8 [Li^+, Na^+, K^+, and NH_4^+].

Wang *et al.* showed the controlled synthesis of AuCu alloy without the use of a surfactant in the synthesis process. Carbon black was used instead of a surfactant, which is detrimental towards catalysis by blocking catalyst active sites. Instead Vulcan XC72 was used as the dispersant which they observed improved the particle size and nanoparticles dispersion of the synthesis method [207].

Au catalysts are very sensitive to the preparation procedures, hence there is a high degree of variation in the oxidation activities of these catalysts. Kung *et al.* reported the problem associated with the use of chloride-containing precursors for supported Au catalyst preparation. The residual chloride has a negative impact on oxidation activity, facilitates the agglomeration of Au particles during heat treatment, and directly suppresses catalytic activity due to the poisoning of active sites [208]. This is the reason for the choice the room temperature synthesis route, washing with deionised water until pH is neutral for the Au and Au-based catalysts in this research work, rather than the high temperature impregnation method. PVP is soluble in a polar solvent and can be easily removed by washing with pure ethanol before use and without blockage of active sites in catalytic applications. NaOH plays the critical role of protective coverage from the reduction of H_2O in the synthesis process.

2.9 Bimetallic Catalysts

Bimetallic catalysts are an important class of heterogeneous catalysts with the combined catalytic properties of two metals to generate bifunctional or multifunctional properties. The structure of bimetallic catalysts strongly depends on several factors, such as synthesis route and conditions, metal-metal bond strength, surface energies of bulk metals and their oxidation state. Liu and co-workers conducted a detailed review of the six different bimetallic catalyst structures (see Figure 2.10) currently investigated: crown-jewel structure, hollow structure, hetero-structure, porous structure, alloyed structure, and core-shell structure [209].
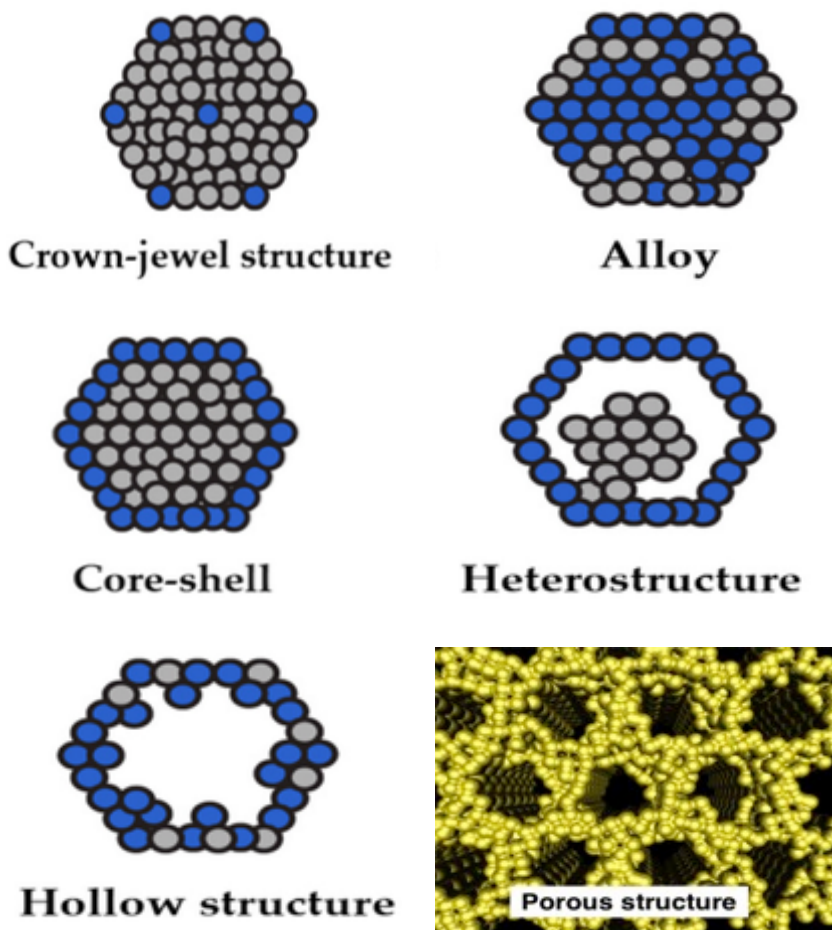
Figure 2.11: Schematic diagram of different bimetallic nanostructures: crown-jewel structure, alloyed structure, core-shell structure, hetero-structure, hollow structure, and porous structure [191]

Controlled structure bimetallic nanoparticles, such as core-shell particles are attractive owing to their novel optical, electronic and catalytic properties when compared to their monometallic counterparts. Core-shell NPs are unique due to their essential nanostructure design when controlled synthesis is used. These can be used to develop new bimetallic nanomaterials with some degree of specificity for catalytic and optical properties [210]. Bimetallic (core-shell) catalysts are of interest from both technological and scientific perspectives for improving the catalytic properties, advancing understanding of catalytic activity and controlling particle structure [190].

Recent efforts in formic acid electrooxidation have shown focused more on bimetallic catalysts due to their slower deactivation, higher reactivity and specificity in the

selection of reaction pathways (resulting in less vulnerability to CO poisoning). The addition of a second metal decreases the *d*-band centre with respect to the Fermi level and thus weakens the adsorption of reactive intermediates. The catalytic and electrocatalytic properties of metals are tuned by controlling the size and morphology of the elements because of the unique inter-metallic interactions.

Recent extensive studies have revealed bimetallic (core-shell) catalysts as promising new catalysts for electrochemical reactions because of their enhanced catalytic efficiency for energy conversion [184]. The core-shell structure provides an excellent method for nanostructuring of Au-based catalysts. They provide good rational tuning of the shell atom geometric distance and the electronic structure through core materials and structures. Jin and coworkers suggested that the shell atoms, when deposited epitaxially (*i.e. deposition of overlayer on a crystalline substrate*) on the core, create some level of tension or compression, which causes reaction species to alter catalytic behaviour and optimise specific reaction mechanisms [211]. Au-shell provides an excellent study for efficient cost design to improve the utilisation of expensive and highly active PGMs by depositing them as thin shells on base metal core nanoparticles [209]. Others focus on improving the catalysis (catalytic activity and selectivity) of the bimetallic catalyst. This will, however, require a controlled synthesis technique. For example, electrochemical syntheses of core-shell bimetallic catalysts do not produce the homogeneous structures. This will hinder or reduce the electrocatalytic activity towards the oxygen reduction reaction (ORR) and the formic acid oxidation reaction.

Core-shell nanoparticles have been identified to have enhanced electrocatalytic activity due to characteristics such as the synergetic property between the layers of the core and shell, the bi-functional contact configuration, high surface-to-volume ratio and the quantum effects due to particle size. In the literature, many researchers have proposed a

combination of strategies to enhance catalytic activity such as chemical/physical methods and experimental conditions. Others are the selection of metal precursors, types of reducing agents, mole ratio variation of precursors and controlling reagents in the procedures of designing a practical core-shell bimetallic particle system [212]. AuCu catalyst is not an exception to the catalytic activities, selectivity and/or deactivation properties of bimetallic catalysts, which can be considerably more favourable than monometallic catalysts [213] and due to the electronic effects with their small size and large surface areas [214]. The catalytic synergy between Cu promotes Au catalysis is not exactly well known for most chemical reactions. However, it is well established that the high surface-to-volume ratio and the contact between core and shell configuration contribute to the enhance electrocatalytic activity. With regards to core-shell nanoparticles, surfactants help to stabilise the highly oxidative copper nanoparticles and ensure they are well dispersed during the synthesis process.

A considerable amount of literature has been published on bimetallic catalysts. These studies have shown that the remarkable ability of bimetallic catalysts to demonstrate a significant increase in reactivity, selectivity and stability of oxidative processes [22, 46, 79, 100, 131, 148, 215]. The synergistic effect of the bimetallic catalyst due to admetals (second metal addition) has been attributed to generating the superior catalytic activity. Liu *et al.* demonstrated the excellent synergistic effect of Cu addition to Au enhanced the catalyst activity for CO oxidation [149, 216]. The performance of DFAFCs electrooxidation processes can be made to be cost efficient by improved utilisation of the anode catalyst via core-shell architecture. Intermetallic catalysts such as alloys have the problem of dissolution of non-metal components leading to poor long-term durability under reaction conditions [186]. Recent trends in controlled synthesis strategy have led to a proliferation of studies for preparing well-defined and durable nanocatalyst structures [207]. Nanostructuring of gold-copper catalysts provides an

efficient design to improve the utilisation of expensive and highly active noble metals as a metal shell (gold) on a copper (core). Hsu and co-workers recently reported that the reason Au/Pd core-shell catalyst demonstrated superior electrochemical stability was due to the electronic effects of Au and Pd in comparison with commercial and monometallic catalysts [217]. Mao *et al.* reported only a 10% metallic loading of Au, in a PdAu/C catalyst with high catalytic activity and stability of 1700 mA mg^{-1} peak current density for ethanol oxidation [218]. The synergistic effects of bimetallic catalysts are the result of combinations of different factors. The interaction of reactants, compositions and experimental condition, limit the direct correlation between bimetallic systems and catalytic properties [104, 219]. Ren and co-workers confirmed that the downshift of the *d*-band centre within catalysts increases lattice strain due to copper addition to the bimetallic catalysts improving the overall catalytic performance of formic acid [114]. A recent review of the literature on factors affecting the catalytic activity of bimetallic catalysts in different chemical reactions is summarised in Figure 2.11.
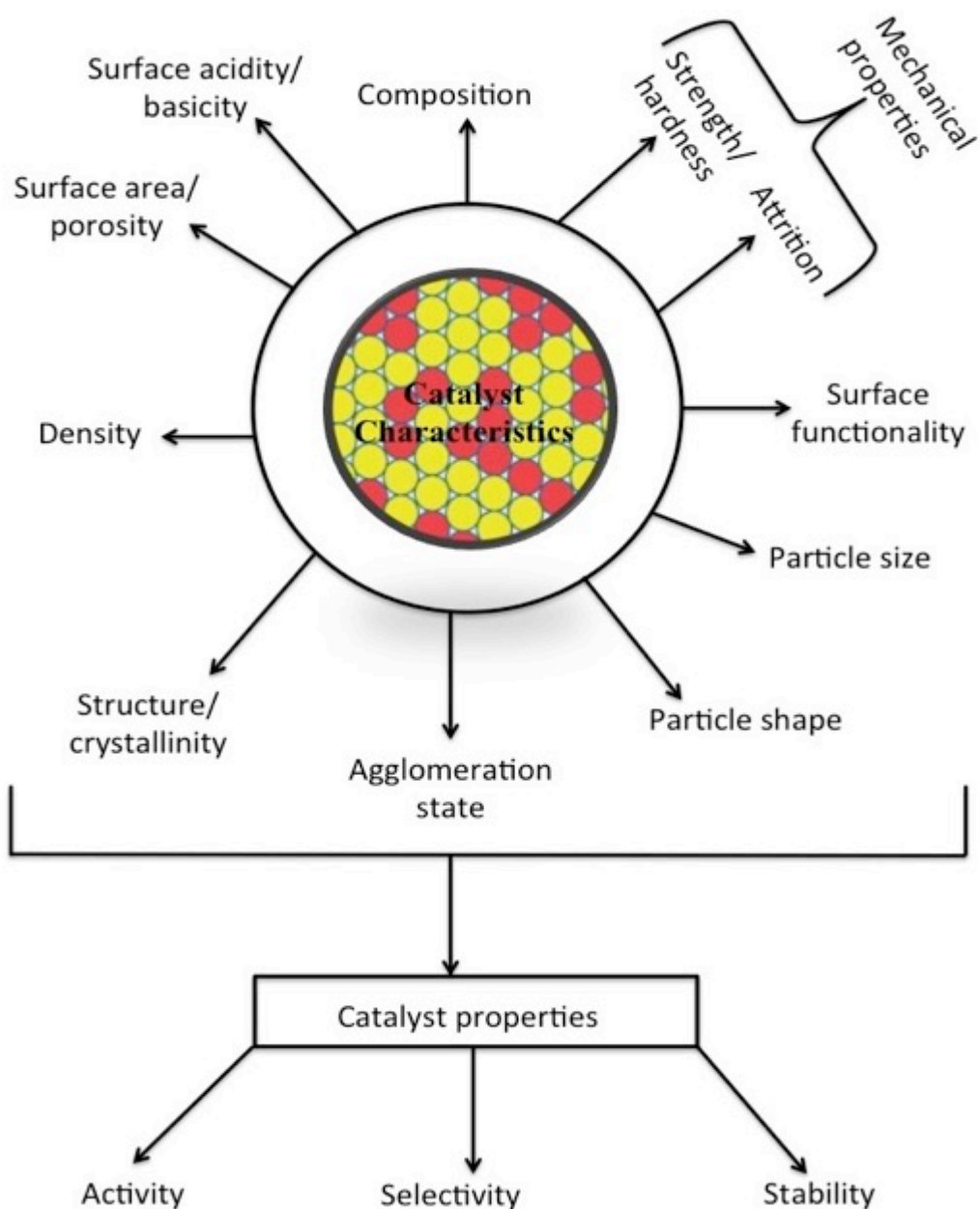
Figure 2.12: Synergistic relationships affecting the catalytic activity of bimetallic catalysts in different chemical reactions [adopted from ref:[191, 220]]

2.9.1 Recent Advances in Electrocatalytic Applications of Bimetallic Catalysts

Some electrochemical oxidation reactions establishing the higher catalytic activity where Au/ or Cu base bimetallic catalysts were employed are presented. Supported AuCu intermetallic nanoparticles on carbon were used for the oxygen-reduction oxidation in 0.1 M KOH; Wang *et al.* confirmed that ordered structured AuCu

nanoparticles exhibited superior catalytic activity compared to Au monometallic catalyst [207]. Cu-Pd nanoparticles alloy on carbon for 0.5 M HCOOH + 0.1 M HClO, with higher resistance to surface poisoning Dai and coworkers compared their findings to Pd and concluded that the enhanced activity was due to the presence of Cu content [68]. Bauer and coworkers studied silica supported AuCu nanoparticle alloy catalysts for CO oxidation reaction, they attributed the catalytic activity to the interplay between the stabilized catalyst with the amount oxide support and alloyed nanoparticles [215], Au-Pd core-shell nanoparticle catalyst were used for formic acid electrooxidation in 0.5 M HCOOH + 0.1 M HClO, Han *et al.* concluded that the morphology and structure along with the synergy between the two metals resulted in high activity [221], AuCu-C electrocatalysts for direct borohydride-hydrogen peroxide fuel cell (0.1 M NaBH4 + 3.0 M NaOH solution). Cu acts as an electronic promoter for Au, and this enhances the catalytic activity and selectivity significantly compared to monometallic counterparts [222]. It is clear that the effect of adding a second metal contributed greatly to the overall performance of the bimetallic catalyst with improved catalytic properties. These properties do not however correlate across all researchers, as there are different parameters observed, such as morphology, structure, selectivity, resistance to poisoning/deactivation. Bimetallic catalysts improved catalytic performance compared to their monometallic counterparts.

2.9.2 Influence and advantages of using copper in bimetallic catalysts

The reason for using Cu to enhance catalytic the activity and stability of Au nanoparticles on a carbon support is mainly due to selective CO removal in fuel cells oxidation processes [68, 69, 223-228]. Cu has much lower *d*-band centre of ca. -2.67

eV and a small atomic size, thus an ideal bimetallic component to tune down the d-band of noble metals (Pd, Au) [229]. Specifically, XPS investigations confirm the effect of d-band centre theory and the influence of admetal formation on the strain and ligand effects. This causes the shift in the d-band centre of primary metals such as Pt or Pd relative to the Fermi level (*the total electrochemical potential for electrons*). This, in turn, can also change the surface chemistry of catalysts by weakening the bonding strength of adsorbates, thus modifying the overall reactivity. The electrocatalytic activity of Pd catalyst for formic acid oxidation increases significantly by a d-band shift of ca. -1.83 eV, taking advantage of the strain and charge transfer effects [130, 229]. Landi and coworkers recently established the key role of copper by confirming that Cu inhibited CO formation on Fe-promoted CuO/CeO_2 with easier CO_2 desorption at a higher temperature [230]. Lee and Chen demonstrated that incorporation of a Cu ion into the CeO_2 lattice increased the oxygen storage capacity and removal of CO in the H_2 stream by suppressing H_2 oxidation in FCs operation on $Au/CuO-CeO_2$ catalysts [231-234].

The addition of a second metal enhances the behaviour of the active metal in the bimetallic catalysts. Differences in morphology, electronic, geometric and compositions have been controlled and have demonstrated improved performance due to modification of the second metal. Several groups have reported the applications such as Ni, Sn [235], Co, Fe [236], Cu [216, 225, 237], Ag [238], and Pd [218, 239]. For example, Mao *et al.* demonstrated the effect of the electronic structural modification on Pd by Ru, Pt and Au. Using XPS analysis to investigate the electron structures and valence states of the catalysts, they observed the existence of electron interaction between Pd and the modified metal. The Pd d-band centre shifts for Ru, Pt and Au are 0.5, 0.6, and 0.4 eV. The electronic change showed enlargement in the ECSA for Pd/C, PdRu/C, PdPt/C and

PdAu/C as 65, 60, 62.8 and 67.8 m^2 g^{-1}, respectively. Overall, PdAu/C showed better performance and about twice the stability than the other three catalysts [218].

The relative lack of control of the metallic nanostructure at the synthesis level in bimetallic catalysts remains a subject of considerable academic and industrial interest. This lack of control can lead to size and compositional variations, agglomeration of nanoparticles and a mixture of monometallic and bimetallic particles [213]. Investigation of the new synthesis routes for the bimetallic catalysts is crucial for high performance and efficient catalyst utilisation to be achieved.

Chapter 3 Experimental Techniques

3.1 Introduction

In the previous chapter, a review of catalyst preparation methods, the catalysis of gold nanoparticle and applications were presented. Also, descriptions of various physicochemical properties influencing catalyst performance were discussed. This chapter describes the different experimental techniques employed for the preparation and physicochemical characterisation of catalysts. The scientific principles, fundamental theories and the reason for the choice of technique are presented.

The characterisation of energy storage/conversion systems and nanomaterials is based on the evaluation of physicochemical properties such as composition, purity, energy content, and stability. For nanomaterials, several characteristics such as particle shape/ size, surface composition, structure, porosity/pore size, surface charge/energy, are crucial. Detailed investigations to understand these parameters, which influence the catalyst behaviour in energy systems is vital for its development. The choice of the technique will be to correlate the properties of the synthesis materials with the exact structure of the particles, e.g. core-shell structure. Addressed below are brief descriptions of different techniques used to examine specific physicochemical properties of the nanomaterials.

3.2 Electrochemical Measurement: Cyclic Voltammetry (CV)

Cyclic voltammetry (CV) is the most widely used electrochemical method, providing information on the thermodynamics of redox and adsorption processes, and the kinetics of the electron transfer reaction. CV is an electrochemical measurement technique to determine the half potential linear ramp with time to obtain a peak current versus potential plot called a voltammogram [240]. During CV experiments, the voltage on the working electrode (WE) is scanned linearly with time from no reaction to where oxidation or reduction of the species takes place in the analyte under investigation. Oxidation will occur if the working electrode potential rises above the equilibrium potential, whereas reduction occur if it is below the equilibrium potential [241, 242]. The peak currents is inversely proportional to the concentration of the electrolyte, demonstrating CV as an excellent quantitative analytical technique. The main relevant parameters obtained from a cyclic voltammogram are the two peak currents and the two peak potentials (anodic and cathodic). There are two primary processes where CV analysis is often used firstly, to determine if a process, reversible (or Nernstian) – meaning fast electron transfer process or mass transport-limited. The Randle-Sevcik model can describe the peak current in this process (see Equation 3.1), where *n* is the number of electrons, *A* electrode area in cm^2, *C* is the concentration of electroactive species, (mol cm^{-3}), *D* is the diffusion coefficient (*the value is a measure of the charge-transport rate within the electrolyte film near the electrode surface*), (cm^{2}s^{-1}), and ϑ is the scan rate in V s^{-1}.

$$I_p = (2.65\ x\ 10^5)n^{\frac{3}{2}}ACD^{\frac{1}{2}}\vartheta^{\frac{1}{2}} \hspace{3cm} 3.1$$

The second process, irreversible/quasi-reversible (slow electron transfer processes), is when the electrode kinetics are slower than the rate of diffusion [243].

Limitations of CV technique

Cyclic voltammetry provides very little or no information on the identity species in the electrolyte. In the case of the determination of the mechanism of two or more closely spaced charge transfer reactions, it is challenge in convoluting the resulting current-voltage asymmetry. Another setback in CV technique is that the voltammogram lends themselves poorly to quantitative equations of the parameters.

3.3 Physicochemical Characterization Techniques for Nanocatalysts

It is essential to understand the catalytic behaviour of catalysts by the comprehensive knowledge of their chemical and physical properties, which in turn help in the development of the major performance indicators. Profound insights on the different characterisation techniques provide information in understanding and analysing the various properties of catalyst (see Figure 3.1).
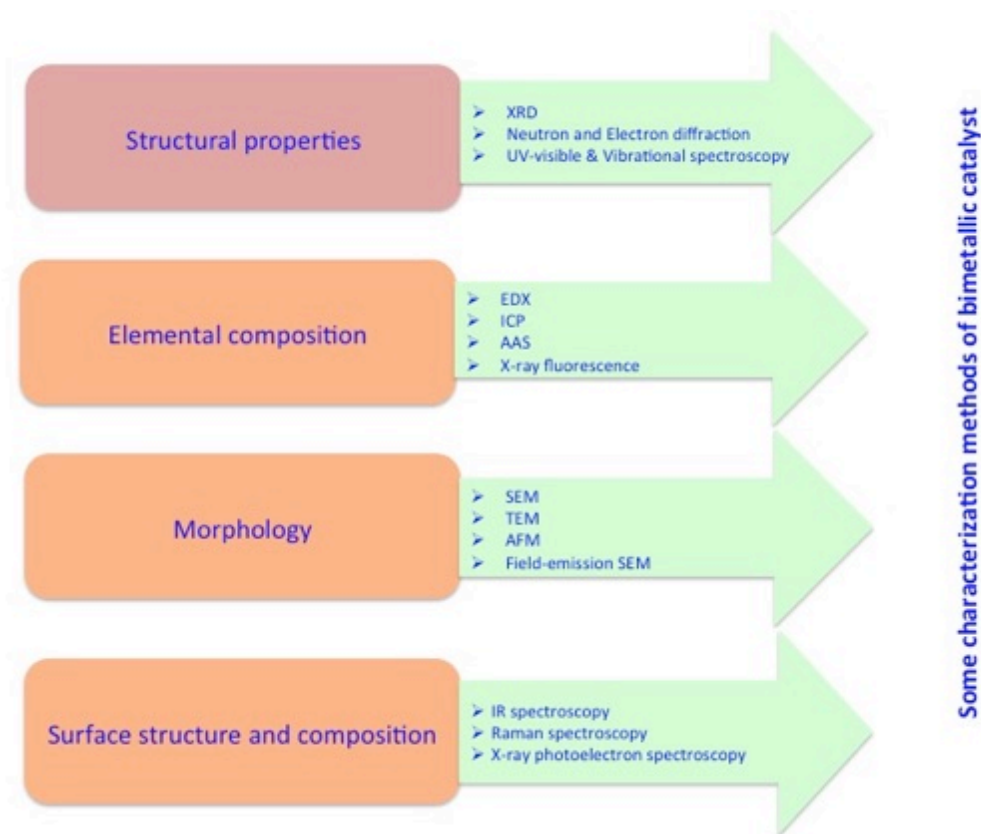
Figure 3.1: Some techniques for chemical and physical characterisation used to investigate various catalysts properties [adopted from ref:[191]]

Figure 3.1 shows some physical and chemical characterisation techniques used to investigate various catalysts properties. The different characterisation techniques elucidate the chemical and physical properties of the material being studied, for example, surface structure and composition (XPS, Raman), morphology and structure (TEM, AFM), elemental composition (EDS, ICP) and structure properties (XRD, UV-Vis), thus providing a holistic analysis of the given material.

3.3.1 X-ray diffraction (XRD)

X-ray methods are nondestructive elemental and structural analysis techniques. XRD gives structural and qualitative information of nanomaterials. It is based on wide-angle elastic scattering of a sufficiently short wavelength resulting in a diffraction pattern of crystalline materials. The interference occurs because of the lattice spacing of the crystal planes of atoms by the Miller's indices (*hkl*), resulting in different reflections from plane to plane according to Bragg's law: $2d_{hkl}\ sin\theta_{hkl} = n\lambda$. There are three main components in XRD, *a beam source* (e.g. Cu, Al, Mo, Mg, Fe, Cr), *a goniometer* (measure an angle or allow an object to rotate to a precise angular position), and *a detector*. XRD is a tool for characterising crystalline size, interplane spacing (*d-spacing*), lattice parameters, shape and lattice distortion by long-range order [244].

X-rays generated from targeted materials, (e.g. Cu) is excited using an electron beam to eject inner shell electrons and replaced by higher outer orbital electrons. This produces characteristic X-rays of the target material which are filtered and concentrated into a monochromatic incident beam that is then focused on the sample. The interaction of the sample surface with the X-ray beam produces intense reflected X-ray from constructive interference when Bragg's conditions are satisfied. Constructive interference is the difference in the travel path of the incident X-ray, which is equal to the wavelength multiplied by an integer. The diffracted X-ray leaving the crystal at the same incident angle are detected, processed, and counted through a range of 2Theta angles, as the sample is scanned. The identified diffraction peaks are compared with the diffraction pattern of standard reference materials retained in the International Centre for Diffraction Data (ICDD) [191, 245]. XRD can precisely detect changes in lattice parameters in a random alloy, which is different to their monometallic counterpart. The

ratio of the two alloys are evaluated using Vegard's law [246] and Rietveld analysis for crystal structure refinement [247].

Some advantages of XRD technique include its non-destructive nature, high sensitivity, reliability, depth profiling and short experimental time (< 20 minutes). However, the acquisition of information from XRD for a small nanoparticle with fewer than a hundred atoms becomes difficult. As small particles may have an amorphous form and interatomic length may change [190].

3.3.2 Transmission electron microscopy (TEM)

The limitations of the human eyes led to the development of magnifying objects, such as the glass lenses and subsequently light microscopes. The light microscope is limited in its resolution for nanosize objects, such as catalyst nanoparticles used in catalysis and nanotechnology. The catalysts prepared in this thesis as small as 2-10 nm metal nanoparticles require magnifications which the light microscope cannot analyse. Nanotechnology requires resolution below 100 nm, which is beyond the light microscope. Rayleigh criterion (Equation 3.2) provides the improvement in the resolution of the light microscope limitation for small nanosized analysis.

$$\delta = \frac{0.61 \lambda}{\mu \sin\beta} \qquad\qquad 3.2$$

where δ is the minimum distance which can be resolved for a specific wavelength, λ is the wavelength, μ the reflection index and β the semi-angle of the lens. For visible light, this limits the resolution to approximately 300 nm, hence the need to decrease the wavelength to improve the resolution. Another advancement to improve resolution was

by the Louis de Broglie formulation, which is given by Equation 3.3 inspired by Einstein's photon description of electromagnetic radiation. This enhances the resolution power required for small nanosized analysis, proposed by the modification of the wavelength given by:

$$\lambda = \frac{h}{p} \ with \ p = \frac{mv}{\sqrt{1-(^v/_c)^2}}$$
$$3.3$$

where h is Planck's constant, p the relativistic momentum, m the rest mass, v the velocity of the particle and c the speed of light in vacuum. With Equation 3.3, an electron accelerating over 100 keV corresponds to an electron wavelength of 0.037 Å, but imperfect electromagnetic lenses lead to significant astigmatism limiting electron microscopes to about 0.1 nm [248, 249].

The key question asked about metal nanoparticles is concerned with size, morphology and aggregation state. The shape of nanoparticles on the atomic scale is critical for elucidating the physical properties of nanosized materials [190]. Generally, there are many techniques used to reveal the size and homogeneity of metal nanoparticles. However, TEM is the best technique for size. TEM is the most frequently used electron microscopic technique for characterising nanomaterials. Direct images and chemical information at a special resolution down to the atomic scale (<1 nm) are achievable on a TEM instrument. Figure 3.2 shows a block diagram of the comparison between light-, scanning electron- and transmission electron- microscopy, illustrating the basic components/similarities of the microscopes.
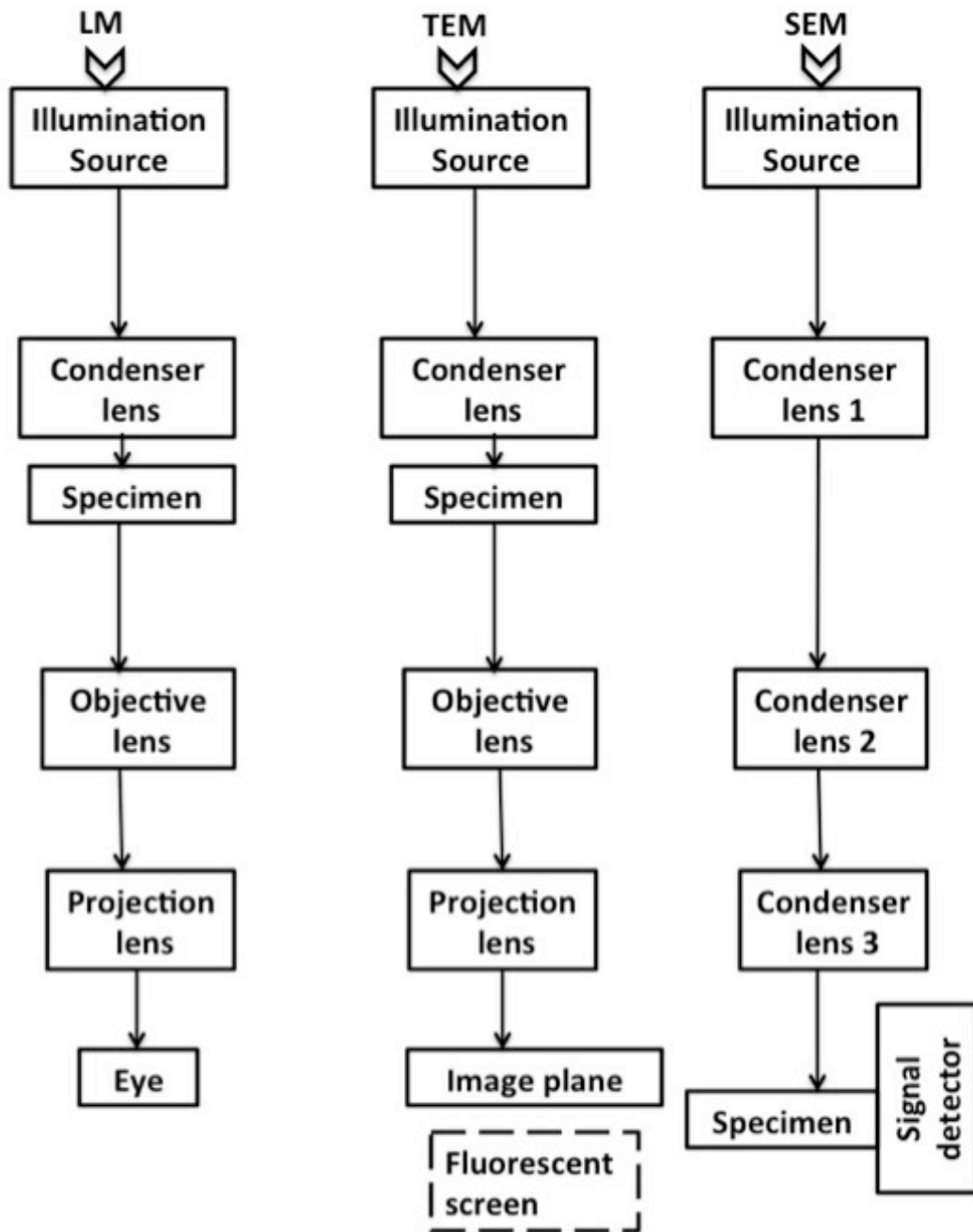
Figure 3.2: Schematic diagrams illustrating the principle of operation and the comparison between conventional light (LM), SEM and TEM microscopes [250]

The principle of conventional TEM mode involves accelerating an electron beam through a specimen causing interaction of incident electrons with the sample. The incident electrons transform into unscattered electron, elastically scattered electrons or

inelastically scattered electrons. The electron diffraction is generated from the electromagnetic lenses projected on a screen by the scattered or unscattered electrons (see Figure 3.2). Then, the amplitude contrast image, a phase-contrast image or a shadow image of varying darkness in relation to the density of unscattered electrons, are formed. TEM and SEM can reveal the size and shape of nanomaterials, degrees of dispersion and aggregation, however, TEM provides better spatial resolution and capacity for additional analytical measurement. There is a significant tradeoff for TEM in that a 3D specimen is being probed by the 2D TEM technique in transmission view leading to depth sensitivity for a single TEM image [244]. Another problem associated with TEM technique is the local probing area distortions, which affect percentage purity due to crystallinity segregation during monolayer formation of the TEM grid [177].

In addition, TEM can be used for chemical analysis when electrons, scattered from the sample, are used to form an image. Selected Area Electron Diffraction (SAED) is used to characterise the crystallographic nature of the sample from a small area of roughly a few microns. Adjusting the back focal plane of the magnetic lenses can generate a SAED pattern. The pattern depends on the orientation and structure of the sample illuminated by the electron beam. For a single thin crystal sample, diffraction shows the pattern of dots or a series of rings for a polycrystalline or amorphous material. The information provided by SAED includes the space group symmetries and the crystal's orientation for the particular crystal phase. In Figure 3.3a She and coworkers (2012), show a diffraction pattern for Ni@Au bimetallic catalyst exhibiting mixed diffraction rings for fcc-Au and fcc-Ni nanoparticles. However, the SAED analysis cannot solely confirm whether the material is core-shell or mixed Au and Ni nanoparticles.
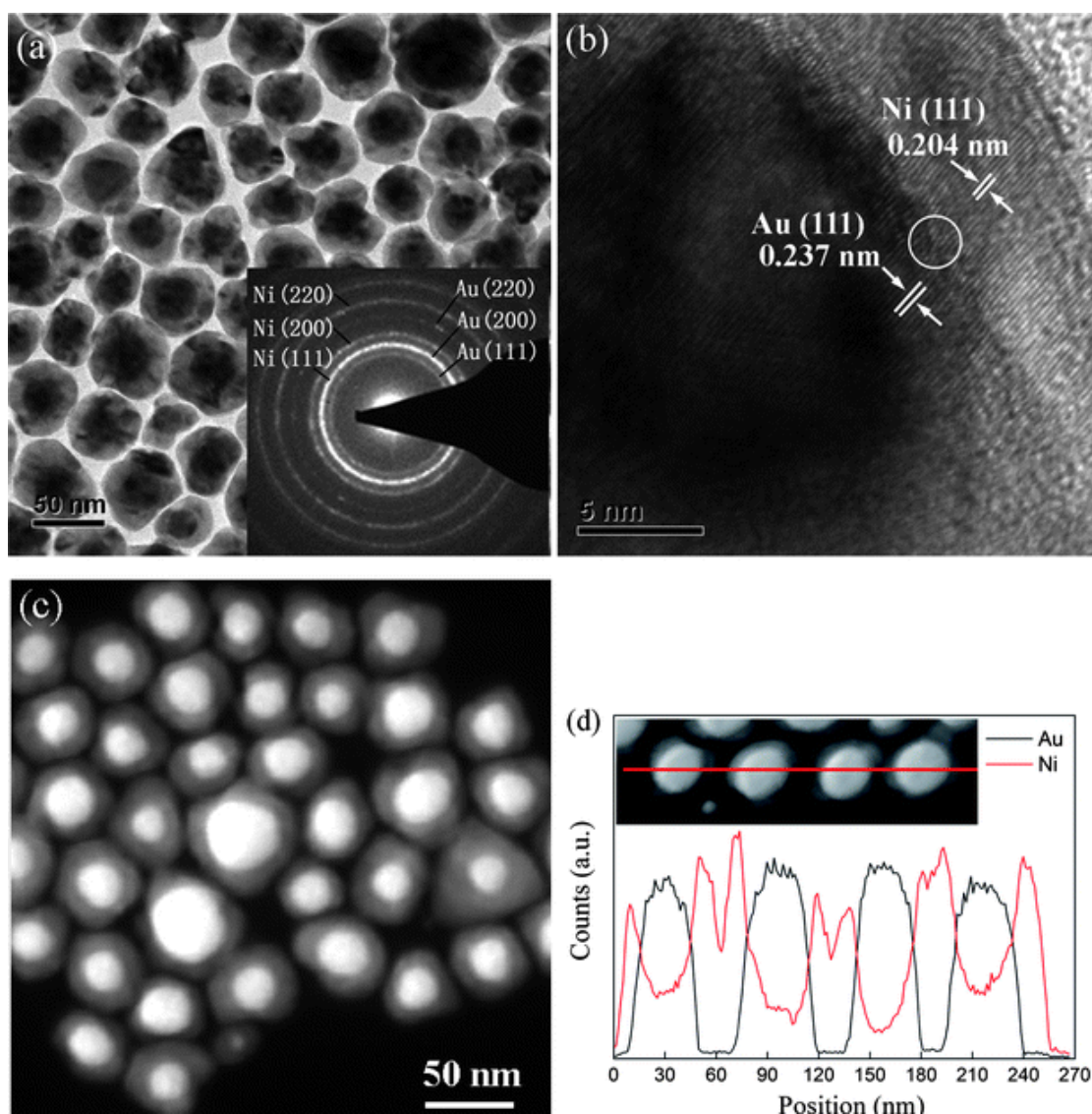
Figure 3.3: Structural characterisation of Au@Ni nanoparticles. (a) Bright-field TEM image with SAED pattern (inset), (b) HRTEM image. The circled area shows the distorted interface between the core and shell. (c) HAADF image showing the contrast between core (appear bright) and shell (appear relatively dark) component. (d) STEM-EDS line-scan analysis with HAADF image (inset). Reused with permission from The Royal Society of Chemistry [251]

High-resolution TEM imaging (see Figure 3.3b-d) can verify the core-shell structure by measuring the lattice fringes from the shell region and the core region to clearly identify the corresponding plane for Au and Ni respectively. As shown in Figure 3.3c-d, the high-angle annular dark-field (HAADF) is another useful technique for confirming the core-shell structure, along with line scan analysis on a single nanoparticle with energy-

dispersive X-ray spectroscopy (EDS) [251]. To convincingly evaluate the structure of a nanoparticle, different techniques are required to establish the physicochemical properties of the nanomaterial and have been investigated as demonstrated by She *et al.* (2012). They were able to distinguish between alloyed (intermetallic bonding) and core shell structure of the Au@Ni nanoparticles catalysts.

3.3.3 Scanning electron microscopy (SEM)

SEM is a surface imaging technique in which highly focused beams of accelerating short wavelength electrons scan across the sample surface. These electrons interact with the sample and generate signals reflecting the atomic composition and topographic detail of the specimen [244]. Usually, SEM can be operated in different scanning modes due to the emission generated by the incident electrons such as back-scattered (elastic), secondary electron (inelastic) or transmission. The reflected or back-scattered electrons are useful for elemental-specific images while secondary electrons are emitted very close to the specimen surface due to ionisation creating high-resolution topology information. In the transmission SEM mode, it operates like a scanning transmission electron microscope (STEM), where image information results from mass and thickness contrast from electrons, that passed through the specimen [252].

There are some limitations associated with recording SEM images: shrinkage of the specimen and alteration of the characteristics of the nanomaterials due to drying and contrasting processes. There is the problem of destructive sample preparation and significant beam damage due to long exposure of selected areas on the sample [244]. The nature of the phase contrast and the accompanying image generation for smaller particles leads to major uncertainties in size quantification for particles less than 2.5 nm

[253]. SEM results can produce vivid images of the sample surface via secondary electron imaging, with superior resolution to about 1 to 5 nm. Compared to TEM, SEM provides a much greater depth of field, i.e. the depth over which the object remains in focus, yielding a 3-dimensional appearance useful for investigating complex surface topology [254].

3.3.4 Energy dispersive spectroscopy (EDS)

EDS is an alternative analytical technique coupled with TEM or SEM used to investigate the localised chemical composition and electronic structure of nanomaterials [244, 253]. The small area of the sample receives a narrow beam of electrons, emitting X-ray energy from the sample, which is recorded. Then, the electron energy losses are measured as a the spectrum is displayed and then used to correlate the image with quantitative data [191]. The X-rays emitted have characteristic energies by electron beam irradiation with intensities propositional to the concentration of each element in the nanoparticles. The characteristic X-rays are emitted as the electron beam removes inner shell electrons from samples causing a higher energy electrons to fill the shell and release energy [254]. EDS is useful in elemental composition of small areas of the sample image in either TEM or SEM and for identification of defects and mapping of the samples. EDS is particularly useful in that it is quick to use for quantitative analysis of samples of different geometries and structures. However, it is limited due to the challenges of having numerous elemental peaks overlapping, which require careful review to evaluate the spectra.

3.3.5 **Atomic force microscopy (AFM)**

AFM is a powerful 3D visualisation technique with both quantitative and qualitative information at the nanoscale dimension. It can elucidate physical (particle size, morphology, surface texture and roughness), mechanical and electrical properties with high resolution. AFM can be applied to particle characterisation in ambient air, gas (N_2 or Ar), liquid and solid dispersions, and from 1 nm to 8 μm in height [255]. Binnig and Quate (1986) demonstrated the first AFM ideas using an ultra-small probe tip at the end of a cantilever in 1986 [256]. The idea was developed by Wickrasinghe *et al.* in 1987 for an AFM setup with a vibrating cantilever which used the light-lever mechanism [257].

AFM utilises a cantilever (typically silicon or silicon nitride) attached to the end of a piezoelectric displacement actuator with a shape probe to scan the sample surface. At close proximity to the sample surface, the cantilever imposes a bending moment due to the attractive or repulsive (electrostatic and van der Waals) force experienced by the atoms at the probe due to surface interactions. The cantilever deflection is measured with a laser beam onto a split photodiode. The probe displacement is linearly proportional to the deflection. Provided the particles are anchored to the sample surface during a scan, AFM can measure either in direct contact, intermittent contact mode, or non-contact mode [244, 258].

In AFM measurements, nanoparticles (NPs) can be classified into two categories: NPs rigidly attached to a solid structure (e.g. nanocomposites) and those weakly adhering to the substrate (e.g. carbon black). Metal nanocatalysts (e.g. Pd-C, Au-C and AuCu-C) fall under the second category, where metal catalysts are dispersed on carbon black support. Metal NPs with weak adhesion to carbon black substrates must have a greater affinity for the substrate than the AFM probe to avoid NPs attaching to probes. This is

because AFM works by scanning a mechanical probe across the sample surface, therefore, to prevent artefacts on the probe, near or intermittent contact mode is strongly recommended for such specimens. One key advantage of AFM is the ability to measure soft surface materials adhered weakly with van der Waals and adsorption forces making it the preferred choice for nanoparticle measurements/analysis [255, 258, 259]. An interesting feature in AFM applications compared to TEM/SEM, for example, is that it can operate in a nonvacuum environment or in wet conditions [260]. This advantage makes AFM easy to use: it is robust, versatile, has a nonvacuum environment and simple sample preparation procedure.

Like SEM and TEM techniques, AFM can investigate the size, shape, structure, sorption, dispersion and aggregation of nanomaterials. However, there are some limitations to the AFM technique include: the size of the cantilever-although the tip is nanoscale is generally larger than the dimension of the measured nanoparticle, leading to overestimation of the lateral dimension of the samples. Also, the tip can easily collect unavoidable artefacts, which could create an unsuitable tip, and/or poor operating environment for taking measurement [244].

Chapter 4 Experimental Procedures: Preparation and Characterisation

In Chapter 3, the basic theories behind the experimental techniques were elucidated, focusing on the scientific information for the choice of the techniques. In this chapter, the focus is to design a suitable formulation/preparation method for Pd-C, Au-C and AuCu-C catalysts for electrooxidation of formic acid for DFAFCs applications. The technique of choice is determined by how much scientific information is obtainable for the investigation of the chemical/structural properties and the performance characteristics of the as-prepared catalysts. The aim of this work is to develop a new synthesis method, reduced active metal needed and evaluate the electrochemical performance of the anode catalysts. To achieve these objectives systematically, a robust preparation method is crucial.

4.1 Catalyst Preparation

The structure, composition, reaction conditions, and activity of bimetallic catalysts are largely dependent on the synthesis method [191]. Choudhary and Goodman reported that wet conventional impregnation synthesis produced relatively inactive Au catalysts. This suggests the need for modified methods of Au preparation strategy, owing to the strong influence of synthesis on particle size, morphology, oxidation state of gold species, nature of the support, and catalytic activity of gold [261-263]. The majority of gold-catalysed systems have been carried out via a deposition-precipitation method for the catalyst preparation, which does not allow clear distinction and evaluation of a large number influencing parameters due to its complex synthesis processes [263]. To

overcome these complexities, a facile reproducible preparation method, via a one-pot colloidal deposition of gold nanoparticle on the carbon support, is proposed. Sodium borohydride reduction synthesis combined with water-soluble PVP stabiliser is commonly considered the most energy efficient, environmentally benign and contaminant free process [229]. PVP chains have a good affinity for gold, and PVP-stabilised AuNPs show good catalytic activity for a variety of organic reactions. During AuNPs synthesis, PVP molecules adsorb onto the growing metal nuclei as water-soluble surfactants, giving a smooth and pinhole-free shell covering on a well-defined core preventing aggregation [155, 205]. However, to ensure core-shell architecture, irrespective of the synthesis route, controllability of uniformity, intact shell, and reproducibility is neither trivial nor easily achievable. Investigative studies to improve the structural and catalytic properties of gold catalysts through modifications of existing syntheses will lead to new material-driven research strategy and a better scientific understanding of catalyst preparation [99].

4.2   Experimental

4.2.1   Preparation of Pd-C catalysts

Pd-C catalysts were prepared using two methods, based on the type of stabilising agent used to stabilise the Pd nanoparticles, before deposition on Vulcan XC72 carbon. In the first method, boric acid and ammonium fluoride were used as stabilisers, following a modified method by Zhang and coworkers, while the second method used PVP as the stabilising agent.

a. Materials

The materials used in the present work include palladium (II) chloride (5wt% in 10wt% HCl solution) (99.9% Sigma-Aldrich), sodium borohydride (99%, Aldrich), ammonium fluoride (99.99%, Aldrich), boric acid (99.999%, Aldrich), 5 wt.% Nafion solution (99.99%, Aldrich), ethanol (>99%, Aldrich), sulphuric acid (95-97%, Aldrich), formic acid (>95%, Aldrich), ammonia solution in 2 M isopropanol (99%, Aldrich), polyvinylpyrrolidone (PVP, 1.30 mmol of monomeric units, Mw = 40,000, 99.9% Sigma-Aldrich), deionized (DI) water (18.2 $M\Omega.cm^{-1}$, Purelab option ELGA), Vulcan XC72 GP-3860 (Cabot) and sodium hydroxide (General purpose grade, Fisher Scientific). All materials were of analytical grade and used without any further purification.

b. Synthesis of Pd nanoparticles

The production of Pd-$C_{H3BO3 + NH4F}$ involved a reduction method using sodium borohydride, following a modified method proposed by Zhang *et al.* [78, 80, 264]. Briefly, 25 mg ammonium fluoride, 125 mg boric acid and 0.450 ml of 0.282 mol l^{-1} $PdCl_2$ solution were added to 10 ml water. Then, 60 mg Vulcan XC-72 carbon black was added into the above solution. The suspension obtained was sonicated at room temperature for 30 minutes and about 1 ml concentrated ammonia solution was added to adjust the pH to 8-9. In this synthesis method, the suspension was slowly reduced by the dropwise addition of 10 ml of 1 mol l^{-1} solution of sodium borohydride ($NaBH_4$) (~12 wt.% in 3 M NaOH) with sonication for a further 30 minutes. The resultant suspension was filtered using Whatman cellulose nitrate filter paper and then washed with

deionized water for several times. The as-prepared catalyst was then dried in a vacuum oven at 80 $^{\circ}$C for 24 hours.

The same synthesis route was followed for the Pd-C$_{PVP}$ nanoparticles, by changing the stabilising agent to 140 mg (1.26 mmol) of polyvinylpyrrolidone (PVP, Mw = 40,000). Selection, formulation and preparation are central in directing formic acid oxidation exclusively through the dehydrogenation pathway. The effect of the capping agent (PVP) on the catalyst formation with respect to structure, morphology and electrooxidation reaction mechanism was investigated.

Table 4.1: Exact Experimental Composition wt.% Pd-C catalyst (H$_3$BO$_3$+NHF$_3$)

Exact Experimental Composition							
Amount of Each Component by Weight						Theoretical estimate	ICP-AES Result
Run#	NH$_4$F (g)	H$_3$BO$_3$ (g)	C (g)	PdCl$_2$ (µL)	H$_2$O (µL)	Pd g	Wt.% Pd	Wt.% Pd
PdC$_1$	0.0232	0.1267	0.06	450	10000	0.014	18.4	20.6
PdC$_2$	0.0252	0.1252	0.0606	450	10000	0.014	18.2	21

Table 4.2: Exact Experimental Composition wt.% Pd-C catalyst (PVP)

Amount of Each Component by Weight						Theoretical estimate	ICP-AES Result
Run#	PVP (g)	C (g)	PdCl$_2$ (µL)	H$_2$O (µL)	NaBH$_4$ (µL)	Pd g	Wt.% Pd	Wt.% Pd
PdC$_1$	0.1404	0.0604	450	10000	10000	0.014	18.3	54
PdC$_2$	0.1413	0.0594	450	10000	10000	0.014	18.5	43.5

NaBH$_4$ (µL) = 10000, PdCl$_2$ concentration = 0.282 mol. l^{-1}

*Weight of Pd, g = concentration of PdCl$_2$ * volume of PdCl$_2$*Mol. wt. Pd*

*Theoretical wt.% estimate = [(Weight of Pd)/(weight of C + weight of Pd)] *100*

4.2.2 Monometallic Catalyst (Au-C$_{PVP}$) Synthesis

Au-C nanoparticle synthesis involved measuring 140 mg of the stabilizing agent, PVP. The PVP stabiliser is dissolved in 10 ml of deionized water and followed by adding 6.75 ml of degassed 0.0508 mol l^{-1} HAuCl$_4$.3H$_2$O solution. The suspension obtained was sonicated vigorously for 1h. The pH of the solution was adjusted with concentrated ammonia solution to between 8-10. 10 ml of freshly prepared 1mol l^{-1} (in 3 mol l^{-1} NaOH) solution of NaBH$_4$ was added under N$_2$ flow to reduce the Au-C$_{PVP}$ nanoparticles. The suspension was sonicated to for 10 minutes under the protection of high purity nitrogen to obtain a complete reaction. To enable reaction completion, the resulting catalyst was filtered and washed several times with deionized water until no chloride ions (Cl$^-$) were detected in the washing solution. Whatman cellulose nitrate filter paper (0.45 μm pore size) was used for collecting the as-prepared catalyst and was followed by drying at 80 ^{o}C under vacuum for 24 hours to obtain Au-C$_{PVP}$ catalysts.

Table 4.3: Exact Experimental Composition wt.% Au-C catalyst

Exact Experimental Composition								
Amount of Each Component by Weight							Theoretical estimate	ICP-AES Result
Run#	PVP (g)	C (g)	HAuCl$_4$ (μL)	H$_2$O (μL)	NaBH$_4$ (μL)	Au g	Wt.% Au	Wt% Au
AuC$_1$	0.1402	0.006	6750	10000	10000	0.068	92	87.6
AuC$_2$	0.1401	0.006	6750	10000	10000	0.068	92	89.2

*Weight of Au, g = concentration of HAuCl$_4$ * volume of HAuCl$_4$*Mol. wt. Au*

*Theoretical wt.% estimate = [(Weight of Au)/(weight of C + weight of Au)] *100*

4.2.3 AuNPs-C catalyst electrode preparation and sample specification

Specification of commercial gold nanoparticle (Sigma-Aldrich)

Gold nanoparticles – 5 nm diameter, OD 1, stabilized suspension in 0.1 mM phosphate buffered saline (PBS), reactant free. Other parameters: Core size, 3 – 7 nm; Particles/ml 4.92×10^{13} – 6.01×10^{13}; Mass of gold/ml = 6.952×10^{-5}, Molecular weight (Au) = 196.97 g/mol., Concentration = 3.53×10^{-4} mol l^{-1}.

Wt.% Au nanoparticle electrode paste (catalyst loading) preparation

4.6 mL of commercial AuNPs (AuNPs-C$_{commercial}$) (Sigma-Aldrich) was added to 325 μL (50:50) ethanol and Nafion solution and was mixed with 0.004 g of carbon black under vigorous stirring for 3 h. The 10 μL of slurry obtained was spread on the surface of the glassy carbon electrode (OD: 6 mm, ID: 3 mm). The electrode was dried overnight under vacuum at 80 ^{o}C to obtain the working electrode. The theoretical maximum AuNP-C$_{commercial}$ active metal weight = 0.352 mg cm^{-2}.

4.2.4 AuCu-C$_{PVP}$ core-shell bimetallic nanoparticles

AuCu-C$_{PVP}$ catalyst synthesis follows a one-pot, two-stage reduction process. Au and Cu bimetallic nanoparticles were synthesised in one vessel using simultaneous batch reduction. The method reported by Zhang *et al.* used the one-pot synthesis method for Ag-Au bimetallic nanoparticles with an Au shell and Ag core structure. In their work, they employed the rapid injection of NaBH$_4$ at a temperature of 0 ^{o}C [202]. In line with

their work, the key novelty in the preparation method employed in this thesis was (i) choice of reducing agent (*see Section 2.9.9*), (ii) low temperature synthesis (room temperature) and (iii) and the addition of a stabilising agent, PVP (*see Section 2.9.9*). Several parameters are involved in the synthesis of nanoparticles, and all cannot be considered to optimize synthesis, which is not the purpose of this thesis. Zhang and coworkers work at 0 ^{o}C, which represents a challenge in maintaining such temperature accurately. Room temperature synthesis requires no temperature control and reduces the problem of fluctuating temperature during synthesis. The other potential problem is the choice of reducing agent (*see Section 2.9.9* for more details). In this thesis, reduction method using $NaBH_4$ was employed, which generated the problem of hydrogen evolution during synthesis. However, the method was modified to reduce H_2 evolution by the addition of concentrated NaOH, which suppressed hydrogen evolution and the potential hazard with hydrogen release. In their report, Amendola *et al.* observed that high concentration of hydroxyl ions from NaOH decreased the number of water molecules available for the hydrolysis reaction of $NaBH_4$ [265]. Disadvantages of the synthesis process include the challenge of scaling-up the batch process and the amount of synthesised material produced is small approximately < 1g, (*i.e. 20wt% active metal and 80wt% Vulcan XC72 carbon*) of the catalyst. Another factor limiting the production process is the problem of homogeneity of the materials for the catalysts due to mixing materials with different densities and the heterogeneous nature of the catalysts.

In a typical synthesis 140 mg of polyvinylpyrrolidone was measured and dissolved in 10 mL of fresh deionized water (15.0 MΩ.cm, Purelab option ELGA). This was followed by adding deaerated 4.2 mL of 0.062 mol l^{-1} copper sulphate ($CuSO_4.5H_2O$ in H_2O) into the aqueous polyvinylpyrrolidone solution. Argon gas was used to purge the mixture of PVP + $CuSO_4$ solution for approximately 1 hour, to remove dissolved oxygen. Then 10 ml of freshly prepared 1 mol l^{-1} (in 3 mol l^{-1} NaOH) solution of

sodium borohydride ($NaBH_4$) is added under argon flow to reduce the $CuSO_4$-PVP solution, with continuous stirring, and protected with argon gas (Equation 4.1). The reaction was allowed to proceed for 1 hour to yield Cu_{PVP} nanoparticles at room temperature. Then, 6.3 mL of freshly prepared and deaerated (0.0508 mol l^{-1}) $HAuCl_4.3H_2O$ solution was quickly added to the Cu_{PVP} nanoparticle solution and sonicated for 1 h under argon protection (Equation 4.2). As the redox potential of Au^{3+}/Au ($E^o = +1.47$ V) is higher than that of Cu^{2+}/Cu ($E^o = +0.34$ V), Au^{3+} is reduced to Au, and therefore AuCu particles were formed [104].

The proposed two-stage one-pot synthesis route can be represented as shown in Figure 4.1:
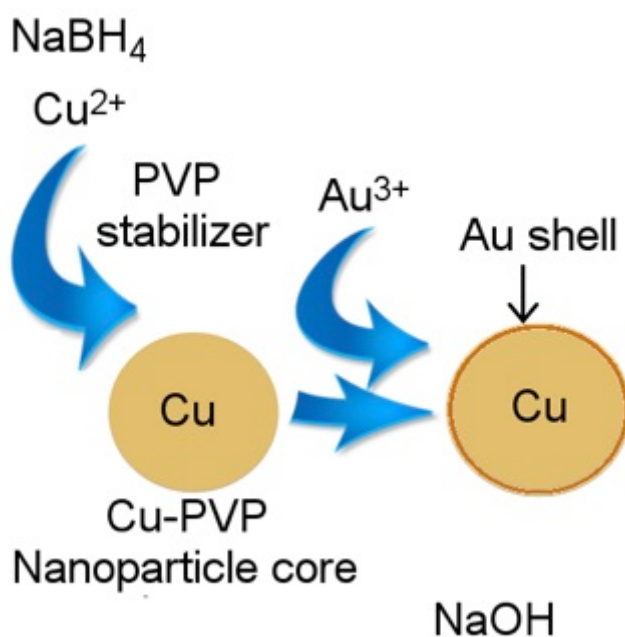
Figure 4.1: Diagram illustrating the use of PVP stabilised chemical reduction synthesis for the preparation of AuCu-C$_{PVP}$ catalyst [104]

The proposed synthesis chemical reaction equations are presented below:

$$CuSO_4 + NaBH_4 + 3H_2O \rightarrow Cu + NaHSO_4 + H_3BO_3 + 3H_2 \qquad 4.1$$

$$2HAuCl_4 + Cu + 8NaBH_4 \rightarrow 2Au:Cu + 8NaCl + 8H_3B + 5H_2 \qquad 4.2$$
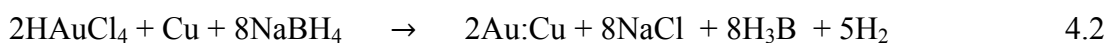
After a few minutes of sol generation, carbon black (Vulcan XC72R GP3860) was added to immobilised the sol under vigorous sonication for 1 hour. The slurry is allowed to settle for 30 minutes until cooled to room temperature. The resulting catalyst was filtered and washed with deionised water until no chloride ions (Cl⁻) were detected in the washing solution. The amount of Vulcan XC72R support was calculated to have a final Au-Cu loading of 20 wt.% of the active metal. The filtered catalyst was vacuum dried overnight at 80 °C to obtain Au-Cu-C$_{PVP}$ catalysts. A typical experimental setup used for the synthesis process is shown in Figure 4.2.

Table 4.44: Exact Experimental Composition wt.% AuCu-C catalyst

Amount of each component by weight				Theoretical estimate			ICP-AES		
Run#	PVP (g)	C (mg)	Au (g)	Cu (g)	Wt.% Au	Wt.% Cu	Wt.% AuCu	Wt.% Au	Wt.% Cu	Wt.% AuCu
AuCu-C$_1$	0.143	60.1	0.063	0.017	45	12	57	45	10.7	56
AuCu-C$_2$	0.140	60.0	0.063	0.017	45	12	57	52.2	6.5	59

* HAuCl$_4$ (µL) = 6300; CuSO$_4$ (µL) = 4200, H$_2$O (µL) = 10000, NaBH$_4$ (µL) = 10000, PVP = 0.140 (g)

Weight of Au, g = concentration of HAuCl$_4$ * volume of HAuCl$_4$*Mol. wt. Au

Weight of Cu, g = concentration of CuSO$_4$ * volume of CuSO$_4$*Mol. wt. Au

Theoretical wt.% estimate = [(Weight of Au)/(weight of C + weight of Au + weight of Cu)] *100

Theoretical wt.% estimate = [(Weight of Cu)/(weight of C + weight of Au+ weight of Cu)] *100
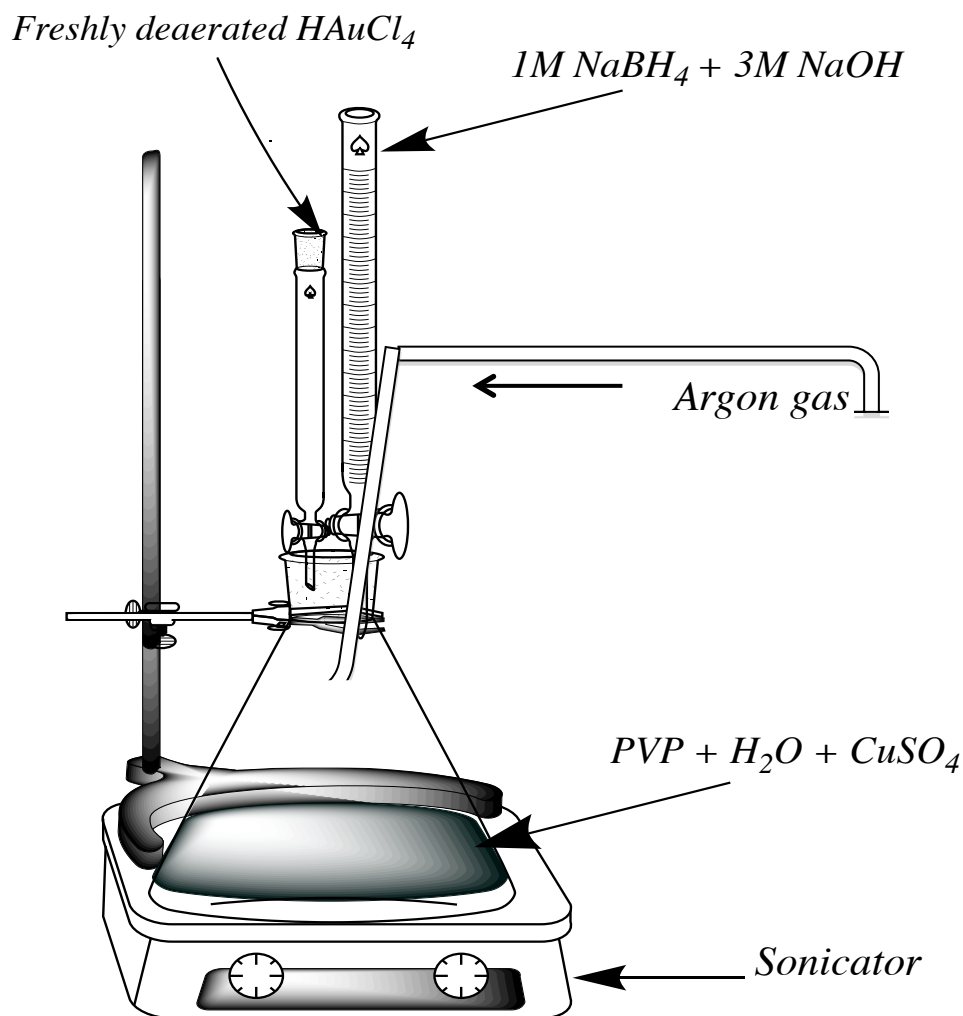
Figure 4.2: Schematic diagram of the catalyst synthesis setup

4.3 **Physical Characterisation of Electrocatalysts**

4.3.1 **X-ray diffraction (XRD)**

X-ray diffraction (XRD) measurements of all catalysts were recorded with a Bruker D2 Phaser diffractometer using a 0.6 mm primary divergence slit without Ni-filtered CuK_α radiation source (λ = 1.5406 Å) at room temperature. The scan time was 0.25 per step from 2θ = 15-90° with a step size of 0.02, operating at 30 kV and 10 mA. The diffraction peaks were indexed using the 2016 International Centre for Diffraction

Database (ICDD). The peak width β and peak position θ and the full width at half-maximum (FWHM) in radians of the Bragg peaks were obtained from curve fitting using PANalytical Data Viewer and Fityk software.

Powder samples preparation

All XRD powder samples were ground well and mixed thoroughly. The sample holder was cleaned carefully and a small amount of catalyst powder was added to fill the central aperture or the 'zero' background silicon wafer specimen holder, depending on the amount of sample. Then a microscope slide was used to level the sample surface and to ensure a random distribution of lattice orientations for peak position characterisation.

4.3.2   Transmission Electron Microscopy (TEM/HRTEM)

All TEM/HRTEM samples were prepared by ultrasonic dispersion in ethanol with one drop (~1 mg.mL^{-1}) of nanoparticle solution onto (a 200 or 300-mesh holey) carbon-coated copper grid and dried in air at room temperature. The TEM images were obtained using a transmission electron microscope (Tecnai T20) operated at 200 kV. DigitalMicrograph software (Gatan, Inc.) was used in the TEM studies to acquire, visualise, analyse and process the digital image data of the catalysts in this study. High-Resolution transmission electron microscopy (HRTEM) was achieved using a Joel 2010FEG HRTEM at 40kV. ImageJ$^{®}$ software analysis was used to estimate the particle diameter from the HRTEM micrographs.

4.3.3 Scanning Electron Microscopy/ Energy Dispersive Spectroscopy (SEM/EDS)

All SEM experiments were performed using Jeol JSM-6010LA analytical SEM at an acceleration voltage of 20 kV, to observe the surface morphology. For all samples, 1 mg of the catalyst sample was dispersed in 1 ml of 95% ethanol and sonicated for 1 minute in a water bath. 10 µl of the paste was dropped onto carbon adhesive tape, mounted onto Joel 10 mm x 10 mm diameter plain stubs, and dried at room temperature. A working distance of 10 – 15 mm was employed for high-resolution measurements. The elemental compositions were verified by EDS maps constructed using the emission lines of Pd, Cu, Au and C, including possible contaminations of chloride ions.

4.3.4 Atomic Formic Microscopy (AFM)

All samples were measured using the Dimension icon (Bruker Ltd, Germany) operating in the soft tapping (ScanAsyst) mode in air at room temperature. About 1 mg of the catalyst sample was dispersed in 1 mL of 95% ethanol and stabilised with ethylamine solution and sonicated for 1 minute in a water bath. A drop of the slurry was dispersed on a freshly cleaved mica surface glued to a metal pad, and dried in air at room temperature before AFM measurements. 3.7 µm thick cantilevers silicon reflective aluminium coating were used throughout the experimental measurements. According to producer's specifications, the spring constant was 26 N/m, the resonance frequency of 300 kHz and radius of the tip was 7 nm [104]. Bruker Nanoscope analysis software version 1.5 was used for all images analysis to determine the nanoparticle size. The particle diameter was estimated by analysis of the AFM micrographs using ImageJ[®]

software. Non-contact mode was used for AFM measurements for all samples because it was the most appropriate for the characterisation of nanoparticles as reported in literature [244, 259].

4.3.5 Thermogravimetric analysis (TGA) experiment to determine Pd content

TGA experiments, conducted on a Mettler Toledo TGA/DSC 1 instrument, were performed using a heating rate of 100 ^{o}C /min, under nitrogen gas flow. The samples were held for 1 minute at 25 ^{o}C under nitrogen flow rate of 50 ml min^{-1}to bring it to steady state condition. It was then heated from 25 ^{o}C to 127 ^{o}C, to evaporate moisture content, and maintained for 10 minutes at 127 ^{o}C to ensure complete removal of moisture from the samples. At a heating rate of 150 ^{o}C/min, the temperature was increased from 127 to 927 ^{o}C, and the sample was soaked for 10 minutes, to allow for the complete removal of all volatile components. Then the furnace was cooled to 824 ^{o}C and the gas flow was switched to oxygen for 30 minutes to ensure complete combustion of the carbon contained in the sample. The sample was then cooled to room temperature. The results were corrected using data from an experimental run using an empty sample pan (blank).

4.3.6 Compositional Analysis

The compositional analysis of the sample comprises two stages. First, the digestion of the solid catalyst sample was digested using aqua regia solution, i.e. 1:3 mixture of nitric acid and hydrochloric acid. Secondly, the Vulcan XC72 carbon support was filtered off the digested metals in solution, before estimating of the weight composition

using Inductively Coupled Plasma Atomic Emission Spectroscopy (ICP-AES), Inductive Coupled Plasma Mass Spectroscopy (ICP-MS), and Flame Atomic Absorption Spectroscopy (AAS).

Preparation of aqua regia solution

The aqua regia solution was prepared by measuring 5 ml concentrated nitric acid (HNO_3) and slowly mixing with 15 ml concentrated hydrochloric acid (HCl) in a Pyrex beaker while gently stirring. This produces volatile fumes and a yellow gas of chlorine and nitrosyl chloride. The aqua regia solution is allowed to cool to room temperature.

Catalyst digestion

All catalyst samples for the ICP analysis were prepared by measuring 1 mg of the catalyst into a beaker and adding 20 ml solution of aqua regia. The sample was heated on a hot plate for 30 minutes to 1 hour at 150 ^{o}C. After digestion of the sample, it was transferred into a 50 ml measuring bottle and 1% HNO_3 was added to fill it to the 50 ml mark.

1. ICP Method

   ➤ ICP-AES was used to estimate the exact metal loading for the catalysts. The measurements were on a Spectro-Ciros-Vision Inductively-Coupled Optical Emission Spectrometer at the Centre for Chemical Instrumentation and Analytical Service, Department of Chemistry, University of Sheffield.

➢ ICP-MS was also employed to measure the exact metal loading of catalysts. All measurements were on a Perkin-Elmer ELAN II DRC inductively coupled plasma spectrometer at the Civil and Structural Engineering Laboratory, Kroto, University of Sheffield.

2. AAS was used to measure the catalyst metal contents for each catalyst sample. All measurements were on a Perkin-Elmer AAnalyst 400 at the Energy & Environmental Laboratory, Chemical & Biological Engineering, University of Sheffield.

4.4   Electrochemical Characterisation of Electrocatalysts

4.4.1   Working electrode preparation

The glassy carbon electrode (diameter = 3 mm) was polished to the mirror by 0.5 and 0.05 μm alumina suspensions sequentially before use. The electrodes were sonicated for 5 minutes prior to each use, followed by washing ultrasonically sequentially with ethanol, acetone and deionized water [266]. After that, the electrode was ready to serve as an underlying substrate of the working electrode.

Catalyst ink

The electrode paste for all samples was prepared by mixing 6 mg of the catalyst, 250 μl C_2H_5OH solution and 250 μl 5wt% Nafion solution by stirring for 1 hour. On the working electrode (inert glassy carbon electrode (OD: 6 mm ID: 3.0 mm)), 10 μl slurry of the catalyst was spread on the surface and the solvent evaporated in air at room

temperature. Figure 4.3 shows the schematic representation of the electrode preparation process.

Weigh Catalyst = 6 mg

Electrochemical setup

Catalyst

Ethanol = 0.25 ml
Nafion solution = 0.25 ml

RE
WE
CE

Working electrode
Geometric area = 0.07 cm^{-2}
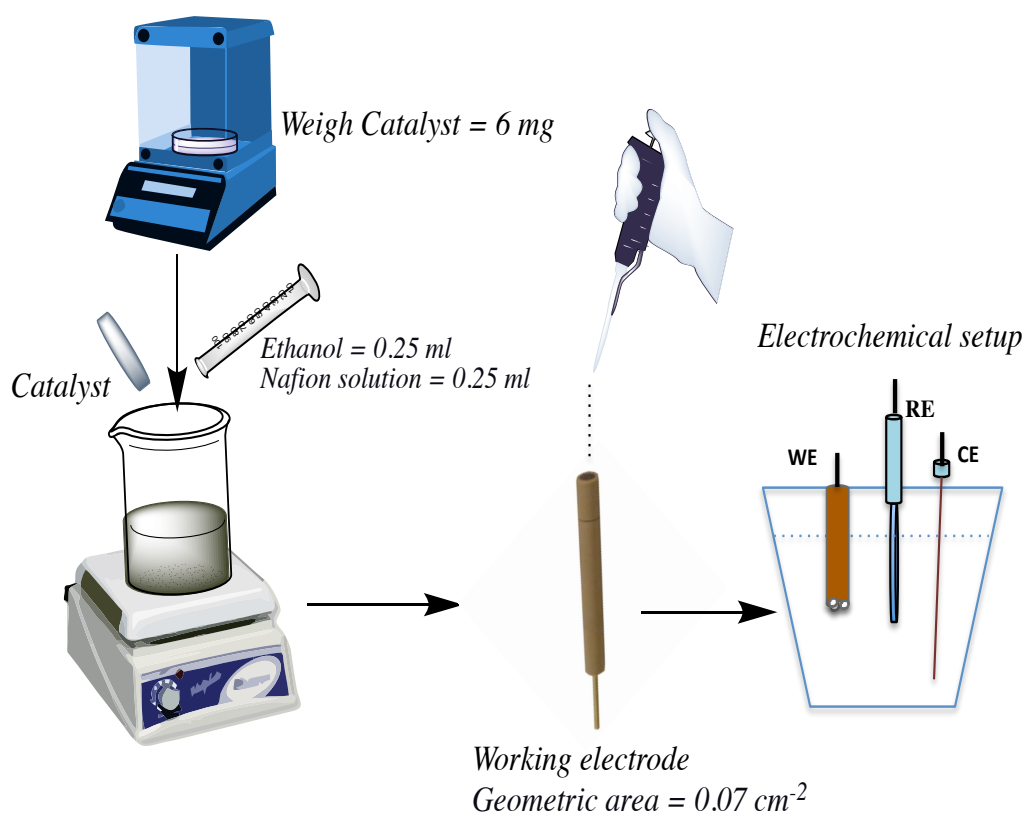
Figure 4.3: A schematic illustration of the electrode preparation used for the electrochemical characterisations

After drying at 80 $^{\circ}$C under vacuum for 12 hours, the working electrode was obtained. The manufacturer gave a value of 0.07 cm^2 for the apparent surface (*geometric*) area of glassy carbon electrode. The specific catalyst loading of approximately 0.35 mg cm^{-2} (electroactive material based on the weight % of the active metal) was deposited on the working electrode for different catalysts (see Table 4.6).

Table 4.5: Electrode catalyst loading based on ICP-AES data

Catalyst	Mass of catalyst, mg	Density of paste, g l^{-1}	Mass of catalyst loading, g ($\times 10^{-4}$)	Wt.% catalyst loading ($\times 10^{-5}$)	Specific catalyst loading, g_{metal} m^{-2} (*ICP-AES*)
Pd-C$_{2PVP}$	5.94	11.9	1.19	5.23	7.5
Pd-C$_{2H3BO3+NHF4}$	6.06	12.1	1.21	2.55	3.6
AuCu-C$_2$	6.1	12.2	1.22	2.44	9.1
Au-C$_2$	6.4	12.8	1.28	2.56	16.5
AuNPs-C	8.0	12.3	1.23	2.46	3.5

4.4.2 Electrochemical cells and testing methodologies

Electrochemical measurements of all catalysts were performed using a conventional three-electrode cell (see Figure 4.3$_{ac}$), with a Solartron Analytical Instrument, model 1400/1470E at ambient temperature. The as-prepared catalyst paste (specific catalysts loading) was deposited on glassy carbon electrodes and used as the working electrode. A Pt wire (0.5 mm diameter) was used as the counter electrode and an Ag/AgCl$_{sat.}$KCl standard electrode (0.256V/NHE or 0.197V/SHE) was used as the reference electrode. High purity argon (N5.0) or nitrogen was fed into the electrolyte in a 50 ml glass bottle for 5-10 minutes to eliminate the dissolved oxygen prior to the electrochemical measurements. After degassing, the setup was allowed to rest for about 2-3 minutes to confirm that gas bubbles were not on the surface of the working electrode before starting the CV experiment. All potentials in the experiments were given versus Ag/AgCl$_{sat.}$KCl reference electrodes using MultiStat-Electrochemistry software. The standard hydrogen electrode (SHE) with 0 V is based on the hydrogen redox reaction at

standard conditions. This allows a small current to be drawn from the system with negligible overpotential; however, the practical application of SHE is limited by the continual gas supply causing measurement disruptions in the half-cell. Instead, silver-silver chloride (Ag/AgCl) in saturated KCl solution with half-reaction

$AgCl\,(s) + \, e^- \, \rightarrow \, Ag\,(s) + \, Cl^-\,(saturated)$ and a relative electrode potential of +0.222 V to SHE at 298 K is an excellent choice. The actual half-cell potential is +1.197 V versus SHE because of the KCl chloride activity, which is not exactly unity.

4.4.3 Electrochemical measurement: Cyclic voltammetry

Cyclic voltammetry experiments were performed in 0.5 M H_2SO_4 in the specified potential range versus reference electrode (Ag/AgCl, KCl_{std}) at a scan rate of 20 mVs^{-1}, to evaluate the electrochemical active surface area of the catalysts. CV employed in 0.5M HCOOH + 0.5M H_2SO_4 at 50 mVs^{-1} established a correlation between electrochemical behaviour and catalytic performance in the oxidation of formic acid. The kinetic parameters and active surface area were evaluated from CV, based on the hydrogen desorption area or oxide reduction peak corresponding to a monolayer of adsorbed hydrogen. All experimental data were analysed using MultiStat Data software for evaluations and calculations.

a. Pd-C catalyst

All Pd-C catalyst electrodes were electrochemically characterised using cyclic voltammetry (CV). To investigate the hydrogen adsorption-desorption peaks (current density and potential positions), 0.5 M H_2SO_4 was used in the potential range of -0.2 to +1.0 V (Ag/AgCl, KCl_{std} [0.197 V vs. NHE]) was performed at a scan rate of 20 mVs^{-1}. The formic acid electrooxidation reaction was investigated in the acid medium using 0.5M HCOOH + 0.5M H_2SO_4 over the potential range of -0.2 and +1.2 V (Ag/AgCl, KCl_{std}) at a scan rate of 50 mVs^{-1} for 50 potential cycles.

b. Au-C, AuNPs-C and AuCu-C catalysts

The Au-C, AuNPs-C and AuCu-C catalysts were investigated using CV experiments performed in 0.5 M H_2SO_4 in the potential range of -0.4 to +1.6 V (Ag/AgCl, KCl_{std}) at a scan rate of 20 mVs^{-1}. Kinetic parameters and active surface area were evaluated from cyclic voltammetry based on the hydrogen desorption area corresponding to a monolayer of adsorbed hydrogen. The electrooxidation reactions of formic acid in acid medium were performed in 0.5M HCOOH + 0.5M H_2SO_4 in the potential range of -0.4 to +1.6V (Ag/AgCl, KCl_{std}) at a scan rate of 50 mVs^{-1}.

4.4.4 Chronoamperometry

Chronoamperometry (CA) is an electroanalytical technique for the investigation of the catalyst stability, kinetics, mechanism and the determination of diffusion coefficients of

the electrochemical system. It involves potential voltage excitation, resulting in a current density response. This response requires semi-infinite linear diffusion (i.e. an unstirred solution, linear diffusion to the electrode surface, a planar electrode and a supporting electrolyte to ensure the absence of ion migration) and no other reactions. To investigate the stability and durability of all catalysts in acid medium, chronoamperometric experiments were performed for fixed potential of 0.6 V for 5000 seconds. For Pd-C catalysts, the comparison between the PVP and NH_4F + H_3BO_3 synthesis routes at fixed potentials of 0.1, 0.3 and 0.6 V for 5000 seconds was investigated.

4.5 Summary of the method development

The chemical reduction synthesis of the Pd-C catalyst followed the modified method by Zhang and coworkers (2006) is summarised in Figure 4.4.
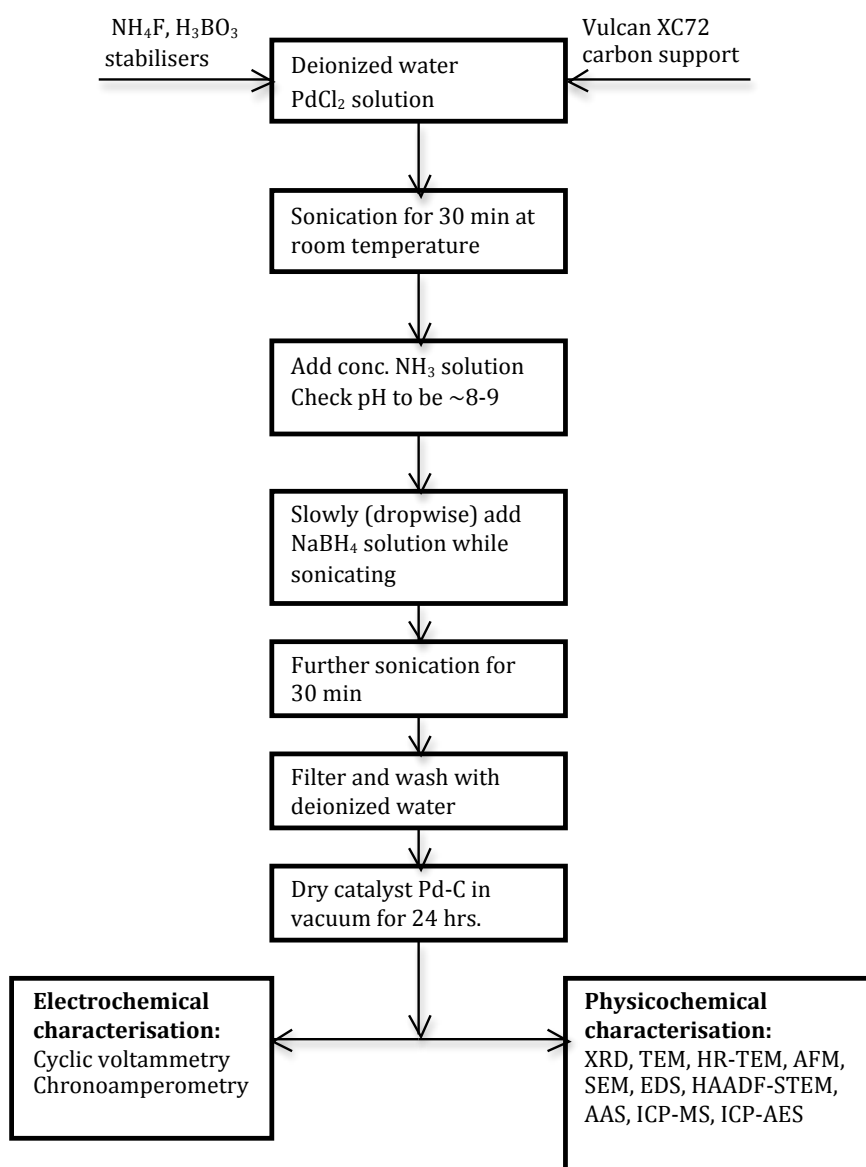
Figure 4.4: Block flow diagram of the experimental methods, physicochemical and electrochemical characterisations [264]

In the work Zhang *et al.*, ammonium fluoride and boric acid were used as stabilising agents and sodium borohydride as a reducing agent. In this thesis, a modification of the method was made, by using 1 M solution of sodium borohydride (~12 wt.% in 3 M NaOH). The NaOH was added to suppress the hydrogen evolution reaction. The prepared catalysts were washed with DI water until the pH is neutral, i.e. no chloride ions remained and other residuals were thoroughly washed off. A further change was to use PVP as the stabiliser for the Pd-C catalyst and compared the effect of stabilisers

(better dispersion and smaller particle sizes) on the physical/electrochemical characteristics of the catalysts. The catalysts prepared by the modified Zhang *et al.* method were denoted as Pd-C$_{H3BO3 + NH4F}$ and Pd-C$_{PVP}$, respectively. Subsequently, all other catalysts (mono- and bi-metallic) were prepared using PVP as the stabilising agent.

4.5.1   Modifications to the Pd-C catalyst synthesis

- The synthesis method was established and parameters were varied to investigate the effect of synthesis conditions on the catalyst product. The catalyst was tested electrochemically and various physical characteristics of the products were estimated.

- Metal content was estimated using ICP-AES for Pd-C$_{H3BO3 + NH4F}$, which showed a low metal content of the synthesised products (*see Table 5.2, Appendix A: Table 9*).

4.5.2   Modifications to the Au and Au-based catalysts

- AAS and ICP-MS data was used to estimate of the metal compositions (see Tables 6.1, 7.2 and Appendix A-Table 3 for details). The wt.% of the active metal was low with wide variations in the amount of active metal (Au) in the catalyst, using both AAS and ICP-MS techniques.

- Further development of the method included increasing the active metal content by:

- o Increasing the concentration of the Pd precursor used. The low metal content was attributed to the possibility of systematic (weight/concentration) error in the precursor used in the synthesis prepared from solid $PdCl_2$ in the laboratory.

- o Focus should be on the increase the weight of the active metal to 20 wt.%, since the % yield was low (ca. $10 - 30\%$) of the wt.% theoretical estimate.

4.5.3 Limitations/Recommendations of the methodology

- Water evaporation over time - this may change the concentration

- Evolution of hydrogen gas during reduction process due to dissociation of water

- When mixing materials (heterogeneous) with different densities, it is generally impossible to achieve a completely homogeneous material.

- The problem of active metal composition variation due to the heterogeneous nature of the sample. The actual weight of metal nanoparticles attached to the carbon black is unknown.

- Variation in the active metal composition, due to synthesis conditions not being optimized.

- The mechanical energy generated due to the sonication process could result in a change of temperature (heat released into the system) in the water bath.

- A temperature control system would be required to optimise the synthesis process to correct for the possible change in temperature.

- Error in concentration due to volume change is common – pipette errors.

- Most common is dilution errors, which lead to concentration errors especially in trace element analysis such as ICP, AAS.

- The possibility of the metal nanoparticles not being anchored onto the carbon support (heterogeneous material), could lead to error in ICP data due to a weight error in the sampling of the catalysts for ICP analysis.

The wide variability of the ICP analysis data could be minimised following the recommendations of Biella and coworkers and Chen *et al.*. In their work, they estimated the metal composition of the catalysts using a filtrate after the sodium borohydride reduction. The approach is used as a means to investigate leaching of the very small AuCu nanoparticles and to eliminate the problem of uneven dispersion of metal nanoparticle on the carbon support (*mixed heterogeneous solids*), both of which contribute to the errors in the digestion method. Their findings showed the composition of the catalyst is consistent with the theoretical calculation from the preparation procedure [16, 267].

Chapter 5   Performance of the Direct Formic Acid Fuel Cell with Electrochemically Modified Pd-C Anode Catalyst

In Chapter 4, detailed experimental techniques were presented. In this chapter, palladium, a member of the platinum group metals, is investigated to evaluate the effect of the synthesis route on the catalyst's physical and electrochemical characteristics, and its overall performance in FAO. Reduction of active metal loading (less mass) and improved dispersion of the nanoparticles on the carbon support will provide a high surface area distribution and enhances the catalytic activity. In this chapter, a new anode material is prepared via room temperature synthesis, which increases Pd utilisation by lowering the amount of active metal loading. Kinetic parameters are obtained using three electrode half-cell cyclic voltammetry techniques to elucidate the performance and mechanism of the FAO.

In this investigation, carbon supported Pd nanocatalysts were prepared by chemical reduction with sodium borohydride and using polyvinyl pyrrolidone as the capping agent at room temperature. Detailed physical characterisations of catalysts were obtained by Thermogravimetric analysis (TGA), transmission electron microscopy (TEM), X-ray diffraction (XRD), atomic force microscopy (AFM), scanning electron microscopy (SEM), and X-ray energy dispersive spectroscopy (EDS). The electroactivity and stability of the catalysts towards formic acid electrochemical oxidation were measured by cyclic voltammetry (CV) and chronoamperometry (CA).

5.1   **Results**

5.1.1   **Thermogravimetric analysis (TGA) analysis to determine Pd content**

Table 5.1: Weighted mass analysis of the Vulcan XC72 carbon support

S/N	[a]Sample wt. (in)	[b]Wt.% (TGA data)	[c]Exact wt., mg	[d]Weighted Mass, mg
XC72-C$_1$	0.8762	1.5719	0.0138	0.0121
XC72-C$_2$	1.3467	1.4357	0.0193	0.0260
XC72-C$_3$	1.2405	1.7674	0.0219	0.0272
XC72-C$_4$	1.4450	1.0659	0.0154	0.0223
XC72-C$_5$	1.4778	1.1280	0.0167	0.0246
XC72-C$_6$	1.1050	3.1131	0.0344	0.0380
XC72-C$_7$	1.2613	4.5249	0.0571	0.0720
XC72-C$_8$	0.6450	6.4546	0.0416	0.0269
XC72-C$_9$	1.0730	5.5936	0.0600	0.0644
XC72-C$_{10}$	0.9497	3.8986	0.0370	0.0352
Weighted average, mg				**0.035±0.018**

*Exact wt., mg = (a*b)/100; weighted mass = b*c

The blank basis for the analysis was 10 samples of the carbon support (Vulcan XC72) as shown in Table 5.1. The sample analyses give an estimated weighted mass of ash (residue from Vulcan XC72) of 0.035±0.018 mg. Figure 5.1 shows the TGA proximate analysis technique used to determine the metal content of the Pd-C catalysts. From Figure 5.1, the average active Pd metal weight % in the Pd-C catalyst samples analysed was 3.5±0.18 wt.%: about 20% yield of the theoretical estimated weight of the active metal loading before synthesis.
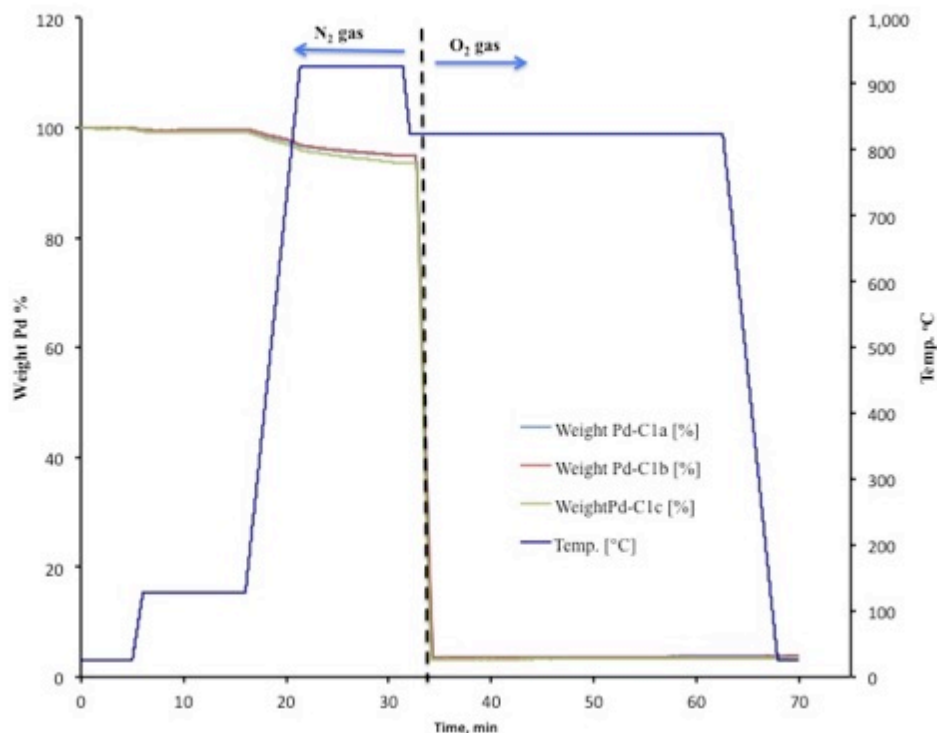
Figure 5.1: TGA proximate analysis curves for Pd-C$_{6H3BO3 + NH4F}$(PdC13) catalyst samples

5.1.2 Compositional analysis for Pd-C catalysts

Table 5.2 shows the compositional analysis for the Pd catalysts, demonstrating the chronological development of the catalyst synthesis procedure (*see details in Appendix A, Table 9*). The PdC13 synthesis showed very low metal deposition on the carbon support; this could be due to the incomplete deposition or reduction of the metal precursors and possible precursor dilution errors. Catalyst syntheses were not performed at optimised conditions; however, the concentration of the precursor was increased during the method development and also by using a commercially available PdCl$_2$ solution. Improved active metal loading can be observed in the subsequent synthesis products PdC16 and PdC17. The PdC17 sets show an average metal loading (triplicate

runs) close to the theoretical maximum of 20wt.% for Pd-C$_{PVP}$ (20.8±1.1) and Pd-C$_{H3BO3 + NH4F}$ (23.2±3.3).

Table 5.2: Catalyst composition analysis results for Pd-C catalysts

Sample #	Theoretical estimate wt.%	ICP wt.%	TGA wt.%
PdC13			
Pd-C$_{1H3BO3 + NH4F}$	16.3	1.9	
Pd-C$_{2H3BO3 + NH4F}$	9.1	1.2	
Pd-C$_{5H3BO3 + NH4F}$	13.1	1.4	
Pd-C$_{6H3BO3 + NH4F}$	16.8	1.9	3.5
Pd-C$_{7H3BO3 + NH4F}$	20.0	2.4	
Pd-C$_{10H3BO3 + NH4F}$	20.0	2.3	
PdC16			
Pd-C$_{1PVP}$	19.2	54	
Pd-C$_{2PVP}$	19.4	43.5	
Pd-C$_{1H3BO3 + NH4F}$	18.4	20.6	
Pd-C$_{2H3BO3 + NH4F}$	18.2	21	
PdC17			
Pd-C$_{1H3BO3 + NH4F}$	20.0	27.2	
Pd-C$_{2H3BO3 + NH4F}$	20.0	23.3	
Pd-C$_{3H3BO3 + NH4F}$	20.0	19.1	
Avg. Wt.%		**23.2±3.3**	
Pd-C$_{1PVP}$	20.0	22.3	
Pd-C$_{2PVP}$	20.0	20.5	
Pd-C$_{3PVP}$	20.0	19.7	
Avg. Wt.%		**20.8±1.1**	

The deviation could be ascribed to the heterogeneous nature of the catalysts, the metal deposited on Vulcan XC72 carbon, the poor dispersion of the nanoparticles on the support (e.g. agglomeration as observed in Figure 5.2), and the poor mixing of metals and carbon (e.g. dispersion), affecting the material sampling in the compositional analysis. The method development for the synthesis process requires optimisation of the different conditions (temperature, precursor concentration, stirring/sonication process, reduction time, and reducing agent flow rate) for improved active metal loading on the Vulcan XC72 carbon black support. In particular, the effect of these limitations can be observed in Table 5.2 PdC16 (Pd-C_{PVP1} and Pd-C_{PVP2}) samples showed complete deviation from the theoretical maximum weight because the metal nanoparticles were probably mostly settled at the bottom of the sample bottle, resulting in weight/sampling error (*e.g. sample AuCu-C_{6PVP} Appendix A: Table* 9). Another possible scenario could be due to the conversion of the Vulcan XC72 carbon into CO2 during the synthesis process. This would account for the relative increase in the weight of Pd metal beyond the theoretical maximum. Pd-C_{PVP2} with 43.5 wt.% was used for the various physical and electrochemical characterisations throughout the thesis and denoted as Pd-C_{PVP2} $_{(43.5\%)}$ except otherwise stated.

5.1.3   Scanning electron microscopy with X-ray microanalysis (SEM/EDS)

SEM/EDS were used to investigate the Pd-C catalyst's morphology, particle size and dispersion (see Figure 5.2), and chemical elemental mapping (see Figure 5.3) was used to determine and confirm the elements in the Pd-C catalyst. Figure 5.2 depicts the SEM images showing the morphology of Pd-C catalysts with 5 and 10 µl dilutions on a carbon tape.
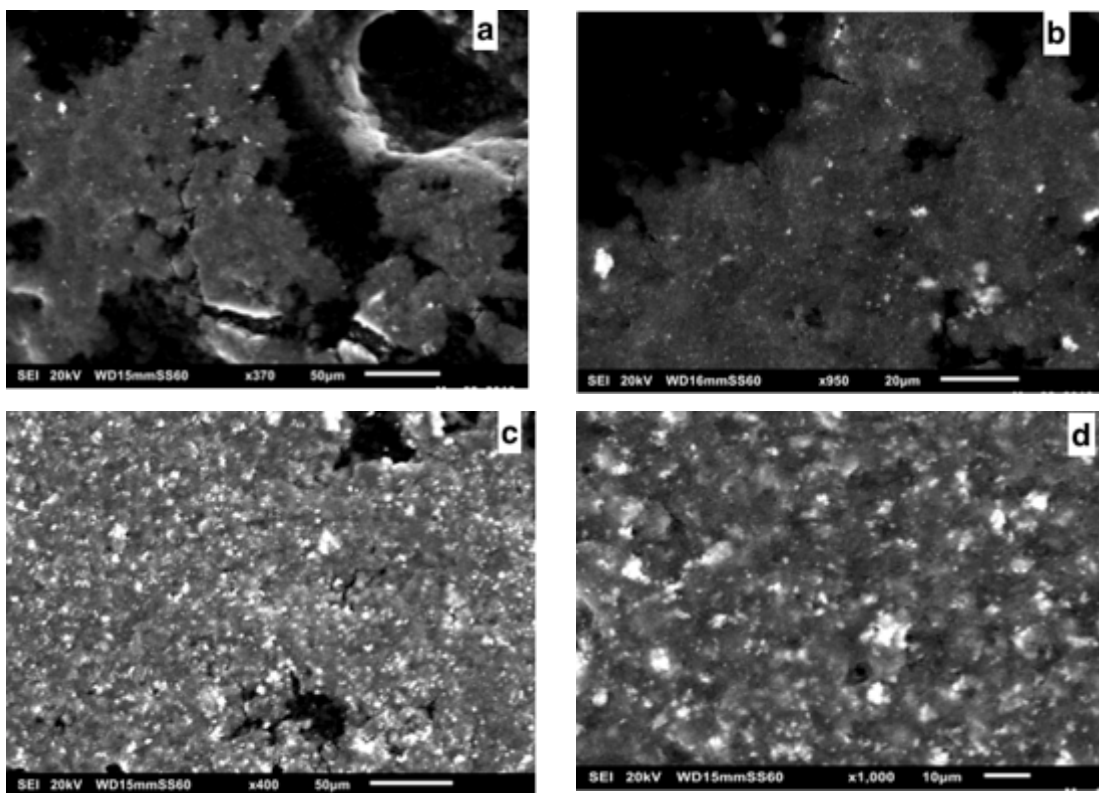
Figure 5.2: SEM micrographs of Pd-C$_{PVP2\ (43.5\%)}$ (PdC16) catalysts: (a and b) with 5 µl and (c and d) with 10 µl dilution

Chemical	Mass %	Atom %
Pd	31.43	4.92
C	68.58	95.08
Total	100	100
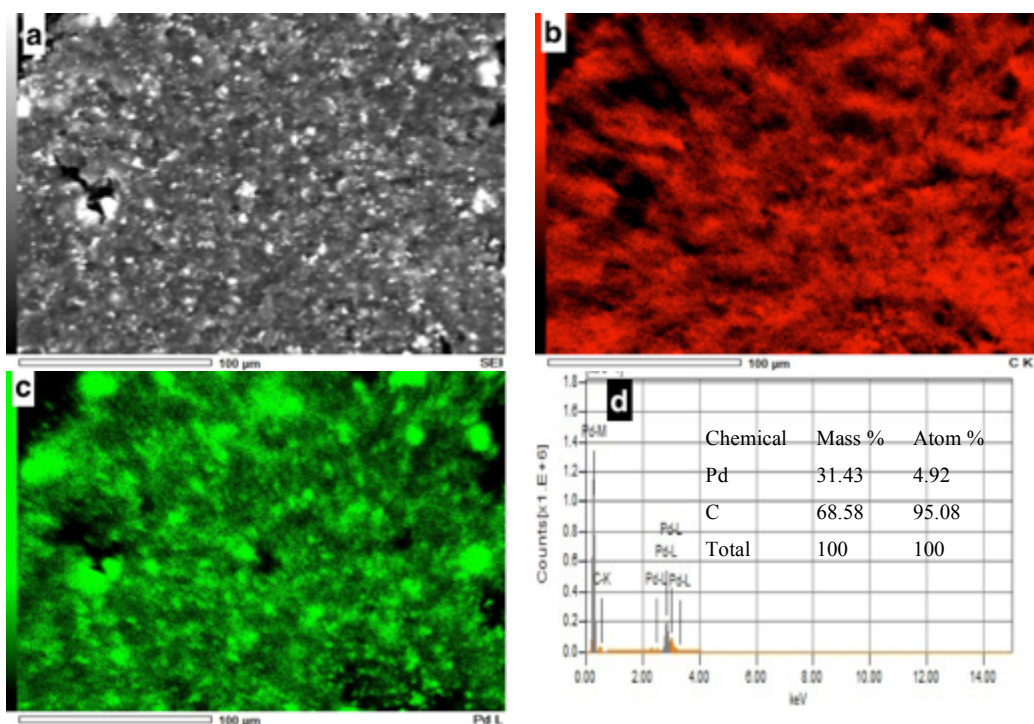
Figure 5.3: SEM-EDS of Pd-C$_{PVP2\ (43.5\%)}$ (PdC16) catalysts: (a) SEM images of 10 µl paste (b) Carbon support element map (c) Pd metal element map (d) Quantitative element mapping

Figure 5.3 shows a representation of the SEM (Figure 5.3a) and corresponding EDS from the same region on the sample (Figures b and c). The composition maps were constructed using the emission lines of Pd and C. The SEM/EDS data particle size analysis gives much larger values, which is expected as EDS provides information from the surface of the Pd-C$_{PVP2 (43.5\%)}$ catalyst, which is residual on the carbon black support and the carbon tape holder [268]. Figure 5.3d show the elemental distribution maps and the atomic ratios deviate from the expected values. The deviation could be ascribed to the area mapping technique of the SEM, which measures the whole area exposed for the particular analysis. The value of the atomic ratio will vary with the position of the electron beam on the sample surface. This is in agreement with previously reported work by Gogate (2016), by the critical assessment of the methods to determine the particle size in supported metals. They concluded that the nature of the phase contrast and the accompanying image generation for smaller particles leads to major uncertainties in size quantification for particle less than 2.5 nm [253].

5.1.4 Atomic formic microscopy analysis
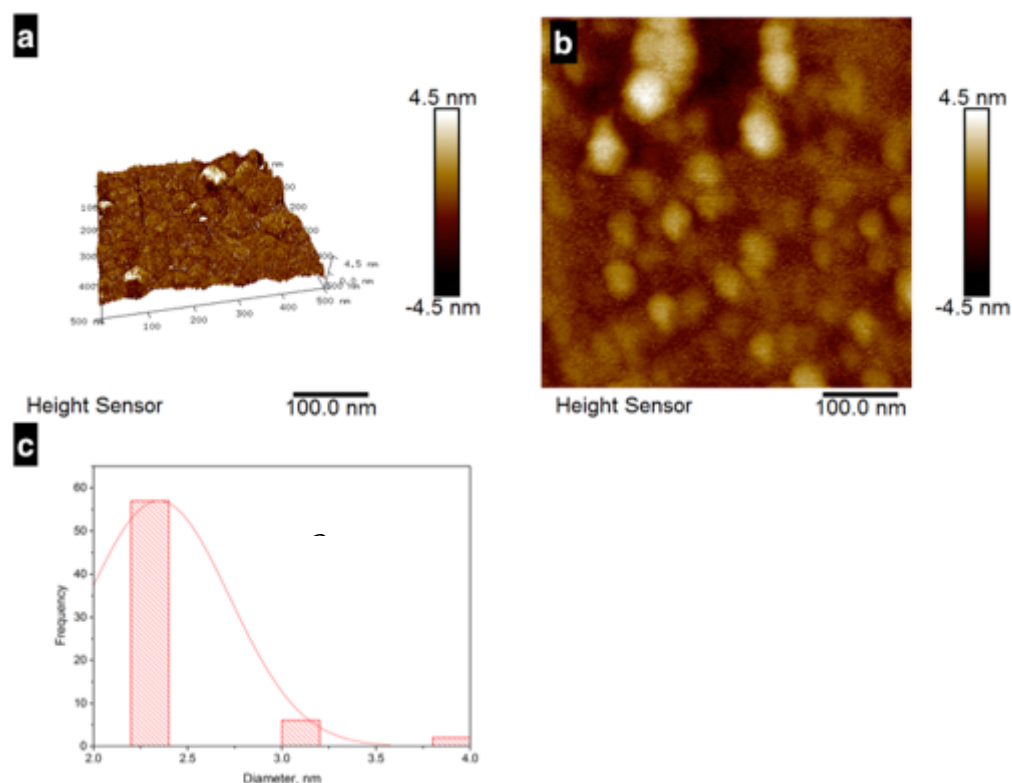
Figure 5.4: Pd-C$_{PVP2\ (43.5\%)}$ catalyst AFM images- (a) 3D image with phase contrast, (b) 2D image, (c) Particle size profile

Figure 5.4 shows the AFM images and profile for Pd-C$_{PVP2\ (43.5\%)}$ catalyst, showing well-dispersed Pd nanoparticles on carbon. Deposition on a mica surface demonstrated the presence of polydisperse, spherical, flattened nanoparticles of Pd, and rough surfaces. The morphological characteristics (height and phase measurements) of Pd-C$_{PVP2\ (43.5\%)}$, see Figure 5.4a, show the surface roughness and the topography of the Pd nanoparticles observed as quasi-spherical shaped Pd nanoparticles. The morphological features show continuous island-like structures with varying thickness and size. These small valleys, the island from visual inspection show surface height relative of nanoparticles to the centre plane at 4.5 nm. The AFM image estimated the

nanoparticles average size of the nanoparticles at ca. 2.4 nm (see Figure 5.4c), which is affected by the degree of surface roughness.

5.1.5 Transmission Electron Microscopy Analysis

Figure 5.5 shows TEM images of Pd-C nanoparticles dispersed on a carbon black support. The high-resolution transmission electron microscopy (HRTEM) shows a selected single Pd crystallite showing the lattice fringes and intra-distance atomic spacing of the Pd crystal. High angle-annular dark-field scanning transmission electron microscopy (HAADF-STEM) was used because of the better contrast of precipitates in TEM and strong chemical/structural sensitivity at the atomic scale. There are about 1200 Pd NPs per sample, determined using ImageJ 1.48 V for estimating the particle size distribution and fitted with Gaussian-Lorentzian product function. Figure 5.5b shows a typical high-angle-annular dark-field (HAADF) image of the nanoparticles. There are spherical and quasi-spherical nanoparticles that are sparingly dispersed on the carbon support because of the low metal loading of Pd-C [Pd-C$_{6H3BO3 + NH4F}$] (~1.9 wt.% ICP-AES) see Table 5.2 and Appendix A – Table 9).
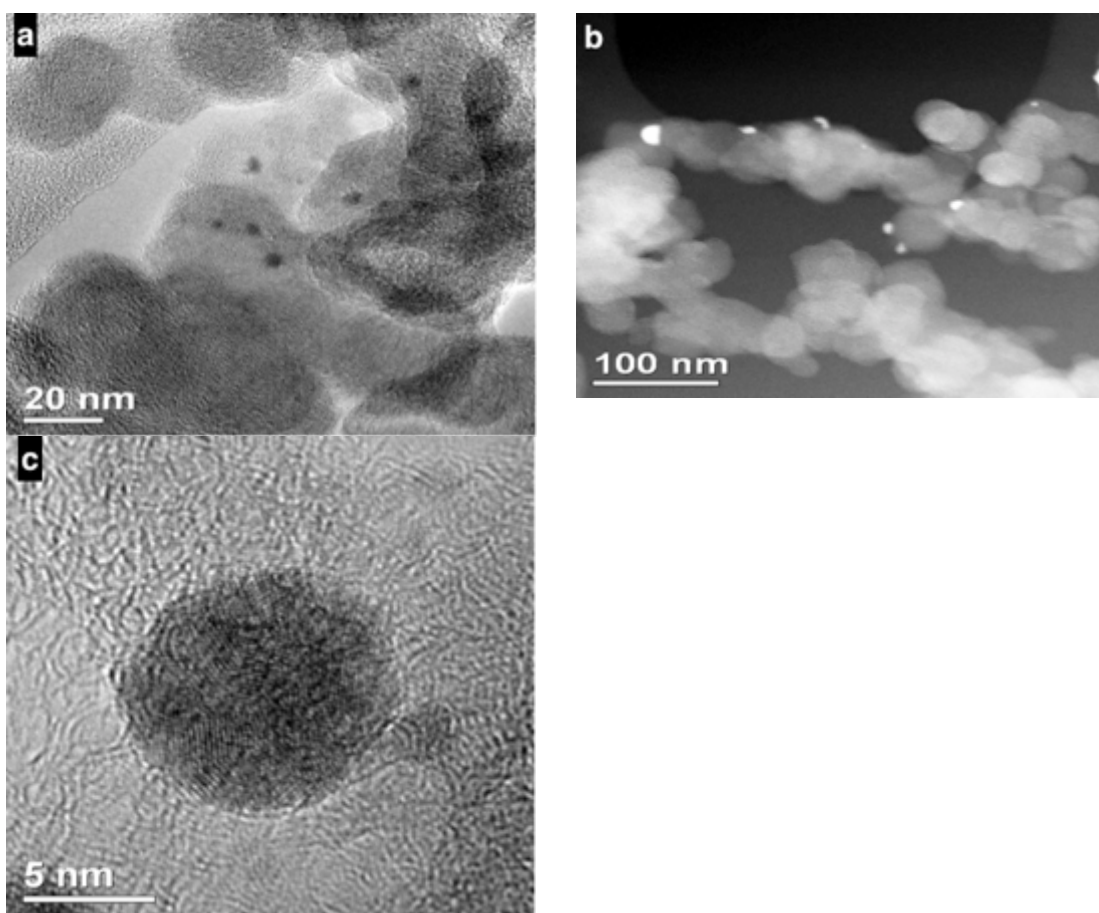
Figure 5.5: HRTEM images of Pd-C catalysts – (a) particle distribution, (b) HAADF-STEM (Z-contrast) image of Pd on carbon support (bright dots correspond to Pd atoms), (c) selected single Pd crystallite

5.1.6 Crystallographic Analysis

Figure 5.6 shows that the pattern of the triplicate samples (*Appendix A, Tables 10 and 11*) Pd-C$_{PVP}$ (*PdC17*) exhibited diffraction peaks of (111), (200), (220) (311) and (222), indexed with (JCPDS No. 46-1043) at 2theta values of 39.75, 45.48, 67.67, and 80.93 for the Pd-C$_{PVP}$ and 39.84, 46.10, 67.35, and 81.21 for Pd-C$_{H3BO3+NH4F}$ catalysts, respectively. The average peak positions for the three samples provide information about the translational symmetry of the Pd-C catalysts. The shape and broad width of the peaks demonstrate possible deviation from a perfect crystal, that is, the possible

presence of defects and microstrain on the nanoparticles. The broad diffraction peak located at approximately 24.6° is associated with the Vulcan XC72 carbon support (C 002), matching the graphite carbon pattern in JCPDS, File No. 56-0159.
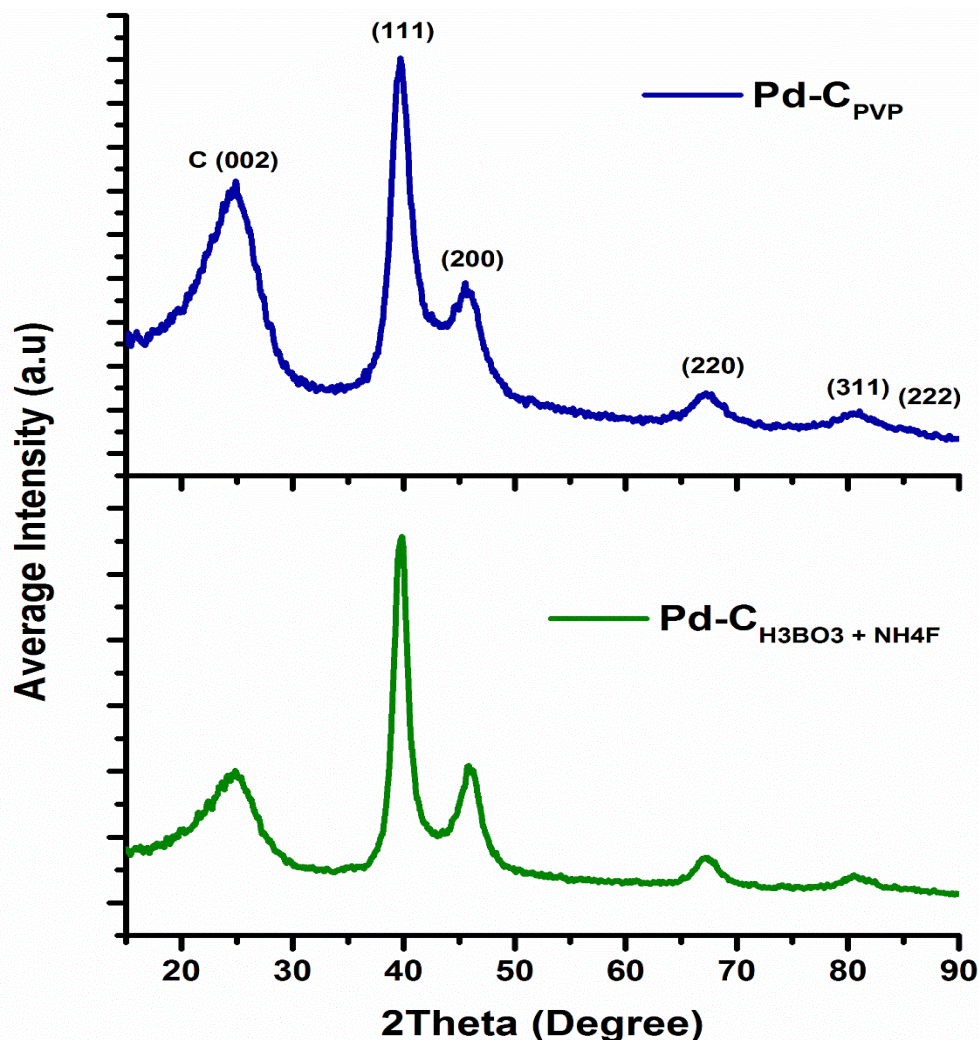
Figure 5.6: XRD patterns of Pd-C$_{PVP}$ and Pd-C$_{H3BO3+NH4F}$ catalysts with major peaks marked (JCPDS No. 46-1043)

5.1.7 Particle size analysis

The average crystallite size of the Pd particles were calculated from the Bragg peaks using Debye-Scherrer's formula, owing to its influence on metal properties including hardness and strength [82, 118, 207]:

$$D_p = \frac{K\lambda}{\beta_{\frac{1}{2}} Cos\theta} = \frac{0.94\lambda}{\beta_{\frac{1}{2}} Cos\theta} \hspace{4cm} 5.1$$

where D_p is the average particle size, K is the shape factor, λ is the wavelength of the X-ray, $\beta_{1/2}$ is the width (in radians) of the diffraction peaks at half height, and θ is the Bragg angle of the (220) peak. All lattice strain for the (200) facets, $\beta_{1/2,}$were analysed using PANalytical B.V Data Viewer software. In Debye-Scherrer's equation, the analysis is largely based on a cubic crystal model. The crystallite shape factor which can be approximated to 0.9 in the absence of shape information. Using an approximation method in 1918, Scherrer evaluated the shape factor, K and obtained a numerical value: $2\left(In\frac{2}{\pi}\right)^{\frac{1}{2}}$ = 0.93. However, different approximations and different definitions of the half-value breadth ($\beta_{\frac{1}{2}}$) of the diffraction beam gave different shape factor values [269]. When the size of the particles is sufficiently small, the diffraction pattern is broadened by an amount inversely proportional to the crystallite size. The actual value of the shape factor depends on: (i) the definition of the 'breadth (peak width), (ii) the definition of the crystal size, (iii) the crystallite shape, and (iv) the crystallite-size distribution. Langford and Wilson, in their excellent discussion, concluded that the most common values of K are: 0.94 for full width at half maximum (FWHM) and 0.89 for integral breadth of spherical crystals with cubic symmetry. They concluded that the actual value of K varies from 0.62 to 2.08 [270]. XRD can only measure the crystallite size of the crystalline materials via Scherrer's equation. The crystallite (coherently scattered domain of the material) size is the size of a single crystal inside the grain or particle. Grains (containing multiple mis-oriented domains) are volumes inside crystalline materials, with specific orientations.
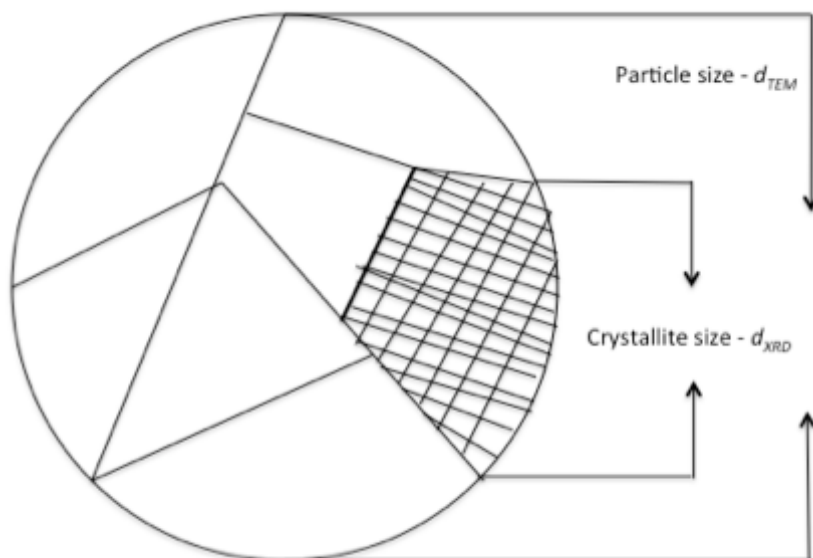
Figure 5.7: Schematic diagram of the size obtained by TEM and XRD peak broadening analysis. In the case of single-crystal nanoparticles, crystallite size and particle size are the same.

Generally a combination/agglomeration of small crystallites sizes gives a particle and several particles combined give a grain (see Figure 5.7). A more accurate technique for the measurement of grains, particles size and shape for nanomaterials is small angle x-ray scattering (SAXS), which can then be confirmed using visual techniques such as TEM and SEM.

X-ray diffraction line broadening will occur for crystalline particle smaller than 100 nm. This instrumental broadening effect is caused by the particle size and lattice strain (measure of the distribution of lattice constants) interaction with the x-ray beam. The crystallite sizes for all catalysts were estimated using the corrected line broadening analysis for standard LaB_6 [271, 272]. A Lorentzian profile fit for the crystal peaks was used and evaluated the instrument broadening was calculated to be 0.05 nm as shown in Figure 5.8. The lattice parameters and *d*-spacing were estimated for all catalysts

according to Bragg's law for the (200) plane using Equation 5.2:

$$a = \frac{(\sqrt{h^2+k^2+l^2} \; x \; \lambda)}{2sin\theta} \text{ and } d_{hkl} = \frac{\lambda}{2sin\theta} \tag{5.2}$$

where a is the lattice parameter, hkl are the Miller indices, θ is the Bragg angle, d_{hkl} is the d-spacing.
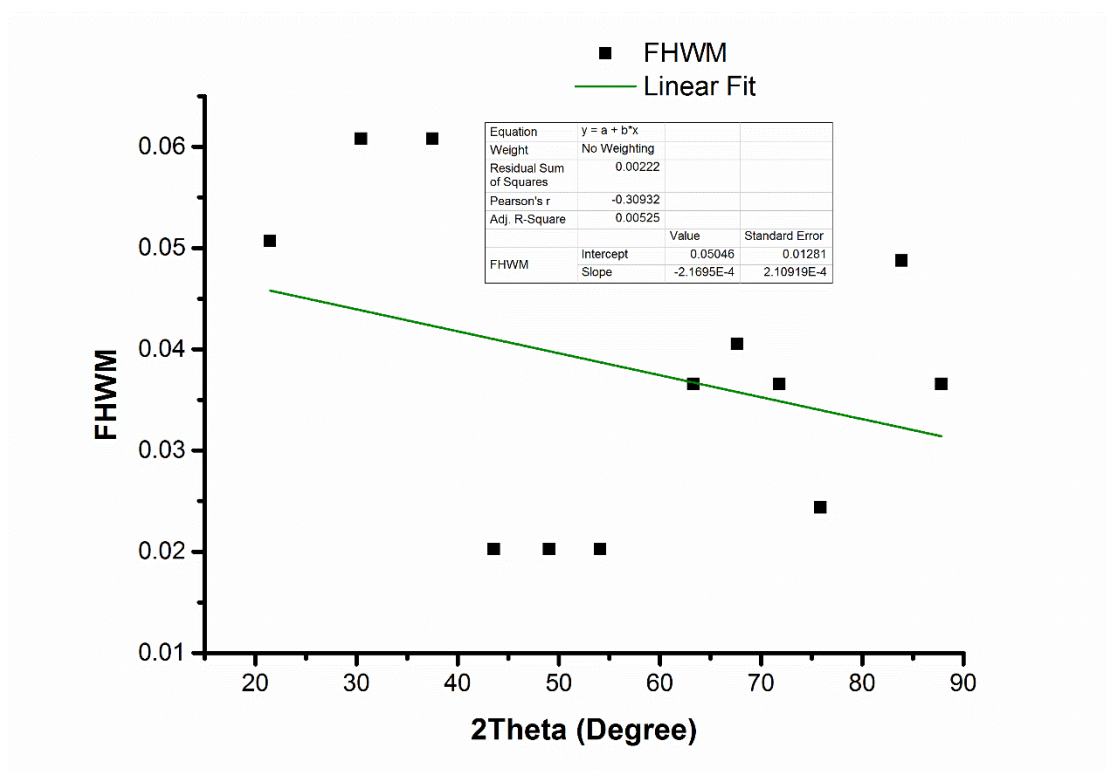
Figure 5.8: Line broadening analysis for standard LaB₆ used to eliminate instrumental broadening effect of the crystallite size estimation

Using Equation 5.1 the average Pd crystallite size from the (200) peak was estimated to be 1.4 nm and 4.4 nm for Pd-C$_{PVP}$ and Pd-C$_{H3BO3 + NH4F}$, respectively, consistent with data obtained from TEM analysis results for other samples. No external layer of oxide phase or a residual capping agent was observed in the analysis. The relative crystallinity of Pd (200) and carbon black (C 002) of the Pd-C catalyst was 2.57 and 2.30 for Pd-

C_{PVP} and Pd-$C_{H3BO3\ +\ NH4F}$, respectively, indicating well-ordered crystalline Pd nanoparticles. The intensity ratio of the (111) peak to (200) peak, calculated from JCPDS card data of the Pd-C catalyst samples (increase from 1.67 to 2.73 and 2.47) for Pd-C_{PVP} and Pd-$C_{H3BO3\ +\ NH4F}$, respectively. Indicates the preferential orientation of the (100) facets in Pd nanoparticles as confirmed in previous literature [92, 273-275], and agrees with the CV experiment. Furthermore, the total surface area of catalyst was estimated from the XRD crystal plane (200) peak using Equation (5.2) [240].

$$S_{XRD} = \frac{6000}{\rho * d} \hspace{4cm} 5.2$$

where S_{XRD} is the surface area in m^2 g^{-1}, d is the average particle size (nm) calculated from the Debye-Scherrer's equation, and ρ is the density of palladium (ρ_{Pd} = 12.0 g cm^{-3}). The surface area, S_{XRD} calculated from the XRD data for the as prepared Pd-C catalysts were 357.1 m^2 g^{-1} and 113.6 m^2 g^{-1} for Pd-C_{PVP} and Pd-$C_{H3BO3\ +\ NH4F}$, respectively, confirming the effect that the PVP stabiliser generates smaller particle sizes and larger surface areas [276, 277]. The difference in the surface area of the catalysts is due to the approximation of Debye-Scherrer's equation, that all particles are all spherical. The TEM, SEM, and AFM images show the particles are not wholly spherical, the defects, corners and carbon support will increase the overall ECSA determined electrochemically. This suggests an enhanced electrocatalytic activity for the FAO reaction and a large Pd surface site per gram of catalyst.

5.1.8 Electrochemical Measurement: Cyclic voltammetry (CV)

CV experiments are used to evaluate the electrocatalytic activity of the Pd-C catalysts in acid media. All experiments were performed at room temperature. Nitrogen or argon gas to deaerated the solutions of formic acid/or sulphuric acid solutions potentials were measured versus Ag/AgCl$_{sat.}$KCl reference electrode.

i. *Electrochemical surface area estimation and analysis*

The cyclic voltammetry technique is useful for estimating the electrochemically active surface area (ECSA) of a catalyst. The Pd-carbon black supported catalyst was used for CV experiments in nitrogen-saturated 0.5 M H_2SO_4 at a scan rate of 20 mVs^{-1} at room temperature. The ECSA is the area of hydrogen adsorption/desorption peaks representing the number of active sites on a catalyst [278]. The ECSA provides the active available surface site of the catalyst for the electrochemical reaction. The ECSA was estimated using the MultiStat data software analysis and is presented in Table 5.3 from the ICP-AES wt.% of the active metal, assuming 100% Faradaic efficiency of the redox process. The ECSA and Pd utilisation increased with decreasing scan rate but rate is lower than 5 mVs^{-1}, the effect of mass transfer caused a drop in utilisation and ECSA. In electrochemical reactions, current density scales with the reaction surface (interfacial) area, i.e. indicating improved performance of the catalyst.

Table 5.3: *Physicochemical and electrochemical parameters of Pd-C$_{2PVP}$ (43.5 wt.%) catalysts*

Scan rate, [mV s^{-1}]	[a]Q, [C cm^{-2}]	[a]ECSA, [m^2.g^{-1} Pd]	[b]Pd surface site, [Pd sites. g$_{cat.}$* x10^{21}]	[c]Pd utilisation, %	[d]Mass activity, [mA g^{-1}]	[e]Specific activity, [mA m^{-2}* x10^{-9}]	[f]Roughness factor, R$_f$ * x10^9
100	0.095	60.0	1.79	16.8	211.3	0.15	0.86
50	0.154	97.5	2.91	27.3	159.5	7.12	1.39
20	0.220	139.4	4.17	39.0	99.6	3.11	1.99
10	0.318	201.9	6.04	56.5	76.1	1.64	2.88
5	0.428	271.7	8.13	76.1	15.7	0.25	3.88
2	0.187	119.0	3.56	33.3	9.9	0.36	1.70

[a] Estimated from CV at 20 mVs^{-1}, [b] Calculated by: [ECSA/CSSA], [c], Calculated by: [ECSA/CSA]*100, [d] Calculated by: Current density sum of adsorption peaks divided by W$_{Pd}$, [e] Calculated by: Current density sum of adsorption peaks divided by ECSA, [f] Calculated by: ECSA/geometric surface area of electrode. Assuming cross sectional surface area (CSSA) of surface Pd atom taken as 0.0787 nm^{-2}.[279, 280]

From Figure 5.9 Pd-C catalysts exhibited a well-defined hydrogen adsorption-desorption region of -0.2 to +0.15 V, a double layer capacitance region +0.18 to +0.5 V and an oxygen region +0.5 to +1.0 V versus Ag/AgCl$_{sat.KCl}$ [118, 281, 282]. The CV curves were consistent with polycrystalline Pd on the carbon support electrode in acid media [281] and consistent with the XRD profile (Figure 5.6). In the three main regions, a characteristic voltammetric signature was observed: in the hydrogen adsorption-desorption region (b) represents hydrogen extraction from α-PdH, (a) represents extraction of hydrogen from the β-PdH hydrogen desorption and (h) is H absorption to

form α-PdH and β-PdH (d and e) both show oxide formation, (f) represents oxide stripping (g) is H adsorption and (c) is the double layer capacitance region [281].
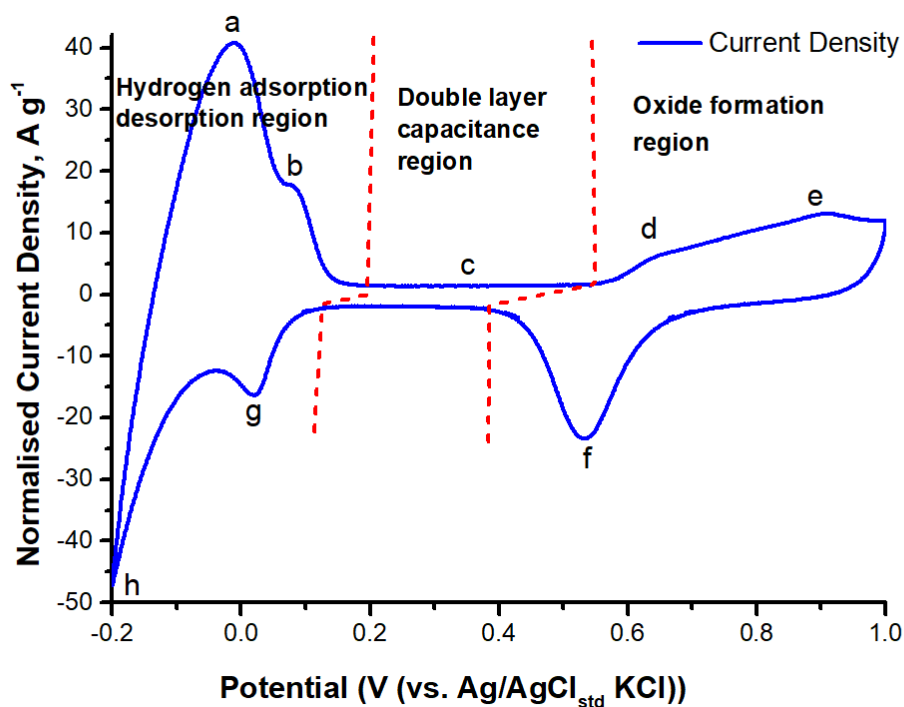
Figure 5.9: Cyclic voltammetry of Pd-C catalyst in 0.5 M H₂SO₄ solution at a scan rate of 20 mVs⁻¹ (10th cycle)

The ECSA of the Pd-C catalyst was obtained from the CV curve shown in Figure 5.9. The electrochemical active surface area (ECSA) was evaluated from the coulombic charge of the hydrogen adsorption-desorption after subtraction of the double layer capacitance charge (Equation 5.3) [118]. This is the area under each peak, which represents the charge involved in the redox processes.

$$ECSA = \frac{Q_H}{210 \text{ x } W_{Pd}}$$

5.3

where W_{Pd} is the Pd catalyst loading (g cm^{-2}) and Q_H is the total charge associated with the monolayer adsorption of hydrogen on the polycrystalline Pd surface(C cm^{-2}). The results calculated above are much higher because the value of 210 μC cm^{-2} is for a plane surface electrode [111]. The electrodes used in this experiments were polished glassy carbon electrodes with Pd catalyst paste in carbon black support. This accounts for the larger surface compared with the theoretical calculations. The cross-sectional surface area is taken as 0.0787 nm^{-2} of surface Pd atom [279, 280]. The specific Pd catalyst loading, amount of catalyst paste on the working electrode was 0.75 mg cm^{-2} for Pd-C$_{2PVP (43.5 wt.\%)}$ and 0.36 mg cm^{-2} for Pd-C$_{2H_3BO_3 + NH_4F}$ electrodes.

The chemical surface area (CSA) of the Pd catalyst was calculated using Equation 5.4 [283]:

$$CSA = \frac{6}{\rho d} \qquad\qquad 5.4$$

where ρ is the density of Pd (12 g cm^{-3}), d (in nm) is the estimated mean particle diameter (SEM, TEM, XRD). The active chemical surface area of the catalyst was calculated, using the XRD surface area, to be 357.1 m^2 g^{-1} for Pd-C$_{2PVP (43.5 wt.\%)}$ and 113.6 m^2 g^{-1} for Pd-C$_{2H_3BO_3 + NH_4F}$ electrodes, indicating a larger well-dispersed structure for the Pd-C$_{2PVP}$ active site available for oxidation of formic acid.

Figure 5.10 shows the comparison of scan rate on the oxidation-reduction (redox) peak positions of the Pd-C$_{2PVP(43.5 wt.\%)}$ catalyst. There are positive oxidation potential shifts and negative potential shifts with scan rate in the reversed cycle.
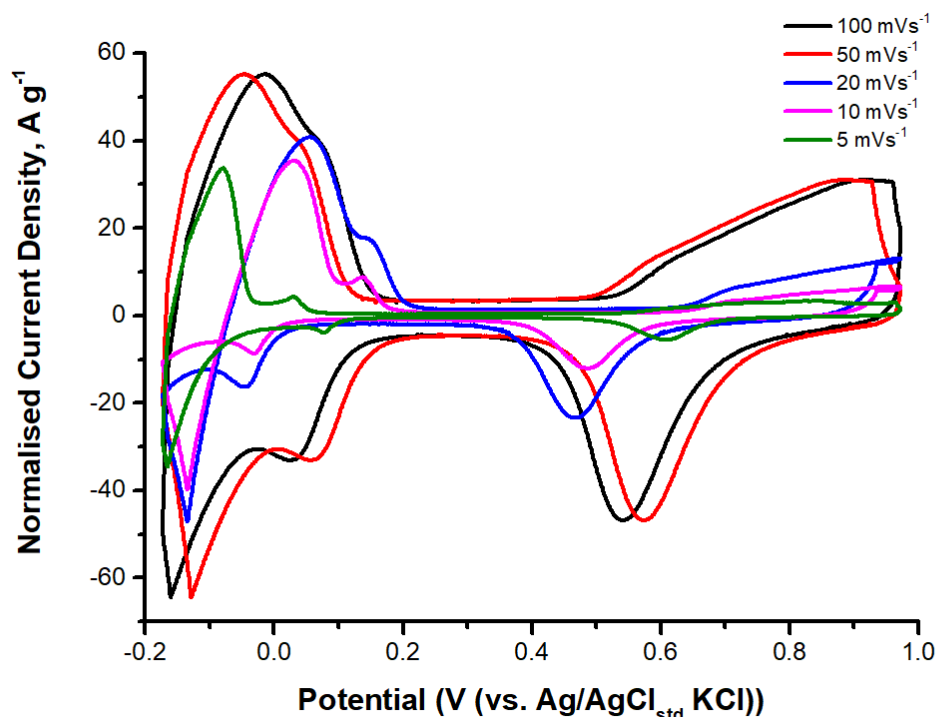
Figure 5.10: Cyclic voltammetry of Pd-C$_{2PVP (43.5 wt.\%)}$ catalyst in 0.5 M H$_2$SO$_4$ solution at different scan rate on potential shift (10th cycle)

The effects of scan rate on the different oxidation-reduction (redox) peak positions of the Pd-C$_{2PVP (43.5 wt.\%)}$ catalysts were investigated. Figure 5.10 shows that at anodic potentials greater than 0.6 V, for all scan rates except 100 mVs^{-1}, it was observed that the oxidation peaks decreased due to the formation of Pd oxide and/or adsorbed oxygenated species (Pd-OH$_{ads}$ or Pd-O$_{ads}$). In the reversed scan, a large anodic current was generated after the reduction of the oxygenated species to metallic Pd at approximately +0.5 V, which agrees with previous literature [118]. The better resolution of the peaks around -0.1 and +0.24 V can be associated with the distribution of surface atoms on the (111) and (110) crystal planes, edge and corner sites of the catalysts [108].

Figure 5.11 evaluates the electrocatalytic performance of the Pd-C$_{2PVP (43.5 wt.\%)}$ catalysts CV experiments were recorded in 0.5 M H$_2$SO$_4$ solution + 0.5 M HCOOH solution at a

scan rate of: (A) 50 mVs^{-1} and (B) different scan rates (50th cycle) from a potential range -0.2 to +1.2 V. From Figure 5.11a, four oxidation peaks and two reverse scan peaks are observed. The main oxidation peak and Pd oxide peak are at about +0.18 V and +0.52 V, respectively.
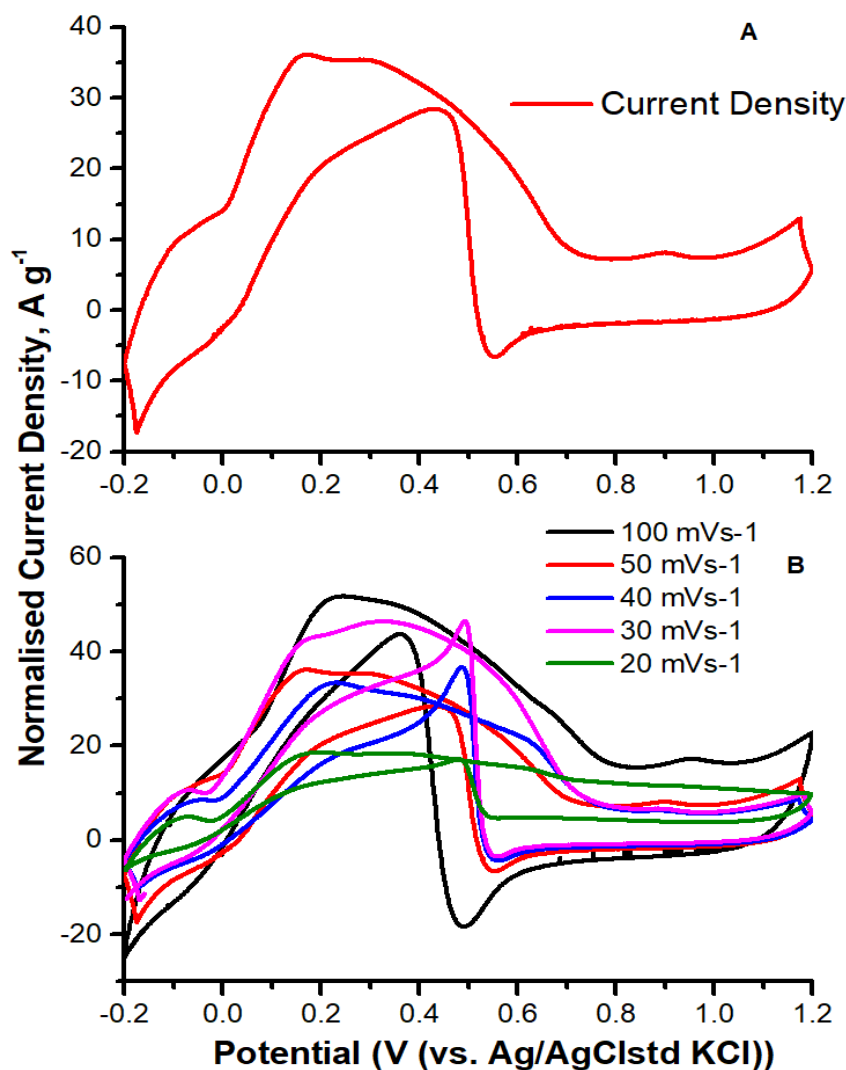
Figure 5.11: Cyclic voltammogram of Pd-C$_{2PVP(43.5\ wt.\%)}$ catalysts in 0.5 M H$_2$SO$_4$ solution + 0.5 M HCOOH solution at a scan rate of: (A) 50 mVs^{-1} and (B) different scan rates (50th cycle).

Figure 5.12 shows the long-term durability of the Pd-C catalysts, was investigated using chronoamperometric measurements at 0.1, 0.3 and 0.6 V (vs. $Ag/AgCl_{sat.KCl}$ [0.197 V vs. NHE]). The stability experiments of the PVP stabilised route shows that the Pd-$C_{2PVP(43.5\ wt.\%)}$ catalysts demonstrated superior catalytic stability in an acid medium than the Pd-$C_{2H_3BO_3\ +\ NH_4F}$ under similar conditions for all potentials (see Figure 5.12. The initial and final current densities for both catalysts are presented in Table 5.4.
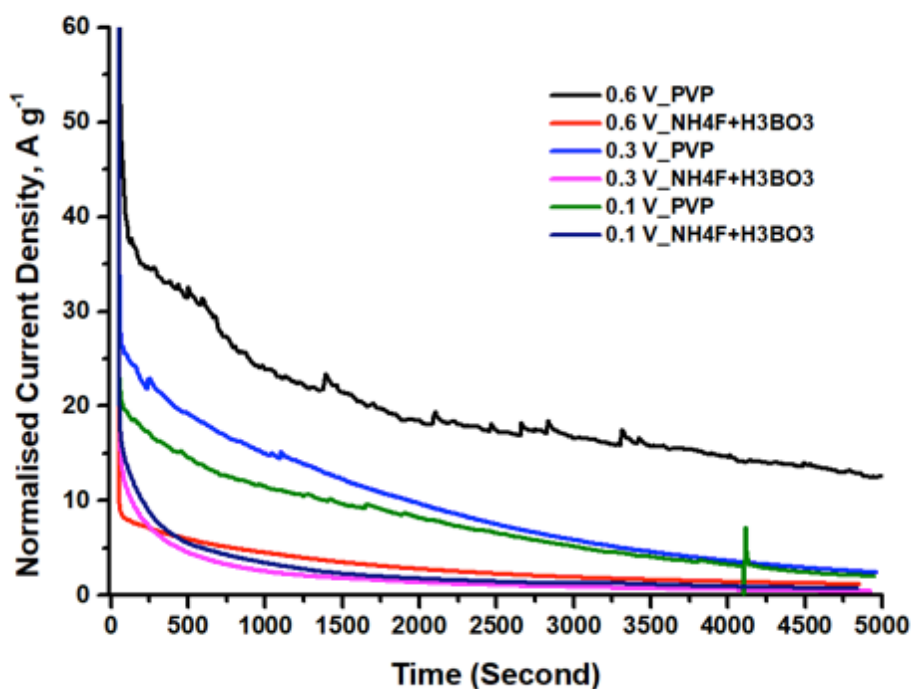
Figure 5.12: Chronoamperometric curve of the Pd-$C_{2PVP(43.5\ wt.\%)}$ vs. Pd-$C_{2H_3BO_3\ +\ NH_4F(21\ wt.\%)}$ electrodes in a 0.5 M H_2SO_4 solution + 0.5 M HCOOH solution at different potentials and room temperature.

Table 5.4: Comparison of the Pd-C$_{2PVP\,(43.5\,wt.\%)}$ and Pd-C$_{2H_3BO_3\,+\,NH_4F\,(21\,wt\%)}$ catalysts stability at 0.6 V with amount of initial and final current densities

Catalysts Run #	Initial Current Density, A/cm^{-2}	Initial Current Density, A g^{-1}	Final Current Density, A/cm^{-2}	Final Current Density, A g^{-1}
Pd-C$_{1\,H_3BO_3\,+\,NH_4F}$	0.078	21.67	0.000425	0.12
Pd-C$_{2\,H_3BO_3\,+\,NH_4F}$	0.068	18.89	0.000394	0.11
Pd-C$_{3\,H_3BO_3\,+\,NH_4F}$	0.062	17.22	0.000482	0.13
Mean	**0.069**	**19.26**	**0.0004**	**0.12**
Pd-C1$_{PVP}$	**0.275**	36.67	**0.009321**	1.24
Pd-C2$_{PVP}$	**0.147**	19.6	**0.008496 4**	1.13
Pd-C3$_{PVP}$	0.157	25.73	0.013438	1.79
Mean	**0.193**	**27.33**	**0.0104**	**1.39**

5.2 Discussion

The synthesis reaction, particle size, morphology and dispersion of Pd-C catalysts are influenced by the synthesis temperature and the PVP stabiliser. TEM images offer insights into the atomic arrangement and morphology of the Pd-C nanoparticles. Figure 5.5a and b show TEM/HRTEM images of Pd-C$_{6H3BO3\,+\,NH4F}$] (~1.9 wt.% ICP-AES) with an average crystallite size of 1.4 nm and a TEM particle size of ca. 5.1 nm. The HRTEM (Figure 5.5c) of a single Pd nanoparticle on a carbon support shows lattice fringes with approximately 1.945 Å interfringe distances, which compares well with the (200) interplanar distance of the Pd face-centred cubic structure. Yang and coworkers confirm, in their studies, that the Pd single phase exposed the (100) plane surface of the fcc structure [275] and demonstrated the highest electrocatalytic activity when compared to the other low index planes. Their findings imply that the Pd (100) planes are the best for practical formic acid fuel cell applications. In addition, the low reduction reaction temperature is generally slow and cannot provide enough energy for

the Ostwald ripening process (i.e. small crystals or particles dissolving and re-depositing onto larger crystals or particles) and anisotropic growth [284]. Another reason for the unique structure of the Pd-C$_{PVP}$ catalyst could be ascribed to the influence of the PVP, acting as both surfactant and mild reducing agent as reported by Dang *et al.* [285, 286] *(see Section 2.9.9 for more details)*. PVP stabilised the palladium particles as single particles in solution and prevents any recrystallisation that leads to large particle formation/or agglomeration. Significant zig-zag features on the exterior of the Pd-C$_{PVP}$ demonstrate the high density of atomic defects present. Also, the low-temperature reduction, as opposed to a higher temperature (>120 ^{o}C) that leads to aggregation, and in synergy with the PVP stabiliser may be the cause of the unique edges and a well dispersed particles and narrow particle size distribution of 1.4 nm Pd nanocatalysts. PVP can be capped on the surface of Pd particles creating a bond between Pd and O/or N [287] for improved dispersion and greater anchorage on carbon supports [288].

5.2.1 Crystallinity and structural analysis

In order to determine the Pd crystallite structure from the XRD analysis and to understand the effect of preferred orientation of crystal planes, texture coefficient ($TC_{(hkl)}$) analysis was used. The texture coefficient measures the relative degree of preferred orientations among crystal planes in polycrystalline materials and was calculated using Halls method for each crystal plane of the XRD powder pattern of Pd-C catalyst, using Equation (5.5) [118, 289]:

$$TC_{(hkl)} = \frac{I_{(hkl)_i}/I_{o(hkl)_i}}{\frac{1}{n}\Sigma n \frac{I_{(hkl)_n}}{I_{o(hkl)_n}}} \qquad\qquad 5.5$$

where $TC_{(hkl)}$ is the texture coefficient of the facet [hkl], $I_{(hkl)}$ is the intensity of the (hkl) reflection of the sample (Pd-C catalyst), $I_{o(hkl)}$ is the intensity of the (hkl) reflection of a polycrystalline bulk sample (Pd bulk) and 'n' is the number of reflections taken into account. When the texture coefficient is unity, this means the facet has no preferred orientation. Texture coefficient value above unity indicates that the crystal planes are preferentially grown facets. The bulk palladium fcc structure (matching JCPDS, File No. 46-1043) was used for calculating the D_p and texture coefficient of the different facets of the Pd-C catalyst (see Figure 5.13).
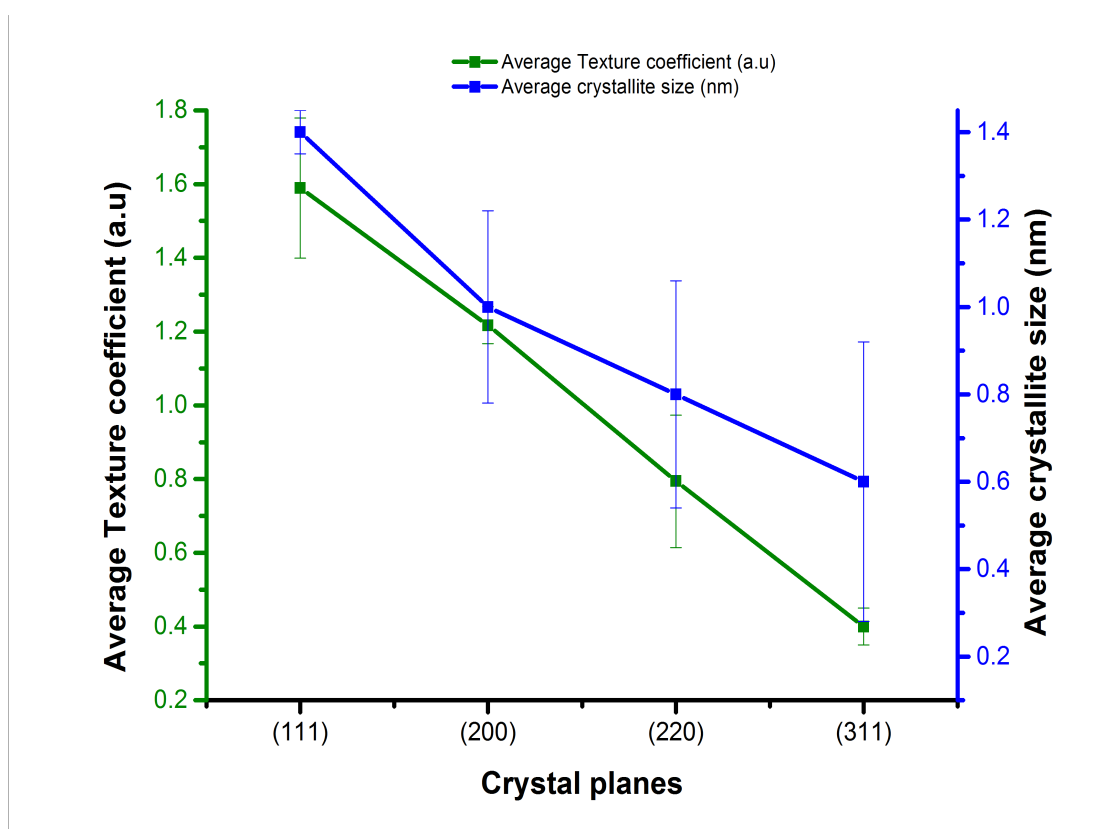
Figure 5.13: Average crystallite size (using Equation 5.1) and texture coefficient (using Equation 5.5) of Pd-C$_{PVP}$ catalysts particles from XRD powder pattern

Figure 5.13 presents the texture coefficient and average crystallite size for the PdC17 synthesis samples. The mean crystallite size for the crystal planes showed a decreasing trend from low index plane to the higher facets. According to the Bragg angle, the average crystallite size should decrease when moving from lower to higher index planes. The trend could be ascribed to the preferential orientation of the Pd (111) facet over the other index planes. The Pd (111) plane agrees with previous reports [289]. However, the deviation of the higher index planes (e.g. (311) from the (111) could be due to the effect of particle size in the x-ray scattering technique. The average crystallite sizes for Pd-C$_{PVP}$ (*single sample run*) ranged from 1.4 to 1.7 nm with the (311) plane have a large particle size of 16.5 nm. Also, the (200) and (311) crystal planes have higher average crystallite sizes than the other planes, which is consistent with previous literature [289] (*see Appendix A, Figure 1*).

The most favoured geometric parameters for Pd nanoparticles are the two most active crystal planes, Pd (100) and Pd (111). These influence the electronic and geometric characteristics of the catalyst activity for electrooxidation, notably the reaction steps (*adsorption, desorption, surface diffusion and redox reactions*) at the electrode-electrolyte interface. In summary, Figure 5.13 gives a better representation of the crystallographic characterisation for the Pd-C catalysts.

Generally, when moving from lower to higher Bragg angles, the average particle size is expected to decrease. The increase (decrease) from unity of the texture coefficient indicates a higher (lower) degree of preferential orientation of the particular Miller plane compared to the bulk Pd. The atomic structure and the crystal planes exposed are a function of the XRD scattering intensities, which in turn correspond to the changes in atomic densities within the material [290]. For comparison, the XRD analysis of all Pd

catalysts were further investigated and demonstrated the preferential formation of the highly reactive (100) and (111) crystal planes. Figure 5.14 shows the shift to lower angles on the XRD pattern of Pd-C$_{PVP}$, confirming the smaller crystallite size compared to commercial Pd-C and Pd-C$_{H_3BO_3+NH_4F}$. An XRD for a commercially available Pd-C$_{commercial}$, showed that the PVP synthesis route has smaller, well-dispersed and fully resolved polycrystalline materials compared to the Pd-C$_{commercial}$.
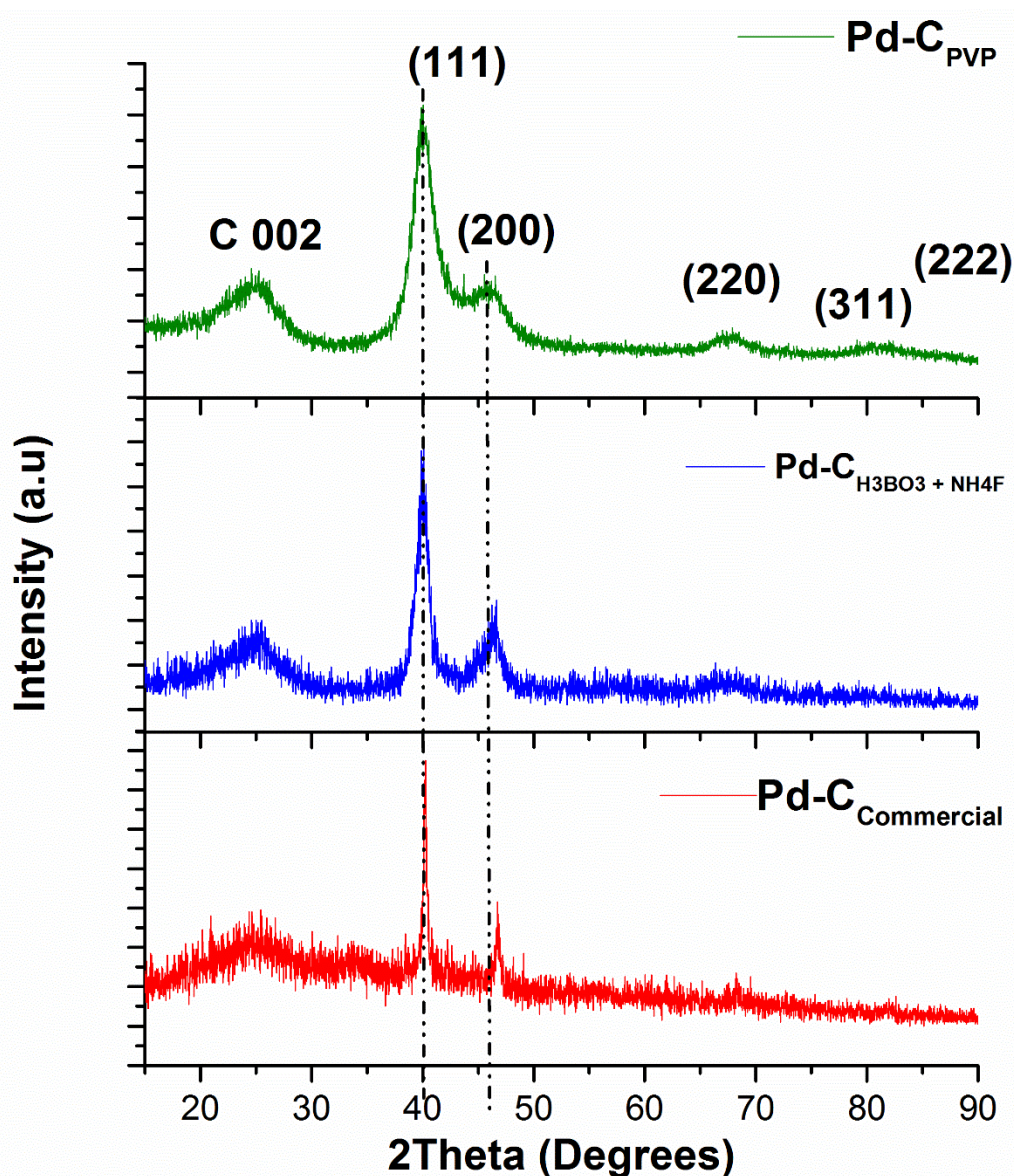
Figure 5.14: XRD patterns of Pd-C catalysts with major peaks marked (JCPDS No. 46-1043)

The XRD diffraction peak is associated with a particular reflection inside the crystal unit cell and individual peak relates to the crystallite size. The broader the peak, the smaller the crystallite size, from Figure 5.14; for example, the peaks increase in width (broader) from Pd-C$_{commercial}$ (21.9 nm) < Pd-C$_{H_3BO_3+NH_4F}$ (4.4 nm) < Pd-C$_{PVP}$ (1.4 nm), respectively.

5.2.2 Oxidation activity and nature of the surface kinetics

In order to investigate the oxidation activity and nature of the surface kinetics of the Pd-C catalyst in acid medium, cyclic voltammetry experiments at different scan rates were performed (see Figures 5.10 and 5.11b). All electrochemical investigations of the catalysts were normalised relative to the ICP-AES weight % in the electrode for efficient comparison of the catalyst activities and performance evaluation.

Figure 5.15 shows similar CV responses of the Pd-C catalysts from different synthesis routes. The CV profiles of the Pd-C$_{PVP}$ (*active metal loading 0.75 mg cm^{-2}*) and Pd-C$_{H_3BO_3 + NH_4F}$ (*active metal loading 0.36 mg cm^{-2}*) electrodes confirm the similarity in crystalline structures. The anodic peak position is in agreement with previously reported work by Hu *et al.*, confirming the crystalline structure for the Pd (111) and Pd (100) crystal planes in 0.5 M H$_2$SO$_4$ [130]. The Pd-C$_{H_3BO_3 + NH_4F (21 wt.\%)}$ evidently shows superior intensity peaks (Figure 5.15a) on all redox regions: hydrogen adsorption-desorption, metal oxidation and oxide reduction, respectively.
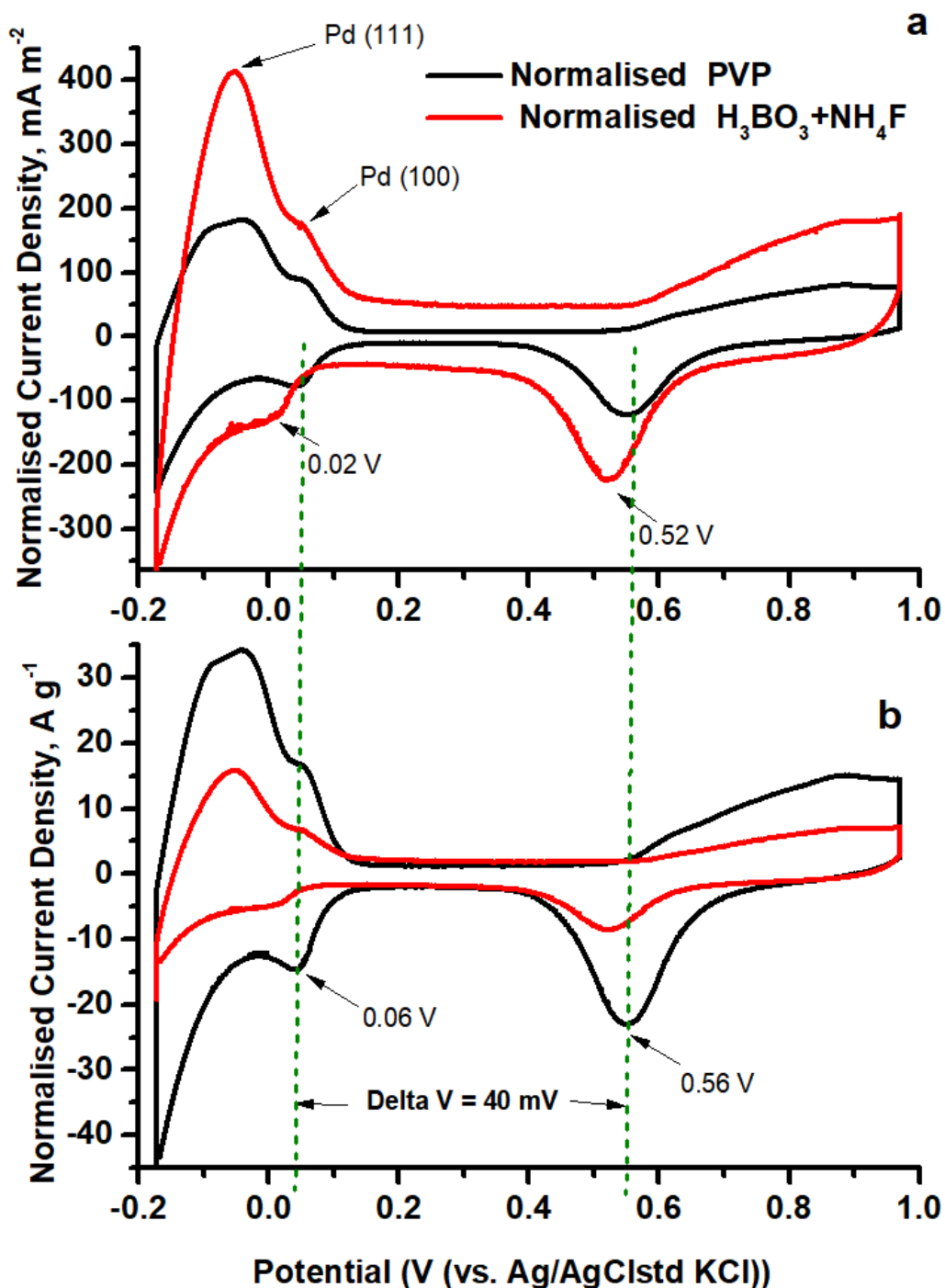
Figure 5.15: Comparison of catalyst activity with synthesis route between Pd-C$_{2PVP\ (43.5\ wt.\%)}$ vs. Pd-C$_{2H_3BO_3\ +\ NH_4F\ (21\ wt\%)}$ for 0.5 M H$_2$SO$_4$ solution at a scan rate of 20 mVs^{-1}.

This is presumably due to the specific activity, 417.0 mA m^{-2}, which is about 2.3 times higher than the Pd-C$_{PVP}$ (182.1 mA m^{-2}). Notably, the first anodic peak (H desorption) shifts negatively in Pd-C$_{H_3BO_3\ +\ NH_4F}$, suggesting weakened adsorption energy due to a lower *d*-band shift compared to Pd-C$_{PVP}$ electrodes which is confirmed by XRD

126

analysis (see Figure 5.14). However, the Pd-C$_{PVP}$ catalyst shows better overall electrochemical and physicochemical properties (ECSA, CSA, Pd %utilisation) than Pd-C$_{H_3BO_3 + NH_4F}$ on mass activity basis (Figure 5.15a). In addition, Pd-C$_{PVP}$ electrodes evidently indicate higher roughness factor R_f, implying a larger Pd surface (see Table 5.6), the existence of several crystalline facets, and a large ECSA with available active sites for increased catalytic performance.

A careful inspection of Figure 5.15, reveals the sharp PdO reduction peak of Pd-C$_{H_3BO_3 + NH_4F}$ appears precisely at the same potential (ca. 0.52 V) confirming larger mass-specific chemical active sites for the oxidation reaction [128]. The hydrogen adsorption-desorption peaks are sharp and well resolved due to the influence of the crystalline facets corresponding to the (100) and (111) planes (Figure 5.15) [130, 291]. The improved performance can be attributed to the distribution of surface atoms on the (111) and (110) crystal planes, edge and corner sites of the catalysts [108]. Also, the Pd-C$_{PVP (45 wt.\%)}$ consistently shows improved catalytic enhancement, which is a factor of 2.2-fold higher with an average mass activity of 34.2 mA mg^{-1}Pd (I_f/I_b = 5.5) compared to Pd-C$_{H_3BO_3 + NH_4F}$ electrodes (15.8 mA mg^{-1}Pd and I_f/I_b = 4.5). This result indicates the large negative onset potential shift, indicating that both Pd-C$_{PVP}$ and Pd-C$_{H_3BO_3 + NH_4F}$ electrodes proceeds mainly by a dehydrogenation (direct) oxidation pathway and defeating the CO poisoning (indirect) at a higher potential [128]. The small shoulder peaks at about 0.5 V on the forward oxidation scan can be attributed to the oxidation of absorbed (e.g. CO-like) species [282]. It appears that Pd-C$_{PVP}$ catalysts under the same electrochemical conditions exhibit better catalytic activity for formic acid electrooxidation compared to Pd-C$_{H_3BO_3 + NH_4F}$ electrodes because of the quick removal of poisoning species from the catalyst surface. The increase in

oxidation results from an increase in the active surface area (ECSA) of the catalysts and enhanced crystallographic properties, especially the highly reactivity Pd (100) planes [291].

Table 5.5: Summary of the crystallographic parameters of Pd-C catalysts

Parameters	Pd-C$_{PVP}$ (43.5 wt.%)	Pd-C$_{H3BO3+NH4F}$ (21 wt.%)	Pd Card 46-1043
Avg. Surface area (m^2 g^{-1}$_{active\ metal}$)	357.1	113.6	
Crystallite size (nm) 200 plane	1.4	4.4	
Relative crystallinity (111 plane)	2.57	2.30	
Intensity ratio (111) to (200)	2.732	2.468	
Intensity ratio (111) to (200) PDF Card	1.671	1.671	
Lattice parameter, a (Å) (200 plane)	3.962	3.889	3.89
d-spacing (Å) (200 plane)	1.981	1.945	1.945
Peak position, 2θ (Degree) (200 plane)	45.76	46.67	46.659
Atomic radius (Å) (200 plane)	1.401	1.375	1.375

The average crystallite size, lattice parameter, *d*-spacing and atomic radius were calculated from the XRD peaks and presented in Table 5.5. In Table 5.5, the lattice constants show an enhanced value from 0.389 nm for bulk Pd [46-1043] to 0.3962 nm and 0.3889 nm for Pd-C$_{PVP}$ and Pd-C$_{H3BO3+NH4F}$ catalysts, respectively. The increased lattice constants indicate the expansion of the Pd unit cell due to the enhanced atomic radii of the synthesised Pd catalysts and the influence of the stabilising agents on the synthesis route. The difference in crystal properties of the Pd-C catalysts compared to

those of the bulk could be ascribed to the effect of the small nanoparticle size altering the d-band energetics and interatomic lattice properties of the nanostructures.

The electrocatalytic performance of Pd-C catalysts towards formic acid oxidation is presented in Figure 5.16. The electrochemical oxidation of formic acid electrooxidation was investigated with the Pd-C$_{PVP}$ and Pd-C$_{H_3BO_3 + NH_4F}$ electrodes for 0.5 M H$_2$SO$_4$ solution + 0.5 M HCOOH solution at a scan rate of 50 mVs^{-1} (Figure 5.16). In this study, all CV results shown are for the 50th cycle in 0.5 M H$_2$SO$_4$ solution + 0.5 M HCOOH solution to confirm the removal of any surface oxides, leaving pure Pd nanocatalysts.

The particle size of the catalyst's nanoparticle is the most significant factors that dominates the electrochemical activities of formic acid oxidation. It affects both the mass activity and the specific activity of the oxidation processes. From Figure 5.16, the average specific current for Pd-C$_{2PVP (43.5 wt.\%)}$ and Pd-C$_{2H3BO3 + NH4F (21 wt\%)}$ nanocatalysts was 53.9 (at 0.3 V vs. Ag/AgCl) and 97.1 (at 0.2 V vs. Ag/AgCl) mA mg^{-1}, respectively. With decreasing particle size, the mass activity increases and the specific activity should decrease, if the surface defects in the nanoparticle structure were significant enough. However, the durability of the catalyst will decrease significantly due to the Gibbs-Thomson effect [292] (*the influence of nanoscale curvature causing a reduction of the electrochemical potential of the nanoparticle compared to bulk material*). It is clear that high activity and catalyst durability cannot be simultaneously achieved in heterogeneous electrochemical reactions due to the different interplay of several factors (*see sections 2.9.4, 2.9.7 and 2.9.8 for details*).
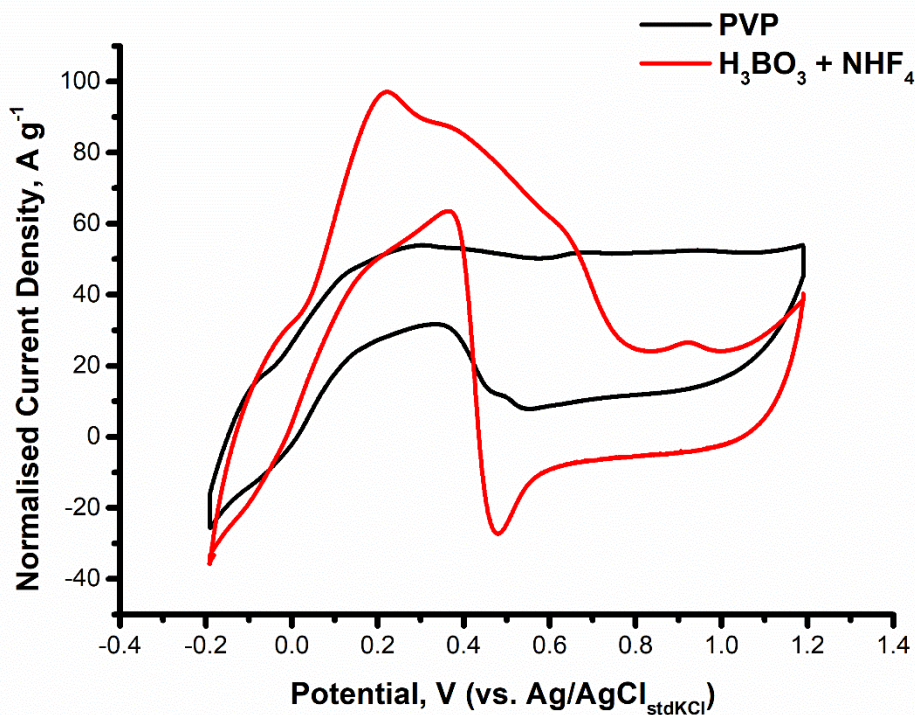
Figure 5.16: Comparison of catalyst activity on synthesis route Pd-C$_{2PVP\ (43.5\ wt.\%)}$ vs. Pd-C$_{2H_3BO_3\ +\ NH_4F\ (21\ wt\%)}$ for 0.5 M H$_2$SO$_4$ solution + 0.5 M HCOOH solution at a scan rate of 50 mVs^{-1} (50th cycle)

The Pd-C$_{PVP}$ electrodes show better activity (DFAFCs region less than 0.3 V [282]) with a very low onset potential of -0.037 V compared to Pd-C$_{H_3BO_3\ +\ NH_4F}$ electrodes at 0.017 V. However, the oxidation activity of the Pd-C$_{H_3BO_3\ +\ NH_4F}$ electrodes showed superior mass and specific activities compared with the Pd-C$_{PVP}$ electrodes. This could account for the differences in the electrooxidation of formic acid for both catalysts, where Pd-C$_{2H_3BO_3\ +\ NH_4F\ (21\ wt.\%)}$ shows improved mass activity with a factor of 1.8 compared to the Pd-C$_{2PVP\ (43.5\ wt.\%)}$ catalyst (*see section 4.5.3 for more details when using ICP data*). Pd-C$_{2H_3BO_3\ +\ NH_4F\ (21\ wt.\%)}$ consistently shows an enhanced activity for formic acid electrooxidation reaction than Pd-C$_{2PVP\ (43.5\ wt.\%)}$ at the same reaction conditions. Pd-C$_{2H_3BO_3\ +\ NH_4F\ (21\ wt.\%)}$ catalysts also display a lower activity compared to a recently published similar work by Zhang *et al.* where they used reduced graphene oxide, and Vulcan XC72 supports. In their report, a Pd/PW$_{12}$/RGO (955 mA mg^{-1} and

130

particle size = 7.5 nm) catalyst demonstrated enhanced activity by a factor 1.2 and 2.3 in comparison to Pd/C[20 wt.%] (786 mA mg^{-1}) and Pd/RGO (419 mA mg^{-1} and particle size = 12.9 nm), respectively [282]. They attributed the improved activities to the larger specific surface area, superior electrical conductivity and excellent chemical stability of the graphene support.

Table 5.6: Catalytic performance of the Pd-C2PVP (43.5 wt.%) vs. Pd-C2H3BO3 + NH4F (21 wt%) nanocatalysts

Parameters	Pd-C$_{PVP}$ catalysts	Pd-C$_{H3BO3 + NH4F}$ catalysts
[a]ECSA, m^2.g$_{-1}$ Pd	188.4	38.3
CSA, m^2.g$_{-1}$ Pd	357.1	113.6
[b]Pd surface site, Pd sites. g$_{cat.}$ (x10^{20})	23.9	4.87
[c]Pd utilisation, %	52.7	33.7
[d]Mass activity (H$_2$SO$_4$), A g^{-1}	34.2	15.8
[e]Specific activity (H$_2$SO$_4$), mA m^{-2}	182.1	412.7
[f]Roughness factor, R$_f$ (x10^6)	25.1	5.48
Onset potential, V	-0.037	0.017
E$_p$, V	0.31	0.22
Avg. Current density, mA cm^{-2}	40.5	37.8
Avg. Specific activity (HCOOH), mA m^{-2} $_{Pd}$	0.29	2.54
Avg. Mass activity (HCOOH) mA mg^{-1} $_{Pd}$	53.9	97.1
I$_f$/I$_b$	5.5	4.5

[a] Estimated using Equation 5.3 from CV at scan rate of 20 mVs^{-1}, [b] Calculated by: [ECSA/CSSA], [c], Calculated by: [ECSA/CSA]*100, [d] Calculated by: Current density sum of adsorption peaks divided by W$_{Pd}$, [e] Calculated by: Mass activity divided by ECSA, [f] Calculated by: ECSA/geometric surface area of electrode. Assuming cross sectional surface area (CSSA) of surface Pd atom taken as 0.0787 nm^{-2}. Roughness factor = ECSA/geometric surface area, CSA from Equation 5.2; I$_f$, forward peak current density, I$_b$, backward peak current density.

The deactivation of Pd catalysts (e.g. poisoning from non-CO organic species) during FAO is not well understood and still requires more studies to elucidate the surface reaction at the nanoscale level [128]. Some other factors that could play a role in the overall activity of FAO include the anions from the supporting electrolyte (e.g. SO_4^{2-}), crystallographic parameters and the structure/morphology of the catalyst. Cheng and Gyenge ascribed the enhanced performance of the catalyst to a combination of factors, which include improved fuel mass transfer, more efficient removal of CO_2 gas from the anode catalyst, and better utilisation of the catalyst [40].

5.2.3 Stability of the catalysts for formic acid electrooxidation reactions

Chronoamperometric tests were used to investigate the stability of the catalysts for formic acid electrooxidation reactions. Figure 5.12 exhibits current density vs. time obtained at 0.6, 0.3 and 0.1 V vs. $Ag/AgCl_{sat.KCl}$ for $Pd-C_{PVP}$ vs. $Pd-C_{H_3BO_3 + NH_4F}$ electrodes in a 0.5 M H_2SO_4 solution + 0.5 M formic acid solution at room temperature. The chronoamperometric curves show an early stage rapid oxidation current drop. This is due to: (a) the interfacial catalyst-electrolyte electric\double layer charging process upon stepping the potential to a new value and (b) accumulation of adsorbed species (CO, hydrocarbons and oxygenates) on the electrode surface, decreasing the available active sites [111]. The oxidation current for the $Pd-C_{PVP}$ demonstrated superior catalytic activities for formic acid oxidation, with an initial current density of 193.2 mA cm^{-2} to 69.5 mA cm^{-2} and a final or residual current density after 5000 seconds at 10.4 mA cm^{-2} to 0.43 mA cm^{-2}. This is ascribed to the polyvinylpyrrolidone stabiliser being a polar soluble polymer, aiding the anchorage of nanoparticles and ease of removal, with no contamination or blocking of the active Pd-C site, compared to boric acid-ammonium fluoride route for electrooxidation processes [275]. This further confirms that the Pd-

C_{PVP} synthesis route is more electrochemically stable for formic acid electrooxidation than with Pd-C$_{H_3BO_3 + NH_4F}$ electrodes as observed in CV experiments. Figure 5.12 reveals that the electrochemical stability of Pd-C$_{2PVP (43.5 \, wt.\%)}$ for formic acid oxidation is superior to that of Pd-C$_{2H_3BO_3 + NH_4F (21 \, wt\%)}$. At the end of the chronoamperometry experiment, Pd-C$_{2PVP (43.5 \, wt.\%)}$ displays an enhanced activity of 11.6 times the current decay of the Pd-C$_{2H_3BO_3 + NH_4F (21 \, wt\%)}$ catalyst.

Further optimisation of the Pd-C catalysts could be achieved by investigating the effect of the formic acid solution on catalyst corrosion (deactivation, degradation) during electrooxidation processes. Mechanistic studies at the electrode interface could help determine the influence of reactive formate intermediates in FAO, such as CO and other intermediate species that slow/or poison the Pd active sites. XPS could be used to investigate the effect of the d-band shift of Pd metal (i.e. s-orbital contraction, d-orbital expansion), leading to weakening of the intermediate chemisorption effect, while improving the Pd resistance to surface oxide formation. Another approach to enhance the oxidation reaction is to use a rotating disc electrode to reduce/eliminate the challenges of the mass transport limitation at the electrode-electrolyte interface. For more strategies to improve the overall activity, see section 4.5.3.

5.2.4   Mechanism at the electrode-electrolyte interface

The mechanism can be evaluated using the relationship between the peak current and the scan rate. The oxidation current and potential of formic acid electrooxidation increased with scan rate (see Figure 5.11 for CV profile). The scan rate studies were

carried out to assess the electrochemical processes at the electrode-electrolyte interface (i.e. diffusion or adsorption controlled). The peak current density increased linearly with the square root of the scan rate (2-100 mVs^{-1}), indicating the system is diffusion controlled rather than by electron transfer kinetics [283]. The equation can be expressed as (see Figure 5.17).

$$I_{pa} \ (mA) = 6.3884 \vartheta^{\frac{1}{2}} \left(V^{\frac{1}{2}} s^{\frac{1}{2}} \right) - 14.7, (r = 0.9995) \qquad\qquad 5.6$$

where I_{pa} is the peak current density in mA, ϑ is the scan rate in $V^{\frac{1}{2}} s^{\frac{1}{2}}$.
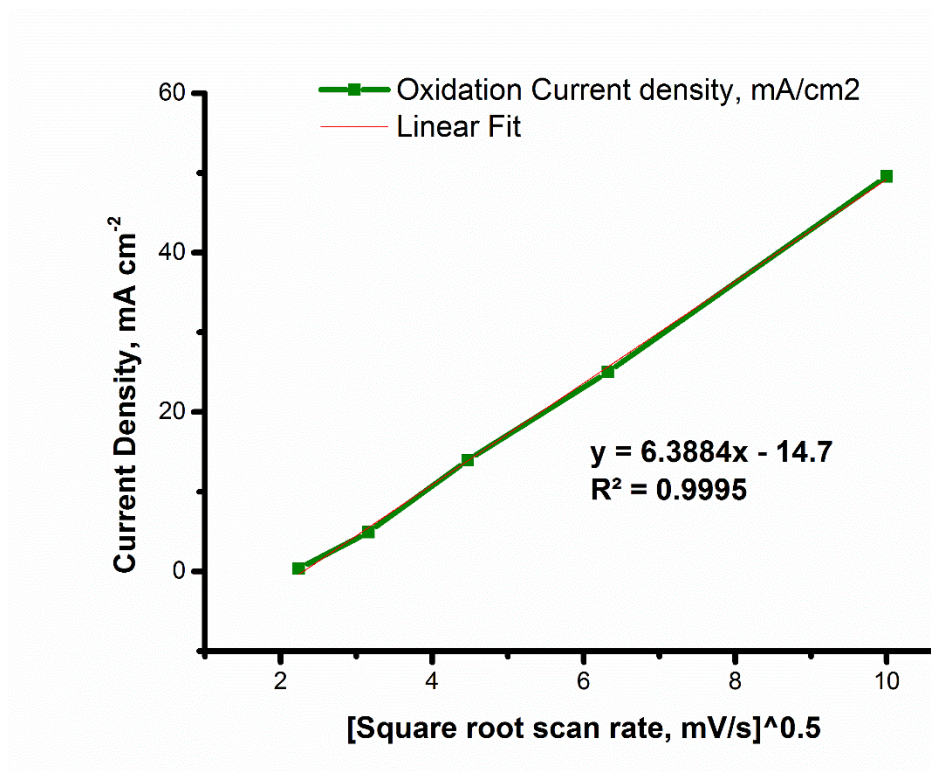
Figure 5.17: Dependence of oxidation peak current on the square root of scan rate of Pd-C$_{2PVP \ (43.5 \ wt.\%)}$ catalyst in 0.5 M H$_2$SO$_4$ solution at different scan rate on potential shift (10th cycle) .

To establish the surface kinetics, Figure 5.18 shows the linear relationship between potential peaks versus the logarithm of the scan rate, with increasing positive potential shift with the increase in scan rate, confirming that the oxidation of formic acid at the Pd-C electrode surface is an irreversible process [81].
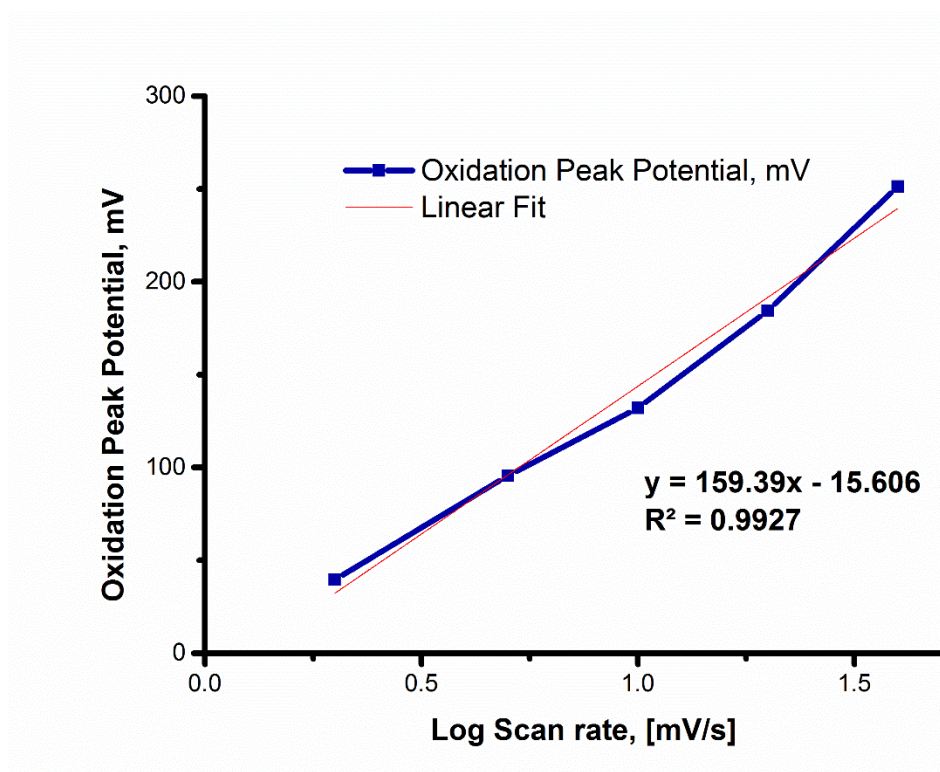
Figure 5.18: Dependence of oxidation peak potential on the logarithm of scan rate of Pd-C$_{2PVP\ (43.5\ wt.\%)}$ catalyst in 0.5 M H$_2$SO$_4$ solution at different scan rate on potential shift (10th cycle) used to estimate the effect of diffusion controlled process at the electrode surface.

The diffusion from the bulk solution to the electrode surface is represented as:

$$I_{pa}\ (mA) = 159.39 \log \vartheta\ (Vs^{-1}) - 15.606, (r = 0.9927) \qquad 5.7$$

Figure 5.19 shows a linear plot of the logarithm of anodic peak current versus the logarithm of the scan rate with a slope of 0.98, which is higher than the theoretical value of 0.5 for a purely diffusion controlled process [293]. The equation can be expressed as:

$$I_{pa}\ (mA) = 0.9795 \log \vartheta\ (Vs^{-1}) - 0.2165, (r = 0.9854) \qquad\qquad 5.8$$
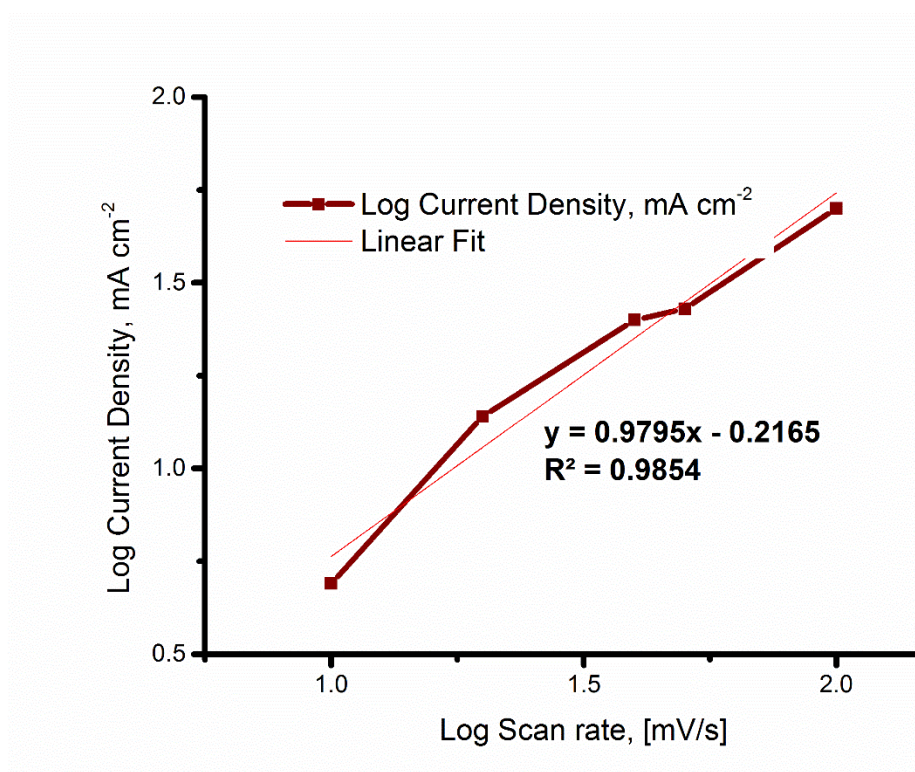
Figure 5.19: Linear relation between the logarithm of the peak current and the logarithm of scan rate of Pd-C$_{2PVP\ (43.5\ wt.\%)}$ catalyst in 0.5 M H$_2$SO$_4$ solution at different scan rate on potential shift (10th cycle) .

These findings indicate that the second anodic peak in the electrooxidation process is controlled by a surface-controlled reaction (rate-determining step (RDS)), while oxidation at higher potentials is a mass transport-limited (irreversible) process.

5.3 Conclusion

A low mass loading of palladium catalyst on a carbon support, with high performance and stability in the acid medium, was prepared by a one-pot sodium borohydride-polyvinylpyrrolidone synthesis. The addition of a high concentration of hydroxyl ions suppressed hydrogen evolution and generated a unique morphology-tunable Pd-C$_{PVP}$

catalyst. The electrooxidation of the Pd-C$_{PVP}$ catalyst in sulphuric acid shows a higher activity (53% utilisation) for formic acid oxidation than in Pd-C$_{H3BO3 + NH4F}$ the catalyst (34% utilisation). The improved catalytic performance is attributed to the effect of the stabiliser and the specific Pd structure promoting oxidation of adsorbed intermediate species. The adsorption-desorption peak currents are higher in Pd-C$_{PVP}$ than in Pd-C$_{H3BO3 + NH4F}$ electrodes, suggesting that the electrochemical surface area (ECSA = 371.5 m^2 g^{-1}) of Pd-C$_{PVP}$ is larger than Pd-C$_{H3BO3 + NH4F}$ as confirmed by XRD analysis. However, the oxidation activity of the Pd-C$_{H3BO3 + NH4F}$ electrodes showed superior mass and specific activities than the Pd-C$_{PVP}$ electrodes. This could account for the differences in the electrooxidation of formic acid for both catalysts, where Pd-C$_{2H3BO3 + NH4F (21 wt.\%)}$ shows improved mass activity with a factor of 1.8 compared to the Pd-C$_{2PVP (43.5 wt.\%)}$ catalyst. The catalyst structural properties were determined by XRD, TEM, SEM and AFM. CV is used to characterise electrochemically the Pd-C$_{PVP}$ working electrodes to elucidate the kinetic parameters in the formic acid electrolyte. Results suggest that the controlled morphologies/nanostructures of Pd-C as a robust anodic catalyst will play a significant role in catalyst cost and utilisation for practical direct formic acid fuel cells (DFAFCs) technology.

However, the oxidation of formic acid at Pd anode is limited by the instability of Pd and the effect of slow deactivation processes on the electrode. Hence there is need to develop new, active, robust, inexpensive and efficient catalysts to overcome these challenges.

Chapter 6 Performance of the direct formic acid fuel cell with electrochemically modified Au nanoparticles on carbon black anode catalyst

In the previous chapter, Pd catalyst synthesis showed that the PVP stabilised route to be promising. Gold nanoparticle catalysis will be investigated in this chapter for performance evaluation of the stability properties of DFAFC and the effect of the specific catalyst loading on the electrooxidation activity. Bulk gold is the most stable of all metals, and was hence considered to be an inert catalyst, however, at the nanoscale, it has been recognised as an active and highly selective catalyst. The focus here is the use of gold to develop efficient, cost-effective solutions for energy storage/conversion applications. The choice of gold is based on its unique nobility property (for more details see section 2.9.3): Au is the only metal with an endothermic chemisorption energy in an oxygen atmosphere [294]. However, Au nanoparticles (below 5 nm) show catalytic activity, even temperature at 0 ^{o}C. There has not yet been a systematic study to understand precisely the activity of Au catalyst in FAO.

6.1 Results

6.1.1 Transmission Electron Microscopy Analysis

Figure 6.1a shows that the morphology and size of the reduced Au-C$_{PVP(87.6 \text{ wt.\%})}$ nanoparticles are well dispersed and anchored on the surface of the carbon black support.
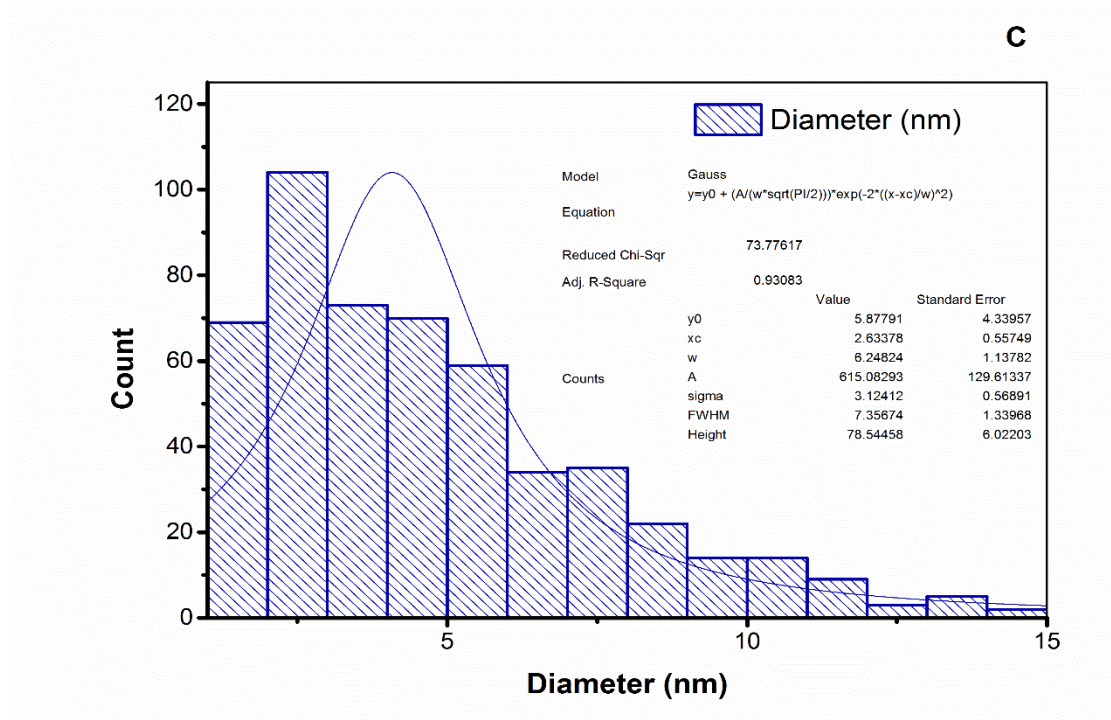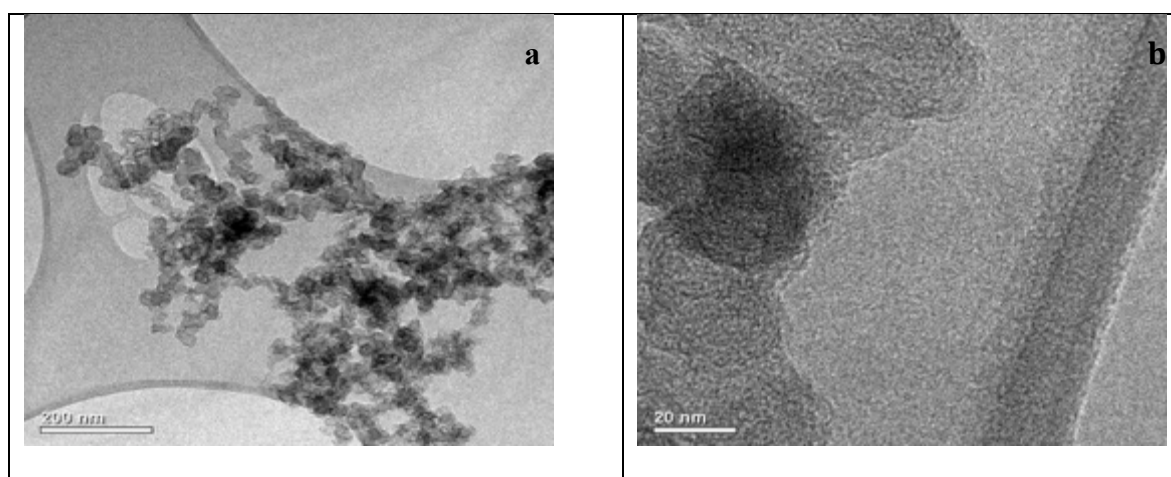
Figure 6.1: Representative TEM images of Au-C$_{PVP(87.6\ wt.\%)}$ catalysts – (a) particle distribution, (b) selected single Au crystallite, (c) Histogram profile

Figure 6.1b shows spherical shaped Au particles with defective corners and edges. The size distribution histogram gives particles sizes in the region of 1-15 nm, with a majority of the particles in the 1-6 nm range (see Figure 6.1c). The mean Au particle size was evaluated as a surface-area weighted diameter from a collection of over 250 particles on the TEM image from an arbitrarily chosen area. The number of active sites available for the electrooxidation reaction could significantly enhance the dispersivity

139

and small size of the Au nanoparticles (see Table 6.1). All samples were analysed using ImageJ 1.48 V to estimate the particle size distribution and fitted with the Gaussian product function.

6.1.2 Crystallographic Analysis

The crystal structures of gold nanoparticles were further characterised by XRD analysis. Figure 6.2 shows that the pattern of AuNPs-C$_{commercial(20\ wt.\%)}$ exhibited diffraction peaks of (111 and (200) at 2Theta values of 37.88 and 43.59, respectively. The diffraction planes were attributed to the (220), (311) and (222) crystal planes, consistent with the fcc gold, were not visibly diffracted, probably due to the Au particles not having corners for proper anchoring on the carbon black. The (200) plane at 44.56^o is the most intense, suggesting that it is the most exposed area of the corresponding facets [295]. The broad diffraction peak located at approximately 24.6^o is associated with the hexagonal structure of the Vulcan XC72 carbon support (C 002), matching graphite carbon with JCPDS, File No. 56-0159.
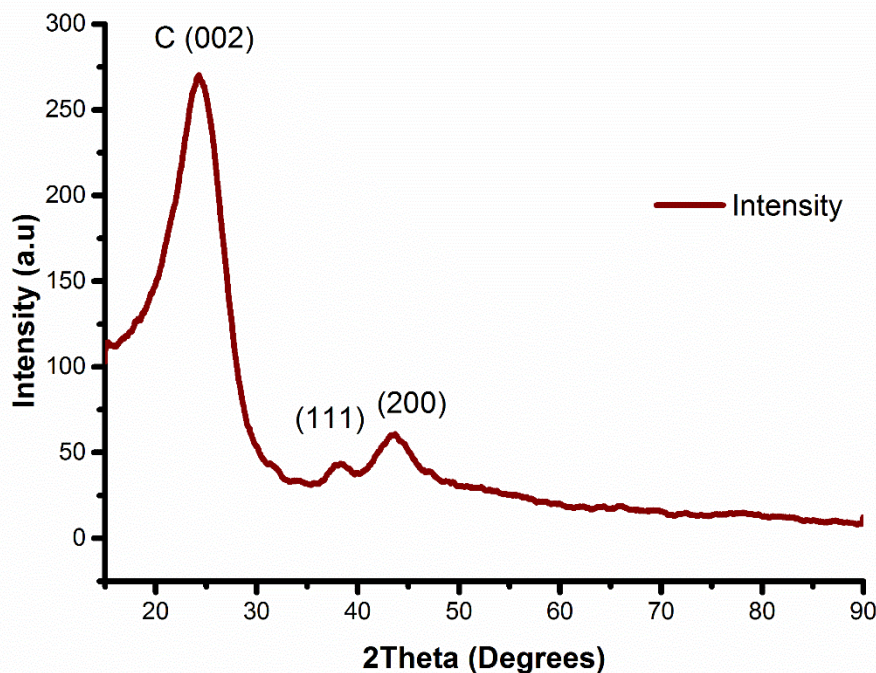
Figure 6.2: XRD patterns of AuNPs-Ccommercial$_{(20\,wt.\%)}$ catalysts with major peaks marked (JCPDS No. 4-0784)

The average crystallite size of the Au particles, were calculated from Debye-Scherrer's Equation 5.3 from the (111) peak, was 4.4 nm, considering only (111) and (200) plane for particle size calculations. The relative crystallinity of peaks (111) versus (200) was 0.27 suggesting that the spherical AuNPs are not well-ordered crystalline particles. The intensity ratio of peaks (111) versus (200) is lower than the standard value estimated from the JCPDS data (1.92 to 1.34), which indicates that the (200) planes dominate in the AuNPs-C$_{commercial}$ catalyst [296]. Furthermore, the total surface area was estimated from Equation 5.4, using an average crystallite size, *d* of 4.4 nm calculated from XRD experimental data, (which is approximately equal to the Au nanoparticle diameter of 5 nm (*manufacturer's value*)) and ρ is the density of gold ($\rho_{Au} = 19.3$ g cm^{-3}). The surface area, S$_{XRD}$ calculated from the XRD data for AuNPs-C$_{commercial}$ catalysts was 63.4 m^2 g^{-1} [297].

6.1.3 Electrochemical Measurement: Cyclic voltammetry (CV)

All CV experiments, to evaluate the electrocatalytic activity of AuNPs-C$_{commercial(20\ wt.\%)}$ catalysts, were in acid media at room temperature. To estimate the electrochemical active surface area (ECSA) of the commercial Au nanoparticles, hydrogen adsorption-desorption (HAD) analysis was performed. The ECSA accounts for the available active sites on the catalyst, which determines the conductive surface available for electron transfer to and fro the electrode surface. At a scan rate of 20 mVs^{-1}, argon or nitrogen saturated sulphuric acid solution was used to investigate HAD peaks, which represent active sites on the AuNPs-C$_{commercial}$ catalysts.
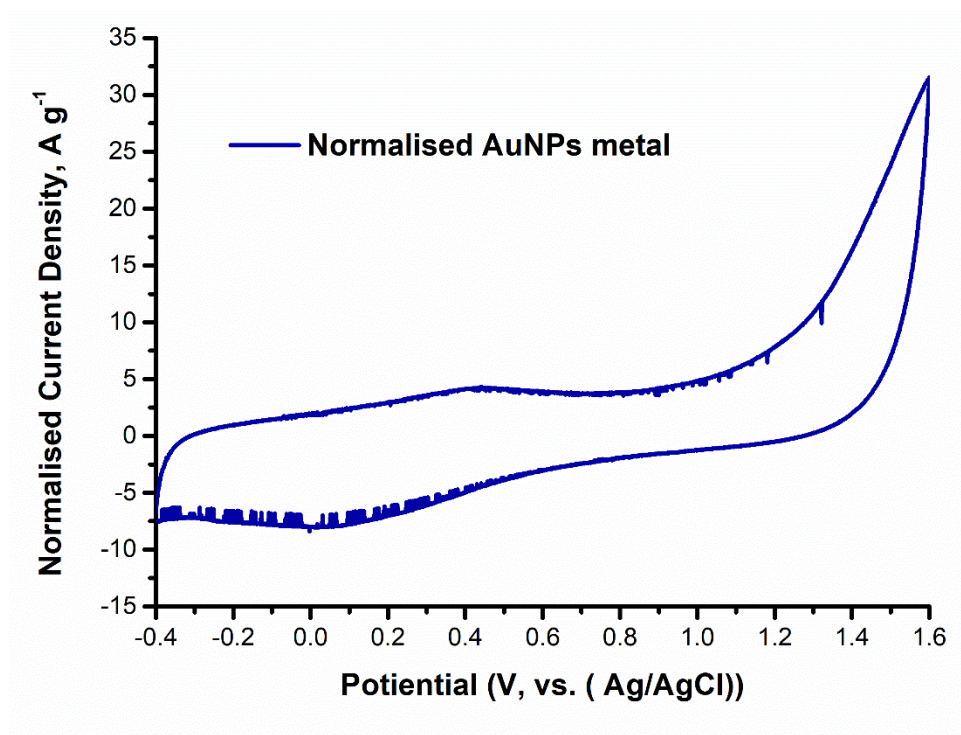
Figure 6.3: Cyclic voltammetry of AuNPs-C$_{commercial(20\ wt.\%)}$ catalyst in 0.5 M H$_2$SO$_4$ solution at a scan rate of 20 mVs^{-1} (10th cycle)

Figure 6.3 shows the hydrogen adsorption/desorption peak on AuNPs-$C_{commercial(20 wt.\%)}$. There is one broad anodic peak at 0.44 V and one cathodic peak at 0.03 V. The results indicate the absence of or very low concentration of AuNPs particles available for electrooxidation activities. The adsorption peak for Au-$C_{PVP(87.6 wt.\%)}$ catalyst had a potential of 0.57 V and a current density of 0.49 mA cm^{-2} indicating the rapid first step of dissociative adsorption of formic acid [266]. The Au oxidation and Au oxide formation peak potentials occurred at 1.47 V (5.63 mA cm^{-2}) and 1.14 V (0.44 mA cm^{-2}), respectively. However, the broad peak is generally associated with the carbon profile rather than the characteristic Au profile in acid medium. The XRD profile (see Figure 6.2) shows very high intensity for carbon compared with the Au nanoparticles.

Table 6.1: Physicochemical properties of AuNPs-Ccommercial$_{(20 wt.\%)}$ and Au-C$_{PVP(87.6 wt.\%)}$ catalysts

Performance Parameters	AuNPs-C	Au-$C_{PVP(87.6 wt.\%)}$
Q, red [mC cm^{-2}]	17.61	83.7
Catalyst wt. loading [g cm^{-2}]* ($\times 10^{-4}$)	3.52	17.2
ECSA [m^2 g^{-1}]	12.5	12.2
CSA [m^2 g^{-1}]^a	62.1	50.1
Catalyst surface site [catalyst sites g^{-1}cat]* ($\times 10^9$)	13.7	13.3
Catalyst utilization (%)^b	20.1	20.8
Current density [HCOOH], mA cm^{-2}	3.21 at 0.56V	0.147at 1.32V
Specific activity, mA m^{-2}	0.73	0.03
Mass activity, mA g^{-1}	9.1	0.42
Roughness factor, R_f* ($\times 10^6$)	1.79	1.74
Initial current density, mA cm^{-2} at 0.6 V	3.8	2.9
Final current density, mA cm^{-2} at 0.6 V* ($\times 10^{-3}$)	3.3	16

a: Calculated by: [ECSA/CSA]*100; b: Calculated by [ECSA/CSSA]

Figure 6.3 exhibited the three characteristic signatures for 0.5 M H_2SO_4 versus Ag/AgCl$_{sat. KCl}$ (0.197 V vs. NHE) reference electrode in acid media. The corresponding response is: (i) the double-layer charging region (ii) the oxide formation region and (iii) the oxide growth or extension region, respectively [298]. This follows the most established mechanism of gold oxidation proposed by Burke and Lee [299] and Conway and group [300-302]. The presence of two anodic peaks is attributed to the sorption mechanism of OH- ions onto different crystallographic facets, which is in agreement with the previous literature [303, 304]. In their work, they showed that the anodic peaks that appeared at about 1.13 V and 1.33 V were associated with Au oxidation, which they ascribed to the influence of different crystal structure of the catalyst. On the AuNPs-C CV profile, no identifiable peaks were found compared to Au-C$_{PVP}$ with anodic peaks at 1.36 V and 1.46 V (anodic E_a), respectively. On the reverse scan, the Au oxide reduction peak is at 0.84 V (cathodic E_p) of oxides formed. Table 6.1 summarises the physicochemical properties of the AuNPs-C$_{commercial(20 wt.\%)}$ and the Au-C$_{PVP(87.6 wt.\%)}$ catalysts. For the AuNPs-C$_{commercial}$ catalyst, the Au metal loading was 3.52 mg cm^{-2}, the columbic charge for 0.5 M H_2SO_4 at a scan rate of 20 mVs^{-1} was 17.61 mC cm^{-2}, giving an estimated electrochemical surface area of 12.5 m^2 g^{-1}. The roughness factors (ratio of the real to the geometric surface area) of the electrodes were evaluated by integration of the oxide reduction peaks. Here, the assumption that the electrode is covered by one monolayer of adsorbed oxygen, with a charge transfer of 400 µC cm^{-2}, was used throughout the experimental analysis [266, 305-307]. The cross-sectional surface area (CSSA) of the Au atom is taken as 0.0913 nm^{-2} to calculate the chemical surface area (CSA) of each catalyst using Equation 5.2 [308], where ρ is the density of the Au (19.32 g cm^{-3}).
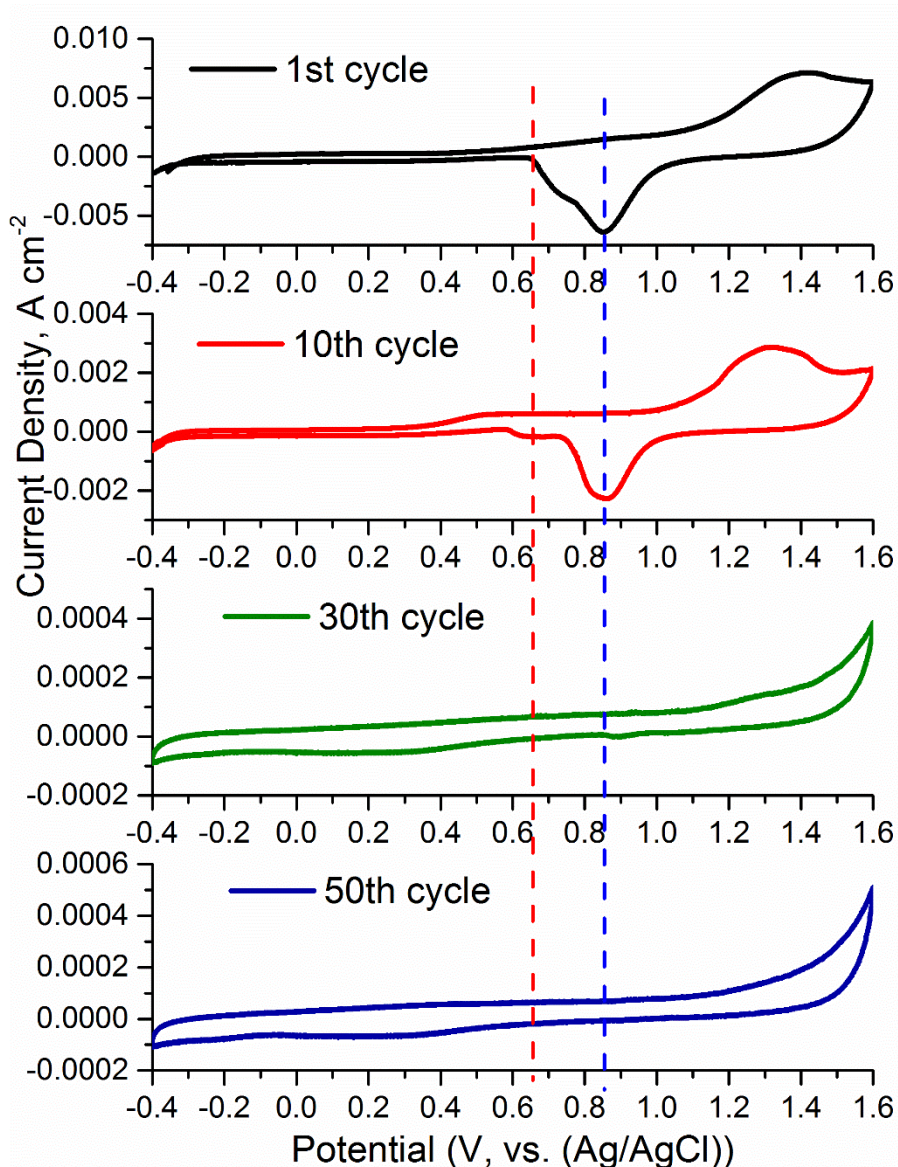
Figure 6.4: Au-$C_{PVP(87.6\ wt.\%)}$ catalyst electrooxidation with increase in 0.5 M H_2SO_4 solution + 0.5 M HCOOH solution at a scan rate of 50 mVs^{-1} (nth cycle).

Figure 6.4 shows that the peak position and potential value of the anodic mass-specific current density decreases with time at higher potential, while the backwards scan moved to lower potentials (more negative). The profile of the 10th cycle shows two anodic peaks at 1.32 V (with 2.87 mA cm^{-2}) and a shadow peak at 0.53V (with 0.59 mA cm^{-2}) and two cathodic peaks in the reverse scan: the oxide reduction peak appears at 0.86 V with 2.26 mA cm^{-2}, with a shadow peak at 0.68 V. After the 30th cycle, the anodic scan

only has one shadow peak at 1.31 V with a current density of 0.15 mA cm^{-2}. The oxide reduction peak is at 0.89 V, with a broad second peak at 0.16 V and a current density of 0.055 mA cm^{-2}. At the 50th cycle, the shift peak position negatively to a lower potential for the second (shadow) peak (-0.22 V) while the oxide reduction peak remained at 0.162 V with a current density of 0.067 mA cm^{-2}. The anodic and cathodic peak positions continue to shift and the current density decreases with the increasing cycle number. Although presently the Au reaction mechanism in acid medium is not clear, it is widely reported that there is a possible deactivation of the catalyst due to poisoning of active sites/or rapid deactivation processes. Gold catalysts are considered to be poor in acid medium when compared to alkaline conditions with slightly higher oxidation activity [309].

6.2   **Discussion**

Figure 6.5 shows a well defined tetragonal fcc crystalline structure with ICCD card JCPDS 4-0784 for both Au-C$_{PVP}$ and AuNPs-C$_{commercial}$ catalysts. The crystalline nature of Au nanoparticle and the method of dispersion on the carbon support has a strong influence on the structure, morphology and reactivity. Figure 6.5a Au-C$_{PVP(87.6\ wt.\%)}$ clearly demonstrates higher crystallinity after deposition/dispersion on carbon black compared to the AuNPs-C$_{commercial(20\ wt.\%)}$ (see Figure 6.5b), as shown in the XRD diffraction intensities. The higher resolution of the different crystal planes indicated well-anchored Au-C$_{PVP}$ nanoparticles on the support, and also a smaller Au particle size with improved catalytic activity.
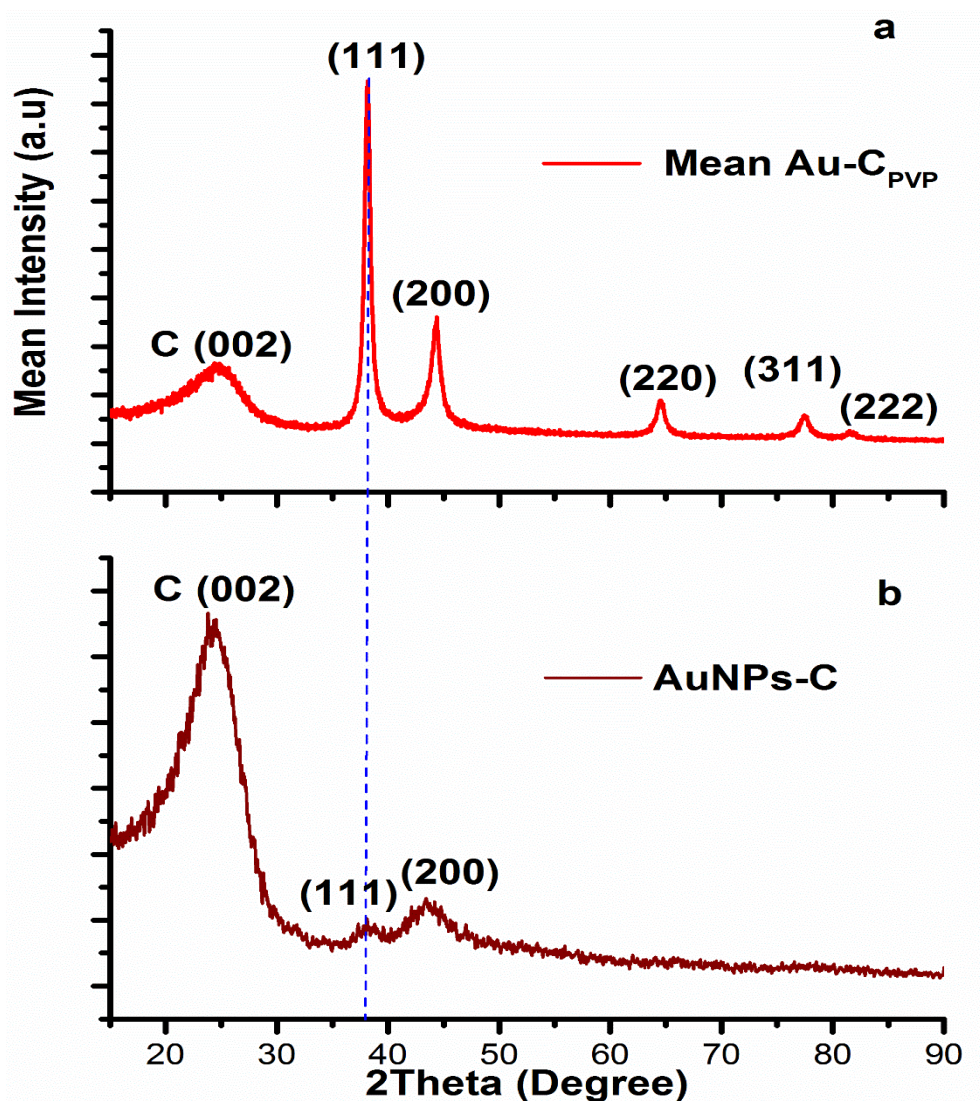
Figure 6.5: XRD patterns of Au-C$_{PVP(87.6\ wt\%)}$ and AuNPs-C$_{commercial(20\ wt\%)}$ catalysts with major peaks marked (JCPDS No. 4-0784)

The average relative crystallinity is 2.17 for Au-C$_{PVP(87.6\ wt.\%)}$ and 0.27 for AuNPs-C$_{commercial\ (20\ wt.\%)}$ catalysts respectively, indicating better crystallinity of Au-C$_{PVP(87.6\ wt.\%)}$ than AuNPs-C$_{commercial\ (20\ wt.\%)}$ [310]. These results confirm the distinct characteristic profile of Au oxidation of sulphuric acid (see Figure 6.6). The highly amorphous nature of the AuNPs-C indicates the possibility of very few AuNPs nanoparticles being attached to the Vulcan XC72 support; the Au characteristic peaks were absent in the CV profile but a broad carbon profile peak has present in Figure 6.6

below. These results indicate the formation of zero valent Au^0 form after the chemical reduction process.

The surface area, S_{XRD} calculated from the XRD data for as-prepared AuNPs-C$_{commercial}$ $_{(20\ wt\%)}$ was 63.4 m^2 g^{-1} which was larger than that for Au-C$_{PVP\ (87.6\ wt.\%)}$ (58.6 m^2 g^{-1}). The Au-C$_{PVP}$ catalyst demonstrated a similar percentage utilisation (22.2 for AuNPs-C$_{commercial}$ and 20.8 for Au-C$_{PVP}$) even though the ICP data showed different active metal loading. The limitation of the assumption, that all particles are spherical in shape does not include the additional surface contribution of the edges/corners.

Table 6.2: Summary of the crystallographic parameters for Au catalysts

Parameters	Au-C	AuNPs-C	Au PDF Card 4-0784
Avg. Surface area (m^2 g^{-1}$_{active\ metal}$)	58.6	63.4	
Avg. Crystallite size (nm) 200 plane	5.3	1.8	
Avg. Relative crystallinity (111 plane)	2.17	0.27	
Avg. Intensity ratio (111) to (200)	2.282	1.344	
Intensity ratio (111) to (200) PDF Card	1.923	1.923	
Avg. Lattice parameter, a (200 plane)	4.082	4.150	4.079
Avg. d-spacing (Å) (200 plane)	2.041	2.075	2.039
Avg. Peak position, 2θ (Degree) (200 plane)	44.35	43.59	44.39
Atomic radius (Å) (200 plane)	1.443	1.467	1.442

The Au-C$_{PVP(87.6 \text{ wt.\%})}$ catalyst gave an average lattice parameter of 4.082, which is in good agreement with the JCPDS Au bulk card (no. 4-0784) value of 4.079. However, the commercial AuNPs dispersed in VulcanXC72 carbon showed a higher estimated lattice parameter value of 4.15. The estimated d-spacing calculated from the diffraction patterns for the Au-C$_{PVP(87.6 \text{ wt.\%})}$ and AuNPs-C$_{(20 \text{ wt.\%})}$ catalysts was 2.041 and 2.075, respectively. Au-C$_{PVP(87.6 \text{ wt.\%})}$ catalyst showed excellent agreement based on the negligible shift in 2θ, the lattice parameter and the d-spacing for the (200) crystal planes of 0.07%, and 1.74% for AuNPs-C$_{commercial(20 \text{ wt\%})}$, respectively. The obtained values for the PVP synthesised Au catalyst are in good agreement with the literature [297] and the JCPDS card 4-0784 (Au bulk) value of 2.039.
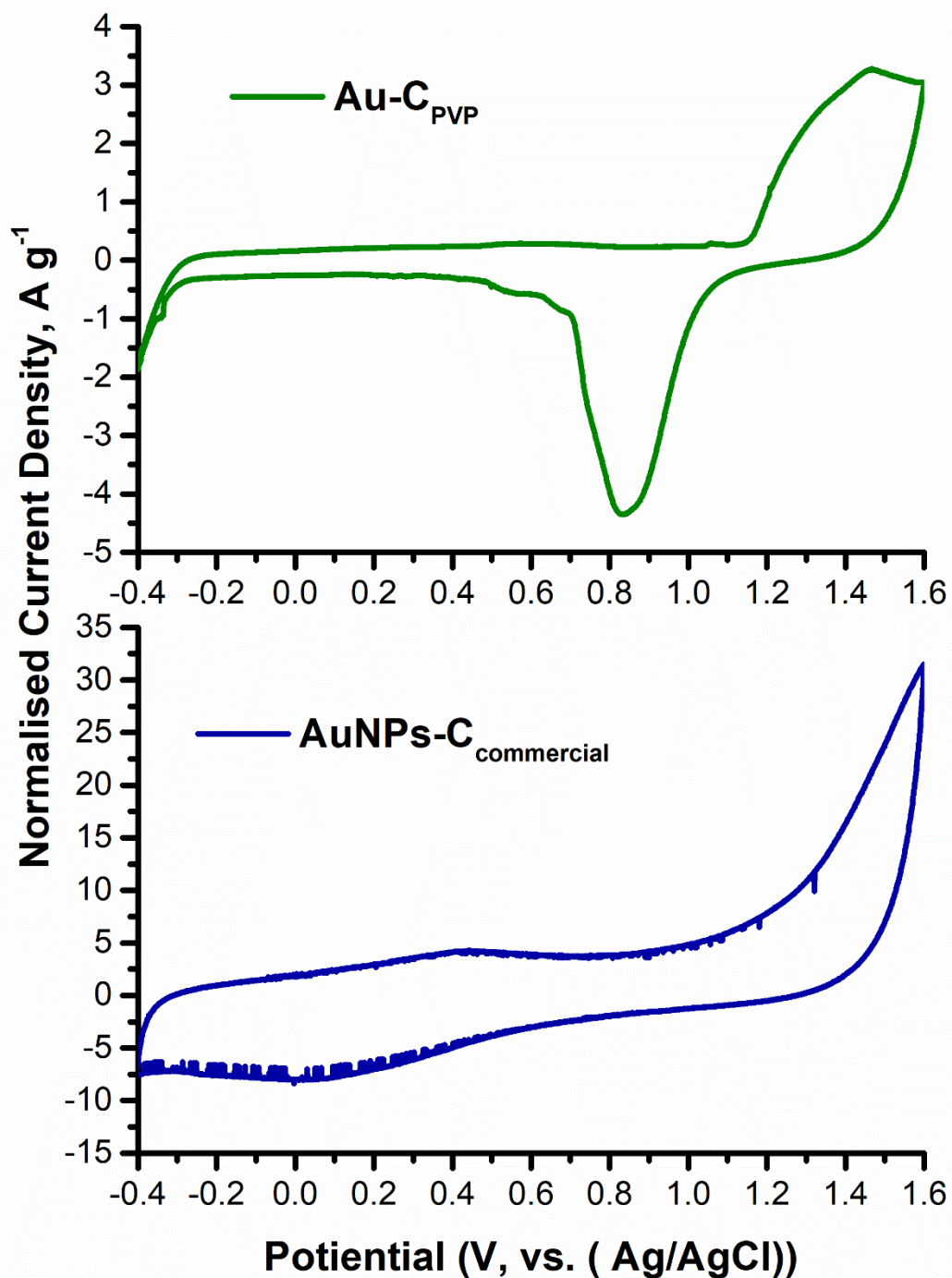
Figure 6.6: Comparison of catalyst activity between AuNPs-C$_{commercial\ (20\ wt.\%)}$ and Au-C$_{PVP\ (87.6\ wt.\%)}$ for 0.5 M H$_2$SO$_4$ solution at a scan rate of 20 mVs^{-1} (10th cycle)

From Figure 6.6, it is certain that after potential cycling the Au surface is cleaned by efficiently eliminating surfactants and residual organic materials from the nanoparticle surface [311]. This may be attributed to different crystal Au nanostructures in each catalyst, such as cubic or exposed phase during the electrocatalytic reaction [312]. Au-

C_{PVP} gave the unique characteristic of an Au catalyst for H_2SO_4 electrooxidation, while AuNPs-$C_{commercial}$ tend to be limited by the hydrogen evolution reaction and tend toward the carbon characteristic profile in an acid medium. On the reverse scan, the oxide reduction peak of Au-$C_{PVP(87.6 wt.\%)}$ is at 0.84 V, while that of AuNPs-$C_{commercial(20 wt.\%)}$ appears at 0.03 V, indicating a higher resistance to surface oxides and covering of the catalyst active site. Also, the ECSA of AuNPs-$C_{commercial(20 wt.\%)}$ is 12.5 m^2 g^{-1} and Au-$C_{PVP(87.6 wt.\%)}$ has an equivalent surface area of 12.2 m^2 g^{-1}. However, Au-$C_{PVP(87.6 wt.\%)}$ showed the characteristic Au nanoparticles oxidation profile, which could be due to the selective blockage of the less reactive (100) and (110) planes. This may be attributed to the more exposed (111) facet in the Au-C_{PVP} Au-$C_{PVP(87.6 wt.\%)}$ catalyst, which demonstrated superior intensity, compared to AuNPs-$C_{commercial(20 wt.\%)}$ [312].
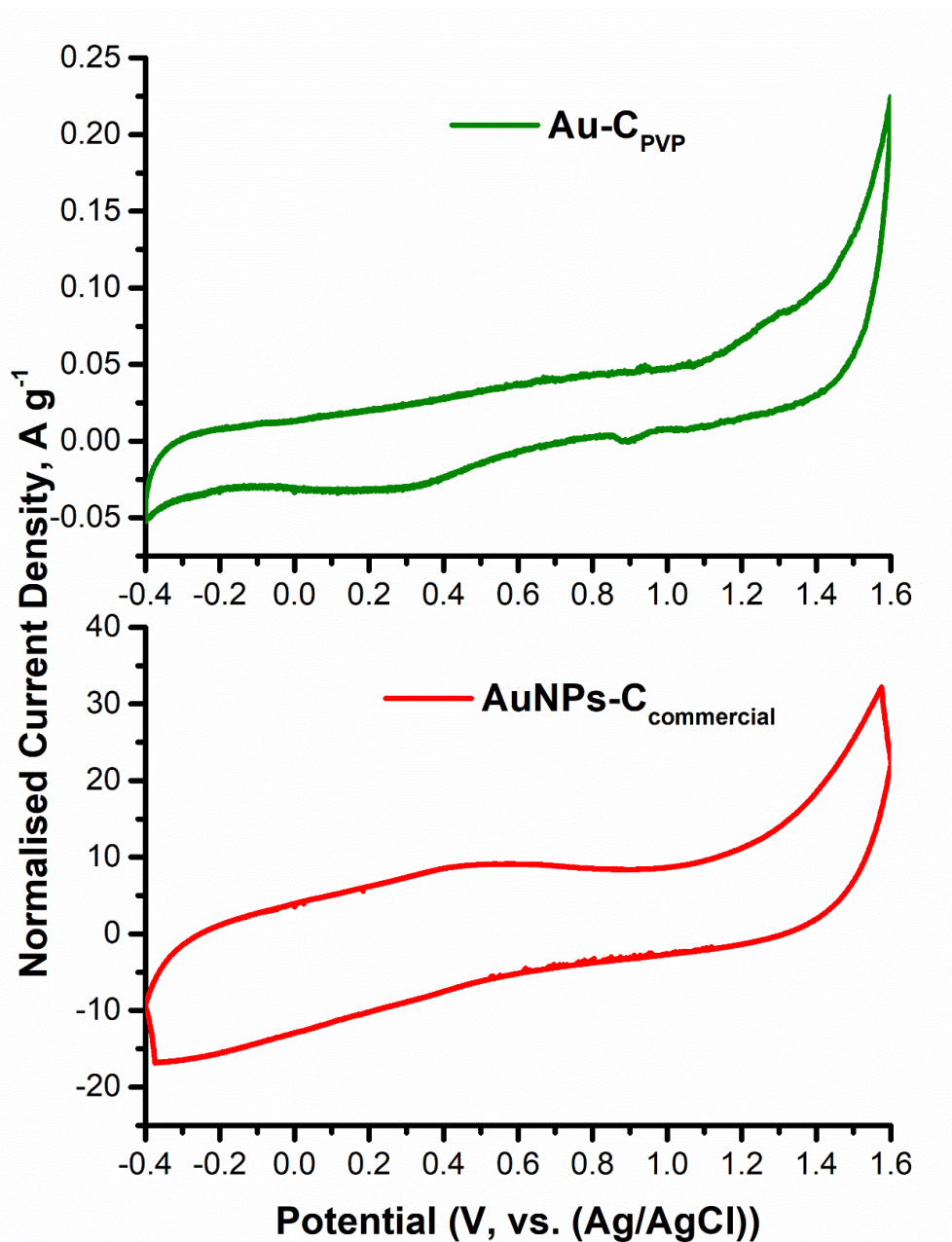
Figure 6.7: Comparison of catalyst activity between AuNPs-C$_{commercial(20\ wt.\%)}$ and Au-C$_{PVP(87.6\ wt.\%)}$ for 0.5 M H$_2$SO$_4$ solution + 0.5 M HCOOH solution at a scan rate of 50 mVs^{-1} (30th cycle)

Chen *et al.* (2007) demonstrated that gold carbon supported catalysts possessed high formic acid tolerance and considered them suitable as a cathodic catalyst for DFAFC. It can be observed that the electrocatalytic activity for oxidation of formic acid demonstrated by Au-C catalyst has a good performance [104]. The higher potential of Au-C$_{PVP(87.6\ wt.\%)}$ FAO indicates higher stability of the oxide(s) formed but reduced

stability on the reverse scan at the voltammetric peak of about 1.29 V with a current density of 0.14 mA cm^{-2}, compared to the current density of 3.18 mA cm^{-2} (0.52 V) for AuNPs-C$_{commercial(20\ wt.\%)}$ under same experimental conditions. In agreement with earlier reports, it has been confirmed that FAO does not depend on the mass-transport conditions, irrespective of the scan rate. The peak region (1.2-1.6 V) was consistent with the FAO profile of Au-C$_{PVP(87.6\ wt.\%)}$, unlike the AuNPs-C$_{commercial(20\ wt.\%)}$ catalyst kinetics [150, 266]. This is because of the formation of oxygen-containing surface species (surface-bonded hydroxyl species) on the Au electrode at potentials near 0.5 V vs. RHE on clean Au (100). The potential region does not give clear evidence inherent to the surface roughness, but the larger background current of AuNPs-C$_{commercial(20\ wt.\%)}$ is due to the presence of the carbon support and the smaller particle size [313] which probably detached from the carbon support. Cherevko *et al.* investigated the oxide formation region of Au electrode (2013) with a 3-electrode cell and scanning flow cell setups were used to. They attributed the variation in the oxidation characteristics from the electrode diversity to the electrode preparation (influence of grain size, exposed surface orientation, purity), polishing and cleaning procedure, and the affinity of gold to poisoning by impurities [305].
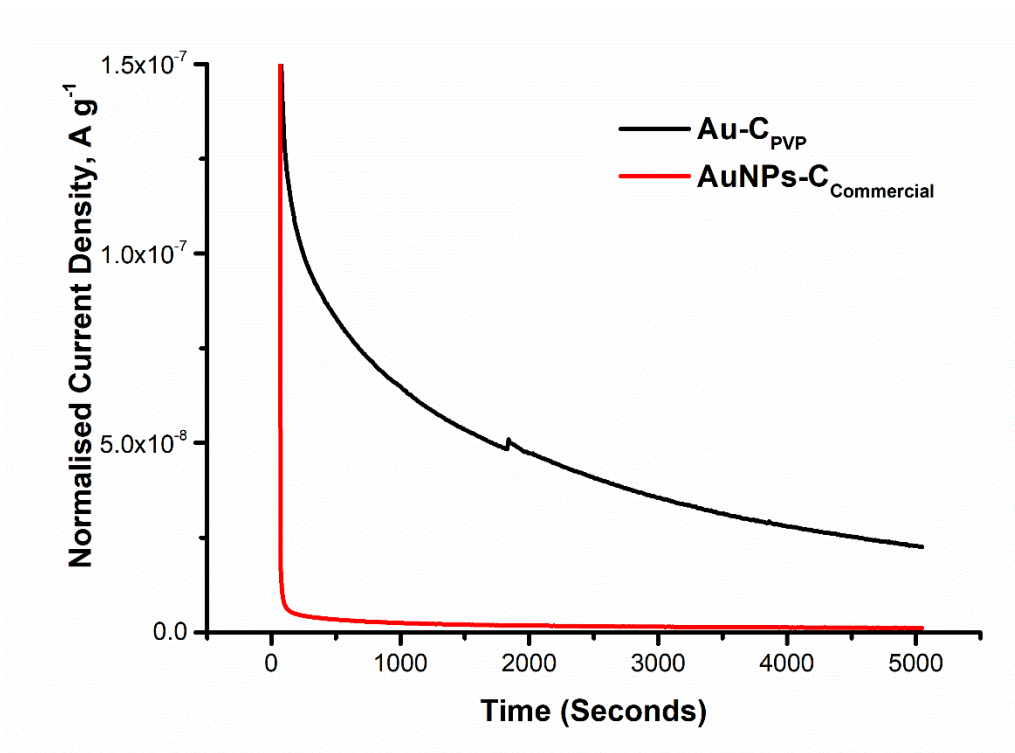
Figure 6.8: Chronoamperometric curve of the AuNPs-C$_{commercial(20\ wt.\%)}$ and Au-C$_{PVP(87.6\ wt.\%)}$ electrodes in a 0.5 M H$_2$SO$_4$ solution + 0.5 M formic acid solution at 0.6 V.

The stability of the Au-C$_{PVP(87.6\ wt.\%)}$ catalyst is due to the surface adsorption and reactivity of Au nanoparticles in the PVP synthesis route, which formed unique morphologies/nanostructures and an adequate number of low coordination surface atoms through down-sizing [314]. Figure 6.8 shows the chronoamperometry of Au-C$_{PVP(87.6\ wt.\%)}$ and AuNPs-C$_{commercial(20\ wt.\%)}$ electrodes in 0.5 M H$_2$SO$_4$ solution + 0.5 M formic acid solution at 0.6 V potential versus Ag/AgCl$_{sat.\ KCl}$ (0.197 V vs. NHE). Au-C$_{PVP(87.6\ wt.\%)}$ demonstrated superior catalytic resistance to catalyst decay with time. The higher current density could be indicative of a high activity because of the larger ECSA of AuNPs-C$_{commercial(87.6\ wt.\%)}$ (see Table 6.1).

6.3 Conclusion

Au-C$_{PVP(87.6 \text{ wt.\%})}$ catalysts were synthesised by a PVP-stabilised sodium borohydride reduction method at room temperature and the electrochemical performance was investigated. The synthesised Au-C$_{PVP(87.6 \text{ wt.\%})}$ nanoparticle had the majority of particles in the 1-6 nm range. The Au-C$_{PVP(87.6 \text{ wt.\%})}$ catalyst provided a consistent Au oxidation activity compared to the AuNPs-C$_{commercial}$, showing a lower onset potential with a well characterised Au electrooxidation profile with all characteristic peaks on both the anodic and cathodic sweeps. Results revealed that the high electrooxidation activity of the Au-C$_{PVP(87.6 \text{ wt.\%})}$ catalyst was related to the intrinsic properties of Au-C$_{PVP(87.6 \text{ wt.\%})}$ nanoparticles. The specific synthesis route led to an apparent change in the morphology with corners and defective edges for Au particle anchorage to the carbon support. The surface atoms are easier to oxidise, and hence the higher electrocatalytic activity is comparable with AuNPs-C$_{commercial(20 \text{ wt.\%})}$ catalysts. The Au-C$_{PVP(87.6 \text{ wt.\%})}$ catalyst possesses high formic acid tolerance and improved stability for DFAFC electrooxidation. However, regarding the electrocatalytic activity of both Au catalysts there have been some reports that hydrogen adsorption/absorption on/into metal generates strain in the lattice, leading to reorganisation of less active surface states [315]. Adams *et al.* (2014), Antolini and Gonzalez (2011) have demonstrated the enhanced reactivity of bimetallic catalysts compared to the monometallic Au for electrooxidation reactions [115, 316]. In Chapter 7, an AuCu bimetallic catalyst will be investigated for the electrooxidation of formic acid in acid medium. The study serves as an insight into understanding the formulation and preparation of a better catalyst for FAO, especially bimetallic catalysts, owing to their synergistic geometric and electronic properties.

Chapter 7 Performance of the direct formic acid fuel cell with electrochemically modified AuCu-C anode catalyst

7.1 Introduction

In chapter 6, AuNPs-C$_{commercial}$ and Au-C$_{PVP}$ PVP-stabilised chemically reduced nanoparticle catalysts were compared by their electrochemical and physical/chemical characterisations. This chapter is an investigation into the influence of the PVP stabiliser on the surface geometry/nanostructure of bimetallic electrocatalysts, which consist of copper nanoparticles completely covered by a monolayer of polycrystalline gold on a high-surface-area carbon support. To determine the physicochemical and electrochemical properties of the bimetallic AuCu on the carbon black support, a one-pot- two-stage synthesis route was employed at low temperature. For gold layer deposition to occur, the copper precursor is stabilised with PVP in solution before it is reduced with sodium borohydride, forming Cu-PVP stabilised nanoparticles. The addition of highly concentrated sodium hydroxide in a ratio of 1M NaBH$_4$: 3M NaOH decreases the number of water molecules available for the hydrolysis reaction during the reduction reaction stage. The concentrated NaOH suppressed hydrogen evolution, allowing copper and gold nanoparticles to be freely disperse in the colloidal state without aggregating into large particles, before immobilisation on the carbon support. The synthesis strategy is a facile and scalable approach to preparing AuCu-C$_{PVP}$. The PVP preparation method is confirmed to be reproducible and produces consistent core-shell bimetallic catalysts with unique geometric structure. The AuCu-C$_{PVP}$ catalyst demonstrated superior catalytic activity for FAO at room temperature, compared with monometallic Au nanoparticles with specific metal loading. Detailed physical/electrochemical characterisations were performed, to correlate the AuCu-C$_{PVP}$

core-shell bimetallic structure and the catalytic properties with the Au-C$_{PVP}$ monometallic nanoparticles. The AuCu-C$_{PVP}$ core-shell structure is one solution to reducing the cost of the anode catalyst, improving utilisation, and enhancing the performance of DFAFCs electrooxidation processes. Some sections of this chapter have been published already by Oseghale and others [104].

Finally, an overall discussion of the thesis is presented, by comparing the critical physical and electrochemical properties of the catalysts (AuCu-C$_{PVP}$, Au-C$_{PVP}$, AuNPs-C$_{commercial}$, Pd-C$_{PVP}$, and Pd-C$_{H3BO3 + NH4F}$) was evaluated.

7.2   Results

7.2.1   Hydrogen Adsorption-Desorption Analysis

From Figure 7.1, AuCu-C$_{PVP(45\ wt.\%)}$ catalyst exhibits three main current sensitivity maxima on the positive scan (anodic) at ca. -0.22 V, 0.25 V and 0.50 V, and on the negative backwards scan at ca. 1.0 V, 0.27 V and -0.075 V [299].
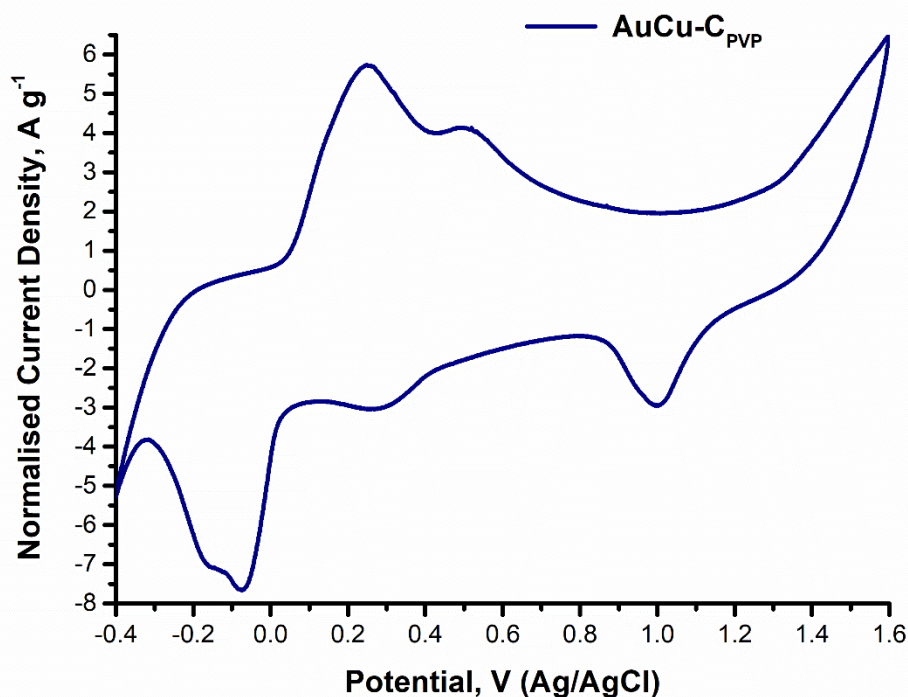
Figure 7.1: Cyclic voltammetry of AuCu-C$_{PVP(45\ wt.\%)}$ catalyst in 0.5 M H$_2$SO$_4$ solution at a scan rate of 20 mVs^{-1} (10th cycle)

Generally electrocatalytic (-0.22 V, 0.25 V, 0.50 V) activities of oxidizable compounds on gold do not react before the onset of monolayer oxide species formation at ca. 1.36 V. However, the reaction of formic acid on the as-prepared AuCu-C$_{PVP(45\ wt.\%)}$ evidently shows high reactivity for formic acid electrooxidation, which is in agreement with literature [298]. Tian and coworkers (2003) investigated the Au activity in aqueous H$_2$SO$_4$ using an electrochemical quartz crystal nanobalance, confirming the potential range for Au oxide formation. The real area of the hydrogen adsorption-desorption peaks (ECSA) of the polycrystalline AuCu-C$_{PVP(45\ wt.\%)}$ represents the available number of active sites on the catalyst for electrocatalytic reactions [278], estimated to 61.8 m^2 g^{-1} using Equation 5.1. It suggests that AuCu-C$_{PVP(45\ wt.\%)}$ displays enhanced electrocatalytic activity and better performance for formic acid oxidation reactions in comparison with monometallic catalysts (AuNPs-C$_{commercial(20\ wt.\%)}$ and Au-C$_{PVP(87.6\ wt.\%)}$).

7.2.2 Crystallography of AuCu-C$_{PVP(45 wt.\%)}$ and Au-C$_{PVP(87.6 wt.\%)}$ catalysts

The crystal phases of the AuCu-C$_{PVP(45 wt.\%)}$ catalysts were characterised using XRD as shown in Figure 7.2. The diffraction peaks match very well with the tetragonal Au crystalline structure (JCPDS 4-0784).

Table 7.1 Crystallographic parameters for the Au and Au-based catalysts

Parameters	Au-C	AuNPs-C*	AuCu-C	Au PDF card 4-0784	Cu PDF card 4-0836	AuCu PDF card 01-072-5241
Avg. Surface area (m^2 g-1active metal)	58.6	63.4	238.9			
Crystallite size (nm) 200 plane	5.3	1.8	1.3			
Relative crystallinity (200 plane)	2.17	0.27	3.31			
Intensity ratio (111) to (200)	2.282	1.344	2.36			
Intensity ratio (111) to (200) PDF Card	1.923	1.923	1.923			
Lattice parameter, a (200 plane)	4.082	4.150	4.088	4.079	3.615	4.009
d-spacing (Å) (200 plane)	2.041	2.075	2.044	2.039	1.808	2.004
Peak position, 2θ (Degree) (200 plane)	44.35	43.59	44.28	44.392	50.433	45.201
Atomic radius (Å) (200 plane)	1.443	1.467	1.445	1.442	1.278	1.417

Compared with the reflections of Au-C$_{PVP(87.6 wt.\%)}$ catalysts, the diffraction facets of AuCu-C$_{PVP(45 wt.\%)}$ catalysts show a shift to higher angles due to the presence of the Cu contents. For example, the Au-C$_{PVP(87.6 wt.\%)}$ (200) diffraction peaks appeared at about

44.35°, whereas there is a shift to 44.28° for the AuCu-C$_{PVP}$ catalysts. The marked decrease in the mean *d*-spacing could be attributed to the shift in the lattice contraction between the metals (Au, Cu) because of their difference in lattice spacing [114]. The data of the average crystallite sizes, lattice parameters, relative crystallinities and the interplanar distance (d-spacing) of the Au and Au-based catalysts are listed in Table 7.1.
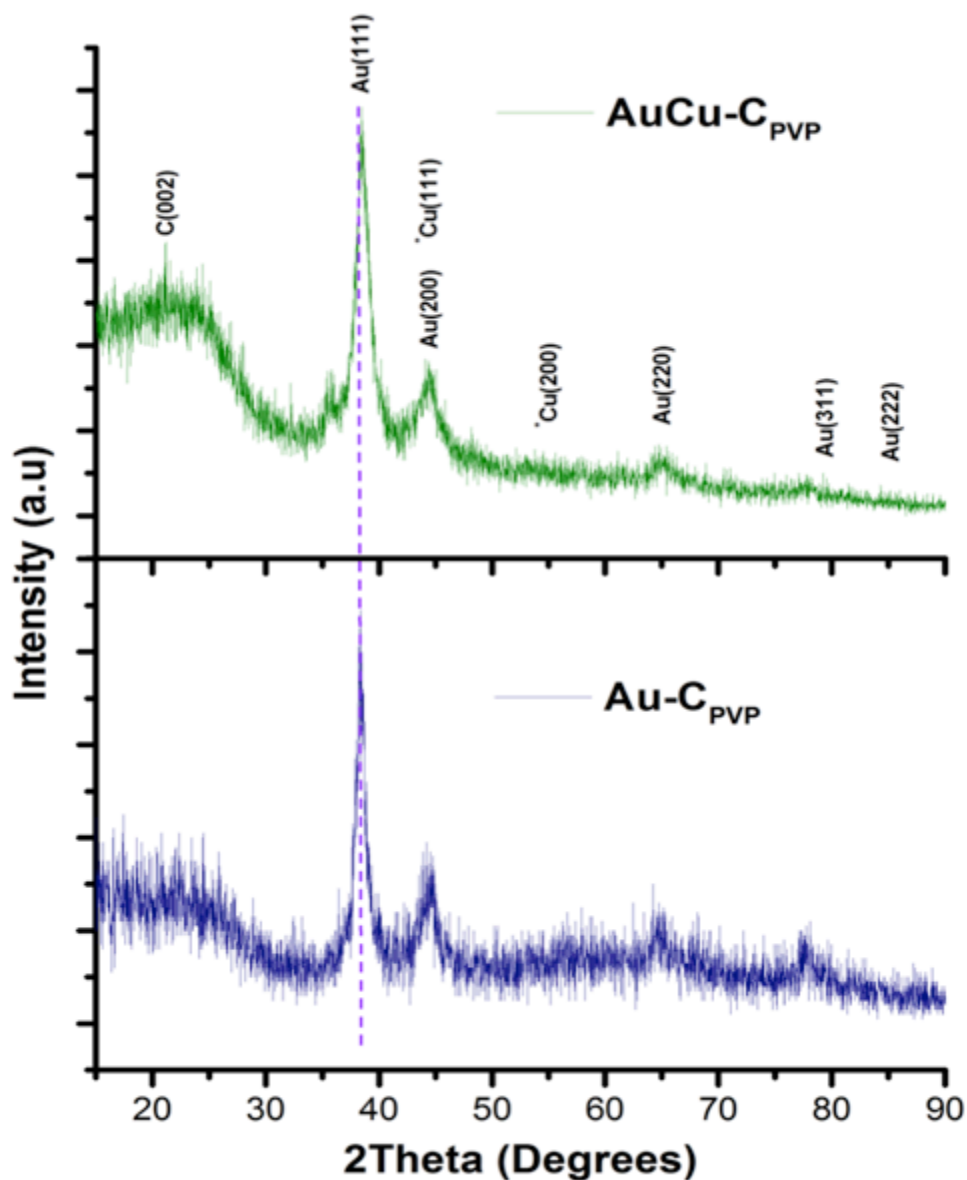
Figure 7.2: XRD patterns of Au-C$_{PVP(87.6 wt.\%)}$ and AuCu-C$_{PVP(45 wt.\%)}$ catalyst.

The crystal planes for copper and copper oxides are not reflected on the AuCu-C$_{PVP(45 wt.\%)}$ catalyst samples. These findings suggest a gold (shell) monolayer coverage of the

copper (core) nanoparticle. There were no impurity phases detected on the diffraction patterns for the entire AuCu-C$_{PVP(45\ wt.\%)}$ sample, indicating the formation of pure and highly polycrystalline fcc-AuCu-C$_{PVP(45\ wt.\%)}$ nanoparticles. AuCu-C$_{PVP(45\ wt.\%)}$ nanoparticles will show reflections according to the selection rules for crystal diffraction, where the Miller indices (*hkl*) are all odd or all even: Au (111), Au (200), Au (220), Au (311), and Au (222). The above results suggest the formation of the core-shell structure, because of the absence of the superlattice reflections of (001) and (110) and the splitting reflections of (200)/(002) and (220)/(202) which substantiate the none-formation of ordered intermetallic (alloy) structures [207, 215, 317]. From Figure 7.2, comparisons of the XRD diffraction patterns show that the absence of alloy or intermetallic bond structure formation in the AuCu-C$_{PVP(45\ wt.\%)}$ catalysts (2θ = 38.4, 44.3, 64.8 and 77.8) and matched with (negligible shift from) pure Au nanoparticles (2θ = 38.3, 44.4, 64.6 and 77.7).

Furthermore, compared to monometallic Au phase changes, which increase the diameter, bimetallic particles can be differentiated, as opposed to monometallic mixtures, by overlapping lines of two individual nanoparticles. The spectrum of bimetallic nanoparticles is generally wider than the monometallic nanoparticles or their counterpart mixtures [190]. Using Debye-Scherrer's equation (Equation 5.3), the mean crystallite size (*d*) of the catalysts was estimated and compared subsequently with TEM, SEM, and AFM particle size. [58, 144]. The peak width β and peak position θ were obtained from curve fitting using PANalytical Data Viewer software.

7.2.3 The Role of Copper Content

The ratio of the intensities of Au (111) and the carbon peaks is the relative crystallinities of Au nanoparticles, that is: 3.31 for AuCu-C and 2.17 for Au-C$_{PVP(87.6\ wt.\%)}$ catalysts. The presence of an amorphous component or contaminant phase can be inferred from the degree of relative crystallinity of the sample and is confirmed from the estimates that Au-C$_{PVP(87.6\ wt.\%)}$ and AuCu-C$_{PVP(45\ wt.\%)}$ are well-defined crystalline nanoparticles on a carbon support. It is observed that a higher d space ($d_{111} = 2.3234$ Å) for the AuCu-C$_{PVP(45\ wt.\%)}$ catalyst could be due to the lower 2θ peak of (111) of Au ($d_{111} = 2.3503$ Å) because of the incorporation of Cu atoms, indicating the possible formation of a core-shell structure on the carbon support [310]. AuCu-C$_{PVP(45\ wt.\%)}$ catalyst showed no reflections for metallic Cu or its Cu oxides, suggesting that Cu exists as highly dispersed core species as demonstrated in similar work by Duan and co-workers [186]. Compared with the pure Au pattern, AuCu-C$_{PVP(45\ wt.\%)}$ shifted slightly to lower angles, indicating a change in the d-band due to Cu content and suggests that the copper nanoparticles are completely covered in core-shell architecture. To further validate the observations (see Table 7.1), the Au$_{0.8}$Cu$_{0.2}$alloy (JCPDS 1-072-5241) or Cu$_{0.508}$ Au$_{0.492}$ (JCPDS 4-018-5478) phase pattern for AuCu-C$_{PVP\ (45\ wt.\%)}$ does not match the alloys, as there is a shift to lower angles due to the effect of the core-copper nanoparticles. The average lattice parameters were estimated from Bragg's law, based on the (200) crystal planes, and are listed in Table 7.1. For example, the AuCu-C$_{PVP\ (45\ wt.\%)}$ catalyst properties based on the shift in 2θ, the changes in the lattice parameter and d-spacing, show a very small mismatch for the (200) crystal planes of 0.25%, 0.24%, and 0.24%, respectively. The structure of the AuCu-C$_{PVP\ (45\ wt.\%)}$ catalyst can hardly be differentiated (only by XRD pattern analysis) to be either core-shell or alloy structures. The lattice contraction is due to the difference in lattice spacing between two metals in solution, and is ascribed to Vegard's law [114]. Using Equation 7.1, the extent of

alloying ($\chi_{AuCu_{PVP}}$) was estimated from Vegard's law based on the lattice parameter data:

$$(\chi_{AuCu_{PVP}}) = a_{AuCu_{PVP}} - a_{Au\ 4-0784} - k\chi_{AuCu_{PVP}} \qquad 7.1$$

where the constant, k is 0.124 Å [318], $a_{AuCu_{PVP}}$ is the lattice parameter for AuCu-C$_{PVP}$, and $a_{Au\ 4-0784}$ is the lattice of the bulk Au (PDF card 4-0784). The value of $\chi_{AuCu_{PVP}}$ was 0.07%. The very low extent of alloying could be ascribed to the low temperature synthesis route and suggests a core-shell structure.

Recent reports by Wang and co-workers confirmed that Cu has much lower d-band centre of ca. -2.67 eV and a small atomic size, thus an ideal bimetallic component to tune down the d-band of noble metals (Au) [229]. Furthermore, AuCu-C$_{PVP(45wt.\%)}$ X-ray scattering did not show a mixture of Au and Cu crystal planes of the physical mixtures of individual gold and copper nanoparticles. The key reason for using Cu to enhance catalytic activity and stability of Au nanoparticles on a carbon support is because of the beneficial selective CO removal in fuel cell oxidation processes [68, 223-228, 319].

7.2.4 The Influence of Crystal Planes and the Texture Coefficient on the Preferential Orientation Gold Catalysts

From XRD analysis, the gold crystallite structure can be evaluated from the knowledge of the preferential orientation of crystal planes and the $TC_{(hkl)}$ calculations. The $TC_{(hkl)}$ of the crystal plane directly influences the performance and reliability of the nanocatalyst in the reaction environment. Furthermore, it represents the structural, conductivity, electronic and electrical properties, which drastically affect the texture of the catalyst

material. Using Equation 5.5 (*see Section 5.2.1 for more details*), the $TC_{(hkl)}$ was estimated from Halls method for each crystal plane of the XRD powder pattern of Au-C$_{PVP(87.6\ wt.\%)}$ and AuCu-C$_{PVP(45\ wt.\%)}$ catalysts [118, 289].

To estimate the D$_p$ and $TC_{(hkl)}$ of the different facets of the Au-C$_{PVP(45\ wt.\%)}$ and AuCu-C$_{PVP(45\ wt.\%)}$ catalyst particles, the bulk gold fcc structure matching (JCPDS, File No. 4-0784) was used (see Figure 7.3).
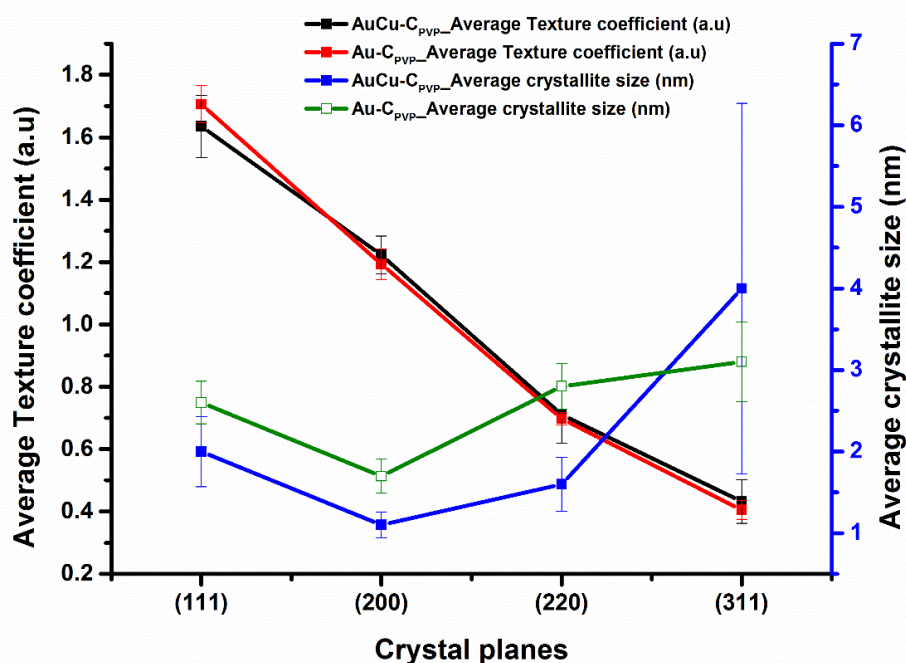
Figure 7.3: The influence of the texture coefficient and average crystallite size on the Au-C$_{PVP(17.9\ wt.\%)}$ and AuCu-C$_{PVP(19.3\ wt.\%)}$ catalysts structure

For the Au-C$_{PVP(17.9\ wt.\%)}$, the $TC_{(hkl)}$[111] and [200] crystal planes were 1.71 and 1.19, respectively while the $TC_{(hkl)}$[111] and [200] of the AuCu-C$_{PVP(19.3\ wt.\%)}$ were 1.64 and 1.22, indicating a preferential crystallographic orientation (growth) along these planes. The other planes for both catalysts were lower than one, which shows a consistent trend with the literature [320] for similar noble metals [289].

7.2.5   Nanostructure and Morphological Analysis of the Catalysts

To understand the nanostructure and surface morphology of the various catalysts, microscopic and spectroscopic measurements were performed. To gain an understanding of the role of surface morphological changes on the prepared catalysts and the surface mechanisms at the electrode interface in the electrochemical reactions, the planes exposed and their relative areas are required. Catalyst samples were investigated using a combination of methods: TEM, AFM, SEM and EDS.
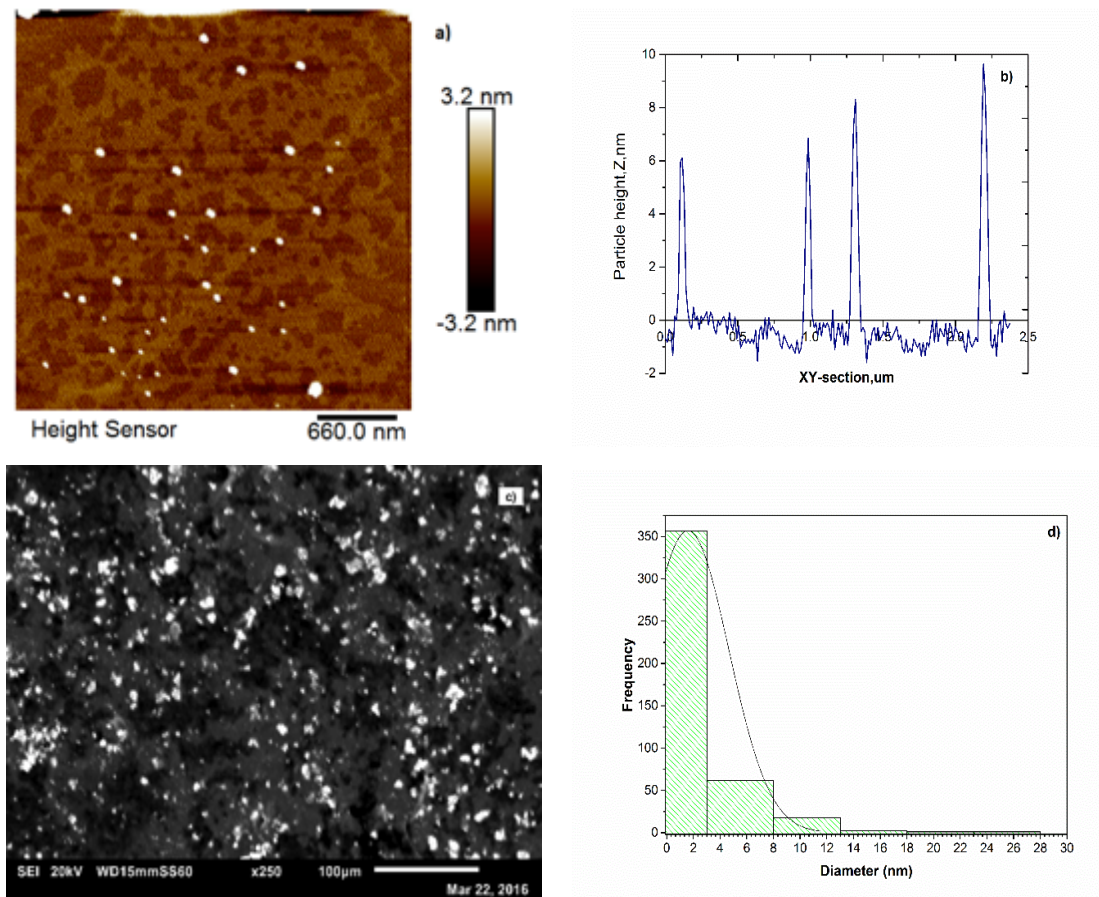
Figure 7.4: Surface morphology of AuCu-C$_{PVP}$ catalyst: a) AFM image topology, b) AFM section analysis of the particle size, c) SEM image of the nanoparticles, d) SEM particle size profile
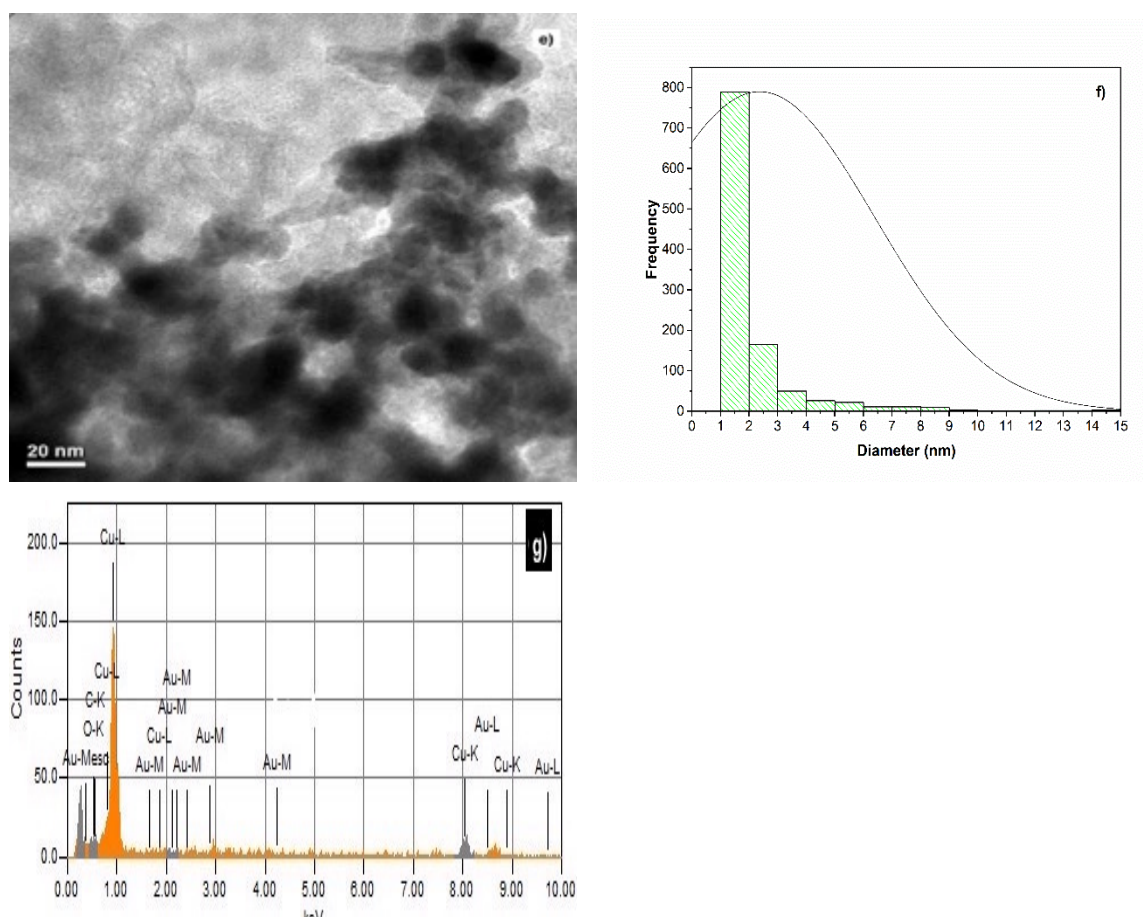
Figure 7.4 continued: Surface morphology of AuCu-C$_{PVP}$ catalyst: e) TEM image, f) TEM particle size distribution, and g) EDS elemental mapping

In Figure 7.4 it can be clearly observed that the Au nanoparticles show a range of particle sizes from 1-14 nm and are well dispersed on the carbon support, from various microscopic analyses. From the histograms and AFM section analysis, a few agglomerations can be seen, but the core-shell structure also unfolded. The EDS results may suggest the formation of a AuCu-C$_{PVP}$ core-shell, which is in fairly good agreement with the XRD core-shell structure evaluation ($\chi_{AuCu_{PVP}}$ = 0.07%). The EDS results confirm that no chloride ions or any other contaminates or artefacts were in the samples investigated. Figure 7.4a shows the surface morphology of the AuCu-C$_{PVP}$ catalyst deposited on a freshly cleaved mica sheet, and shows quasi-spherical well-dispersed nanoparticles. The AFM images were further analysed using cross-section analysis of the image (Figure 7.4b) to elucidate particle size by comparing the peak

166

heights of AuCu-C$_{PVP}$ nanoparticles arising from the surface of the carbon black substrate.

The particle size (height of peaks) observed from the section analysis show AuCu-C$_{PVP}$ nanoparticles anchored on carbon black with a particle size range between 1-14 nm. The average particle size estimated from the AFM images is 8.5 ± 0.56 nm, a bit larger than the TEM values because of the limited high-resolution of AFM measurements due to the convolution of tip width [321, 322]. Figures 7.4c and 7.4d show an SEM micrograph with well-dispersed particles of AuCu-C$_{PVP}$ catalysts and histogram with a mean D$_p$ distribution of 3.5 ± 0.31 nm, along with few agglomerate particles observed. EDS elemental mapping confirmed the presence of Au and Cu nanoparticles dispersed on a carbon support (see Figure 7.4g). Approximately 1120 AuCu-C$_{PVP\ (45\ wt.\%)}$ particles in the TEM image were used to obtain the average D$_p$ of 1.4 ± 0.11 nm. Furthermore, over 90% of the observed particles (see Figure 7.4d and f) were in the range of 1 to 10 nm, which is in good agreement with XRD, AFM and SEM analysis results. These confirm that the TEM particle sizes represent a few single crystals of AuCu or grains.

7.2.6   Electrocatalytic performance of AuCu-C$_{PVP}$ for formic acid oxidation

The cyclic voltammogram for the electrooxidation activity of formic acid in acid media on the AuCu-C$_{PVP(45\ wt.\%)}$ catalyst is shown in Figure 7.5. From the profile of HCOOH oxidation, the main oxidation peaks are located at 0.55 V and 1.49 V and a current density of 2.95 (3.78 mA mg^{-1}) and 25.8 mA cm^{-2} (33.1 mA mg^{-1}), respectively.
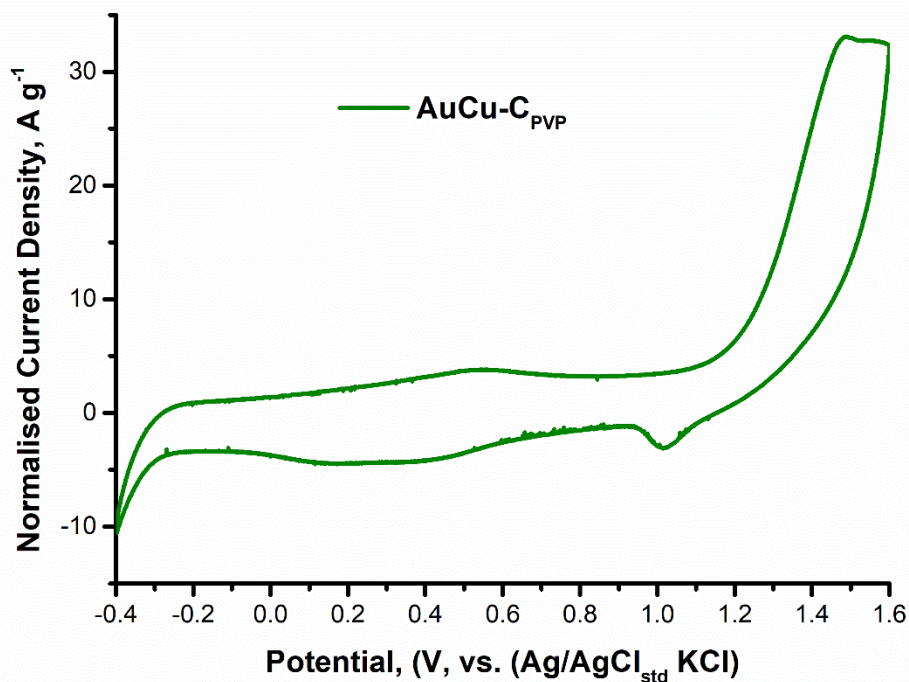
Figure 7.5: Cyclic Voltammogram of AuCu- $C_{PVP(45\,wt.\%)}$ for 0.5 M H_2SO_4 solution + 0.5 M HCOOH solution at a scan rate of 50 mV s^{-1}, 25 ^{o}C (50th cycle)

The catalyst tolerance to the poisoning species in gold improved significantly, due to the elimination of residual carbon species (e.g. carbon monoxide (CO_{ads})) from the Au surface. In the reverse scan, the peak appears just after 0.4 V (the anodic oxidation potential) indicating fast removal of oxidation products. Strasser at al (2010) confirmed that compression from the Pt shell modified the d-band structure of the AuPt core-shell nanoparticles decreasing the absorption energy of the reaction intermediates [323]. On the contrary, Au monometallic catalysts show a lower peak potential ca. 0.8 V, due to the absence of the electronic coupling effect of the Cu content in AuCu-$C_{PVP(45\,wt.\%)}$ catalyst [151, 217, 324]. From the estimated electrochemical surface areas, AuCu-$C_{PVP(45\,wt.\%)}$ catalysts can provide at least 4.1 times higher specific ECSA for catalysis in comparison to Au-$C_{PVP(87.6\,wt.\%)}$ monometallic catalysts.

7.2.7 Current density decay for formic acid oxidation

Chronoamperometry is an effective electrochemical technique for investigating the electrooxidation activities of the catalyst stability in acid medium. Figure 7.6 shows the CA response of 0.5 M H_2SO_4 + 0.5 M HCOOH at a potential of 0.6 V versus Ag/AgCl$_{sat}$KCl for 3000 and 5000 seconds. All catalyst electrodes showed current density decay with formic acid oxidation. The decay was gradual in both AuCu-C$_{PVP}$ electrodes but showed a lower decay in the 5000 seconds stability test. The current density shows a gradual decline during the first 20 seconds, attributed to the accumulation of toxic intermediate species (e.g. (CO$_{ads}$), formate radical (HCOO$_{ads}$)) before reaching steady state after 45 seconds. The initial and final current densities for AuCu-C$_{PVP(45\ wt.\%)}$ were 20.87, 28.85 and 0.97, 0.30 mA cm^{-2}, after 3000 and 5000 seconds, respectively.

This demonstrates the promising electrochemical durability of the AuCu-C$_{PVP(45\ wt.\%)}$ nanoparticles in a long-term stability test. The results confirm the existence of the electronic coupling between the Au (shell) and Cu (core) structure, compared to the Au monometallic catalysts.
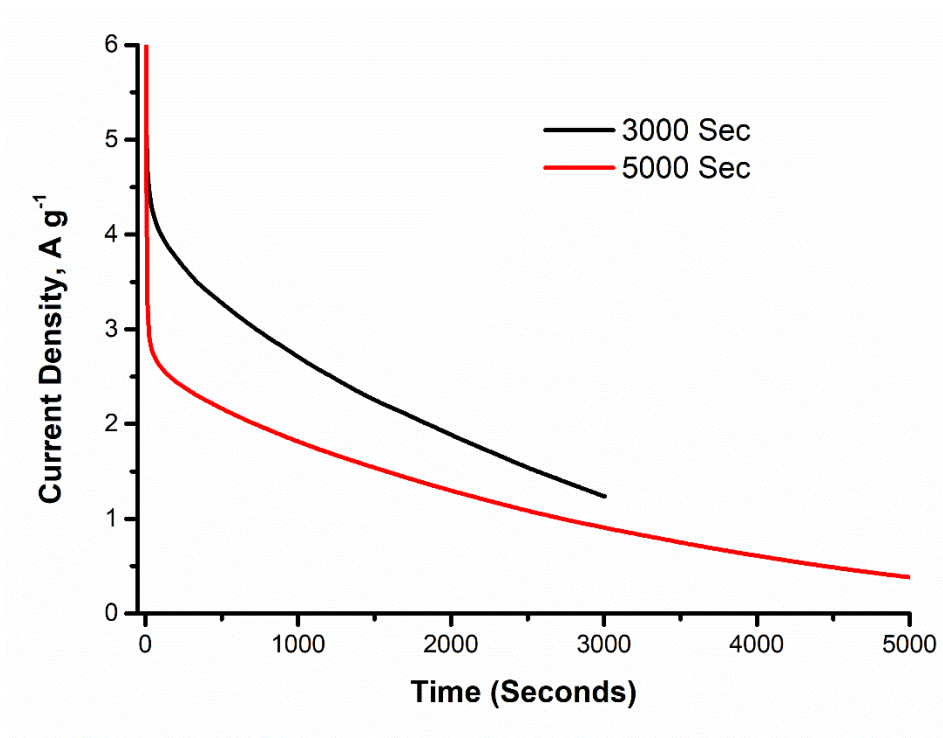
Figure 7.6: Chronoamperometry experiment at 0.6 V at 3000 and 5000 seconds of AuCu-C$_{PVP(45\ wt.\%)}$ catalysts in 0.5 M HCOOH + 0.5 M H$_2$SO$_4$ solution

7.3   Discussion

From a crystallographic viewpoint, the XRD data confirms that the Au-C$_{PVP(87.6\ wt.\%)}$ and AuCu-C$_{PVP(45\ wt.\%)}$ largely favours the (111) orientation. The (111) and (200), even though parallel planes showed the difference in crystallite size and texture, imply that the $TC_{(hkl)}$ varies between the polycrystalline, bulk sample and the nanoparticles. The average D_p (1.3 ± 0.11 nm) estimated from XRD confirmed the same particle size due to the large sample size used in the TEM analysis, indicating the polycrystalline nature of the AuCu-C$_{PVP(45\ wt.\%)}$ catalysts. The synthesis route for Au-C$_{PVP(87.6wt.\%)}$ and AuCu-C$_{PVP(45wt.\%)}$ catalysts confirmed that small nanoparticles of Au could be prepared by well designed and tuned preparation strategy. Compared with earlier reports that carbon surface materials are acidic with low isoelectric points, and can react with Au^{3+} as reducing agent to form large gold nanoparticles during reduction reaction step [102].

170

The modified preparation method can produce a well-dispersed narrow distribution of small Au and Au-based nanoparticles on a carbon black support with negligible agglomeration or large particles. From Figure 7.3, the XRD data confirms that the Au and AuCu nanoparticles were largely grown preferentially in the (111) orientation. In particular, both catalysts show low, consistent error bars across the crystal planes. Each catalyst displays a similar trend of decreasing average texture coefficient from low to higher facets. The average crystallite sizes show increasing error bars which are consistent with the XRD pattern (see Figure 7.2) with reducing diffraction intensities. The Au (111) planes predicted for the Au and Au-based catalysts are consistent with the previous report by Melaine *et al.* (2007) [325].

The ECSA of AuCu-C_{PVP} was 61.8 m^2 g^{-1} compared with 12.2 m^2 g^{-1} for the Au-$C_{PVP(87.6 wt.\%)}$ catalyst, with mass activities of 33.1 mA g^{-1} and 0.08 mA g^{-1}. This demonstrates the superior catalytic properties of the bimetallic AuCu-C_{PVP} catalyst over the monometallic Au-$C_{PVP(87.6 wt.\%)}$. The electrocatalytic enhanced activity is attributed to the synergistic effect of AuCu-$C_{PVP(45 wt.\%)}$ catalysts due to the addition of Cu metal [103, 114, 319], its bimetallic properties, particle size, carbon support, and reaction conditions. On the basis of the dependency of maximum current densities and ECSA for both Au catalysts, the smaller particle size (1.3 nm, 61.8 m^2 g^{-1}) of the AuCu-C_{PVP} indicates that formic acid is more accessible to be oxidised than Au-$C_{PVP(87.6 wt.\%)}$ (5.3 nm, 12.2 m^2 g^{-1}). This finding indicates that the Au catalyst is less active in acidic electrolytes compared to the alkaline media but is active towards the O_2 reduction in both electrolytes. Also, they observed that a AuPt bimetallic catalyst showed significant catalytic activity by modifying the property of a Pt in the acidic electrolyte [326]. The higher FAO current density of AuCu-$C_{PVP(45 wt.\%)}$ compared to the Au-$C_{PVP(87.6 wt.\%)}$

catalyst is indicative of faster reaction rate, particle size/electronic effects and the large available ECSA for the reaction. Another reason for the highly efficient and selective electrochemical oxidation reaction of AuCu-C$_{PVP(45\ wt.\%)}$ could be the synergistic geometric and electronic effects attributed to the gold-copper bimetallic nanoparticle. In their report, Kim and co-workers (2014) find that two factors dictate the activity of gold-copper bimetallic nanoparticles with the intermediate binding effects – the electronic and geometric effects on the nanoparticles [151].

The performance criteria seem to be dependent on lattice contraction associated, with the electronic effect of the bimetallic structure increasing coordination of unsaturated Au and Cu nanoparticles for small molecule hydrocarbons. For example, experimental and computational estimates show that the bond dissociation energy values of Cu, Ag and Au are relatively high and also thermodynamically stable [327]. They concluded that Au is catalytically more active at low temperature (200-300K, compared with Pd and Pt at 400-800K). The difference in the mechanism is ascribed to the electrophilicity (*ability to attract electrons*) of Au towards catalytic species. Another key influential factor is the adsorption of PVP on the surface preventing agglomeration and growth of nanoparticles for the improved catalytic activity of AuCu-C$_{PVP(45\ wt.\%)}$ in the acid medium as confirmed by Wang and co-workers [328]. The lower onset potential for formic acid oxidation reaction above confirmed that the AuCu-C$_{PVP(45\ wt.\%)}$ catalyst could be attributed to the removal of intermediate species and improved electrocatalytic activity.

Figure 7.5 confirmed that the high electrooxidation activity of AuCu-C$_{PVP(45\ wt.\%)}$ catalyst was related to the intrinsic properties of the bimetallic nanoparticle structure. The surface reactivity and adsorption of AuCu-C$_{PVP(45\ wt.\%)}$ nanoparticle can be tuned due to structural defects and the adequate number of low-coordination surface atoms

through down-sizing [314] (see Section 2.9.7). The particle size plays a key factor along with the bimetallic properties of AuCu nanoparticles in enhancing the catalytic activity of the AuCu-C$_{PVP}$ catalyst for FAO. Furthermore, another factor is the effect of the mass presence of the (111) plane of the Au surface. The investigation of the comparison of electroactivity between (111) and (100) plane of Au structure in KOH [314], methanol [295] and formic acid [150] electrooxidation have been previously reported. It is believed that the underlying structures (lattice strain), i.e. geometric effects, play a key role in improving the catalytic properties of the Au outer surface [205].

The perturbation in the orbital of Au, due to the loss of valence electrons to the Cu atoms might be the result of the electronic surface energy of Au, to achieve improved electrochemical performance of the catalyst [114, 319]. The weak chemisorption energy resulting from the electronic surface energy leads to the fast removal of poisonous species during formic acid oxidation from catalyst active sites [114]. This is observed by the immediate reaction with the Au oxide reduction peak at ca. 1.0 V and the second cathodic peak at ca. 0.17 V, respectively. Moreover, these could be attributed to the known facts that Au atoms at steps, corner and defect positions in small particles have a bottom coordination number and d-band state. These bring the energy gap much closer to the Femi level compared to the crystallographic planes, given strong interaction between Au $5d$ and O $2p$ valence states [152].

7.4   Conclusion

At the atomic scale gold catalysts display unique catalytic properties regarding the electrochemical oxidation reactions in formic acid. AuCu-C$_{PVP(45\,wt.\%\,Au)}$ catalysts with a core-shell structure were prepared by a PVP-stabilised chemical reduction method

generated narrow average particle size of 1.3 ± 0.11 nm. The XRD analysis confirmed the absence of superlattice and splitting reflections, suggesting a core shell structure AuCu nanoparticles instead of an alloy evident by the lower angle shift of all the diffraction planes. CV experiments clearly demonstrated that AuCu-$C_{PVP(45 \text{ wt.% Au})}$ catalyst has a superior catalytic activity for FAO when compared with monometallic with Au-$C_{PVP(87.6 wt.%)}$ catalyst. The enhanced electrochemical activity may be due to the electronic effects of the core-shell structure and the increased coordination of unsaturated Au and Cu for FAO. Also, the improved absorption strength were influenced by the Cu metal content in the AuCu-$C_{PVP(45 \text{ wt.% Au})}$ between the active sites and the absorbed species on the catalyst surface. The PVP stabiliser played a significant role in the anchorage of the Au shell on the Cu nanoparticles in solution. It can be concluded that the stronger metal-metal interaction influenced the preferential reduction of the Au shell covering the Cu-PVP stabilised nanoparticles rather than on carbon support. The fact that Au coated Cu in a core-shell arrangement is supported with XRD, CV, SEM and TEM results. These findings can provide useful guidance for tunable design protocols for HCOOH oxidation in acid solution. The presence of atomic defects such as steps, corners, edges, and kinks is the basis for the origin of high catalytic activity in the catalysts. The highly reproducible and superior FAO performance, together with ease of incorporation into existing fuel cell membranes, makes it an attractive candidate for actual low-temperature fuel cell applications.

7.5 Overall Discussion

The XRD analysis for all catalysts showed no external layer of oxide phases or residual capping agent (see Figures 5.12 and 7.7). All the as-prepared catalysts demonstrated

high relative crystallinity with the decreasing order AuCu-C_{PVP} > Pd-C_{PVP} > Pd-$C_{H3BO3 + NH4F}$ > Au-C_{PVP} > AuNPs-$C_{commercial}$, indicating well-ordered crystalline metal nanoparticles. The intensity ratio of the (111) peak to (200) peak (calculated from JCPDS card data) of the Pd-C_{PVP} catalyst samples (an increase from 1.67 to 2.73) indicated the preferential orientation of the (100) facets in Pd nanoparticles as confirmed in previous literature [92, 273-275].

Yang and coworkers (2014) confirm that the Pd single phase exposes the (100) plane surface of the fcc structure [275]. The overall superior activities of the Pd-C_{PVP} catalysts compared to the other catalysts demonstrated that the (100) plane of Pd nanoparticles is the most reactive plane. The morphology of the Pd-C_{PVP} surface reflects the presence of edges and corners, and enhanced the catalytic performance in the electrooxidation of formic acid on the Pd surfaces. For comparison, the XRD analysis of all Pd catalysts was further investigated, demonstrating the preferential formation of the highly reactive 100 and 111 crystal planes. In Figure 5.12, the shift to lower angles on the XRD pattern of Pd-C_{PVP} confirmed the smaller crystallite size compared to Pd-$C_{commercial}$ and Pd-$C_{H3BO3 + NH3F}$.

.
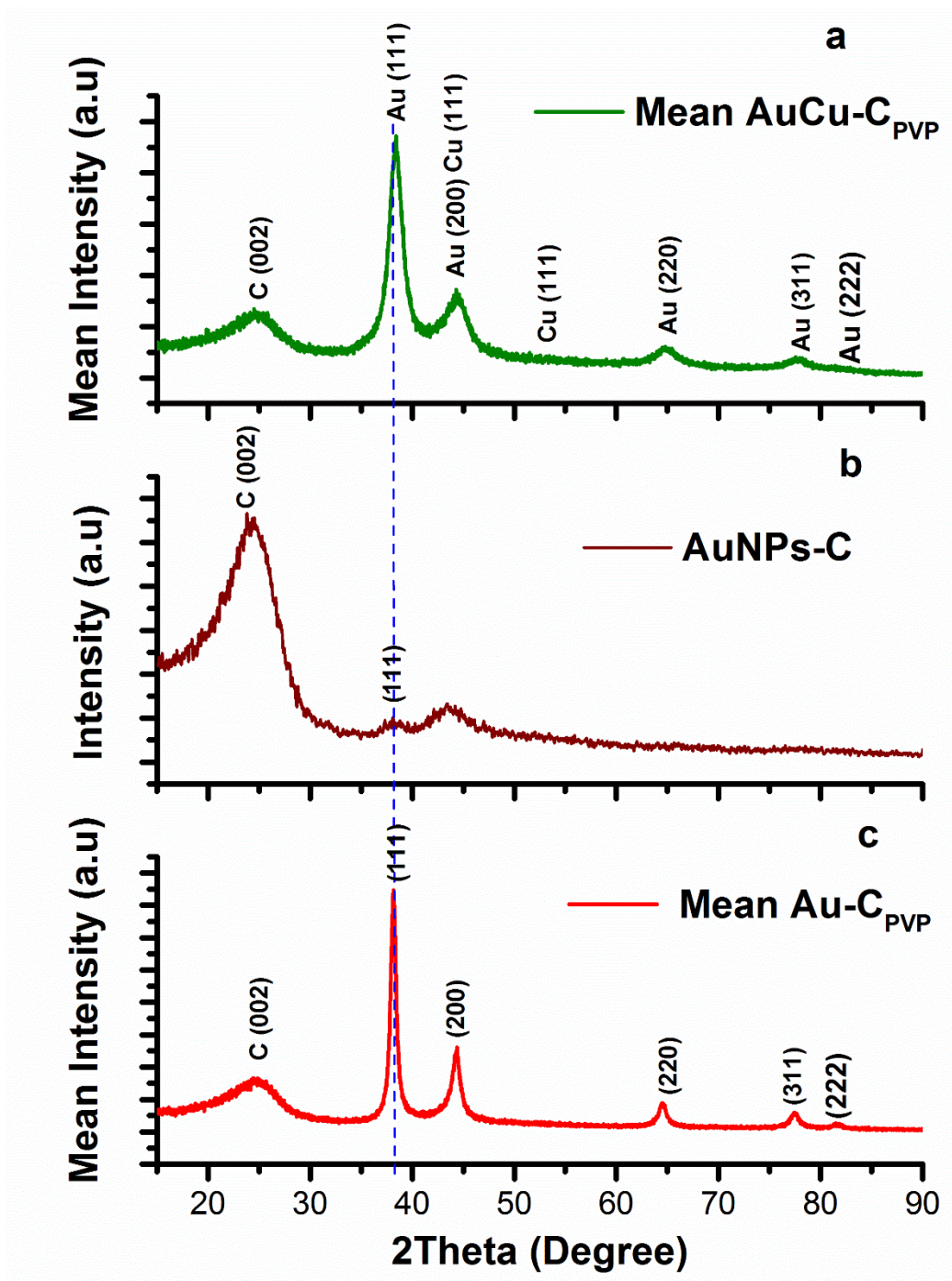
Figure 7.7: Comparison of the XRD patterns of Au-C$_{PVP(87. 6wt.\%)}$, AuCu-C$_{PVP(45wt.\%)}$ and AuNPs-C$_{commercial(20wt.\%)}$ catalyst.

For Au and Au-based catalysts, the XRD analysis showed that the (111) plane at 38.36^o is the most intense, which suggested that it is the most exposed area of the corresponding facets [295]. The intensity ratio of the (111) peak to the (200) peak is lower than the standard value estimated from the JCPDS data (from 1.92 to 1.34),

which indicates that the (200) planes dominate in the AuNPs-C$_{commercial}$ catalyst [296]. The relative crystallinity was 3.31 for AuCu-C$_{PVP(45wt.\%)}$, 3.09 for Au-C$_{PVP(87.6wt.\%)}$ and 0.27 for AuNPs-C$_{commercial(20wt.\%)}$ catalysts respectfully, indicating increasing crystallinity of AuCu-C$_{PVP}$, Au-C$_{PVP}$ and AuNPs-C$_{commercial}$ catalysts [310]. The degree of crystallinity of the nanoparticles influences the catalyst structure such as the optical, magnetic, conductivity and electrical properties of the catalysts. It is generally accepted that the reactivity could be enhanced by improving crystallinity (e.g. electronic effect), which is attributed to the improved electron transport from the conduction band of the Au to the surface adsorbed species [329].

Table 7.2: Comparison of the crystallographic parameters for the different catalysts

Parameters	Pd-C$_{PVP}$	Pd-C$_{H3BO3+NH4F}$	Au-C	AuNPs-C	AuCu-C
Avg. Surface area (m^2 g$^-$$_{1\ active\ metal}$)	357.1	113.6	58.6	63.4	238.9
Crystallite size (nm) 200 plane	1.4	4.4	5.3	4.4	1.3
Relative crystallinity	2.57	2.30	3.09	0.27	3.31
Intensity ratio (111) to (200)	2.73	2.47	2.76	1.34	2.36
Intensity ratio (111) to (200) PDF Card	1.671	1.671	1.923	1.923	1.923
Lattice parameter, a (200 plane)	3.962	3.889	4.082	4.150	4.088
d-spacing (Å) (200 plane)	1.981	1.945	2.041	2.075	2.044
Peak position, 2θ (Degree) (200 plane)	45.76	46.67	44.35	43.59	44.28
Atomic radius (Å) (200 plane)	1.401	1.375	1.443	1.467	1.445
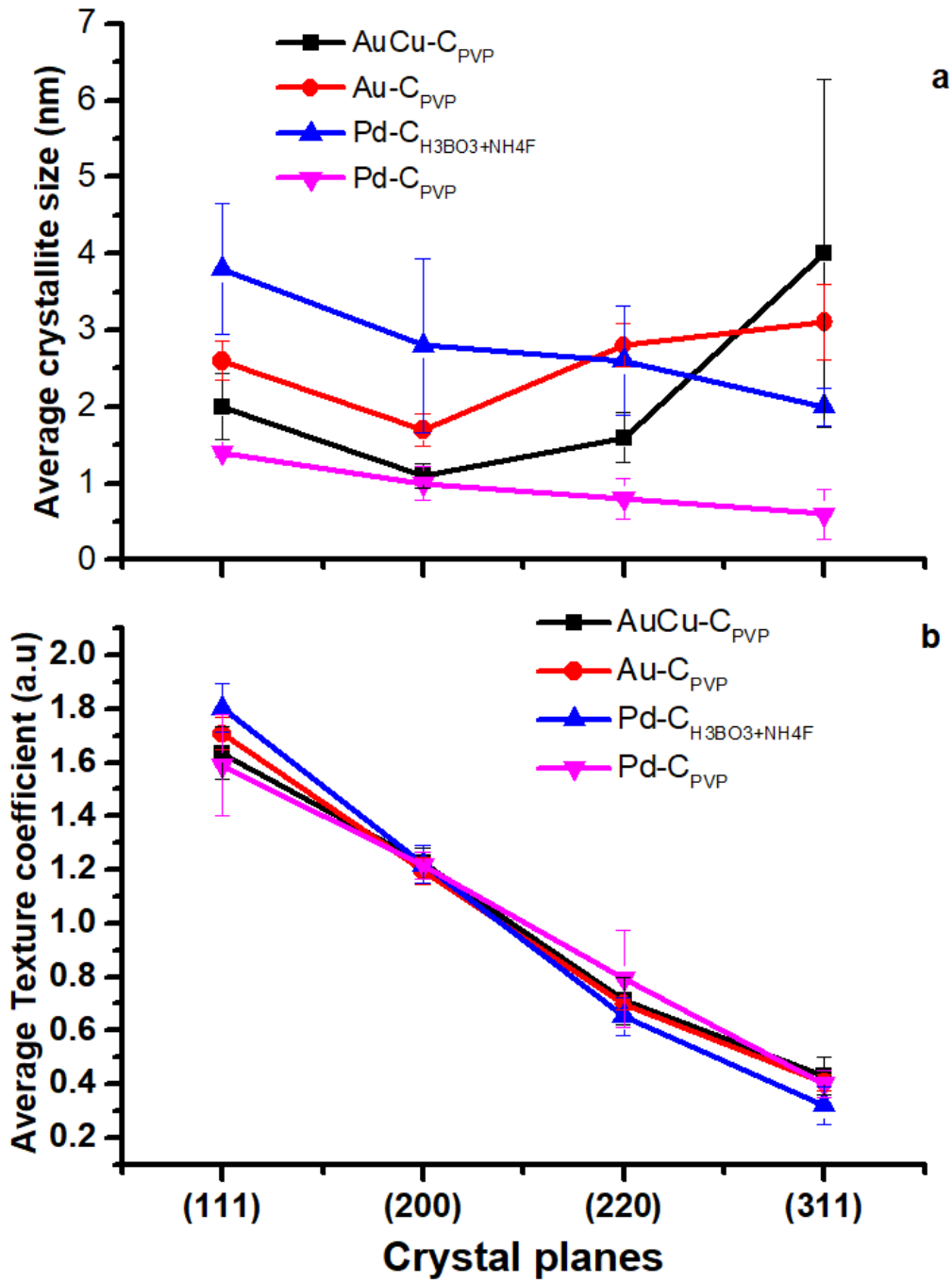
Figure 7.8: Comparison of the texture coefficient and average crystallite size for Au-C_{PVP}, AuCu-C_{PVP}, Pd-C_{2PVP} and Pd-$C_{2H_3BO_3 + NH_4F}$ catalysts

Figure 7.8 presents a comparison of the texture coefficient and average crystallite size for Au-C_{PVP}, AuCu-C_{PVP}, Pd-C_{2PVP} and Pd-$C_{2H_3BO_3 + NH_4F}$ catalysts (SYN17). The crystallite sizes are consistent, with a decreasing trend from low to higher index planes. For all the catalysts, the average crystallite sizes display preferential crystallographic

growth for the (111) plane. In particular, Pd-C$_{2PVP}$ shows low, consistent error bars across the crystal planes compared with the others. All catalysts display a similar trend of decreasing average texture coefficient from low to higher facets. The (200) plane shows little deviation from across the crystal planes. All catalysts demonstrated high average texture coefficient with decreasing order: Pd-C$_{H3BO3 + NH4F}$ > Au-C$_{PVP}$ > AuCu-C$_{PVP}$ > Pd-C$_{PVP}$, indicating well-ordered crystalline nanoparticles for the (111) preferential orientation. The average crystallite size (Figure 7.8a) showed consistency between the increase of crystallite size and the increase in crystal plane from low angles to higher angles, except for Pd-C$_{H3BO3+NH4F}$ (220). The degree of preferred orientation among the crystal planes was analysed and presented in Figure 7.8b [289]. A three-fold hexagonal-like symmetry orientation is predicted for the as-prepared Au and Au-based catalysts for the Au (111) plane, which is consistent with previous literature [325]. The (111) plane at 38.36^o is the most intense, which suggested that it is the most exposed area of the corresponding facets [295].

The strain and ligand effects are with associated the Cu content in the AuCu-C$_{PVP(45wt.\%)}$, which causes a structural change from the crystallographic position. This causes a shift in the *d*-band centre of primary metals such as Au relative to the Fermi level. This may change the surface chemistry of AuCu-C$_{PVP(45wt.\%)}$ catalysts by weakening the bonding strength of adsorbates, thus modifying the overall reactivity [130, 229]. Also, Ren *et al.* (2014) confirmed in their work the effect of Cu addition on the enhanced activity of formic acid oxidation due to the increase in lattice strain of PdCu, improving the overall catalytic performance [114]. Further investigation of the surface chemistry is required to understand the effect of the *d*-band shift and the weakening of the bonding strength of poisonous species on the electrode surface (e.g. in-situ techniques - In-situ Surface-

Enhanced Raman Spectroscopy (SERS) and Attenuated Total Reflectance Fourier Transform Infrared Spectroscopy (ATR-FTIR)).

The mass activity for the Pd-C$_{\text{H3BO3 + NH4F(21wt.\%)}}$ electrodes, with an average of 97.1 mA mg$^{-1}_{\text{Pd}}$, shows a 1.8 fold higher performance than the Pd-C$_{\text{PVP(43.5 wt.\%)}}$ catalysts electrodes (53.9 mA mg$^{-1}_{\text{Pd}}$) under the same electrochemical conditions when compared on the basis of the ICP-AES metal content. However, the Pd-C$_{\text{PVP(43.5 wt.\%)}}$ catalyst synthesis demonstrated more efficient metal dispersion and physicochemical properties than the H$_3$BO$_3$ + NH$_4$F synthesis route. The efficient performance of the PVP synthesis route can be understood from the desorption peak analysis for H$_2$SO$_4$ solution CV experiments. The PVP catalysts demonstrated a higher ECSA of 188.4 m^2 g$^{-1}_{\text{Pd}}$ than the H$_3$BO$_3$ + NH$_4$F electrodes at 38.3 m^2 g$^{-1}_{\text{Pd}}$ in the reverse scan directions. The change can be attributed to the higher available ECSA for the oxidation reaction due to the fast removal of product and intermediate species from the Pd active sites and less deactivation of the active sites. A more comprehensive investigation of the underlying mechanisms still needs to be undertaken, for example via in-situ electrode surface mechanistic experiments, such as, using ATR-FTIR.

The ECSA of the catalysts decreases in the order Pd-C$_{\text{PVP}}$ > AuCu-C$_{\text{PVP}}$ > Pd-C$_{\text{H3BO3 + NH4F}}$ > AuNPs-C$_{\text{commercial}}$ > Au-C$_{\text{PVP}}$ (Table 7.4), indicating that the addition of Cu in AuCu-C$_{\text{PVP}}$ increases the dispersion of Au on the carbon support [87]. The smaller the average particle size and lower the relative crystallinity of the Au particles, the larger the ECSA [296, 330]. The larger ECSA and subsequent higher current density AuCu-C$_{\text{PVP}}$ could be due to the selective blockage of the less reactive (100) and (110) planes. This may be attributed to the more exposed (111) facet in the Au catalysts, which

demonstrated superior intensity [312]. A small particle size and lower relative crystallinity usually would correspond to a larger ECSA of the catalysts. From the estimated electrochemical surface areas, AuCu-C$_{PVP(45wt.\%)}$ catalysts can provide a value of the specific ECSA at least 5.1 times higher for catalysis as compared with Au monometallic catalysts (see Figure 7.9). It is proposed that this improved catalytic activity is due to the synergistic effect of Cu content in the AuCu-C$_{PVP(45wt.\%)}$ catalysts [69, 103, 114, 319], bimetallic properties, particle size, the carbon support, and reaction conditions. Previous studies by Liu *et al.* (2001, 2012) have demonstrated the enhanced activity for the oxidation of CO with Cu addition to Au [149, 216]. On the basis of the dependency of maximum current densities and ECSA for Au catalysts, it is thought that the smaller particle size of AuCu-C$_{PVP(43.5wt.\%)}$ indicates that formic acid is more easily oxidised than on monometallic Au nanoparticles (*electronic/geometric effects*). The effect of the shell atoms (Au) on the core (Cu) may have created some level of tension or compression, as confirmed by Jin and coworkers (2012), which altered the catalytic behaviour and optimised the specific reaction path for the AuCu-C$_{PVP(45wt.\%)}$ catalysts. Form an economic viewpoint, the Au-shell provides an efficient cost design to improve the utilisation of expensive active metal by depositing thin shells on Cu (core) nanoparticles. In a recent report, Mao *et al.* (2016) successfully demonstrated that with only a 10% metallic loading of Au in PdAu/C, high catalytic activity and a stability of up to 1700 mA mg^{-1} peak current density for ethanol oxidation was achieved [218]. However, the direct correlation between bimetallic catalyst systems and catalytic properties remains a challenge. The overall performance indeed would be a combination of several factors such as the interaction of reactants, compositions and experimental conditions.
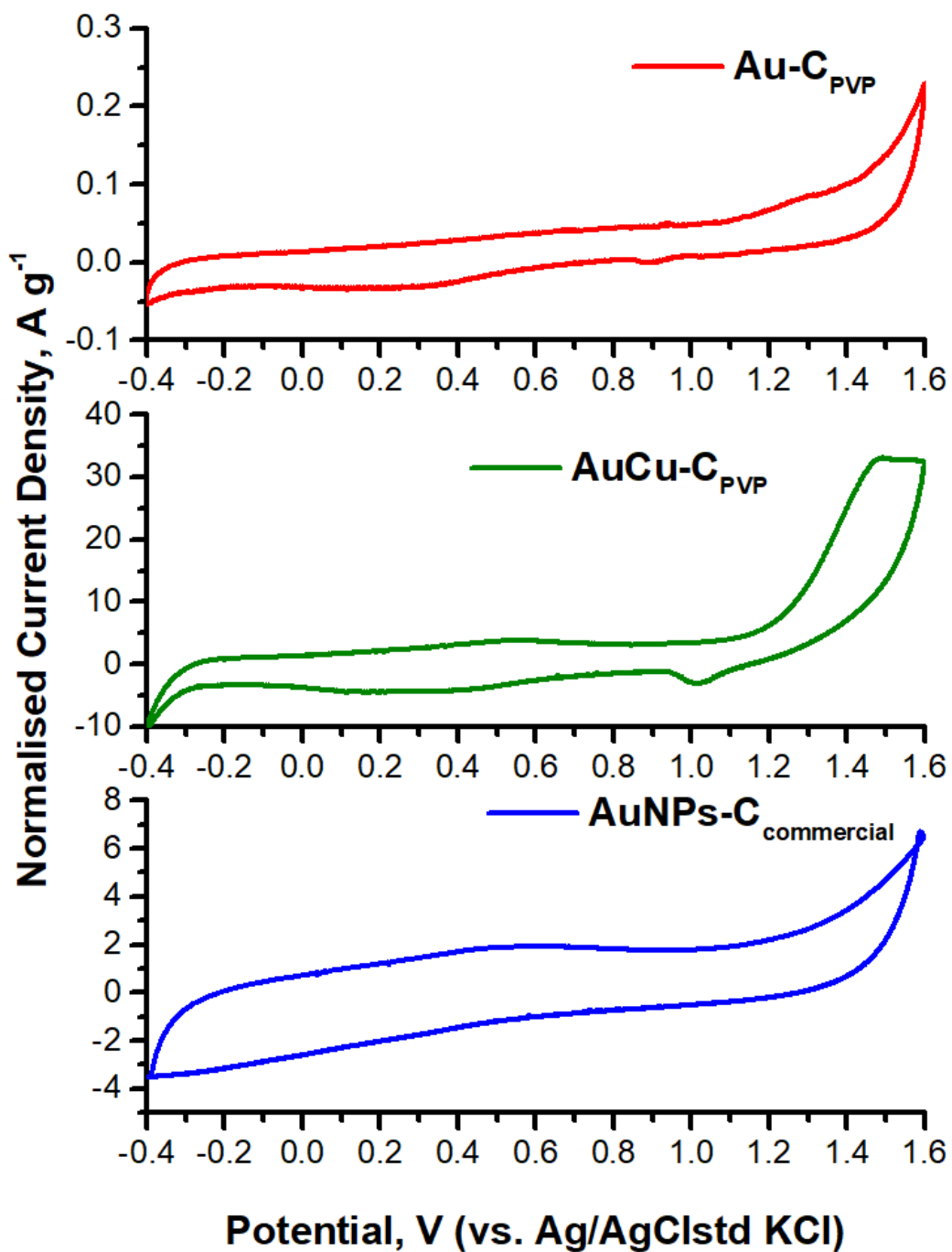
Figure 7.9: Catalyst loading weight normalized CV profile for Au-C$_{PVP(87.6\ wt.\%)}$, AuNPs-C$_{commercial(20\ wt.\%)}$ (30th cycle) and AuCu- C$_{PVP(45\ wt.\%)}$ (50th cycle) for 0.5 M H$_2$SO$_4$ solution + 0.5 M HCOOH solution at a scan rate of 50 mVs^{-1}

In the synthesis strategy route for Pd and Au catalysts, where PVP is used as the stabiliser in preparation, a unique morphology and structure is achieved. The PVP stabilises the metal nanoparticles (Au, Cu, Pd) as single particles in solution and avoids

any recrystallisation and agglomeration. This is because a thin layer of PVP capped on the surface of metal particles, creates bonds between the metal and oxygen species (O) for improved dispersion and greater anchorage on the carbon support. In the morphology of the as-prepared nanoparticles, there is a significant zigzag feature on the exterior of the as-prepared PVP stabiliser for $Au-C_{PVP(87.6wt.\%)}$, $AuCu-C_{PVP(45wt.\%)}$ and $Pd-C_{PVP(43.5wt.\%)}$, less significant in $AuNPs-C_{Commercial(20wt.\%)}$ and $Pd-C_{H3BO3 + NH4F(21wt.\%)}$ nanocatalysts, demonstrating the presence of high density of atomic defects. The energy efficient low-temperature reduction as opposes to a higher temperature ($>120\ ^oC$) that leads to aggregation, may be the cause of the unique edges and the well dispersed and narrow distribution of $Pd-C_{PVP}$ (1.4 nm), $AuCu-C_{PVP}$ (1.4 nm), $Au-C_{PVP}$ (5.3 nm) and 4.4 nm for the $Pd-C_{H3BO3 + NH4F}$ nanocatalysts.

7.5.1 The influence of physicochemical properties on the electrochemical activities of the catalysts

The physicochemical properties such as the high roughness of the Pd nanoparticle surface (see Table 7.5), the existence of several crystalline facets, and the large ECSA available active sites are presumably the reasons for the increased catalytic performance. Notably, the first anodic peak showing hydrogen desorption shifts negatively in $Pd-C_{PVP}$, suggesting a weakened adsorption energy due to a lower d-band shift compared to $Pd-C_{H3BO3 + NH4F}$ electrodes. Furthermore, the TEM, SEM, and AFM images show the particle are not perfectly spherical and the defects, corners and carbon support will increase the overall ECSA determined electrochemically. This gives the enhanced electrocatalytic activity for FAO reaction and the large Pd surface site per gram of catalysts ($25.1x10^6$ for $Pd-C_{PVP}$ compared with $5.5x10^6$ for $Pd-C_{H3BO3 + NH4F}$

nanocatalysts). This confirms that the unique strategy of low temperature PVP stabiliser influences the morphology and structure of the as-prepared catalysts. The observed peak potential drops are probably due to the accumulation of intermediates on the reactive surface (blocking-site effect).

The Pd-C_{PVP} electrodes show better activity (DFAFCs region less than 0.3 V) with a very low onset potential of -0.037 V compared to Pd-$C_{H3BO3+NH4F}$ electrodes at 0.017 V. However, the Pd-$C_{H3BO3+NH4F}$ shows improved catalytic enhancement which is a factor of 1.8 fhigher with an average mass activity of 97.1 mA g^{-1}Pd (I_f/I_b = 5.5) compared to 53.9 mA g^{-1}Pd (I_f/I_b = 5.5) for Pd-C_{PVP} electrodes (see Figure 5.14). This result indicates that the large negative onset potential shift which occurs in both Pd-C_{PVP} and Pd-$C_{H3BO3 + NH4F}$ electrodes, proceeds mainly by the dehydrogenation (direct) oxidation pathway, defeating the CO poisoning (indirect) at a higher potential [128]. The high turnover rates and the dehydrogenation (CO-free) pathway for formic acid oxidation on Au catalysts are confirmed by previous reports [331]. The increase in oxidation results from an increase in the active surface area (ECSA) of catalysts and crystallographic properties, depending on the preferential crystal facets, especially the highly reactive Pd (100) and Au (111) planes [291].

It can be seen that the position of the main anodic peaks potentials that improved the performance activity of Au-C_{PVP} and AuCu-C_{PVP} are at 1.29 V and 1.49 V with a corresponding current density of 0.147 mA cm^{-2} and 25.8 mA cm^{-2}, respectively (see Figure 7.9). The peak potential is lower by about 200 mV but occurs at higher current densities in AuCu-C_{PVP} catalysts. This indicates that the decrease of oxidation of formic acid is apparently due to PdO and AuO formation and their subsequent removal in the

reserve sweep [332-334]. The mass activity of the catalysts demonstrated that the Pd-C catalysts exhibited higher activities (53.9 mA g^{-1} for Pd-C$_{PVP}$ and 97.1 mA g^{-1} for Pd-C$_{H3BO3 + NH4F}$) than the Au and Au-based catalysts. For Au and Au based catalysts, the mass activities increase in the order of AuCu-C$_{PVP}$ > AuNPs-C$_{commercial}$ > Au-C$_{PVP}$, confirming the excellent activity of bimetallic AuCu-C$_{PVP}$ (61.8 mA g^{-1}) [103, 114, 319]. In agreement with an earlier report, it has been confirmed that FAO does not depend on the mass-transport conditions, irrespective of the scan rate. The peak region (1.2-1.6 V) was consistent with the FAO profile of Au-C$_{PVP}$ unlike the AuNPs-C$_{commercial}$ catalyst kinetics [150, 266]. In their report, Beltramo *et al.* (2005), confirmed that there was no evidence for CO formation on gold during formic acid oxidation, using in-situ SERs, first-principle DFT calculations and differential electrochemical mass spectroscopy. The electrocatalytic properties of Au-C$_{PVP(87.6wt.\%)}$ and AuCu-C$_{PVP(45wt.\%)}$ core-shell catalysts strongly influenced the kinetics due to their sensitivity to environmental changes in the reaction phase. Their unusual shape could bring different, special contributions to the electron transfer processes because of their morphology and structure. These findings make gold and gold-based nanocatalysts excellent candidates for the fabrication of energy storage devices, fuel cells and the electrochemical sensors.

As shown in Table 7.3, AuCu-C$_{PVP}$ exhibited the largest mass activity under the operating conditions used, which confirming the very high electrocatalytic activity. This result is consistent with the physical characterisations from TEM, XRD and CV measurements. The enhanced the catalytic activity of AuCu-C$_{PVP(45wt.\%)}$ catalyst for formic acid electrooxidation could be due to the electronic effect of Cu and Au. Another reason could be due to zero valent Au gaining *d*-electron, which improving the removal of absorbed intermediate species on the catalyst active site. Ren and co-workers recently confirmed that the copper content within Pd-shell Cu-core catalysts increases lattice

strain in nanocrystals, thus leading to a downshift of the *d*-band centre with an overall

improved catalytic performance [114].

Table 7.3: Comparative summary of performance parameters for Au based and Pd catalysts

Parameters	AuCu-C_{PVP}	Au-C_{PVP}	AuNPs-$C_{commercial}$	Pd-C_{PVP}	Pd-$C_{H3BO3 + NH4F}$
ECSA, $m^2 g^{-1}$	61.8	12.2	12.5	188.4	38.3
CSA, $m^2 g^{-1}$	357.1	58.6	62.1	357.1	113.6
Current Density, mA cm^{-2}	25.8	0.147	3.21	35.1	28.3
Specific Activity, mA m^{-2}	0.15	0.07	0.73	0.26	0.38
Mass Activity, mA g^{-1}	33.1	0.09	9.1	53.9	97.1
Roughness factor, R_f	8.83×10^6	8.71×10^6	1.79×10^6	2.69×10^7	5.54×10^6
Initial current density, mA mg^{-1}	37.1	1.7	12.6	261.1	193.1
Final current density, mA mg^{-1}	0.38	7.7×10^{-3}	9.7×10^{-4}	14.1	1.1

There is an initial, gradual decay for all catalyst types; however, the Pd-C_{PVP} catalyst

exhibits the highest initial current density and the slowest current decay compared with

electrodes of other catalysts (Pd-C_{PVP} > Pd-$C_{H3BO3 + NH4F}$ > AuCu-C_{PVP} > Au-C_{PVP} >

AuNPs-$C_{commercial}$) (see Figure 7.10). The observed oxidation current densities for the

catalysts demonstrated that the catalytic activities for formic acid oxidation. The initial

and final or residual current densities after 5000 seconds are present in Table 7.3.
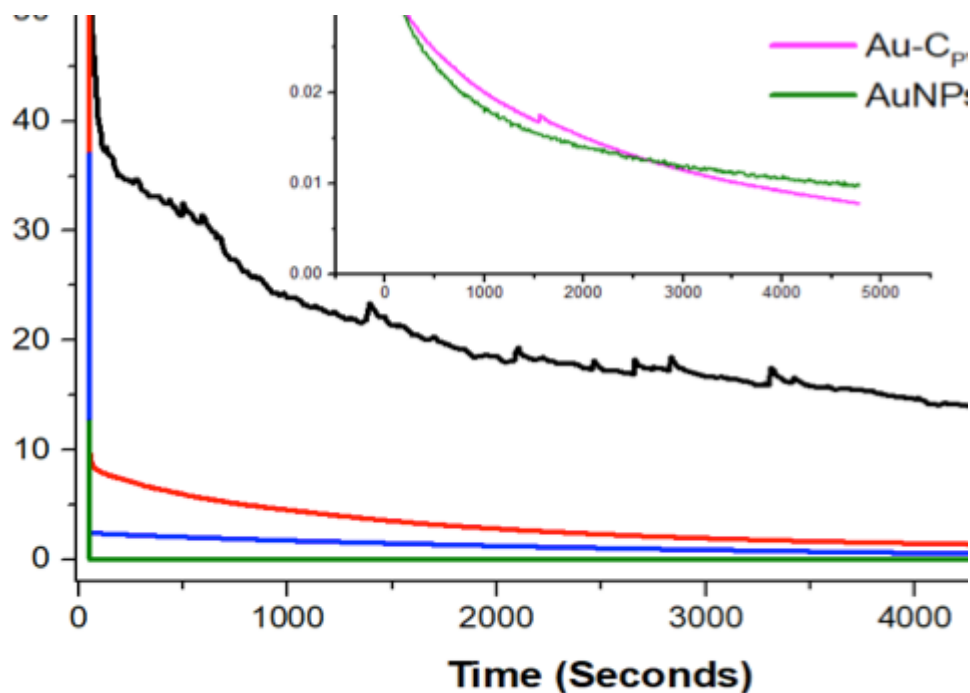
Figure 7.10: Comparison of chronoamperometry experiment for 5000 seconds at 0.6 V of AuCu-C$_{PVP(45wt.\%)}$, Au-C$_{PVP(87.6wt.\%)}$, AuNPs-C$_{commercial(20wt.\%)}$, Pd-C$_{PVP(43.5wt.\%)}$, and Pd-C$_{H3BO3\ +\ NH4F(21wt.\%)}$ catalysts in 0.5 M HCOOH + 0.5 M H$_2$SO$_4$ solution

The stability of Pd-C$_{PVP}$ is ascribed to the polyvinylpyrrolidone stabiliser as a polar soluble polymer, capping the nanoparticles to produce the unique outer surface structure for effective reactions. Pd-C$_{PVP}$ showed superior overall catalytic activity because the PVP stabiliser aided nanoparticle anchorage and ease of removal with no contamination or blocking of the active site compared to the boric acid-ammonium fluoride route for electrooxidation processes [275]. This demonstrates the superb electrochemical durability of the AuCu-C$_{PVP(45wt.\%)}$ nanoparticles in long-term stability tests. The results confirm the existence of the electronic coupling between the Au (shell) and Cu (core) structure, compared to the Au monometallic catalysts. The high surface-to-volume ratio and the contact between the core and shell configuration contributed to the enhanced electrocatalytic activity. AuCu-C$_{PVP(45wt.\%)}$ nanoparticles do not exhibit poor long-term stability because of dissolution of non-noble metals [186].

The higher activity of Pd catalysts may be due to the standard attributes of palladium or platinum-transition metals, which are active as larger particles and even as single macroscopic crystals. Also, the low melting point of Pd as compared with Au makes it a challenging task to achieve small particle sizes [335]. More investigation is still required to ascertain the exact mechanism of gold and gold bimetallic catalysts for formic acid oxidation.

Chapter 8   Conclusions and Future work

8.1   Conclusions

Gold-copper core-shell nanoparticles can serve as highly active catalysts for the formic acid electrooxidation reaction. This thesis aimed to understand the catalysts synthesis strategy, microstructure and electrochemical properties of the prepared catalysts to be used in direct formic acid fuel cell applications.

- A one-pot sodium borohydride reduction room temperature synthesis was used for the as-prepared catalysts in the presence of a polyvinylpyrrolidone stabiliser. The addition of a high concentration of hydroxyl ions suppressed hydrogen evolution, enabling an environmentally friendly synthesis procedure. The new synthesis route generated unique morphology-tunable catalysts with higher electrochemical activities for formic acid oxidation. The performance and stability of the PVP-stabilised catalyst enhanced the catalytic properties. This was attributed to the effect of PVP capping the nanoparticles and the specific structure that promotes fast oxidation of absorbed intermediate species.

- Pd-C$_{H3BO3 + NH4F}$ catalysts demonstrated superior electrocatalytic activity for formic acid oxidation with an activity 1.8 times higher than Pd-C$_{PVP}$. The physical characterisation determined by XRD, TEM, SEM and AFM confirmed the modified structural properties of Pd-C$_{PVP}$ catalysts as demonstrated with the high mass activity of 97.1 mA mg^{-1} for Pd-C$_{H3BO3 + NH4F}$ compared to 53.9 mA

mg^{-1} for Pd-C$_{PVP}$. From the mass activity of the catalysts, Pd-C$_{PVP}$ showed a superior performance of over 44.5% for formic acid electrooxidation reactions compared to Pd-C$_{PVP}$ catalysts. Results suggest that the controlled morphologies/nanostructures of Pd-C$_{PVP}$ as a robust anodic catalyst will play a significant role in catalyst cost (less material use due to small particle size) and utilisation for practical DFAFCs technology.

- The Au-C$_{PVP(87.6wt.\%)}$ catalysts provided a higher ECSA for electrocatalytic activity than AuNPs-C$_{commercial}$, showing a lower onset potential, with a well characterised Au electrooxidation profile, with all characteristic peaks on both the anodic and cathodic sweeps. The specific synthesis route led to apparent changes in the morphology with corners and defective edges for better Au particle anchorage and reactivity. Au-C$_{PVP(87.6wt.\%)}$ catalysts possess high formic acid tolerance and are considered suitable for DFAFC electrooxidation. The insights gained through this study will serve as a foundation for the formulation and preparation of better catalysts for FAO, especially bimetallic catalysts owing to their synergistic geometric and electronic properties.

- A gold-copper catalyst on a carbon support with high performance and stability, in acid medium was prepared by a one-pot sodium borohydride-polyvinylpyrrolidone synthesis. The electrooxidation of the catalyst showed 72% higher activity for formic acid oxidation than a commercial gold nanoparticle catalyst. The improved catalytic performance was attributed to the electronic synergistic effect of copper and specific gold structure, promoting oxidation of adsorbed intermediate species. The enhanced electrochemical

190

activity was attributed to the formation of a core-shell structure, which results in an increased coordination of unsaturated Au and Cu for small molecule hydrocarbons. Also, the Cu content improved the absorption strength between active sites and the adsorbate on the catalysts. The use of PVP stabiliser showed sufficient coverage of Cu nanoparticles, which aided in the anchorage of the Au shell on the Cu-PVP. It is reasonable to conclude that Au reduced preferentially and covered the PVP-protected Cu particles rather than the carbon because of the stronger metal interaction. The highly reproducible and superior FAO performance, together with ease of incorporation into existing fuel cell membranes, make it an attractive candidate for actual fuel applications. However, gold-based catalysts show promise in the elimination of the formation of poisonous species (e.g. low onset potential) and demonstrate enhanced activity compared to Pd catalysts. Both Pd synthesis routes showed higher mass activities for formic acid electrooxidation in this current work.

- Compared with the XRD reflection for Au-C catalysts, the diffraction planes of AuCu-C$_{PVP(45wt.\%)}$ catalysts shifted to higher angles due to the presence of Cu. For example, Au-C$_{PVP}$ (200) shifted from 44.62° to lower 44.18° because of the lattice contraction between metals with different lattice spacing, indicating the reason for the marked decrease in the mean d-spacing and indicating the absence of alloy or bimetallic bond structure. Furthermore, the formation of individual Au and Cu nanoparticles formation was ruled out, as the X-ray scattering of the physical mixtures would have exhibited completely different XRD patterns. The EDS results suggested the formation of on AuCu-C$_{PVP(45wt.\%)}$ core-shell particles, which is in fairly good agreement with the XRD core-shell structure evaluation.

The EDS elemental mapping confirmed the presence of Au and Cu dispersed on a carbon support. The electrochemical evaluation of the AuCu-C$_{PVP(45wt.\%)}$ catalyst shows a 98.7% higher activity for formic acid oxidation compared to Au-C$_{PVP(87.6wt.\%)}$ catalyst. The stability test of the AuCu-C$_{PVP(45wt.\%)}$ catalysts showed better resistance to poisoning, particularly due to its unique structure and ease of removal with no contamination or blocking of the active sites.

8.2 Suggestions for future work

8.2.1 Validation of synthesis route and application in battery technology

Preliminary results show great promise for gold-based catalysts in possible Nickel-iron battery applications. The synthesis route developed for a core-shell bimetallic catalyst is validated, although detailed analytical and physicochemical characterisation is still required to confirm its physical structure and electrochemical performance. Figure 8.1 shows the crystal phases of the AuPd-C core-shell structure and the Au-C$_{PVP(87.6wt.\%)}$ using XRD analysis. The electrochemical stability of the AuPd-C$_{PVP}$ catalyst after 250 cycles demonstrates strong stability and improved performance in an alkaline medium (see Figure 8.2).
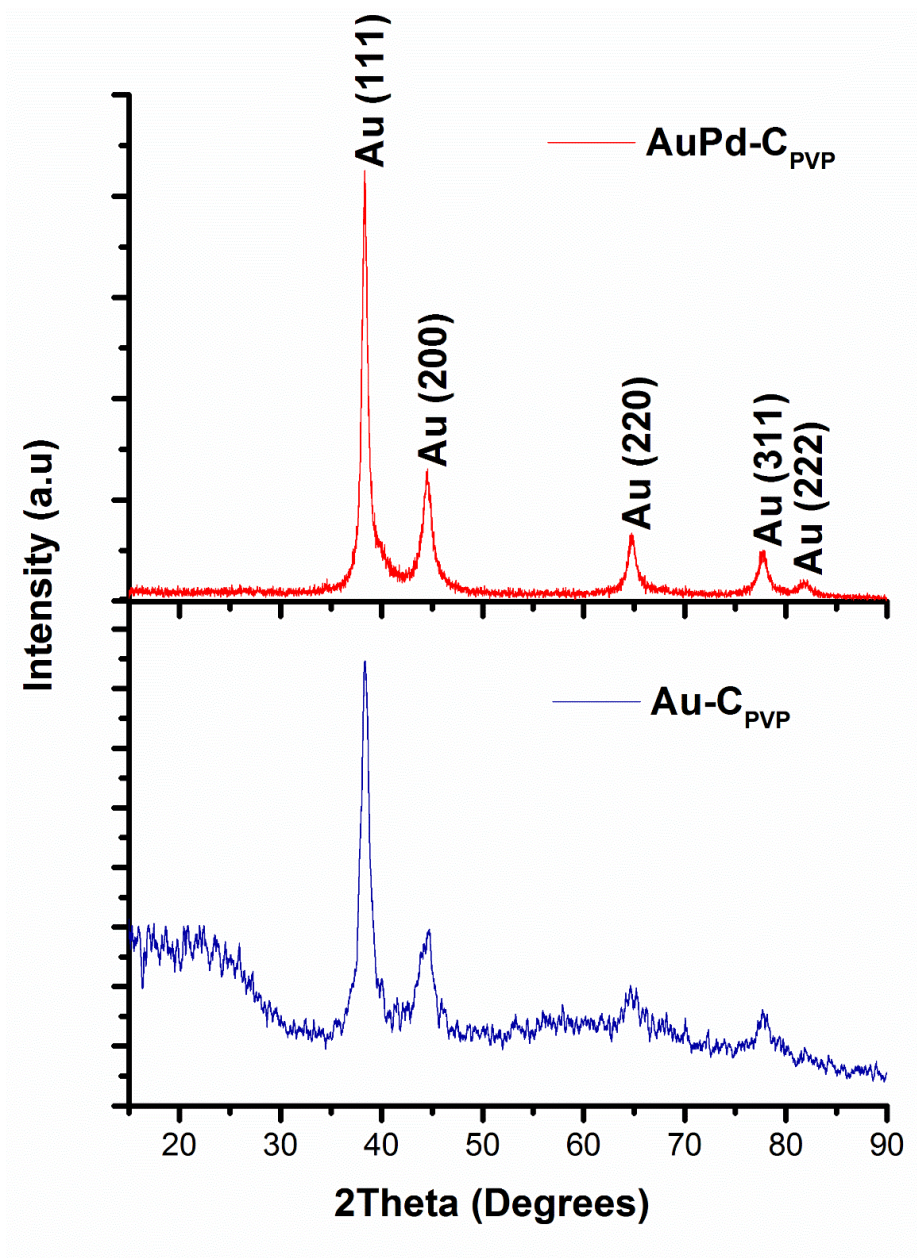
Figure 8.1: Comparison of the XRD patterns of Au-C$_{PVP}$ and AuPd-C$_{PVP}$ catalysts.
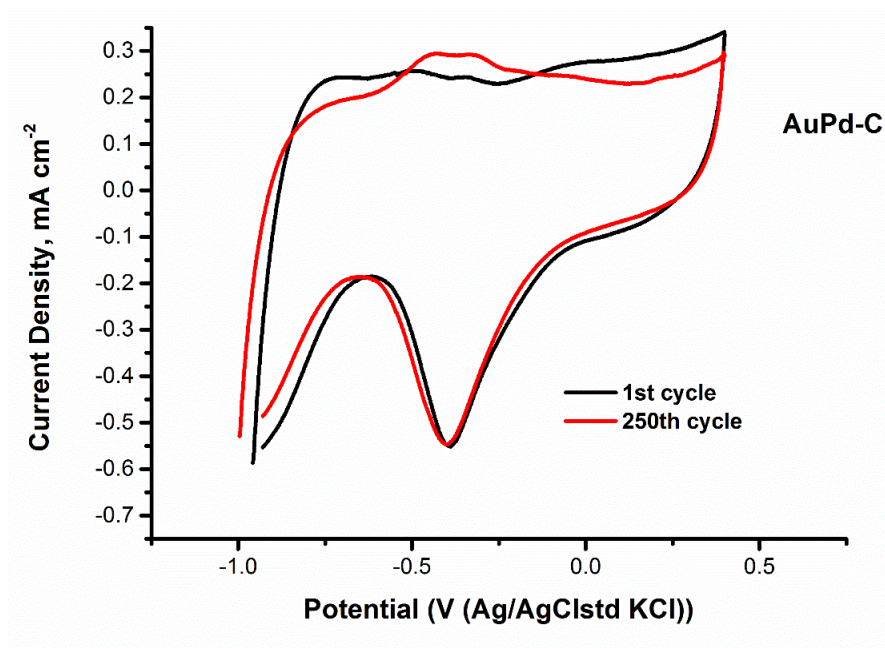
Figure 8.2: Cyclic Voltammogram of AuPd- C_{PVP} for 1 M KOH electrolyte at a scan rate of 50 mV s^{-1}, 25 ^{o}C (1st and 250th cycle)

8.2.2 To investigate the mechanism and electrode kinetics of as-prepared catalysts
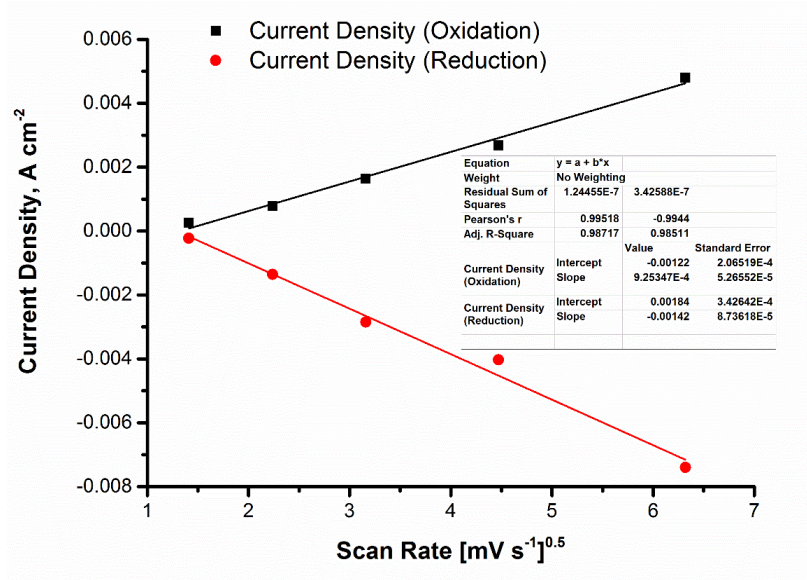
Figure 8.3: The plot of peak current density vs. the square root of scan rates for 0.5M HCOOH containing 0.5M H$_2$SO$_4$ solution at the AuCu-C_{PVP} catalyst electrode.

The Randles-Sevcik plot (see Equation 3.1) shows a linear plot, indicative of a fast electron transfer process for both oxidation and reduction scan directions (see Figure 8.3). The evaluation of the diffusion coefficient D from the slope is 3.44 x10^{-5} cm s^{-1}, suggesting that the charge-transport rate within the liquid film, near the electrode surface, is fast and consequently gives a higher standard rate constant. The preliminary results show AuCu catalyst would be electro-catalytically activities and investigation of the mechanism is vital in understanding the kinetic behaviour in acid medium. In-situ SERs and differential function theory (DFT) analysis would elucidate the surface-bonded intermediate (HCOO$_{ad}$, COOH) during oxidation.

8.2.3 Investigation of the bifunctional-surface model using quantum-chemical analysis

To gain insight into bimetallic catalysed electrochemical oxidation reactions experimental studies can be combined with DFT calculations, which enable consideration of the pivotal role of the oxygen, adsorbed species on the metal surfaces and aiming to correlate this with the catalytic activity. Bimetallic catalysts have been proven to increase catalytic activity on the basis of the bifunctionality surface model. However, alloyed catalysts have shown to be unstable, owing to the alloying components leaching under electrochemical conditions, resulting in surface rich noble metals.

REFERENCES

[1] IEA. Key World Energy Statistics 2016 (KWES). 2016.
[2] Olah GA. After Oil and Gas: Methanol Economy. Catalysis Letters. 2004;93:1-2.
[3] Boudghene Stambouli A, Traversa E. Fuel cells, an alternative to standard sources of energy. Renewable and Sustainable Energy Reviews. 2002;6:295-304.
[4] Haan JL. Electrochemistry of formic acid and carbon dioxide on metal electrodes with applications to fuel cells and carbon dioxide conversion devices. Thesis, University of Illinois at Urbana-Champaign. 2010.
[5] Badwal S, Giddey S, Munnings C, Bhatt A, Hollenkamp A. Emerging electrochemical energy conversion and storage technologies. Frontiers in Chemistry. 2014;2:1-28.
[6] Stambouli AB. Fuel cells: The expectations for an environmental-friendly and sustainable source of energy. Renewable and Sustainable Energy Reviews. 2011;15:4507-20.
[7] Ter-Gazarian AG. Energy Storage for Power Systems: Institution of Engineering and Technology; 2011.
[8] Ha S, Adams B, Masel RI. A miniature air breathing direct formic acid fuel cell. Journal of Power Sources. 2004;128:119-24.
[9] Sanborn Scott D. Electrochemical technologies: At the summit of civilization's energy conversion and storage evolution – Where they will stay. International Journal of Hydrogen Energy. 2011;36:9401-4.
[10] Hur JI, Kim C-J. Miniature fuel-cell system complete with on-demand fuel and oxidant supply. Journal of Power Sources. 2015;274:916-21.
[11] Kirubakaran A, Jain S, Nema RK. A review on fuel cell technologies and power electronic interface. Renewable and Sustainable Energy Reviews. 2009;13:2430-40.
[12] Bonifácio, Almir O. N, L M. High Performance Carbon Supported Palladium Catalyst in Anodes of Proton Exchange Membrane Fuel Cell. Int J Electrochem Sci, . 2013;8:159 - 67.
[13] Aslam NM, Masdar MS, Kamarudin SK, Daud WRW. Overview on Direct Formic Acid Fuel Cells (DFAFCs) as an Energy Sources. APCBEE Procedia. 2012;3:33-9.
[14] Wee J-H. Contribution of fuel cell systems to CO2 emission reduction in their application fields. Renewable and Sustainable Energy Reviews. 2010;14:735-44.
[15] Haseli Y, Naterer GF, Dincer I. Comparative assessment of greenhouse gas mitigation of hydrogen passenger trains. International Journal of Hydrogen Energy. 2008;33:1788-96.
[16] Biella, Francesca Porta, Laura Prati, Rossi M. Surfactant-protected gold particles: new challenge for gold-on-carbon catalysts. Catalysis Letters. 2003;90:23-9.
[17] Shao Y, Liu J, Wang Y, Lin Y. Novel catalyst support materials for PEM fuel cells: current status and future prospects. Journal of Materials Chemistry. 2009;19:46.
[18] Zhang Q, Yue R, Jiang F, Wang H, Zhai C, Yang P, et al. Au as an efficient promoter for electrocatalytic oxidation of formic acid and carbon monoxide: a comparison between Pt-on-Au and PtAu alloy catalysts. Gold Bulletin. 2013;46:175-84.

[19] Zhang Y, Weaver MJ. Application of surface-enhanced Raman spectroscopy to organic electrocatalytic systems: decomposition and electrooxidation of methanol and formic acid on gold and platinum-film electrodes. Langmuir. 1993;9:1397-403.

[20] Andújar JM, Segura F. Fuel cells: History and updating. A walk along two centuries. Renewable and Sustainable Energy Reviews. 2009;13:2309-22.

[21] Zhang, Shao Y, Yin G, Lin Y. Recent progress in nanostructured electrocatalysts for PEM fuel cells. Journal of Materials Chemistry A. 2013;1:4631.

[22] Yu X, Pickup PG. Recent advances in direct formic acid fuel cells (DFAFC). Journal of Power Sources. 2008;182:124-32.

[23] Rice C, Ha S, Masel RI, Waszczuk P, Wieckowski A, Barnard T. Direct formic acid fuel cells. Journal of Power Sources. 2002;111:83-9.

[24] Choi S-I, Herron JA, Scaranto J, Huang H, Wang Y, Xia X, et al. A Comprehensive Study of Formic Acid Oxidation on Palladium Nanocrystals with Different Types of Facets and Twin Defects. ChemCatChem. 2015;7:2077-84.

[25] Léger J-M. Mechanistic aspects of methanol oxidation on platinum-based electrocatalysts. Journal of Applied Electrochemistry. 2001;31:767-71.

[26] Spiegel CS. Designing & Building Fuel Cells. New York: McGraw Hill; 2007.

[27] Kamarudin SK, Daud WRW, Ho SL, Hasran UA. Overview on the challenges and developments of micro-direct methanol fuel cells (DMFC). Journal of Power Sources. 2007;163:743-54.

[28] Ghosh S, Raj C. Pt-Pd nanoelectrocatalyst of ultralow Pt content for the oxidation of formic acid: Towards tuning the reaction pathway. J Chem Sci. 2015;127:949-57.

[29] Ouellette D, Cruickshank CA, Matida E. Experimental Investigation on the Performance of a Formic Acid Electrolyte-Direct Methanol Fuel Cell. Journal of Fuel Cell Science and Technology. 2013;11:021003-.

[30] Fang Y-L, Miller JT, Guo N, Heck KN, Alvarez PJJ, Wong MS. Structural analysis of palladium-decorated gold nanoparticles as colloidal bimetallic catalysts. Catalysis Today. 2011;160:96-102.

[31] Matsumoto F, Chandrani Roychowdhury, Francis J. DiSalvo z, Abruña aHcD. Electrocatalytic Activity of Ordered Intermetallic PtPb Nanoparticles Prepared by Borohydride Reduction toward Formic Acid Oxidation. Journal of The Electrochemical Society,. 2008;155 B148-B54

[32] Wilde CP, Zhang M. Profiles of adsorption during the oxidation of small organic molecules: oxidation of formic acid at polycrystalline Pt in acid solutions. Journal of the Chemical Society, Faraday Transactions. 1994;90:1233-40.

[33] Jeong K-J, Miesse CM, Choi J-H, Lee J, Han J, Yoon SP, et al. Fuel crossover in direct formic acid fuel cells. Journal of Power Sources. 2007;168:119-25.

[34] Rice C. Catalysts for direct formic acid fuel cells. Journal of Power Sources. 2003;115:229-35.

[35] Wang X, Hu J-M, Hsing IM. Electrochemical investigation of formic acid electro-oxidation and its crossover through a Nafion® membrane. Journal of Electroanalytical Chemistry. 2004;562:73-80.

[36] Uhm S, Lee HJ, Lee J. Understanding underlying processes in formic acid fuel cells. Phys Chem Chem Phys. 2009;11:9326-36.

[37] Moret S, Dyson PJ, Laurenczy G. Direct synthesis of formic acid from carbon dioxide by hydrogenation in acidic media. Nat Commun. 2014;5.

[38] Zhu Y, Ha SY, Masel RI. High power density direct formic acid fuel cells. Journal of Power Sources. 2004;130:8-14.

[39] Baik SM, Han J, Kim J, Kwon Y. Effect of deactivation and reactivation of palladium anode catalyst on performance of direct formic acid fuel cell (DFAFC). International Journal of Hydrogen Energy. 2011;36:14719-24.

[40] Cheng TT, Gyenge EL. Novel catalyst-support interaction for direct formic acid fuel cell anodes: Pd electrodeposition on surface-modified graphite felt. Journal of Applied Electrochemistry. 2009;39:1925-38.

[41] Kim J, Yu J, Lee H, Kim J, Kim Y, Han J, et al. Effect of temperature, oxidant and catalyst loading on the performance of direct formic acid fuel cell. Korean Journal of Chemical Engineering. 2005;22:661-5.

[42] Ha S, Larsen R, Masel RI. Performance characterization of Pd/C nanocatalyst for direct formic acid fuel cells. Journal of Power Sources. 2005;144:28-34.

[43] Pan Y, Zhang R, Blair SL. Anode Poisoning Study in Direct Formic Acid Fuel Cells. Electrochemical and Solid-State Letters. 2009;12:B23-B6.

[44] Larsen R, Ha S, Zakzeski J, Masel RI. Unusually active palladium-based catalysts for the electrooxidation of formic acid. Journal of Power Sources. 2006;157:78-84.

[45] Qi Z, Kaufman A. Open circuit voltage and methanol crossover in DMFCs. Journal of Power Sources. 2002;110:177-85.

[46] Rees NV, Compton RG. Sustainable energy: a review of formic acid electrochemical fuel cells. Journal of Solid State Electrochemistry. 2011;15:2095-100.

[47] Larminie JaD, A. Fuel Cell Systems explained. Second ed. West Sussex: John Wiley & Sons Ltd; 2009.

[48] Tibdewal S, Saxena Ua, Gurumoorthy AVP. Hydrogen economy vs. methanol economy. international Journal of Chemical Sciences. 2014;12:1478-86.

[49] Ghosh TK, Prelas MA. Energy Resources and Systems

Volume 2: Renewable Resources. London: Springer; 2011.

[50] Yilanci A, Dincer I, Ozturk HK. A review on solar-hydrogen/fuel cell hybrid energy systems for stationary applications. Progress in Energy and Combustion Science. 2009;35:231-44.

[51] Jeong I, Kim J, Pak S, Nam SW, Moon I. Optimum operating strategies for liquid-fed direct methanol fuel cells. Journal of Power Sources. 2008;185:828-37.

[52] Methanol-Institute. Methanol Safe Handling Manual. 2013.

[53] Methanol-Institute. Methanol Gasoline Blends. 2016.

[54] Iwasita T. Electrocatalysis of methanol oxidation. Electrochimica Acta. 2002;47:3663-74.

[55] Pojanavaraphan C, Luengnaruemitchai A, Gulari E. Effect of support composition and metal loading on Au catalyst activity in steam reforming of methanol. International Journal of Hydrogen Energy. 2012;37:14072-84.

[56] Srinivasan S. Fuel Cells From Fundamentals to Applications. New York: Springer Science and Business Media, LLC; 2006.

[57] Hamnett A. Mechanism and electrocatalysis in the direct methanol fuel cell. Catalysis Today. 1997;38:445-57.

[58] Liu Z, Hong L, Tham MP, Lim TH, Jiang H. Nanostructured Pt/C and Pd/C catalysts for direct formic acid fuel cells. Journal of Power Sources. 2006;161:831-5.

[59] Batista EA, Malpass GRP, Motheo AJ, Iwasita T. New mechanistic aspects of methanol oxidation. Journal of Electroanalytical Chemistry. 2004;571:273-82.

[60] Li Z, Li M, Han M, Zeng J, Li Y, Guo Y, et al. Preparation and characterization of carbon-supported PtOs electrocatalysts via polyol reduction method for methanol oxidation reaction. Journal of Power Sources. 2014;268:824-30.

[61] Teliz E, Díaz V, Pérez I, Corengia M, Zinola CF. Carbon supported Pt, Ru and Mo catalysts for methanol electrooxidation. International Journal of Hydrogen Energy. 2012;37:14761-8.

[62] Liao S, Holmes K-A, Tsaprailis H, Birss VI. High Performance PtRuIr Catalysts Supported on Carbon Nanotubes for the Anodic Oxidation of Methanol. Journal of the American Chemical Society. 2006;128:3504-5.

[63] Choi J-H, Jeong K-J, Dong Y, Han J, Lim T-H, Lee J-S, et al. Electro-oxidation of methanol and formic acid on PtRu and PtAu for direct liquid fuel cells. Journal of Power Sources. 2006;163:71-5.

[64] Long NV, Ohtaki M, Hien TD, Randy J, Nogami M. A comparative study of Pt and Pt–Pd core–shell nanocatalysts. Electrochimica Acta. 2011;56:9133-43.

[65] Han SD, Choi JH, Noh SY, Park K, Yoon SK, Rhee YW. Performance characterization of direct formic acid fuel cell using porous carbon-supported palladium anode catalysts. Korean Journal of Chemical Engineering. 2010;26:1040-6.

[66] Viva FA. Studies on Direct Methanol, Formic Acid and Related Fuel Cells in Conjunction with the Electrochemical Reduction of Carbon dioxide, Chemistry, University of Southern California, Los Angeles 2009.

[67] Bagotski VS. Fuel Cells: Problems and Solutions. New York: John Wiley and Sons Inc; 2012.

[68] Dai L, Zou S. Enhanced formic acid oxidation on Cu-Pd nanoparticles. Journal of Power Sources. 2011;196:9369-72.

[69] Hu, Scudiero L, Ha S. Electronic effect on oxidation of formic acid on supported Pd–Cu bimetallic surface. Electrochimica Acta. 2012;83:354-8.

[70] Al-Akraa IM, Ahmad M. Mohammad, Mohamed S. El-Deab,Bahgat E. El-Anadouli. Development of Tailor-Designed Gold-Platinum Nanoparticles Binary Catalysts for Efficient Formic Acid Electrooxidation. Int J Electrochem Sci,. 2012;7:3939 - 46.

[71] Feng Y-Y, Zhang G-R, Xu B-Q. Catalytic Pd-on-Au nanostructures with improved Pd activity for formic acid electro-oxidation. RSC Advances. 2013;3:1748.

[72] EG&G Technical Services I. Fuel Cell Handbook. Seventh Edition ed. West Virginia: U.S. Department of Energy; 2004.

[73] An H, Cui H, Zhou D, Tao D, Li B, Zhai J, et al. Synthesis and performance of Pd/SnO2–TiO2/MWCNT catalysts for direct formic acid fuel cell application. Electrochimica Acta. 2013;92:176-82.

[74] Hong P, Liao S, Zeng J, Huang X. Design, fabrication and performance evaluation of a miniature air breathing direct formic acid fuel cell based on printed circuit board technology. Journal of Power Sources. 2010;195:7332-7.

[75] Kristian N, Yu Y, Gunawan P, Xu R, Deng W, Liu X, et al. Controlled synthesis of Pt-decorated Au nanostructure and its promoted activity toward formic acid electro-oxidation. Electrochimica Acta. 2009;54:4916-24.

[76] Lee, Jeon H, Uhm S, Lee J. Influence of underpotentially deposited Sb onto Pt anode surface on the performance of direct formic acid fuel cells. Electrochimica Acta. 2008;53:6089-92.

[77] Sáez A, Expósito E, Solla-Gullón J, Montiel V, Aldaz A. Bismuth-modified carbon supported Pt nanoparticles as electrocatalysts for direct formic acid fuel cells. Electrochimica Acta. 2012;63:105-11.

[78] Simonov AN, Simonov PA, Parmon VN. Formic acid electrooxidation over carbon-supported nanoparticles of non-stoichiometric palladium carbide. Journal of Power Sources. 2012;217:291-5.

[79] Yu X, Pickup PG. Codeposited PtSb/C catalysts for direct formic acid fuel cells. Journal of Power Sources. 2011;196:7951-6.

[80] Zhang L, Tang Y, Bao J, Lu T, Li C. A carbon-supported Pd-P catalyst as the anodic catalyst in a direct formic acid fuel cell. Journal of Power Sources. 2006;162:177-9.

[81] Wang Y, Wu B, Gao Y, Tang Y, Lu T, Xing W, et al. Kinetic study of formic acid oxidation on carbon supported Pd electrocatalyst. Journal of Power Sources. 2009;192:372-5.

[82] Cuesta A, Cabello G, Osawa M, Gutiérrez C. Mechanism of the Electrocatalytic Oxidation of Formic Acid on Metals. ACS Catalysis. 2012;2:728-38.

[83] Liu Y, Wang Y, Deng C, Wu B, Gao Y. Kinetic study of formic acid oxidation on carbon supported platinum electrocatalyst. Electrochemistry. 2010;78:662-5.

[84] Lu G-Q, Crown A, Wieckowski A. Formic Acid Decomposition on Polycrystalline Platinum and Palladized Platinum Electrodes. The Journal of Physical Chemistry B. 1999;103:9700-11.

[85] Miyake H, Okada T, Samjeske G, Osawa M. Formic acid electrooxidation on Pd in acidic solutions studied by surface-enhanced infrared absorption spectroscopy. Physical Chemistry Chemical Physics. 2008;10:3662-9.

[86] Zhou WP, Lewera A, Larsen R, Masel RI, Bagus PS, Wieckowski A. Size Effects in Electronic and Catalytic Properties of Unsupported Palladium Nanoparticles in Electrooxidation of Formic Acid. The Journal of Physical Chemistry B. 2006;110:13393-8.

[87] Liu, Wang L, Wang G, Deng C, Wu B, Gao Y. High active carbon supported PdAu catalyst for formic acid electrooxidation and study of the kinetics. Journal of Physical Chemistry C. 2010;114:21417-22.

[88] Zhang Z, Zhou X, Liu C, Xing W. The mechanism of formic acid electrooxidation on iron tetrasulfophthalocyanine-modified platinum electrode. Electrochemistry Communications. 2008;10:131-5.

[89] Dai L. Functionalization of Graphene for Efficient Energy Conversion and Storage. Accounts of Chemical Research. 2012;46:31-42.

[90] Williams M, Horita T, Yamagi K, Sakai N, Yokokawa H. Basic Electrochemical Thermodynamic Studies of Fuel Cells Using MALT2. Journal of Fuel Cell Science and Technology. 2009;6:021301-.

[91] Meng H, Zeng D, Xie F. Recent Development of Pd-Based Electrocatalysts for Proton Exchange Membrane Fuel Cells. Catalysts. 2015;5:1221.

[92] Cao, Song L, Tang J, Xu J, Wang W, Chen Z. Enhanced activity of Pd nanoparticles supported on Vulcan XC72R carbon pretreated via a modified Hummers method for formic acid electrooxidation. Applied Surface Science. 2013;274:138-43.

[93] Perego C, Villa P. Catalyst preparation methods. Catalysis Today. 1997;34:281-305.

[94] Sanders IJ, Peeten TL. Carbon Black: Production, Properties, and Uses: Nova Science Publishers; 2011.

[95] Bevilacqua M, Bianchini C, Marchionni A, Filippi J, Lavacchi A, Miller H, et al. Improvement in the efficiency of an OrganoMetallic Fuel Cell by tuning the molecular architecture of the anode electrocatalyst and the nature of the carbon support. Energy & Environmental Science. 2012;5:8608-20.

[96] Wu B, Hu D, Kuang Y, Liu B, Zhang X, Chen J. Functionalization of Carbon Nanotubes by an Ionic-Liquid Polymer: Dispersion of Pt and PtRu Nanoparticles on Carbon Nanotubes and Their Electrocatalytic Oxidation of Methanol. Angewandte Chemie International Edition. 2009;48:4751-4.

[97] Soo LT, Loh KS, Mohamad AB, Daud WRW, Wong WY. An overview of the electrochemical performance of modified graphene used as an electrocatalyst and as a catalyst support in fuel cells. Applied Catalysis A: General. 2015;497:198-210.

[98] Lam E, Luong JHT. Carbon Materials as Catalyst Supports and Catalysts in the Transformation of Biomass to Fuels and Chemicals. ACS Catalysis. 2014;4:3393-410.

[99] Ma Z, Dai S. Development of novel supported gold catalysts: A materials perspective. Nano Research. 2010;4:3-32.

[100] Zhu Y, Jin R, Sun Y. Atomically Monodisperse Gold Nanoclusters Catalysts with Precise Core-Shell Structure. Catalysts. 2011;1:3-17.

[101] Van Bokhoven JA, Miller JT. Electronic and geometric structures of small gold metal particles: Particles size effects and the relationship to catalytic activity. 2007. p. 582-4.

[102] Ma Z, Dai S. Development of novel supported gold catalysts: A materials perspective. Nano Research. 2011;4:3-32.

[103] Redina EA, Greish AA, Mishin IV, Kapustin GI, Tkachenko OP, Kirichenko OA, et al. Selective oxidation of ethanol to acetaldehyde over Au–Cu catalysts prepared by a redox method. Catalysis Today. 2015;241, Part B:246-54.

[104] Oseghale, Abdalla AH, Posada JOG, Hall PJ. A new synthesis route for sustainable gold copper utilization in direct formic acid fuel cells. International Journal of Hydrogen Energy. 2016;41:19394-6401.

[105] Haruta M, Daté M. Advances in the catalysis of Au nanoparticles. Applied Catalysis A: General. 2001;222:427-37.

[106] Broaddus E, Wedell A, Gold SA. Formic Acid Electrooxidation by a Platinum Nanotubule Array Electrode. International Journal of Electrochemistry. 2013;2013:1-7.

[107] DandanTu, Wu B, Wang B, Deng C, Gao Y. A highly active carbon-supported PdSn catalyst for formic acid electrooxidation. Applied Catalysis B: Environmental. 2011;103:163-8.

[108] Godinez-Salomon FA-E, E ; Hallen-Lopez, M. Electrochemical study of the Pt nanoparticles size effect in the formic acid oxidation. International Journal of Electrochemical Science. 2012;7:2566-76.

[109] Guo JW, Zhao TS, Prabhuram J, Wong CW. Preparation and the physical/electrochemical properties of a Pt/C nanocatalyst stabilized by citric acid for polymer electrolyte fuel cells. Electrochimica Acta. 2005;50:1973-83.

[110] Lović JD, Tripković AV, Gojković SL, Popović KD, Tripković DV, Olszewski P, et al. Kinetic study of formic acid oxidation on carbon-supported platinum electrocatalyst. Journal of Electroanalytical Chemistry. 2005;581:294-302.

[111] Yldz Y, Pamuk H, Karatepe O, Dasdelen Z, Sen F. Carbon black hybrid material furnished monodisperse platinum nanoparticles as highly efficient and reusable electrocatalysts for formic acid electro-oxidation. RSC Advances. 2016;6:32858-62.

[112] Qiu X, Dai Y, Tang Y, Lu T, Wei S, Chen Y. One-pot synthesis of gold–palladium@palladium core–shell nanoflowers as efficient electrocatalyst for ethanol electrooxidation. Journal of Power Sources. 2015;278:430-5.

[113] Hattori M, Einaga H, Daio T, Tsuji M. Efficient hydrogen production from formic acid using TiO2-supported AgPd@Pd nanocatalysts. Journal of Materials Chemistry A. 2015;3:4453-61.

[114] Ren M, Zhou Y, Tao F, Zou Z, Akins DL, Yang H. Controllable Modification of the Electronic Structure of Carbon-Supported Core–Shell Cu@Pd Catalysts for Formic Acid Oxidation. The Journal of Physical Chemistry C. 2014;118:12669-75.

[115] Adams BD, Asmussen RM, Ostrom CK, Chen A. Synthesis and Comparative Study of Nanoporous Palladium-Based Bimetallic Catalysts for Formic Acid Oxidation. The Journal of Physical Chemistry C. 2014;118:29903-10.

[116] Baik SM, Kim J, Han J, Kwon Y. Performance improvement in direct formic acid fuel cells (DFAFCs) using metal catalyst prepared by dual mode spraying. International Journal of Hydrogen Energy. 2011;36:12583-90.

[117] Maniam K, Chetty R. Electrochemical synthesis of palladium dendrites on carbon support and their enhanced electrocatalytic activity towards formic acid oxidation. Journal of Applied Electrochemistry. 2015;45:953-62.

[118] Rezaei M, Tabaian S, Haghshenas D. The Role of Electrodeposited Pd Catalyst Loading on the Mechanisms of Formic Acid Electro-Oxidation. Electrocatalysis. 2014;5:193-203.

[119] Rice C, Ha S, Masel RI, Wieckowski A. Catalysts for direct formic acid fuel cells. Journal of Power Sources. 2003;115:229-35.

[120] Wang R, Liao S, Ji S. High performance Pd-based catalysts for oxidation of formic acid. Journal of Power Sources. 2008;180:205-8.

[121] Wang, Liu J, Liu P, Bi X, Yan X, Wang W, et al. Ultra-thin layer structured anodes for highly durable low-Pt direct formic acid fuel cells. Nano Research. 2014;7:1569-80.

[122] Wang X-M, Xia Y-Y. Synthesis, characterization and catalytic activity of an ultrafine Pd/C catalyst for formic acid electrooxidation. Electrochimica Acta. 2009;54:7525-30.

[123] Wang Y, Toshima N. Preparation of Pd–Pt Bimetallic Colloids with Controllable Core/Shell Structures. The Journal of Physical Chemistry B. 1997;101:5301-6.

[124] Wang, Yan JM, Wang HL, Ping Y, Jiang Q. Pd/C synthesized with citric acid: an efficient catalyst for hydrogen generation from formic acid/sodium formate. Sci Rep. 2012;2:598.

[125] Yu X, Pickup PG. Deactivation/reactivation of a Pd/C catalyst in a direct formic acid fuel cell (DFAFC): Use of array membrane electrode assemblies. Journal of Power Sources. 2009;187:493-9.

[126] Yu X, Pickup PG. Mechanistic study of the deactivation of carbon supported Pd during formic acid oxidation. Electrochemistry Communications. 2009;11:2012-4.

[127] Cheng H, Scott K. Selection of oxygen reduction catalysts for rechargeable lithium–air batteries—Metal or oxide? Applied Catalysis B: Environmental. 2011;108–109:140-51.

[128] Al-Akraa IM, Mohammad AM, El-Deab MS, El-Anadouli BE. Electrocatalysis by design: Synergistic catalytic enhancement of formic acid electro-oxidation at core–shell Pd/Pt nanocatalysts. International Journal of Hydrogen Energy. 2015;40:1789-94.

[129] Xin Z, Wang S, Wang J, Huang X, Ji X, Yao Y, et al. Nanosizing low-loading Pd on phosphorus-doped carbon nanotubes for enhanced HCOOH oxidation performance. Electrochemistry Communications. 2016;67:26-30.

[130] Hu S, Munoz F, Noborikawa J, Haan J, Scudiero L, Ha S. Carbon supported Pd-based bimetallic and trimetallic catalyst for formic acid electrochemical oxidation. Applied Catalysis B: Environmental. 2016;180:758-65.

[131] Haruta M. Size- and support-dependency in the catalysis of gold. Catalysis Today. 1997;36:153-66.

[132] Haruta M. Nanoparticulate Gold Catalysts for Low-Temperature CO Oxidation. Journal of New Materials for Electrochemical Systems. 2004;7:163-72.

[133] Haruta M, Kobayashi T, Sano H, Yamada N. Novel Gold Catalysts for the Oxidation of Carbon Monoxide at a Temperature far Below 0 °C. Chemistry Letters. 1987;16:405-8.

[134] Hutchings GJ, Carrettin S, Landon P, Edwards JK, Enache D, Knight DW, et al. New approaches to designing selective oxidation catalysts: Au/C a versatile catalyst. Topics in Catalysis. 2006;38:223-30.

[135] Ivanova S, Bobadilla LF, Penkova A, Sarria FR, Centeno MA, Odriozola JA. Gold Functionalized Supported Ionic Liquids Catalyst for CO Oxidation. Catalysts. 2011;1:52-68.

[136] Kuralkar M, Ingle A, Gaikwad S, Gade A, Rai M. Gold nanoparticles: novel catalyst for the preparation of direct methanol fuel cell. IET Nanobiotechnology: Institution of Engineering and Technology; 2015. p. 66-70.

[137] Freakley S, He Q, Kiely C, Hutchings G. Gold Catalysis: A Reflection on Where We are Now. Catalysis Letters. 2015;145:71-9.

[138] Lee M, Kim D. Au nanoparticles attached carbon nanotubes as a high performance active element in field effect transistor. Materials Chemistry and Physics. 2016;179:103-9.

[139] Ban Z, Barnakov YA, Li F, Golub VO, O'Connor CJ. The synthesis of core-shell iron@gold nanoparticles and their characterization. Journal of Materials Chemistry. 2005;15:4660-2.

[140] Wagers K, Chui T, Adem S. Effect of pH on the Stability of Gold Nanoparticles and Their Application for Melamine Detection in Infant Formula. 2014;7:15-20.

[141] Della Pina C, Falletta E, Rossi M. Gold catalysis in organic synthesis and material science. Catalysis: Volume 22: The Royal Society of Chemistry; 2010. p. 279-317.

[142] Feng L, Yao S, Zhao X, Yan L, Liu C, Xing W. Electrocatalytic properties of Pd/C catalyst for formic acid electrooxidation promoted by europium oxide. Journal of Power Sources. 2012;197:38-43.

[143] Kwon Y, Lai SCS, Rodriguez P, Koper MTM. Electrocatalytic Oxidation of Alcohols on Gold in Alkaline Media: Base or Gold Catalysis? Journal of the American Chemical Society. 2011;133:6914-7.

[144] Lee JK, Lee J, Han J, Lim TH, Sung YE, Tak Y. Influence of Au contents of AuPt anode catalyst on the performance of direct formic acid fuel cell. Electrochimica Acta. 2008;53:3474-8.

[145] Miao Y-X, Shi L, Sun Q, Li W-C. A highly efficient potassium-treated Au-Cu/Al2O3 catalyst for the preferential oxidation of carbon monoxide. RSC Advances. 2016;6:24603-9.

[146] Zhou N, He B, Wang X, Hu Z. Preparation and characterization of Au@TiO2 core–shell hollow nanoparticles with CO oxidation performance. Journal of Nanoparticle Research. 2014;16:1-11.

[147] Lee S-Y, Jung N, Cho J, Park H-Y, Ryu J, Jang I, et al. Surface-Rearranged Pd3Au/C Nanocatalysts by Using CO-Induced Segregation for Formic Acid Oxidation Reactions. ACS Catalysis. 2014;4:2402-8.

[148] Zhu W, Michalsky R, Metin Ö, Lv H, Guo S, Wright CJ, et al. Monodisperse Au Nanoparticles for Selective Electrocatalytic Reduction of CO2 to CO. Journal of the American Chemical Society. 2013;135:16833-6.

[149] Li X, Fang SSS, Teo J, Foo YL, Borgna A, Lin M, et al. Activation and Deactivation of Au–Cu/SBA-15 Catalyst for Preferential Oxidation of CO in H2-Rich Gas. ACS Catalysis. 2012;2:360-9.

[150] Beltramo GL, Shubina TE, Koper MTM. Oxidation of Formic Acid and Carbon Monoxide on Gold Electrodes Studied by Surface-Enhanced Raman Spectroscopy and DFT. ChemPhysChem. 2005;6:2597-606.

[151] Kim D, Resasco J, Yu Y, Asiri AM, Yang P. Synergistic geometric and electronic effects for electrochemical reduction of carbon dioxide using gold–copper bimetallic nanoparticles. Nature Communications. 2014;5:4948.

[152] Hvolbæk B, Janssens TVW, Clausen BS, Falsig H, Christensen CH, Nørskov JK. Catalytic activity of Au nanoparticles. Nano Today. 2007;2:14-8.

[153] Yang Z, Wu R, Goodman DW. Structural and electronic properties of Au on${\mathrm{TiO}}_{2}(110)$. Physical Review B. 2000;61:14066-71.

[154] Titantah JT, Karttunen M. Multiphase density functional theory parameterization of the interatomic potential for silver and gold. The European Physical Journal B. 2013;86:288.

[155] Zhao P, Feng X, Huang D, Yang G, Astruc D. Basic concepts and recent advances in nitrophenol reduction by gold- and other transition metal nanoparticles. Coordination Chemistry Reviews. 2015;287:114-36.

[156] Häkkinen H, Abbet S, Sanchez A, Heiz U, Landman U. Structural, Electronic, and Impurity-Doping Effects in Nanoscale Chemistry: Supported Gold Nanoclusters. Angewandte Chemie International Edition. 2003;42:1297-300.

[157] Jaksic JM, Krstajic NV, Vracar LM, Neophytides SG, Labou D, Falaras P, et al. Spillover of primary oxides as a dynamic catalytic effect of interactive hypo-d-oxide supports. Electrochimica Acta. 2007;53:349-61.

[158] Kung MC, Davis RJ, Kung HH. Understanding Au-Catalyzed Low-Temperature CO Oxidation. The Journal of Physical Chemistry C. 2007;111:11767-75.

[159] Gong J, Mullins CB. Surface Science Investigations of Oxidative Chemistry on Gold. Accounts of Chemical Research. 2009;42:1063-73.

[160] Haruta M. Chance and Necessity: My Encounter with Gold Catalysts. Angewandte Chemie International Edition. 2014;53:52-6.

[161] Goudeli E, Pratsinis SE. Crystallinity dynamics of gold nanoparticles during sintering or coalescence. AIChE Journal. 2016;62:589-98.

[162] Guisbiers G, Abudukelimu G, Hourlier D. Size-dependent catalytic and melting properties of platinum-palladium nanoparticles. Nanoscale Res Lett. 2011;6:396.

[163] Cameron D, Holliday R, Thompson D. Gold's future role in fuel cell systems. Journal of Power Sources. 2003;118:298-303.

[164] Corti CW, Holliday RJ, Thompson DT. Commercial aspects of gold catalysis. Applied Catalysis A: General. 2005;291:253-61.

[165] Thompson DT. Using gold nanoparticles for catalysis. Nano Today. 2007;2:40-3.

[166] Bond GC. Gold: a relatively new catalyst. Catalysis Today. 2002;72:5-9.

[167] Bone WA, Wheeler RV. The Combination of Hydrogen and Oxygen in Contact with Hot Surfaces. Philosophical Transactions of the Royal Society of London A: Mathematical, Physical and Engineering Sciences. 1906;206:1-67.

[168] Bond GC, Sermon PA. Gold catalysts for olefin hydrogenation. Gold Bulletin. 1973;6:102-5.

[169] Yockell-Lelièvre H, Lussier F, Masson JF. Influence of the Particle Shape and Density of Self-Assembled Gold Nanoparticle Sensors on LSPR and SERS. The Journal of Physical Chemistry C. 2015;119:28577-85.

[170] Sardar R, Funston AM, Mulvaney P, Murray RW. Gold Nanoparticles: Past, Present, and Future. Langmuir. 2009;25:13840-51.

[171] Chandra P, Singh J, Singh A, Srivastava A, Goyal RN, Shim YB. Gold Nanoparticles and Nanocomposites in Clinical Diagnostics Using Electrochemical Methods. Journal of Nanoparticles. 2013;2013:12.

[172] Yamada M, Foote M, Prow TW. Therapeutic gold, silver, and platinum nanoparticles. Wiley Interdisciplinary Reviews: Nanomedicine and Nanobiotechnology. 2015;7:428-45.

[173] Siegel J, Kvítek Oe, Kolská Zk, Slepička P, Švorčík Vc. Gold Nanostructures Prepared on Solid Surface In: (Ed.) DYP, editor. Metallurgy - Advances in Materials and Processes2012.

[174] Rice CA, Wieckowski A. Electrocatalysis of Formic Acid Oxidation. In: Shao M, editor. Electrocatalysis in Fuel Cells: A Non- and Low- Platinum Approach. London: Springer London; 2013. p. 43-67.

[175] Lopez N, Nørskov JK. Catalytic CO Oxidation by a Gold Nanoparticle: A Density Functional Study. Journal of the American Chemical Society. 2002;124:11262-3.

[176] Liu Z-P, Hu P, Alavi A. Catalytic Role of Gold in Gold-Based Catalysts: A Density Functional Theory Study on the CO Oxidation on Gold. Journal of the American Chemical Society. 2002;124:14770-9.

[177] Goubet N, Tempra I, Yang J, Soavi G, Polli D, Cerullo G, et al. Size and nanocrystallinity controlled gold nanocrystals: synthesis, electronic and mechanical properties. Nanoscale. 2015;7:3237-46.

[178] Gramage-Doria R, Reek JNH. New Endeavors in Gold Catalysis—Size Matters. Angewandte Chemie International Edition. 2013;52:13146-8.

[179] Zhang GR, Zhao D, Feng YY, Zhang B, Su DS, Liu G, et al. Catalytic Pt-on-Au nanostructures: Why Pt becomes more active on smaller Au particles. ACS Nano. 2012;6:2226-36.

[180] Zhou X, Xu W, Liu G, Panda D, Chen P. Size-dependent catalytic activity and dynamics of gold nanoparticles at the single-molecule level. Journal of the American Chemical Society. 2010;132:138-46.

[181] Van Bokhoven JA. Catalysis by gold: Why size matters. Chimia. 2009;63:257-60.

[182] Yao Q, Wang C, Wang H, Yan H, Lu J. Revisiting the Au Particle Size Effect on TiO2-Coated Au/TiO2 Catalysts in CO Oxidation Reaction. The Journal of Physical Chemistry C. 2016;120:9174-83.

[183] Bond GC. Chemisorption and Reactions of Small Molecules on Small Gold Particles. Molecules. 2012;17:1716.

[184] Sun X, Li D, Guo S, Zhu W, Sun S. Controlling core/shell Au/FePt nanoparticle electrocatalysis via changing the core size and shell thickness. Nanoscale. 2016;8:2626-31.

[185] Chen T-Y, Liu Y-T, Wang JH, Lee G-W, Yang P-W, Wang K-W. Size Effect of Atomic Gold Clusters for Carbon Monoxide Passivation at Rucore–Ptshell Nanocatalysts. The Journal of Physical Chemistry C. 2016;120:7621-8.

[186] Duan D, Liang J, Liu H, You X, Wei H, Wei G, et al. The effective carbon supported core–shell structure of Ni@Au catalysts for electro-oxidation of borohydride. International Journal of Hydrogen Energy. 2015;40:488-500.

[187] Rue AE, Collinson MM. Size and Shape Control of Gold Nanodeposits in an Array of Silica Nanowells on a Gold Electrode. International Journal of Electrochemistry. 2012;2012:1-9.

[188] Huang R, Shao G, Wen Y, Sun S-G. Tunable thermodynamic stability of Au-CuPt core-shell trimetallic nanoparticles by controlling alloy composition: Insights from atomistic simulations. Physical Chemistry Chemical Physics. 2014.

[189] Campbell CT. The Active Site in Nanoparticle Gold Catalysis. Science. 2004;306:234-5.

[190] Toshima N, Yonezawa T. Bimetallic nanoparticles-novel materials for chemical and physical applications. New Journal of Chemistry. 1998;22:1179-201.

[191] Alshammari A, Kalevaru V, Martin A. Bimetallic Catalysts Containing Gold and Palladium for Environmentally Important Reactions. Catalysts. 2016;6:97.

[192] Prati L, Villa A. The Art of Manufacturing Gold Catalysts. Catalysts. 2011;2:24-37.

[193] Haber J, Block JH, Delmon B. Manual of methods and procedures for catalyst characterization. Pure and Applied Chemistry. 1995;67:1257-306.

[194] !!! INVALID CITATION !!!

[195] Harada M, Asakura K, Toshima N. Catalytic activity and structural analysis of polymer-protected gold/palladium bimetallic clusters prepared by the successive reduction of hydrogen tetrachloroaurate(III) and palladium dichloride. The Journal of Physical Chemistry. 1993;97:5103-14.

[196] Toshima N, Harada M, Yonezawa T, Kushihashi K, Asakura K. Structural analysis of polymer-protected palladium/platinum bimetallic clusters as dispersed catalysts by using extended x-ray absorption fine structure spectroscopy. The Journal of Physical Chemistry. 1991;95:7448-53.

[197] Toshima N, Ito R, Matsushita T, Shiraishi Y. Trimetallic nanoparticles having a Au-core structure. Catalysis Today. 2007;122:239-44.

[198] Toshima N, Kushihashi K, Yonezawa T, Hirai H. Colloidal Dispersions of Palladium–Platinum Bimetallic Clusters Protected by Polymers. Preparation and Application to Catalysis. Chemistry Letters. 1989;18:1769-72.

[199] Toshima N, Yonezawa T, Harada M, Asakura K, Iwasawa Y. The Polymer-Protected Pd-Pt Bimetallic Clusters Having Catalytic Activity for Selective Hydrogenation of Diene. Preparation and EXAFS Investigation on the Structure. Chemistry Letters. 1990;19:815-8.

[200] Toshima N, Yonezawa T, Kushihashi K. Polymer-protected palladium-platinum bimetallic clusters: preparation, catalytic properties and structural considerations. Journal of the Chemical Society, Faraday Transactions. 1993;89:2537-43.

[201] Zhang H, Lu L, Kawashima K, Okumura M, Haruta M, Toshima N. Synthesis and Catalytic Activity of Crown Jewel-Structured (IrPd)/Au Trimetallic Nanoclusters. Advanced Materials. 2015;27:1383-8.

[202] Zhang H, Okuni J, Toshima N. One-pot synthesis of Ag–Au bimetallic nanoparticles with Au shell and their high catalytic activity for aerobic glucose oxidation. Journal of Colloid and Interface Science. 2011;354:131-8.

[203] Pina, F F, M R. Gold catalysis in organic synthesis and material science. Catalysis. 2010;22:279–317.

[204] Behera M, Ram S. Synthesis and characterization of core–shell gold nanoparticles with poly(vinyl pyrrolidone) from a new precursor salt. Appl Nanosci. 2013;3:83-7.

[205] Westsson E, Koper G. How to Determine the Core-Shell Nature in Bimetallic Catalyst Particles? Catalysts. 2014;4:375.

[206] Yadav M, Xu Q. Liquid-phase chemical hydrogen storage materials. Energy & Environmental Science. 2012;5:9698-725.

[207] Wang, Xiao L, Huang B, Ren Z, Tang X, Zhuang L, et al. AuCu intermetallic nanoparticles: surfactant-free synthesis and novel electrochemistry. Journal of Materials Chemistry. 2012;22:15769-74.

[208] Kung MC, Costello CK, Kung HH. CO oxidation over supported Au catalysts. In: Spivey JJ, Roberts GW, editors. Catalysis: Volume 17: The Royal Society of Chemistry; 2004. p. 152-65.

[209] Liu X, Wang D, Li Y. Synthesis and catalytic properties of bimetallic nanomaterials with various architectures. Nano Today. 2012;7:448-66.

[210] Ghosh Chaudhuri R, Paria S. Core/Shell Nanoparticles: Classes, Properties, Synthesis Mechanisms, Characterization, and Applications. Chemical Reviews. 2011;112:2373-433.

[211] Jin M, Zhang H, Wang J, Zhong X, Lu N, Li Z, et al. Copper Can Still Be Epitaxially Deposited on Palladium Nanocrystals To Generate Core–Shell Nanocubes Despite Their Large Lattice Mismatch. ACS Nano. 2012;6:2566-73.

[212] Long NV, Hien TD, Asaka T, Ohtaki M, Nogami M. Synthesis and characterization of Pt–Pd nanoparticles with core-shell morphology: Nucleation and overgrowth of the Pd shells on the as-prepared and defined Pt seeds. Journal of Alloys and Compounds. 2011;509:7702-9.

[213] Wong MS, Alvarez PJJ, Fang Y-l, Akçin N, Nutt MO, Miller JT, et al. Cleaner water using bimetallic nanoparticle catalysts. Journal of Chemical Technology & Biotechnology. 2009;84:158-66.

[214] Lin J-H, Guliants VV. Alumina-supported Cu@Ni and Ni@Cu core–shell nanoparticles: Synthesis, characterization, and catalytic activity in water–gas-shift reaction. Applied Catalysis A: General. 2012;445–446:187-94.

[215] Bauer JC, Mullins D, Li M, Wu Z, Payzant EA, Overbury SH, et al. Synthesis of silica supported AuCu nanoparticle catalysts and the effects of pretreatment conditions for the CO oxidation reaction. Phys Chem Chem Phys. 2011;13:2571-81.

[216] Liu X, Wang A, Zhang T, Su D-S, Mou C-Y. Au–Cu alloy nanoparticles supported on silica gel as catalyst for CO oxidation: Effects of Au/Cu ratios. Catalysis Today. 2011;160:103-8.

[217] Hsu C, Wei M, Wei Z, Liu F. Improving the catalytic activity of Au/Pd core-shell nanoparticles with a tailored Pd structure for formic acid oxidation reaction. RSC Advances. 2016;6:24645-50.

[218] Mao H, Huang T, Yu A. Surface noble metal modified PdM/C (M = Ru, Pt, Au) as anode catalysts for direct ethanol fuel cells. Journal of Alloys and Compounds. 2016;676:390-6.

[219] Villa A, Wang D, Su DS, Prati L. New challenges in gold catalysis: bimetallic systems. Catalysis Science & Technology. 2015;5:55-68.

[220] Jahangiri H, Bennett J, Mahjoubi P, Wilson K, Gu S. A review of advanced catalyst development for Fischer-Tropsch synthesis of hydrocarbons from biomass derived syn-gas. Catalysis Science & Technology. 2014;4:2210-29.

[221] Han J, Zhou Z, Yin Y, Luo X, Li J, Zhang H, et al. One-pot, seedless synthesis of flowerlike Au-Pd bimetallic nanoparticles with core-shell-like structure via sodium citrate coreduction of metal ions. CrystEngComm. 2012;14:7036-42.

[222] Yi L, Song Y, Liu X, Wang X, Zou G, He P, et al. High activity of Au-Cu/C electrocatalyst as anodic catalyst for direct borohydride-hydrogen peroxide fuel cell. International Journal of Hydrogen Energy. 2011;36:15775-82.

[223] Tan KS, Cheong KY. Advances of Ag, Cu, and Ag-Cu alloy nanoparticles synthesized via chemical reduction route. Journal of Nanoparticle Research. 2013;15.

[224] Pojanavaraphan C, Luengnaruemitchai A, Gulari E. Effect of catalyst preparation on Au/Ce1−xZrxO2 and Au–Cu/Ce1−xZrxO2 for steam reforming of methanol. International Journal of Hydrogen Energy. 2013;38:1348-62.

[225] Liao X, Chu W, Dai X, Pitchon V. Bimetallic Au–Cu supported on ceria for PROX reaction: Effects of Cu/Au atomic ratios and thermal pretreatments. Applied Catalysis B: Environmental. 2013;142–143:25-37.

[226] Hussain A. Beneficial Effect of Cu on a Cu-Modified Au Catalytic Surface for CO Oxidation Reaction: A DFT Study. The Journal of Physical Chemistry C. 2013;117:5084-94.

[227] Yin J, Shan S, Yang L, Mott D, Malis O, Petkov V, et al. Gold–Copper Nanoparticles: Nanostructural Evolution and Bifunctional Catalytic Sites. Chemistry of Materials. 2012;24:4662-74.

[228] Hsu C, Huang C, Hao Y, Liu F. Synthesis of highly active and stable Au-PtCu core-shell nanoparticles for oxygen reduction reaction. Physical Chemistry Chemical Physics. 2012;14:14696-701.

[229] Wang L, Zhai J-J, Jiang K, Wang J-Q, Cai W-B. Pd–Cu/C electrocatalysts synthesized by one-pot polyol reduction toward formic acid oxidation: Structural characterization and electrocatalytic performance. International Journal of Hydrogen Energy. 2015;40:1726-34.

[230] Landi G, Di Benedetto A, Colussi S, Barbato PS, Lisi L. Effect of carbon dioxide and water on the performances of an iron-promoted copper/ceria catalyst for CO preferential oxidation in H2-rich streams. International Journal of Hydrogen Energy. 2016;41:7332-41.

[231] Lee D-S, Chen Y-W. Au/CuO–CeO2 catalyst for preferential oxidation of CO in hydrogen-rich stream: Effect of CuO content. International Journal of Hydrogen Energy. 2016;41:3605-12.

[232] Zhu W, Tang K, Li J, Liu W, Niu X, Zhao G, et al. The effect of copper species in copper-ceria catalysts: structure evolution and enhanced performance in CO oxidation. RSC Advances. 2016;6:46966-71.

[233] Cwele T, Mahadevaiah N, Singh S, Friedrich HB. Effect of Cu additives on the performance of a cobalt substituted ceria (Ce0.90Co0.10O2−δ) catalyst in total and preferential CO oxidation. Applied Catalysis B: Environmental. 2016;182:1-14.

[234] Chagas CA, de Souza EF, Manfro RL, Landi SM, Souza MMVM, Schmal M. Copper as promoter of the NiO–CeO2 catalyst in the preferential CO oxidation. Applied Catalysis B: Environmental. 2016;182:257-65.

[235] Correa PdS, da Silva EL, da Silva RF, Radtke C, Moreno B, Chinarro E, et al. Effect of decreasing platinum amount in Pt–Sn–Ni alloys supported on carbon as electrocatalysts for ethanol electrooxidation. International Journal of Hydrogen Energy. 2012;37:9314-23.

[236] Aranishi K, Jiang H-L, Akita T, Haruta M, Xu Q. One-step synthesis of magnetically recyclable Au/Co/Fe triple-layered core-shell nanoparticles as highly efficient catalysts for the hydrolytic dehydrogenation of ammonia borane. Nano Research. 2011;4:1233-41.
[237] Maniecki TP, Mierczynski P, Maniukiewicz W, Bawolak K, Gebauer D, Jozwiak WK. Bimetallic Au–Cu, Ag–Cu/CrAl3O6 Catalysts for Methanol Synthesis. Catalysis Letters. 2009;130:481-8.
[238] Tsao Y-C, Rej S, Chiu C-Y, Huang MH. Aqueous Phase Synthesis of Au–Ag Core–Shell Nanocrystals with Tunable Shapes and Their Optical and Catalytic Properties. Journal of the American Chemical Society. 2013;136:396-404.
[239] Hsu C, Huang C, Hao Y, Liu F. Au/Pd core-shell nanoparticles with varied hollow Au cores for enhanced formic acid oxidation. Nanoscale Res Lett. 2013;8:1-7.
[240] Wu YN, Liao SJ, Su YL, Zeng JH, Dang D. Enhancement of anodic oxidation of formic acid on palladium decorated Pt/C catalyst. Journal of Power Sources. 2010;195:6459-62.
[241] Evans DH, O'Connell KM, Petersen RA, Kelly MJ. Cyclic voltammetry. Journal of Chemical Education. 1983;60:290.
[242] Noel MaV, K. I. Cyclic Voltammetry and the Frontiers of electrochemistry. New Delhi: Oxford and IBH Publishing Co. PVT ltd; 1990.
[243] Wang J. Analytical Electrochemistry, Second edition. Second ed. New York: Wiley-VCH; 2000.
[244] Lin P-C, Lin S, Wang PC, Sridhar R. Techniques for physicochemical characterization of nanomaterials. Biotechnology advances. 2014;32:711-26.
[245] Callister Jr WD, Rethwisch DG. Materials Science and Engineering

An Introduction. 8th ed. New York: John Wiley & Sons, Inc.; 2010.
[246] Denton AR, Ashcroft NW. Vegard's law. Physical Review A. 1991;43:3161-4.
[247] Perego G. Characterization of heterogeneous catalysts by X-ray diffraction techniques. Catalysis Today. 1998;41:251-9.
[248] Nitze F. Synthesis and characterization of palladium based carbon nanostructure-composites and their clean-energy application. Print & Media Umeå, Sweden: Umeå University, Sweden; 2013.
[249] Egerton RF. Physical Principles of Electron Microscopy. Springer Science+Business Media, Inc. 2005.
[250] Researcher Handbook, Central Microscopy Research Facility. The University of Iowa; 2016.
[251] She H, Chen Y, Chen X, Zhang K, Wang Z, Peng D-L. Structure, optical and magnetic properties of Ni@Au and Au@Ni nanoparticles synthesized via non-aqueous approaches. Journal of Materials Chemistry. 2012;22:2757-65.
[252] Bogner A, Jouneau PH, Thollet G, Basset D, Gauthier C. A history of scanning electron microscopy developments: Towards "wet-STEM" imaging. Micron. 2007;38:390-401.
[253] Gogate MR. Recent research advances and critical assessment of methods to determine the particle size in supported metals. Applied Catalysis A: General. 2016;514:203-13.
[254] Liu, Wu J, Chen K, Xue D. Microscopy: Science, Technology, Applications and Education. In: Méndez-Vilas AaD, J. , editor. Morphology Study by Using Scanning Electron Microscopy. Spain: FORMATEX; 2010. p. 1781-92.

[255] Scalf J, West P. Part1: Introduction to Nanoparticle Characterization with AFM. Pacific Nanotechnology, Inc.; 2006.

[256] Binnig G, Quate CF, Gerber C. Atomic Force Microscope. Physical Review Letters. 1986;56:930-3.

[257] Martin Y, Williams CC, Wickramasinghe HK. Atomic force microscope–force mapping and profiling on a sub 100 ‐ Å scale. Journal of Applied Physics. 1987;61:4723-9.

[258] Grobelny J, DelRio FW, Pradeep N, Kim D-I, Hackley VA, Cook RF. Size Measurement of Nanoparticles Using Atomic Force Microscopy. National Institute of Standard and Technology U.S Department of Commerce

Nanotechnology Characterization Laboratory, National Cancer Institute-Frederick; 2009.

[259] Baalousha M, Lead JR. Characterization of natural and manufactured nanoparticles by atomic force microscopy: Effect of analysis mode, environment and sample preparation. Colloids and Surfaces A: Physicochemical and Engineering Aspects. 2013;419:238-47.

[260] Jakub Širc, Radka Hobzová, Nina Kostina, Marcela Munzarová, Martina Juklíčková, Miloslav Lhotka, et al. Morphological Characterization of Nanofibers: Methods and Application in Practice. Journal of Nanomaterials. 2012;2012:14.

[261] Choudhary TV, Goodman DW. Catalytically active gold: The role of cluster morphology. Applied Catalysis A: General. 2005;291:32-6.

[262] Haruta M, Tsubota S, Kobayashi T, Kageyama H, Genet MJ, Delmon B. Low-Temperature Oxidation of CO over Gold Supported on TiO2, α-Fe2O3, and Co3O4. Journal of Catalysis. 1993;144:175-92.

[263] Comotti M, Li W-C, Spliethoff B, Schüth F. Support Effect in High Activity Gold Catalysts for CO Oxidation. Journal of the American Chemical Society. 2006;128:917-24.

[264] Zhang L, Lu T, Bao J, Tang Y, Li C. Preparation method of an ultrafine carbon supported Pd catalyst as an anodic catalyst in a direct formic acid fuel cell. Electrochemistry Communications. 2006;8:1625-7.

[265] Amendola SC, Sharp-Goldman SL, Janjua MS, Spencer NC, Kelly MT, Petillo PJ, et al. A safe, portable, hydrogen gas generator using aqueous borohydride solution and Ru catalyst. International Journal of Hydrogen Energy. 2000;25:969-75.

[266] Xiang J, Wu B-L, Chen S-L. Investigation of the mechanism of the electrochemical oxidation of formic acid at a gold electrode in sulfuric acid solution. Journal of Electroanalytical Chemistry. 2001;517:95-100.

[267] Chen CH, Liou WJ, Lin HM, Wu SH, Borodzinski A, Stobinski L, et al. Palladium and palladium gold catalysts supported on MWCNTs for electrooxidation of formic acid. Fuel Cells. 2010;10:227-33.

[268] Castegnaro MV, Gorgeski A, Balke B, Alves MCM, Morais J. Charge transfer effects on the chemical reactivity of PdxCu1-x nanoalloys. Nanoscale. 2016;8:641-7.

[269] Patterson AL. The Scherrer Formula for X-Ray Particle Size Determination. Physical Review. 1939;56:978-82.

[270] Langford JI, Wilson AJC. Scherrer after sixty years: A survey and some new results in the determination of crystallite size. Journal of Applied Crystallography. 1978;11:102-13.

[271] Chantler CT, Rae NA, Tran CQ. Accurate determination and correction of the lattice parameter of LaB6 (standard reference material 660) relative to that of Si (640b). Journal of Applied Crystallography. 2007;40:232-40.

[272] King HW, Payzant EA. Error Corrections For X-RAY Powder Diffractometry. Canadian Metallurgical Quarterly. 2001;40:385-94.

[273] Lee AF, Baddeley CJ, Hardacre C, Ormerod RM, Lambert RM, Schmid G, et al. Structural and Catalytic Properties of Novel Au/Pd Bimetallic Colloid Particles: EXAFS, XRD, and Acetylene Coupling. The Journal of Physical Chemistry. 1995;99:6096-102.

[274] Vidal-Iglesias FJ, Arán-Ais RM, Solla-Gullón J, Herrero E, Feliu JM. Electrochemical Characterization of Shape-Controlled Pt Nanoparticles in Different Supporting Electrolytes. ACS Catalysis. 2012;2:901-10.

[275] Yang S, Shen C, Tian Y, Zhang X, Gao H-J. Synthesis of cubic and spherical Pd nanoparticles on graphene and their electrocatalytic performance in the oxidation of formic acid. Nanoscale. 2014;6:13154-62.

[276] Cho Y-S, Shin CH, Han S. Dispersion Polymerization of Polystyrene Particles Using Alcohol as Reaction Medium. Nanoscale Res Lett. 2016;11:46.

[277] Hong J, Hong CK, Shim SE. Synthesis of polystyrene microspheres by dispersion polymerization using poly(vinyl alcohol) as a steric stabilizer in aqueous alcohol media. Colloids and Surfaces A: Physicochemical and Engineering Aspects. 2007;302:225-33.

[278] Zhong J, Bin D, Ren F, Wang C, Zhai C, Yang P, et al. Graphene nanosheet-supported Pd nano-leaves with highly efficient electrocatalytic performance for formic acid oxidation. Colloids and Surfaces A: Physicochemical and Engineering Aspects. 2016;488:1-6.

[279] Nutt MO, Hughes JB, Wong MS. Designing Pd-on-Au Bimetallic Nanoparticle Catalysts for Trichloroethene Hydrodechlorination. Environmental Science & Technology. 2005;39:1346-53.

[280] Sarage N, Diallo M, Duncan J, Street A, Sustich R. Nanotechnolgy Application for Clean Water. In: J R, editor. Micro and Nano Technologies. New York: William Andrew Inc; 2009.

[281] Al Abass NA, Denuault G, Pletcher D. The unexpected activity of Pd nanoparticles prepared using a non-ionic surfactant template. Physical Chemistry Chemical Physics. 2014;16:4892-9.

[282] Zhang X, Wang X, Le L, Ma A, Lin S. A Pd/PW12/RGO Composite Catalyst Prepared by Electro-Codeposition for Formic Acid Electro-Oxidation. Journal of The Electrochemical Society. 2016;163:F71-F8.

[283] Liang Y, Wu K, Ge C, Zhou Y, Chen Y, Tang Y, et al. Efficient Anchorage of Palladium Nanoparticles on the Multi-Walled Carbon Nanotubes as Electrocatalyst for the Hydrazine Electrooxidation in Strong Acidic Solutions. Fuel Cells. 2012;12:946-55.

[284] Cao, Chen D, Caruso RA. Surface-Metastable Phase-Initiated Seeding and Ostwald Ripening: A Facile Fluorine-Free Process towards Spherical Fluffy Core/Shell, Yolk/Shell, and Hollow Anatase Nanostructures. Angewandte Chemie International Edition. 2013;52:10986-91.

[285] Thi My Dung D, Thi Thu Tuyet L, Eric F-B, Mau Chien D. The influence of solvents and surfactants on the preparation of copper nanoparticles by a chemical reduction method. Advances in Natural Sciences: Nanoscience and Nanotechnology. 2011;2:025004.

[286] Yan Y, Chen K-b, Li H-r, Hong W, Hu X-b, Xu Z. Capping effect of reducing agents and surfactants in synthesizing silver nanoplates. Transactions of Nonferrous Metals Society of China. 2014;24:3732-8.

[287] García-Aguilar J, Navlani-García M, Berenguer-Murcia Á, Mori K, Kuwahara Y, Yamashita H, et al. Evolution of the PVP–Pd Surface Interaction in Nanoparticles through the Case Study of Formic Acid Decomposition. Langmuir. 2016;32:12110-8.

[288] Shahgaldi S, Hamelin J. Improved carbon nanostructures as a novel catalyst support in the cathode side of PEMFC: a critical review. Carbon. 2015;94:705-28.

[289] Navaladian S, Viswanathan B, Varadarajan T, Viswanath R. A Rapid Synthesis of Oriented Palladium Nanoparticles by UV Irradiation. Nanoscale Res Lett. 2008;4:181.

[290] Kumar M, Kumar A, Abhyankar AC. Influence of Texture Coefficient on Surface Morphology and Sensing Properties of W-Doped Nanocrystalline Tin Oxide Thin Films. ACS Applied Materials & Interfaces. 2015;7:3571-80.

[291] Bhowmik T, Kundu MK, Barman S. Highly active and durable Pd nanoparticles-porous graphitic carbon nitride composite for electrocatalytic oxygen reduction reaction. International Journal of Hydrogen Energy. 2016;41:14768-77.

[292] McCue I, Snyder J, Li X, Chen Q, Sieradzki K, Erlebacher J. Apparent Inverse Gibbs-Thomson Effect in Dealloyed Nanoporous Nanoparticles. Physical Review Letters. 2012;108:225503.

[293] Casella IG. Electrocatalytic oxidation of oxalic acid on palladium-based modified glassy carbon electrode in acidic medium. Electrochimica Acta. 1999;44:3353-60.

[294] Bligaard T, N√∏rskov JK, Dahl S, Matthiesen J, Christensen CH, Sehested J. The Br√∏nsted‚ÄìEvans‚ÄìPolanyi relation and the volcano curve in heterogeneous catalysis. Journal of Catalysis. 2004;224:206-17.

[295] Pedireddy S, Lee HK, Tjiu WW, Phang IY, Tan HR, Chua SQ, et al. One-step synthesis of zero-dimensional hollow nanoporous gold nanoparticles with enhanced methanol electrooxidation performance. Nature Communications. 2014;5:4947.

[296] Chen W, Tang Y, Bao J, Gao Y, Liu C, Xing W, et al. Study of carbon-supported Au catalyst as the cathodic catalyst in a direct formic acid fuel cell prepared using a polyvinyl alcohol protection method. Journal of Power Sources. 2007;167:315-8.

[297] Silva JCM, da Silva SG, De Souza RFB, Buzzo GS, Spinacé EV, Neto AO, et al. PtAu/C electrocatalysts as anodes for direct ammonia fuel cell. Applied Catalysis A: General. 2015;490:133-8.

[298] Tian M, Pell WG, Conway BE. Nanogravimetry study of the initial stages of anodic surface oxide film growth at Au in aqueous HClO4 and H2SO4 by means of EQCN. Electrochimica Acta. 2003;48:2675-89.

[299] Burke LD, Lee BH. An investigation of the electrocatalytic behaviour of gold in aqueous media. Journal of Electroanalytical Chemistry. 1992;330:637-61.

[300] Conway BE. Electrochemical oxide film formation at noble metals as a surface-chemical process. Progress in Surface Science. 1995;49:331-452.

[301] Angerstein-Kozlowska H, Conway BE, Hamelin A, Stoicoviciu L. Elementary steps of electrochemical oxidation of single-crystal planes of Au—I. Chemical basis of processes involving geometry of anions and the electrode surfaces. Electrochimica Acta. 1986;31:1051-61.

[302] Angerstein-Kozlowska H, Conway BE, Hamelin A, Stoicoviciu L. Elementary steps of electrochemical oxidation of single-crystal planes of Au Part II. A chemical and structural basis of oxidation of the (111) plane. Journal of Electroanalytical Chemistry and Interfacial Electrochemistry. 1987;228:429-53.

[303] Hezard T, Fajerwerg K, Evrard D, Colliere V, Behra P, Gros P. Gold nanoparticles electrodeposited on glassy carbon using cyclic voltammetry: Application to Hg(II) trace analysis. Journal of Electroanalytical Chemistry. 2012;664:46-52.

[304] O'Mullane AP, Ippolito SJ, Sabri YM, Bansal V, Bhargava SK. Premonolayer Oxidation of Nanostructured Gold: An Important Factor Influencing Electrocatalytic Activity. Langmuir. 2009;25:3845-52.

[305] Cherevko S, Topalov AA, Zeradjanin AR, Katsounaros I, Mayrhofer KJJ. Gold dissolution: towards understanding of noble metal corrosion. RSC Advances. 2013;3:16516-27.

[306] Rhieu SY, Reipa V. Tuning the Size of Gold Nanoparticles with Repetitive Oxidation-reduction Cycles. American Journal of Nanomaterials. 2015;3:15-21.

[307] Cadle SH, Bruckenstein S. Ring-disk electrode study of the anodic behavior of gold in 0.2M sulfuric acid. Analytical Chemistry. 1974;46:16-20.

[308] Shastri AG, Schwank J. Metal dispersion of bimetallic catalysts via stepwise chemisorption and surface titration: I. Ru □ AuSiO2. Journal of Catalysis. 1985;95:271-83.

[309] Tremiliosi-Filho G, Gonzalez ER, Motheo AJ, Belgsir EM, Léger JM, Lamy C. Electro-oxidation of ethanol on gold: analysis of the reaction products and mechanism. Journal of Electroanalytical Chemistry. 1998;444:31-9.

[310] Xu JB, Zhao TS, Liang ZX. Carbon supported platinum–gold alloy catalyst for direct formic acid fuel cells. Journal of Power Sources. 2008;185:857-61.

[311] Hong JW, Kim D, Lee YW, Kim M, Kang SW, Han SW. Atomic-Distribution-Dependent Electrocatalytic Activity of Au–Pd Bimetallic Nanocrystals. Angewandte Chemie International Edition. 2011;50:8876-80.

[312] Han D-D, Li S-S, Guo Z, Chen X, Liu J-H, Huang X-J. Shape dependent stripping behavior of Au nanoparticles toward arsenic detection: evidence of enhanced sensitivity on the Au (111) facet. RSC Advances. 2016;6:30337-44.

[313] Inasaki T, Kobayashi S. Particle size effects of gold on the kinetics of the oxygen reduction at chemically prepared Au/C catalysts. Electrochimica Acta. 2009;54:4893-7.

[314] Yan S, Gao L, Zhang S, Zhang W, Li Y, Gao L. Synthesis of Au/C catalyst with high electrooxidation activity. Electrochimica Acta. 2013;94:159-64.

[315] Kang HJ, Patra S, Das J, Aziz A, Jo J, Yang H. Effect of aging on the electrocatalytic activity of gold nanoparticles. Electrochemistry Communications. 2010;12:1245-8.

[316] Antolini E, Gonzalez ER. Effect of synthesis method and structural characteristics of Pt–Sn fuel cell catalysts on the electro-oxidation of CH3OH and CH3CH2OH in acid medium. Catalysis Today. 2011;160:28-38.

[317] Chen CH, Liou WJ, Lin HM, Wu SH, Mikolajczuk A, Stobinski L, et al. Carbon nanotube-supported bimetallic palladium-gold electrocatalysts for electro-oxidation of formic acid. Physica Status Solidi (A) Applications and Materials Science. 2010;207:1160-5.

[318] Liu Z, Zhang X, Tay SW. Nanostructured PdRu/C catalysts for formic acid oxidation. Journal of Solid State Electrochemistry. 2012;16:545-50.

[319] Hu S, Scudiero L, Ha S. Electronic effect on oxidation of formic acid on supported Pd-Cu bimetallic surface. Electrochimica Acta. 2012;83:354-8.

[320] Le CH, Nguyen OTT, Nguyen HS, Pham LD, Hoang CV. Controllable synthesis and visible-active photocatalytic properties of Au nanoparticles decorated urchin-like ZnO nanostructures. Current Applied Physics. 2017;17:1506-12.

[321] Diculescu VC, Chiorcea-Paquim A-M, Corduneanu O, Oliveira-Brett AM. Palladium nanoparticles and nanowires deposited electrochemically: AFM and electrochemical characterization. Journal of Solid State Electrochemistry. 2007;11:887-98.

[322] Ju W, Valiollahi R, Ojani R, Schneider O, Stimming U. The Electrooxidation of Formic Acid on Pd Nanoparticles: an Investigation of Size-Dependent Performance. Electrocatalysis. 2015;7:149-58.

[323] Strasser P, Koh S, Anniyev T, Greeley J, More K, Yu C, et al. Lattice-strain control of the activity in dealloyed core–shell fuel cell catalysts. Nat Chem. 2010;2:454-60.

[324] Mayrhofer KJJ, Blizanac BB, Arenz M, Stamenkovic VR, Ross PN, Markovic NM. The Impact of Geometric and Surface Electronic Properties of Pt-Catalysts on the Particle Size Effect in Electrocatalysis. The Journal of Physical Chemistry B. 2005;109:14433-40.

[325] Melanie K, Xudong W, Zhong Lin W, Robert LS. Solid Au nanoparticles as a catalyst for growing aligned ZnO nanowires: a new understanding of the vapour–liquid–solid process. Nanotechnology. 2007;18:365304.

[326] Maye MM, Kariuki NN, Luo J, Han L, Njoki P, Wang L, et al. Electrocatalytic reduction of oxygen: Gold and gold-platinum nanoparticle catalysts prepared by two-phase protocol. Gold Bulletin. 2004;37:217-23.

[327] Soriano E, Marco-Contelles J. Structure, Bonding, and Reactivity of Reactant Complexes and Key Intermediates. In: Soriano E, Marco-Contelles J, editors. Computational Mechanisms of Au and Pt Catalyzed Reactions. Berlin, Heidelberg: Springer Berlin Heidelberg; 2011. p. 1-29.

[328] Wang, Sun S, Huang Z, Zhang H, Zhang S. Preparation and catalytic activity of PVP-protected Au/Ni bimetallic nanoparticles for hydrogen generation from hydrolysis of basic NaBH4 solution. International Journal of Hydrogen Energy. 2014;39:905-16.

[329] Wang X, Sø L, Su R, Wendt S, Hald P, Mamakhel A, et al. The influence of crystallite size and crystallinity of anatase nanoparticles on the photo-degradation of phenol. Journal of Catalysis. 2014;310:100-8.

[330] Tang Y, Zhang L, Wang Y, Zhou Y, Gao Y, Liu C, et al. Preparation of a carbon supported Pt catalyst using an improved organic sol method and its electrocatalytic activity for methanol oxidation. Journal of Power Sources. 2006;162:124-31.

[331] Ojeda M, Iglesia E. Formic Acid Dehydrogenation on Au-Based Catalysts at Near-Ambient Temperatures. Angew Chem Int Ed Engl. 2009;121:4894-7.

[332] Cordi EM, Falconer JL. Oxidation of Volatile Organic Compounds on Al2O3, Pd/Al2O3, and PdO/Al2O3Catalysts. Journal of Catalysis. 1996;162:104-17.

[333] Brimaud S, Solla-Gullón J, Weber I, Feliu JM, Behm RJ. Formic Acid Electrooxidation on Noble-Metal Electrodes: Role and Mechanistic Implications of pH, Surface Structure, and Anion Adsorption. ChemElectroChem. 2014;1:1075-83.

[334] Kibler LA, Al-Shakran M. Adsorption of Formate on Au(111) in Acid Solution: Relevance for Electro-Oxidation of Formic Acid. The Journal of Physical Chemistry C. 2016;120:16238-45.

[335] Liotta L. New Trends in Gold Catalysts. Catalysts. 2014;4:299.

APPENDIX A

Calculation of Diffusion Coefficient for Oxidation-Reduction processes

Using Randles-Sevcik equation: $I_p = 2.69E5 * n^{\frac{3}{2}} * D^{0.5} * A * C * \vartheta^{0.5}$

$Slope\ K = 2.69E5 * n^{\frac{3}{2}} * A * C$

$$D = \sqrt{\frac{K}{2.69E5 * n^{\frac{3}{2}} * A * C}}$$

where, n = 2 electron transfer, A = geometric surface area of electrode

C = concentration of electrolyte (0.5 M HCOOH)

K = slope (9.25 x 10^{-4} for oxidation reaction)

Table 1 shows the previous peer-reviewed articles for the estimation of the 20 wt.% Pd compositions for all catalysts in this thesis.

Table 8.1: %wt. Composition for Pd-C catalysts from literature

[a]PdCl$_2$, mL	[b]Molarity, mol./L	[c]PdCl$_2$, g	[d]Mol. wt. Pd, g/mol.	[f]wt. Pd, g	[g]Carbon black, g	[i]%wt. Pd	Ref.
3.13	0.045	0.02498	106.42	0.015	0.06	20	[264]
		0.0375	106.42	0.023	0.09	20	[92]
3	0.045	0.02394	106.42	0.014	0.06	19	[283]
4.2	4	0.0168	106.42	0.010	0.04	20	[81]
		=a*b*mole.wt.PdCl$_2$		=a*b*d		=(f/(g+f))*100	

Prepared Stock solution from anhydrous PdCl₂ powder

PdCl$_2$ (5wt.% in 10 ml HCl) = 1.2505 g

Concentration (mol./l) = Mass, g/(Mol. Wt., g/mole*Volume, l)

$$= 1.2505 \text{ (g)}/(177.33*0.025)$$

=0.28207 mol./l

Palladium catalysts

Volume of PdCl$_2$ (5wt.% in 10 ml HCl, density, 1.06 g ml^{-1}): 0.45 ml solution

Mass of PdCl$_2$ = Density of PdCl$_2$ * weight % (concentration) of PdCl$_2$ * volume of PdCl$_2$

$$= 1.06 \text{ (g ml}^{-1}) * 0.05 \text{ x } 0.45 \text{ (ml)} = 0.02385 \text{ g PdCl}_2$$

Molecular weight of PdCl$_2$ = 177.326 g mol^{-1}

Numbers of mole PdCl$_2$ = (0.02385 g PdCl$_2$)/(177.326 g mol^{-1}) = 0.0001345 mol. PdCl$_2$

Mass of Pd = Numbers of mole PdCl$_2$ * Molecular weight of Pd

$$= 0.0001345 \text{ mol. PdCl}_2 * 106.42 \text{ g mol}^{-1} = 0.0143 \text{ g Pd}$$

Total catalyst weight = carbon black support + mass of Pd = (0.06 + 0.0143) g

$$= 0.0743 \text{ g}$$

Therefore, Maximum Pd metal loading on the catalyst (Pd$_{Max}$ metal loading) = (Mass of Pd)/(Total catalyst weight)

$$\text{Pd}_{Max} \text{ metal loading} = (0.0143 \text{ g Pd})/(0.0743 \text{ g}) = 19.3 \text{ wt.\% Pd}$$

Table 2: wt.% Pd-C catalyst (H₃BO₃+NHF₃) (SYN17)

	Amount of Each Component by Weight						Theoretical estimate	ICP-AES Result
Run#	NH$_4$F (g)	H$_3$BO$_3$ (g)	C (g)	PdCl$_2$ (μL)	H$_2$O (μL)	Pd g	Wt.% Pd	
PdC$_1$	0.0256	0.1263	0.06	472	10000	0.015	20	27.2
PdC$_2$	0.0254	0.1257	0.06	472	10000	0.015	20	23.3
PdC$_3$	0.0250	0.1250	0.06	472	10000	0.015	20	19.1

Table 3: wt.% Pd-C catalyst (PVP) (SYN17)

	Amount of Each Component by Weight						Theoretical estimate	ICP-AES Result
Run#	PVP (g)	C (g)	PdCl$_2$ (µL)	H$_2$O (µL)	NaBH$_4$ (µL)	Pd g	Wt.% Pd	
PdC$_1$	0.1438	0.0602	472	10000	10000	0.015	20	22.3
PdC$_2$	0.1408	0.0595	472	10000	10000	0.015	20	20.5
PdC$_3$	0.1407	0.0601	472	10000	10000	0.015	20	19.7

PdCl$_2$ concentration = 0.299 mol. l^{-1}

Table 4: wt.% Au-C catalyst (SYN17)

	Amount of Each Component by Weight						**Theoretical estimate**	**ICP-AES Result**
Run #	PVP (g)	C (g)	HAuCl$_4$ (µL)	H$_2$O (µL)	NaBH$_4$ (µL)	Au g	Wt.% Au	Wt.% Au
AuC$_1$	0.1411	0.06	1500	10000	10000	0.015	20	14.8
AuC$_2$	0.1407	0.06	1500	10000	10000	0.015	20	17.9
AuC$_3$	0.1402	0.06	1500	10000	10000	0.015	20	8.3

Table 5: wt% AuCu-C catalyst (SYN17)

		Theoretical estimate			**ICP-AES Result**			**Active metal efficiency**	
Run#	C, g	Wt.% Au	Wt.% Cu	Wt.% AuCu	Wt.% Au	Wt.% Cu	Wt.% AuCu	Au	AuCu
C$_1$	0.06	20	5	25	13.0	3.5	16.5	64.9	66.3
C$_2$	0.06	20	5	25	17.5	3.2	20.7	87.4	82.8
C$_3$	0.06	20	5	25	16.0	3.3	19.3	79.9	77.5
Average wt.%					15.5± 1.9	3.3± 0.2	18.8± 1.7	77.4± 9.3	75.6± 6.9

* HAuCl$_4$ (µL) = 1600; CuSO$_4$ (µL) = 1000, H$_2$O (µL) = 10000, NaBH$_4$ (µL) = 10000
*Weight of Au, g = concentration of HAuCl$_4$ * volume of HAuCl$_4$*Mol. wt. Au*
*Weight of Cu, g = concentration of CuSO$_4$ * volume of CuSO$_4$*Mol. wt. Au*
*Theoretical wt.% estimate = [(Weight of Au)/(weight of C + weight of Au + weight of Cu)] *100*
*Theoretical wt.% estimate = [(Weight of Cu)/(weight of C + weight of Au+ weight of Cu)] *100*

Calculations for specific catalyst loading:

Concentration of catalyst paste = Mass of catalyst/Volume (Nafion+ ethanol)

Volume of catalyst paste each electrode = 10 µl

Electrode area = 0.07 cm^{-2}

Mass of catalyst loading = Concentration*Volume of paste

Wt.% catalyst loading = Mass of catalyst loading* wt.% metal loading

Specific catalyst loading (mg cm^{-2}) = wt.% catalyst loading/ Electrode area

Table 6: Electrode catalyst loading (Electrochemical Experiments) SYN16

8.3 Catalyst	Mass of catalyst, mg	Density of paste, g l^{-1}	Mass of catalyst loading, mg	Wt.% catalyst loading (x10^{-5})	Specific catalyst loading, g m^{-2} (*assuming 20wt% metal loading*)	Specific catalyst loading, g m^{-2} (*ICP-AES wt.% metal loading*)
Pd-C$_{1PVP}$	6.04	12.1	0.121	6.52	3.5	9.3
Pd-C$_{2PVP}$	5.94	11.9	0.119	5.23	3.4	7.5
Pd-C$_{1H3BO3+NHF4}$	6.0	12.0	0.120	2.47	3.4	3.5
Pd-C$_{2H3BO3+NHF4}$	6.06	12.1	0.121	2.55	3.5	3.6
AuCu-C1	6.1	12.2	0.122	2.44	3.5	7.8
AuCu-C2	6.1	12.2	0.122	2.44	3.5	9.1
Au-C1	6.7	13.4	0.134	2.68	3.8	17.2
Au-C2	6.4	12.8	0.128	2.56	3.7	16.5
AuNPs-C	8	12.3	0.123	2.46	3.5	

Table 7: Equal electrode catalyst loading (Electrochemical Experiments) based on ICP-AES data for SYN16 samples

Catalyst	Mass of catalyst, mg	Density of paste, g l^{-1}	Mass of catalyst loading, mg	Wt.% catalyst loading (x10^{-5})	Specific catalyst loading, g m^{-2} (*ICP-AES 20wt% metal loading*)
Pd-C$_{1PVP}$	2.28	4.6	0.0456	4.56	3.52
Pd-C$_{2PVP}$	5.94	5.6	0.056	5.6	3.52
Pd-C$_{1H3BO3+NHF4}$	6.0	12.0	0.120	2.47	3.53
Pd-C$_{2H3BO3+NHF4}$	5.9	11.8	0.118	2.55	3.54
AuCu-C1	2.75	5.5	0.055	2.48	3.54
AuCu-C2	2.38	4.8	0.0476	2.48	3.54
Au-C1	1.375	2.8	0.0275	2.48	3.54
Au-C2	1.375	2.8	0.0275	2.48	3.54
AuNPs-C	8	12.3	0.123	2.46	3.52

Table 8: Fixed active metal loading based on ICP-AES data analysis

Catalyst	Mass of catalyst, (mg)	Wt.% active metal ICP-AES	Active metal weight (mg)	Vulcan XC72 carbon weight (mg)	Nafion bender (mg)	Specific Active metal loading (mg cm^{-2})
Pd-C$_{3PVP}$	6.25	19.7	1.23	5.02	11.6	0.35
Pd-C$_{3H3BO3+NH4F}$	6.42	19.1	1.23	5.19	11.6	0.35
AuCu-C$_3$	6.9	17.5	1.23	5.66	11.6	0.35
Au-C$_2$		17.9	1.23	5.60	11.6	0.35

Compositional Analysis

Table 9: Compositional analysis for the Pd-C, Au-C and AuCu-C catalysts

Sample #	Theoretical estimate wt.%			AAS wt.%			ICP-MS/ICP-AES wt.%		
SYN2013									
Pd-C$_{1H3BO3 + NH4F}$	16.3						1.9		
Pd-C$_{2H3BO3 + NH4F}$	9.1						1.2		
Pd-C$_{5H3BO3 + NH4F}$	13.1						1.4		
Pd-C$_{6H3BO3 + NH4F}$	16.8						1.9		
Pd-C$_{7H3BO3 + NH4F}$	20.0						2.4		
Pd-C$_{10H3BO3 + NH4F}$	20.0						2.3		
SYN2014									
	Au	Cu	AuCu	Au	Cu	AuCu	Au	Cu	AuCu
AuCu-C$_{1PVP}$	7.3	9.1	16.4	1.0	1.9	2.8	3.1	2.1	5.2
AuCu-C$_{2PVP}$	7.3	9.1	16.4	1.7	2.8	4.5	5.0	7.9	12.9
AuCu-C$_{3PVP}$	7.3	9.1	16.4	2.5	0.1	2.6	6.0	3.7	9.7
AuCu-C$_{4PVP}$	7.3	9.1	16.4	1.3	1.2	2.4	8.2	5.0	13.2
AuCu-C$_{5PVP}$	7.3	9.1	16.4	1.6	2.0	3.6	5.0	3.8	9.3
AuCu-C$_{6PVP}$	7.3	9.1	16.4	1.2	1.0	2.2	5.5	3.1	8.1
AuCu-C$_{7PVP}$	7.3	9.1	16.4	2.5	2.2	4.6	8.2	5.7	13.9
AuCu-C$_{8PVP}$	7.3	9.1	16.4	1.6	0.8	2.4	7.0	3.7	10.7
AuCu-C$_{9PVP}$	7.3	9.1	16.4	2.1	1.1	3.3	7.6	5.5	13.1
AuCu-C$_{10PVP}$	7.3	9.1	16.4	2.2	1.2	3.4	4.5	3.1	7.6
SYN2016	Au	Cu	AuCu				Au	Cu	AuCu
AuCu-C$_{1PVP}$	44.8	11.8	56.6				45	10.7	55.7
AuCu-C$_{2PVP}$	45.2	11.8	57.0				52.2	6.5	58.7
Au-C$_{1PVP}$	92						87.6		
Au-C$_{2PVP}$	92						89.2		
Pd-C$_{1PVP}$	19.2						54		
Pd-C$_{2PVP}$	19.4						43.5		
Pd-C$_{1H3BO3 + NH4F}$	18.4						20.6		
Pd-C$_{2H3BO3 + NH4F}$	18.2						21		
SYN2017	Au	Cu	AuCu				Au	Cu	AuCu
AuCu-C$_{1PVP}$	20	4.9	24.9				13.0	3.5	16.5
AuCu-C$_{2PVP}$	20	4.9	24.9				17.5	3.2	20.7
AuCu-C$_{3PVP}$	20	4.9	24.9				16.0	3.3	19.3
Mean							15.5±1.9	3.3±0.2	18.8±1.7
Au-C$_{1PVP}$	20						14.8		
Au-C$_{2PVP}$	20						17.9		
Au-C$_{3PVP}$	20						8.3*		
Mean							**13.7±4.0**		
AuNPs-C	20						-		
Pd-C$_{1PVP}$	20						22.3		
Pd-C$_{2PVP}$	20						20.5		
Pd-C$_{3PVP}$	20						19.7		
Mean							**20.8±1.1**		
Pd-C$_{1H3BO3 + NH4F}$	20						27.2		
Pd-C$_{2H3BO3 + NH4F}$	20						23.3		

Pd-C$_{3H3BO3 + NH4F}$	20						19.1	
Mean							**23.2±3.3**	

Table 9 shows the chronological development of the synthesis procedure for various catalysts. The table shows the progression from very low metal content to higher metal loading on the catalysts.

XRD Calculations for the different catalysts

Table 10: Summary of the average Pd-C$_{PVP}$ (PdC17) catalysts with deviation for Pd [Card 46-1043]

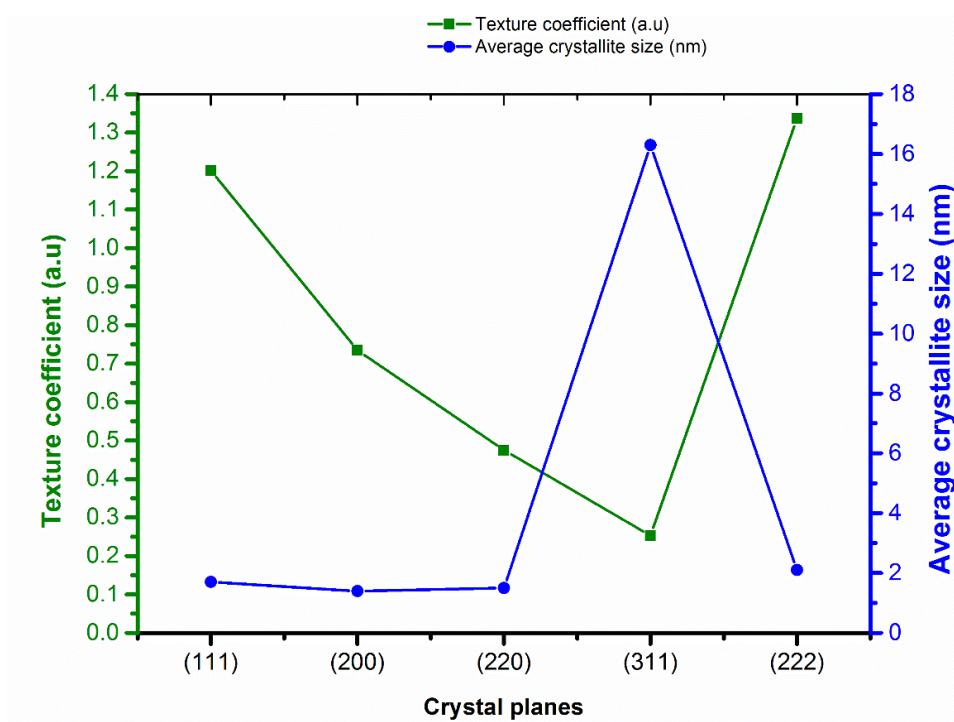|								
111	**39.75**	**0.92**	**2.266**	**0.90**	**3.204**	**0.88**	**1.133**	**0.89**
200	45.48	2.56	1.993	2.43	3.986	2.44	1.409	2.44
220	67.67	0.66	1.384	0.63	3.914	0.62	1.384	0.65
311	80.93	1.44	1.187	1.19	3.937	1.20	1.392	1.23

Figure 1: Average crystallite size and texture coefficient of Pd-C$_{PVP\ (43.5\ wt.\%)}$ catalysts particles from XRD powder pattern

222

Table 11: Summary of the average Pd-C$_{H3BO3 +NH4F}$ (PdC17) catalysts with deviation for Pd [Card 46-1043]

Miller Indices	Peak Position, in 2θ (Degree)	% Difference (2θ)	Peak Position in d (Å)	% Difference (d)	Lattice parameters, a (Å)	% Difference (a)	Atomic radius, R (Å)	% Difference (R)
111	39.84	0.70	2.266	0.90	3.205	0.91	1.133	0.89
200	46.10	1.21	1.967	1.12	3.935	1.15	1.391	1.16
220	67.35	1.14	1.389	0.99	3.930	1.02	1.389	1.01
311	81.21	1.09	1.184	0.94	3.926	0.92	1.388	0.94

Table 12: Summary of the average Au-C$_{PVP}$ catalysts with deviation for Au [PDF Card 4-0784]

Miller Indices	Peak Position, in 2θ (Degree)	% Difference (2θ)	Peak Position in d (Å)	% Difference (d)	Lattice parameters, a (Å)	% Difference (a)	Atomic radius, R (Å)	% Difference (R)
111	38.23	0.12	2.352	0.13	3.327	0.12	1.176	0.15
200	44.38	0.03	2.040	0.05	4.080	0.05	1.442	0.03
220	64.65	0.11	1.441	0.07	4.075	0.10	1.441	0.09
311	77.63	0.11	1.229	0.08	4.076	0.10	1.441	0.06
222	81.55	0.21	1.180	0.22	3.910	0.13	1.382	0.10

Table 13: Summary of the average AuCu-C$_{PVP}$ catalysts with deviation for Au [PDF Card 4-0784]

Miller Indices	Peak Position, in 2θ (Degree)	% Difference (2θ)	Peak Position in d (Å)	% Difference (d)	Lattice parameters, a (Å)	% Difference (a)	Atomic radius, R (Å)	% Difference (R)
111	38.38	0.51	2.344	0.47	3.314	0.51	1.172	0.54
200	44.28	0.25	2.044	0.24	4.088	0.24	1.445	0.23
220	64.7	0.19	1.44	0.14	4.072	0.17	1.440	0.16
311	77.91	0.47	1.226	0.33	4.064	0.39	1.437	0.36

Table 14: Summary of the average AuNPs-C$_{commercial}$ catalysts with deviation for Au [PDF Card 4-0784]

Miller Indices	Peak Position, in 2θ (Degree)	% Difference (2θ)	Peak Position in d (Å)	% Difference (d)	Lattice parameters, a (Å)	% Difference (a)	Atomic radius, R (Å)	% Difference (R)
111	37.81	0.98	2.377	0.93	3.362	0.93	1.189	0.93
200	44.56	0.38	2.032	0.34	4.063	0.37	1.437	0.35

APPENDIX B

Journal publication

C.I. Oseghale, A. H. Abdalla, J. O. G. Posada and P.J. Hall**. *A new synthesis route for sustainable gold copper utilization in direct formic acid fuel cells,* International Journal of Hydrogen Energy, **41** (37): 16394-16401, 2016

Conferences

1. 252nd American Chemical Society National Meeting & Exposition, 21-25 August 2016, Philadelphia, PA, USA
   Title: High performance gold based catalysts and their application as a low cost fuel cell catalyst

2. European Congress and Exhibition on Advanced Materials and Processes, 20-24 September 2015, Warsaw, Poland
   Title: Synthesis and activity of gold copper core-shell catalysts for direct formic acid fuel cells

3. 8th International Conference on Sustainable Energy & Environment Protection, 11-14 August 2015, Paisley, Scotland
   Title: A new synthesis route for sustainable gold copper utilization in direct formic acid fuel cells

4. Fuel Cells 2014 Science & Technology A grove Fuel Cell Event, 3-4 April 2014, Amsterdam, The Netherlands
   Title: Pd-C catalyst as anodic catalyst in direct formic acid fuel cell

5. Electrochem. 2014: Electrochemical Horizon, Loughborough University, 7-9 September, 2014, Loughborough, UK
   Title: Synthesis and activity of AuCu-C core-shell catalysts for direct formic acid fuel cell applications

Departmental seminars/ presentations

CBE PGR Conference, June 18th 2016. *Title: Gold based catalysts and their application as a low cost fuel cell catalyst*